



HAL
open science

Ultrafast electronic, acoustic and thermal properties of metal nanoparticles and clusters

Tatjana Stoll

► **To cite this version:**

Tatjana Stoll. Ultrafast electronic, acoustic and thermal properties of metal nanoparticles and clusters. Other [cond-mat.other]. Université Claude Bernard - Lyon I, 2014. English. NNT : 2014LYO10332 . tel-01128276

HAL Id: tel-01128276

<https://theses.hal.science/tel-01128276>

Submitted on 9 Mar 2015

HAL is a multi-disciplinary open access archive for the deposit and dissemination of scientific research documents, whether they are published or not. The documents may come from teaching and research institutions in France or abroad, or from public or private research centers.

L'archive ouverte pluridisciplinaire **HAL**, est destinée au dépôt et à la diffusion de documents scientifiques de niveau recherche, publiés ou non, émanant des établissements d'enseignement et de recherche français ou étrangers, des laboratoires publics ou privés.

THÈSE DE L'UNIVERSITÉ DE LYON

Délivrée par
l'Université Claude Bernard Lyon 1

École Doctorale Physique et Astrophysique

Diplôme de Doctorat
(arrêté du 7 août 2006)

Soutenue publiquement le 12 décembre 2014
par

Tatjana Stoll

**Ultrafast electronic, acoustic and thermal properties of
metal nanoparticles and clusters**

Directeur de thèse: Fabrice Vallée
Codirectrice de thèse: Natalia Del Fatti

Jury:

M.	Claude	Henry	<i>Rapporteur</i>
M.	Arnaud	Devos	<i>Rapporteur</i>
M.	Francesco	Banfi	<i>Examineur</i>
M.	Patrice	Mélinon	<i>Examineur</i>
Mme.	Natalia	Del Fatti	<i>Codirectrice de thèse</i>
M.	Fabrice	Vallée	<i>Directeur de thèse</i>

Acknowledgments

Le travail de thèse décrit dans ce manuscrit a été effectué de 2011 à 2014 à l'Institut Lumière Matière (ILM) à Lyon. Pour leur accueil je tiens à remercier les directeurs successifs, Christian Bordas et Marie-France Joubert.

Je remercie Claude Henry et Arnaud Devos d'avoir accepté de faire partie du jury en tant que rapporteurs, pour le temps et les efforts qu'ils m'ont accordé par leur lecture soigneuse du manuscrit. Merci également à Francesco Banfi d'avoir bien voulu faire partie de ce jury et d'avoir montré beaucoup d'intérêt pour mes travaux, et finalement merci à Patrice Mélinon d'avoir présidé ce jury.

Ces travaux ont pu être réalisés grâce à un entourage chaleureux et plein d'énergie. Je remercie donc les membres de l'équipe FemtoNanoOptics pour leurs humanités, leurs compétences, leurs sourires, pour les pauses café et les prévisions astronomiques.

Je tiens tout d'abord à remercier les chefs d'équipe, Fabrice Vallée et Natalia Del Fatti, tous deux responsables des conditions de travail très agréables dans un environnement plein d'enthousiasme pour la recherche et d'intelligence. Je remercie Fabrice Vallée pour avoir dirigé ma thèse et pour m'avoir accueilli dans le monde de la recherche avec bienveillance. Ses vastes connaissances de la physique sont impressionnantes et poussent à aller toujours plus loin. Mes remerciements vont également à Natalia Del Fatti, dont l'enthousiasme et les connaissances du monde nanométrique étaient une source d'inspiration. Son optimisme et son énergie m'ont appris à ne jamais abandonner.

Merci à Paolo Maioli, mon formateur tout au long de ce travail de thèse. Toute ma gratitude pour avoir suivi cette thèse de près et au quotidien. Son savoir scientifique, son sens de l'organisation, son ouverture d'esprit et sa curiosité ont particulièrement contribué à la réussite de ce travail. Ses grandes qualités humaines sont à l'origine d'une ambiance relaxée pleine de bienveillance. Merci pour son soutien, sa patience et son amitié.

Toute ma reconnaissance pour Aurélien Crut, compagnon indispensable pendant ces années de travail acharné et sportif doué. Nos discussions scientifiques étaient d'une nature stimulante, ses vérifications numériques de mes travaux parfois primordiales. Je le remercie également pour ses critiques, je reconnais, toujours constructives. Merci beaucoup pour

Acknowledgments

les séances de footing au parc qui m'ont aidé à développer des ambitions en dehors de la recherche.

Je tiens à remercier particulièrement les thésards et post-docs qui étaient à mes côtés pendant ces nombreux moments de joie et de tristesse, de réussite et de désespoir. Merci à Etienne Pertreux qui a montré une patience infinie envers moi, qui m'a illuminé avec ses incroyables connaissances en optique mais qui était surtout un ami précieux dans la salle de manipulation et en dehors. Merci à Anna Lombardi, dont la présence à l'expérience voisine a créé une atmosphère cordiale et rassurante et sans laquelle mon quotidien au laboratoire aurait été beaucoup moins gai. Ma reconnaissance à Denis Mongin qui m'a appris le montage expérimental et qui était un soutien fiable et un pôle de sérénité. Je remercie également les expérimentateurs de la « troisième salle », Samuel Aberra Guebrou ainsi que Jean-Christophe Blancon, avec sa gentillesse, son calme et son génie discret. Merci à Mike Hettich, pour toutes ses histoires curieuses, drôles et encourageantes et pour avoir apporté un petit air de la Forêt Noire au travail. Un grand merci aussi à Lucile Rudkowski pour les moments parfois durs passés ensemble pour rédiger nos travaux dans le même bureau mais que nous avons su surmonter grâce à son grand optimisme et sa force de caractère.

Le succès de mes travaux expérimentaux dépendait cruciallement de mes collaborateurs. C'est pour cela que je tiens à remercier chaleureusement Aude Demessence pour son travail exceptionnel de synthèse. Merci à Matthias Hillenkamp et enfin ma grande reconnaissance à Michel Pellarin, pour la grande fiabilité et l'excellente qualité de ses échantillons.

Je remercie mes amis rencontrés à Lyon qui ont fait de ces années d'apprentissage une période enrichissante et pleine de bonheur et qui rendent mon départ si difficile. Merci à Fosca, Martin, Julien, Catherine et Louison qui m'ont accueilli d'une façon ouverte ce qui encore m'étonne et m'impressionne. Je les remercie pour leur présence et leur amitié dès la première minute. Merci aussi à Elisa, Ioana, Charlotte, Daniel, Franziska et Jean avec lesquels me resteront tant de souvenirs agréables. Merci à ceux que j'ai laissés, à Christine et à Natalie et à ma famille, qui représenteront toujours mon chez moi. Je remercie profondément mes parents pour leur confiance en moi et leur soutien absolu. Merci aussi à mes frères Michael et Alexander qui seront toujours mes grands frères admirés.

Mon dernier merci à David qui m'a accompagné tout au long de ce chemin, qui était présent, avec sa générosité et ses plaisanteries, son sérieux et sa tendresse. Merci d'avoir été à mes côtés.

Contents

Introduction	7
1 Linear and ultrafast properties of noble metal nanoparticles	11
1.1 Dielectric function of bulk and confined noble metals	12
1.1.1 Electronic and lattice properties of bulk noble metals	12
1.1.2 The dielectric function of metals	17
1.1.3 Drude model	19
1.1.4 Interband dielectric function: Rosei model	22
1.2 Confinement effects on linear optical properties	28
1.3 Dynamic evolution of excited noble metals	30
1.3.1 Excitation and time evolution of the free electron gas	30
1.3.2 Time-resolved electron distribution changes	33
1.3.2.a The Boltzmann equation	34
1.3.2.b Electron excitation	35
1.3.2.c Electron-electron interaction	36
1.3.2.d Electron-phonon interaction	38
1.3.2.e Numerical simulations	39
1.4 Time-dependent metal dielectric function changes	41
1.4.1 Electronic contribution	41
1.4.2 Lattice contribution	43
1.5 Ultrafast response of an ensemble of metal nanoobjects	45
2 Size dependence of electronic interactions in metal clusters	49
2.1 Two-colored pump-probe setup	50
2.1.1 Setup 1: Tunable femtosecond laser source	50
2.1.2 Setup 2: Broadband white light pump-probe experiment	53
2.2 Ultrafast electron-lattice interactions in Ag clusters	54
2.2.1 Samples	54
2.2.2 Optical detection of electron-phonon coupling	57
2.2.3 Experimental results	58

Contents

2.2.3.a	Analysis of time-resolved pump-probe signals	58
2.2.3.b	Effects of pump power and size reduction	59
2.2.4	Discussion	62
2.2.4.a	Intermediate size range: size-dependent screening effects .	62
2.2.4.b	Small size range: pump excitation effect	64
2.2.4.c	Small size range: quantum effects	66
2.3	Ultrafast electron-electron interactions in Ag clusters	69
2.3.1	Ultraviolet ultrafast spectroscopy	69
2.3.2	Modeling of the optical detection of the electron thermalization . .	71
2.3.2.a	Optical response of nanoparticles following electron distri- bution changes	72
2.3.2.b	Testing the model: Ag film	75
2.3.3	Experimental results for small particle sizes	78
2.3.3.a	Transient time-resolved signals	78
2.3.3.b	Excitation-dependent dynamics	79
2.3.3.c	Ultrafast transient absorption spectra: size dependence . .	80
2.3.3.d	Electron internal thermalization: size dependence	84
2.3.4	Electronic interactions in Ag clusters: summary	87
2.4	Electron dynamics in thiol-stabilized Au clusters	87
2.4.1	Samples	88
2.4.2	Experiments	91
2.4.2.a	Transient absorption spectra	91
2.4.2.b	Relaxation dynamics	95
2.4.2.c	Signal rise dynamics	98
2.4.3	Summary of observations in Au clusters	100
2.5	Conclusion	101
3	Acoustic response of bimetallic nanoparticles and metal clusters	103
3.1	Macroscopic elastic model	104
3.2	Ultrafast acoustic response of bimetallic nanoparticles	106
3.2.1	Samples	107
3.2.2	Experimental methods	109
3.2.2.a	Time-resolved ultrafast oscillations	110
3.2.2.b	Analysis including size dispersion	112
3.2.3	Analysis of the breathing mode periods	115
3.2.4	Conclusion on the acoustic vibrations of bimetallic nanosystems . .	118
3.3	Ultrafast vibrational spectroscopy of thiol-protected Au clusters	120
3.3.1	Experimental methods	121

3.3.2	Analysis of the Au cluster vibrational frequencies	125
3.3.3	Summary of experiments on small thiol-protected Au clusters	127
3.4	Conclusion	127
4	Thermal relaxation of colloidal gold and gold-silica nanospheres	129
4.1	Experiments	130
4.1.1	Nanoparticle samples	130
4.1.2	Pump-probe experiments	132
4.2	Modeling heat transfer dynamics	135
4.2.1	The Kapitza resistance	136
4.2.2	Bare gold nanospheres	137
4.2.3	Addition of a dielectric shell	141
4.3	Optical detection of heat transfer	144
4.3.1	Derivatives of the absorption spectra	146
4.3.2	Temperature dependence of the dielectric constants	147
4.3.3	Contributions of metal, shell and solution to the observed signal	148
4.4	Results	149
4.4.1	Thermal conductance at gold-liquid interfaces	149
4.4.2	Probe wavelength-dependent optical response	151
4.4.3	Thermal conductance at gold-silica and silica-liquid interfaces	155
4.4.3.a	Estimation of the silica porosity	155
4.4.3.b	Estimation of interface conductances	157
4.4.4	Comparison to photoacoustic experiments	159
4.5	Summary and conclusion	161
	Conclusion	163

Introduction

Reduction of the size of a material to a nanometer scale leads to drastic modifications of its physical and chemical properties. In the case of metal nanoobjects, optical [1], magnetic [2] and vibrational [3] characteristics are affected by size reduction. These effects are associated to changes of electronic and ionic lattice properties of the metals and their increased interaction with the environment, due to an increasing fraction of atoms close to surfaces. For not too small particles (sizes larger than a few nanometers), these modifications can be explained by classical effects, one of the most striking being the appearance of the localized surface plasmon resonance in the optical response. This is due to dielectric confinement, and strongly modifies the color of metal nanosystems [1]. Other phenomena are affected by a simple scaling law (e.g. acoustic vibrations, whose periods scale with diameter) [3, 4] or a more complex evolution with size (electronic interactions within the nanoparticles) [5].

The modified properties compared to bulk metals have aroused great interest in the development of technological applications and have motivated a large number of fundamental studies in the last decades, investigating the effects of nanoobject size, shape and environment. In this context, small nanosystems yielded applications in telecommunications for the doping of optical fibers [6, 7], in medicine as imaging markers and cancer treatment [8, 9], in chemistry for catalysis [10, 11] and in energy development for photovoltaic cells and batteries [12]. In parallel, several techniques were used for the structural characterization of small nanoobjects (high resolution transmission electron microscopy, scanning tunneling microscopy, atomic force microscopy, ...), while the development of femtosecond lasers has enabled the optical study of their out-of-equilibrium ultrafast response.

Recent advances in synthesis methods have allowed to prepare small metal clusters, i.e. nanoobjects in the few nanometer or even sub-nanometer size range [13–15]. These systems are characterized by peculiar physical properties compared to larger nanoparticles, as quantization begins to play an important role leading to an evolution from a “small solid” behavior (quasi-continuum of electronic states in the conduction band) to a molecular-like one (discrete energy states).

Introduction

In this dissertation, the dynamic processes in noble metal nanoparticles and clusters are studied by means of time-resolved optical pump-probe spectroscopy. This experimental technique allows the investigation of distinct physical mechanisms appearing on different timescales, from few femtoseconds to hundreds of picoseconds. Here, metal nanoparticles are excited by the absorption of an ultrafast laser pulse, leading to a succession of different relaxation processes. In the first few hundred of femtoseconds after excitation, the injected energy is redistributed among the electrons by electron-electron scattering (yielding their internal thermalization) and transferred to the ions by electron-lattice interaction (which leads to the full thermalization within the nanoobject). On a longer picosecond timescale these processes can excite acoustic vibrations of the nanoparticles, detected and characterized by time-resolved spectroscopy. The metal nanoobjects finally lose their excess energy, typically within some hundreds of picoseconds, by heat transfer to the environment through their interfaces.

All these fundamental processes are investigated here on nanoparticle ensembles, prepared by physical or chemical techniques, and embedded in a transparent solid matrix or dispersed in a liquid solvent. Investigations on small noble metal clusters and hybrid (bimetallic and metal-dielectric) nanoparticles allow the study of these different aspects. In Chapter 1 the theoretical background of the electronic and optical properties of metal nanoparticles is developed. The emphasis is put on the optical detection of the physical processes at the origin of the ultrafast response of the nanoobjects. For this purpose, all processes induced by an ultrafast laser pulse are quantitatively modeled and their consequence on the optical properties and thus the experimental pump-probe signals are detailed. The nanoobjects are described as “small solids”, being generally characterized by bulk properties, with few modifications due to the increasing role of surfaces.

The transition from this bulk-like behavior to a molecular-like one is experimentally studied for the electronic dynamics (electron-electron and electron-lattice scattering) in silica-embedded silver and thiol-stabilized gold clusters in Chapter 2. The probe wavelengths are selectively chosen in order to study either electron-lattice interactions (via the monitoring of the energy loss of the thermalized electron gas) or electron-electron interactions (by recording the dynamics of specific electronic states close to the Fermi energy). Former measurements have studied these kinetics on noble metal nanospheres in an intermediate size range (3-30 nm diameter), and modifications could be explained in the “small solid” picture introducing reduced screening of electronic interactions close to the surfaces [5, 16–18]. These small adjustments are not sufficient for the nanomaterials studied in this work, where electronic discretization effects become observable.

Acoustic vibrations of bimetallic (alloyed or core-shell) nanoparticles and thiol-stabilized gold clusters are investigated in Chapter 3, in order to elucidate the impact of combining two metals and the effect of size reduction on their mechanical properties. Acoustic de-

tection is shown to be sensitive to the morphology (alloy or core-shell) of the composite nanosystems, in agreement with continuum mechanics simulations describing the vibrational modes of homogeneous or core-shell nanostructures. Former experiments on small platinum nanospheres already showed the validity of continuum mechanics predictions for diameters down to 1.3 nm [19]. Their confirmation is pushed even further in the context of this work, where a quasi-breathing mode is found for clusters of only 25 atoms, in agreement with both classical predictions and molecular dynamics simulations, revealing the robustness of the classical continuum mechanics picture.

In Chapter 4 the mechanisms of heat evacuation of metal and hybrid nanoparticles are addressed on bare and silica-coated gold nanospheres ($D \sim 20$ nm) in different liquid environments. This subject is of great technological interest due to the requirements of fast cooling of nanometric devices [20]. Optical measurements on such systems allow to investigate the impact of thermal interface resistances, which control heat transfer at the nanoscale. In this thesis, a quantitative model describing the time and position-dependent temperature increases in the composite system (metal, silica and solvent), and their impact on the experimentally observable optical properties is developed and used to interpret wavelength-dependent pump-probe experiments. This understanding allows to tune the experimental conditions in order to have access to the thermal response of either the heated environment or the metal nanoparticles, and to extract reliable values for the interface thermal resistances.

Chapter 1

Linear and ultrafast properties of noble metal nanoparticles

The main focus of this thesis is the investigation of the size dependence of fundamental electronic interaction mechanisms of noble metal nanoparticles, especially silver and gold. For this purpose, the accurate study of metal nanoparticle internal dynamics through the measurement of their time-resolved optical response requires detailed modeling of the physical processes involved, which is the main scope of this chapter. The optical response of a small-sized object is characterized by its absorption and scattering cross-sections, σ_{abs} and σ_{sca} , defined as the ratio between absorbed/scattered powers and the intensity of the light incident on the particle, the extinction cross-section σ_{ext} being the sum of σ_{abs} and σ_{sca} [21]. Ultrafast excitation of a nanoparticle leads to a time-dependent modification of σ_{ext} , which can be investigated by time-resolved spectroscopy. These experiments (Fig. 1.1) consist in the perturbation of the metal nanoparticles by a first laser pulse (pump) and the subsequent monitoring of the time-dependent modification of their absorption by measuring the transmission of a second time delayed pulse (probe).

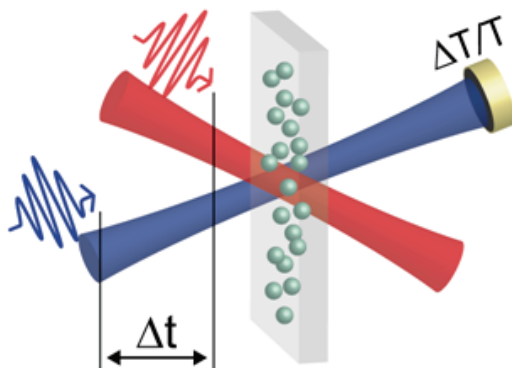


Figure 1.1: Scheme of a pump-probe optical spectroscopy setup.

Neglecting the influence of environment heating on these short timescales and assuming

weak induced changes in the nanoparticle, the variation of its extinction cross-section at probe frequency ω_{pr} and probe delay t , can be expressed by [5]:

$$\begin{aligned}\Delta\sigma_{ext}(\omega_{pr}, t) &= \frac{\partial\sigma_{ext}}{\partial\epsilon_1}(\omega_{pr})\Delta\epsilon_1(\omega_{pr}, t) + \frac{\partial\sigma_{ext}}{\partial\epsilon_2}(\omega_{pr})\Delta\epsilon_2(\omega_{pr}, t) \\ &= a_1(\omega_{pr})\Delta\epsilon_1(\omega_{pr}, t) + a_2(\omega_{pr})\Delta\epsilon_2(\omega_{pr}, t),\end{aligned}\tag{1.1}$$

with $a_{1,2}$ the stationary spectral-dependent plasmonic enhanced σ_{ext} derivatives and $\Delta\epsilon_{1,2}$ the dynamic spectral-dependent modifications of the nanoobject dielectric function $\epsilon = \epsilon_1 + i\epsilon_2$. Time-resolved signals result thus from a combination of the dynamic physical effects under study, and their optical detection, with a spectral sensitivity given by $a_{1,2}$.

In the first section of this chapter we will introduce some basic properties of bulk metals. This will give a short overview on the context of the studies as well as an introduction to some electronic and lattice properties that will be used afterward. Furthermore, tabulated values of characteristic constants of silver and gold are presented, these values being used for computations in this thesis.

The following section introduces the optical properties of bulk noble metals as well as specific characteristics of confined systems. In this context the most striking effect of dielectric confinement, the appearance of the localized surface plasmon resonance (SPR), is presented.

On this background a quantitative model is developed in order to describe the time-resolved optical response of metal nanoobjects. Based on a “small solid” approach, it includes the impact of the out-of-equilibrium conditions (electron excitation and subsequent lattice heating) on the electron energy distribution, the induced modifications of the metal dielectric function, and their influence on the nanoparticle optical response, taking into account plasmonic effects.

1.1 Dielectric function of bulk and confined noble metals

1.1.1 Electronic and lattice properties of bulk noble metals

The noble metals Cu, Ag and Au are organized in a monovalent face-centered cubic (fcc) crystalline lattice. The bulk lattice parameters as well as the atomic structure of these elements are summarized in Table 1.1 [22].

Electrons in a crystal are subject to the periodic potential of the ionic cores formed by the atomic nuclei and all the bound electrons, yielding the description of one electron

1.1. Dielectric function of bulk and confined noble metals

Table 1.1: Atomic structure and lattice parameters \tilde{a} of the noble metals Cu, Ag and Au.

metal	atomic structure	\tilde{a} (Å)
Ag	[Kr]4d ¹⁰ 5s ¹	4.09
Au	[Xe]4f ¹⁴ 5d ¹⁰ 6s ¹	4.08
Cu	[Ar]3d ¹⁰ 4s ¹	3.61

states in terms of Bloch functions:

$$\psi_{n\vec{k}}(\vec{r}) = e^{i\vec{k}\vec{r}} u_{n\vec{k}}(\vec{r}), \quad (1.2)$$

where \vec{r} is the position, \vec{k} the wave vector and $u_{n\vec{k}}$ a periodic function with the same periodicity as the crystal, namely $u_{n\vec{k}}(\vec{r} + \vec{R}) = u_{n\vec{k}}(\vec{r})$, with \vec{R} a lattice vector. When calculating the energy eigenvalues of a Bloch wave, one can identify a continuous variation of the energy $E_n(\vec{k})$ with the index n describing discrete bands. In noble metals, the atomic d orbitals contribute to completely filled and weakly dispersed d-bands whereas the hybridized s-p orbitals form the partially filled p-band. Electrons in this partially filled band (conduction band) are delocalized being thus responsible for most electrical and thermal transport properties, while the deeper filled bands (valence bands) contribute only few to these features. Fig. 1.2 shows a schematic view of the band structure of noble metals. Here, E_F is the Fermi level which describes the energy of the highest occupied electronic state at zero temperature. Electrons in the conduction band are called “quasi-

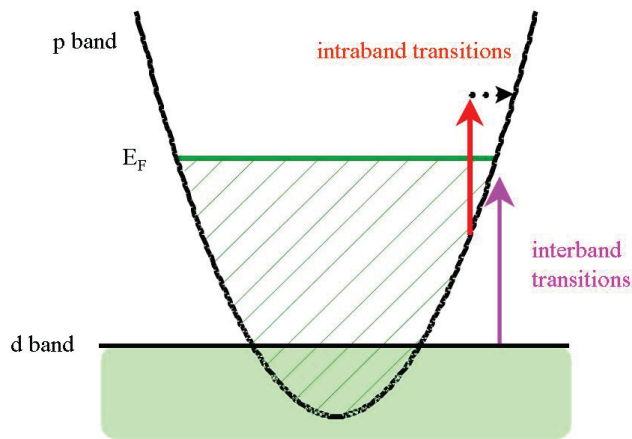


Figure 1.2: Schematic illustration of a metal band structure, showing the weakly dispersed valence band (d-band) and the parabolic conduction band (p-band).

free” as their interaction with the ionic cores is weak and their dynamics is similar to the

Chapter 1. Linear and ultrafast properties of noble metal nanoparticles

one of a free electron gas being characterized by a parabolic dispersion relation:

$$E(\vec{k}) = \frac{\hbar^2 k^2}{2m^*}, \quad (1.3)$$

where m^* is the electron effective mass describing the curvature of the band. In order to determine m^* Eq. (1.3) can be reformulated, leading to:

$$m^* = \hbar^2 \frac{\partial^2 E}{\partial k^2}, \quad (1.4)$$

The resulting density of electron states in a three-dimensional system is given by:

$$\rho(E) = \frac{V}{2\pi^2} \left(\frac{2m^*}{\hbar^2} \right)^{3/2} \sqrt{E}, \quad (1.5)$$

with V the volume of the solid. In this picture, the Fermi energy can be defined by:

$$E_F = \frac{\hbar^2}{2m^*} (3\pi n)^{2/3}, \quad (1.6)$$

where $n = N/V$ describes the conduction electron density of the metal. For many physical effects the value of different energy-dependent quantities around E_F plays an important role. One can thus define the Fermi wave vector $k_F = \sqrt{2m^*E_F}/\hbar$ and Fermi velocity $v_F = \hbar k_F/m^*$, as well as the Fermi temperature $k_B T_F = E_F$. Table 1.2 sums up some important values of the free electron model in silver and gold [22].

Table 1.2: Effective electron mass m^* as a function of the electron rest mass m_e , conduction electron density n , Fermi energy E_F , Fermi wave vector k_F , Fermi velocity v_F and Fermi temperature T_F in Ag and Au.

metal	$m^*(m_e)$	$n(10^{22} \text{ 1/cm}^3)$	E_F (eV)	$k_F(10^8 \text{ 1/cm})$	$v_F(10^8 \text{ cm/s})$	$T_F(10^4 \text{ K})$
Ag	1	5.86	5.49	1.20	1.39	6.38
Au	1	5.90	5.53	1.21	1.40	6.42

The Fermi surface is defined as the surface in k -space separating the occupied and the unoccupied levels of the conduction band at zero temperature. In the case of free electrons it is given by a sphere of radius k_F . The conduction electrons of noble metals being quasi-free, their Fermi surface is similar to the one of a free electron gas, being only slightly modified at the L and X points of the Brillouin zone (see Figs. 1.3(a), 1.3(b) and 1.3(c)) [23]. The occupation probability of an electronic state of energy E at an electron temperature T_e is given by the Fermi-Dirac distribution:

$$f(E) = \frac{1}{e^{\frac{E-E_F}{k_B T_e}} + 1}, \quad (1.7)$$

1.1. Dielectric function of bulk and confined noble metals

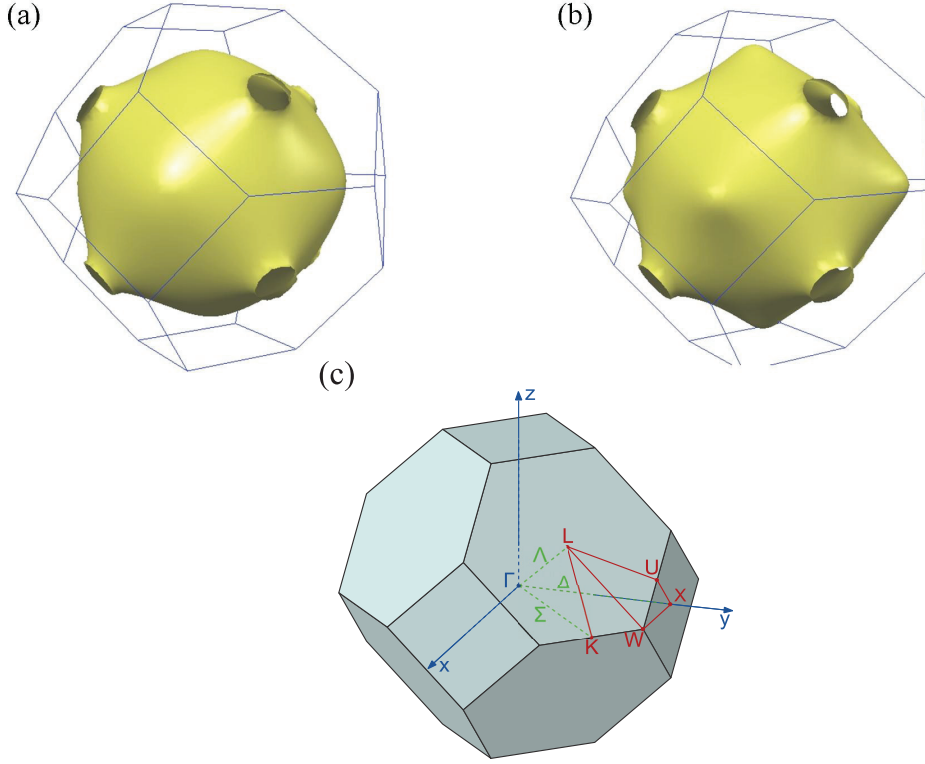


Figure 1.3: Fermi surface in Ag (a) and Au (b) and an illustration of the first Brillouin zone of a fcc lattice (c) and its symmetry lines [23].

where we assumed the chemical potential to be equal to E_F . This is legitimate at room temperature where $T_e \ll T_F$, see Table 1.2.

The electronic contribution to the volumetric specific heat of a metal is given by:

$$c_e(T_e) = \frac{1}{V} \frac{\partial U}{\partial T_e} = \frac{1}{V} \int_0^\infty \epsilon \rho(\epsilon) \frac{\partial f(\epsilon)}{\partial T_e} d\epsilon, \quad (1.8)$$

where U is the internal energy of the system. For $T_e \ll T_F$ in the free electron gas approximation, integration yields a specific heat linear with the electron temperature:

$$c_e(T_e) = \frac{\pi^2 n k_B}{2 T_F} T_e = a T_e. \quad (1.9)$$

The primitive cell of noble metal crystals contains a single atom leading to vibrational normal modes of wave vector q and branch p characterized by a sinusoidal dispersion relation:

$$\omega_{q,p} = \sqrt{\frac{4C_p}{M}} \left| \sin \frac{q\tilde{a}}{2} \right| = \omega_M \left| \sin \frac{q\tilde{a}}{2} \right|, \quad (1.10)$$

where C_p is a constant describing the force between neighboring atoms, \tilde{a} their spacing

Chapter 1. Linear and ultrafast properties of noble metal nanoparticles

and M their mass. Eq. (1.10) represents an acoustic dispersion relation, the frequency $\omega_{q,p}$ being zero for $q = 0$ (see Fig. 1.4). As an alternative to considering lattice vibrations in terms of normal modes it is convenient to introduce the concept of phonons, describing vibrations in a corpuscular picture, in analogy to photons of the electromagnetic field [22]. For each phonon wave vector there are three branches p , one of longitudinal polarization

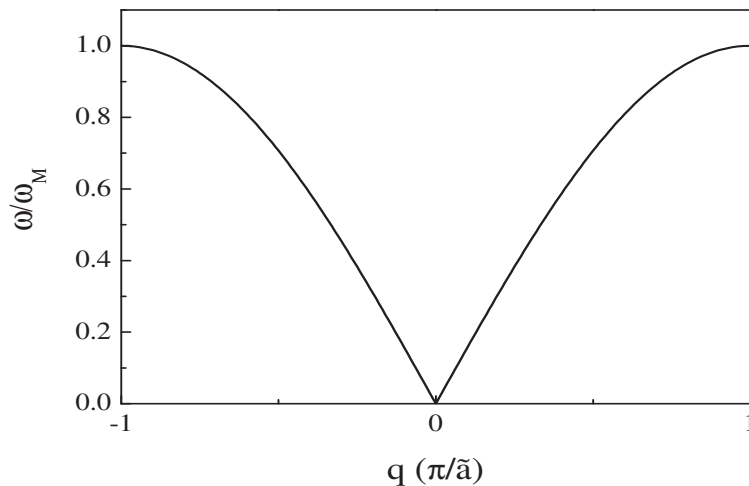


Figure 1.4: Sinusoidal acoustic phonon dispersion relation $\omega(q)$.

and two of transverse polarization (for the longitudinal polarization in Ag $\omega_M \approx 21$ meV). All phonons can be described inside the first Brillouin zone yielding N modes per branch, with N the number of atoms in the crystal. Note that this is a very simplified model, neglecting interactions on a range longer than the neighboring atoms and non-linearities in the potential.

The Debye model is an approximation for short wave vectors. Here, the phonon frequency is considered to be linear with q :

$$\omega = v_D q, \quad (1.11)$$

with v_D the constant sound velocity in the direction of \vec{q} for the longitudinal or transverse branch. The number of possible states in one branch is limited by N . Assuming isotropy, one can thus introduce the Debye wave vector, which constitutes a limit value for phonon wave vectors ($q \leq q_D$).

$$q_D = (6\pi^2 n)^{1/3} = \sqrt[3]{2} k_F, \quad (1.12)$$

where the second identity is only valid for monovalent metals. Analogously it is possible to define the maximum phonon frequency $\omega_D = v_D q_D$ and the Debye temperature Θ , given

1.1. Dielectric function of bulk and confined noble metals

by:

$$\Theta = \frac{\hbar v_D}{k_B} (6\pi^2 n)^{1/3}. \quad (1.13)$$

For temperatures T higher than Θ , all phonon states can be considered to be excited. This corresponds to 215 K and 170 K for Ag and Au, respectively. In thermal equilibrium, the occupancy of phonons of wave vector \vec{q} and polarization p is described by the Bose-Einstein statistics:

$$N(\vec{q}) = \frac{1}{e^{\frac{\hbar\omega_{\vec{q},p}}{k_B T}} - 1}. \quad (1.14)$$

Considering v_D to be independent of polarization, it is thus possible to calculate the phonon contribution to the metal heat capacity according to Eq. (1.8). At room temperature (~ 300 K), the high temperature limit ($T \gg \Theta$) can be applied leading to the classical Dulong-Petit law for the heat capacity at constant volume:

$$c = 3nk_B, \quad (1.15)$$

yielding $c \approx 2.4 \times 10^6$ J/(m³ K) and $c \approx 2.5 \times 10^6$ J/(m³ K) for Ag and Au, respectively.

1.1.2 The dielectric function of metals

The complex dielectric function of a noble metal describes the interaction of electrons with an electromagnetic field of frequency ω . An incident electromagnetic field \vec{E} induces a polarization in the medium, which is introduced in a macroscopic way by Maxwell's equations, where the electric displacement field is given by [24]:

$$\vec{D} = \epsilon_0 \epsilon \vec{E} = \epsilon_0 (1 + \chi) \vec{E}, \quad (1.16)$$

with ϵ_0 the vacuum permittivity, χ the permittivity of the medium and $\epsilon = \epsilon_1 + i\epsilon_2$ the relative dielectric function, where real and dielectric parts are related through the Kramers-Kronig relation [21]. In isotropic media both dielectric function and permittivity are scalar functions of the frequency. The propagation of an incident monochromatic plane wave in the solid is characterized by Helmholtz's equation:

$$\Delta \vec{E} + \frac{\omega^2}{c^2} \epsilon(\omega) \vec{E} = 0, \quad (1.17)$$

its solution being given by:

$$\vec{E}(z, t) = \vec{E}_0 \exp \left[i\omega \left(\frac{\tilde{n}}{c} z - t \right) \right], \quad (1.18)$$

where \tilde{n} describes the complex refractive index $\tilde{n} = n + i\kappa$. It can be related to the complex dielectric constant by:

$$\epsilon_1 + i\epsilon_2 = (n + i\kappa)^2. \quad (1.19)$$

The intensity of the electric field being proportional to $|\vec{E}|^2$ an exponential decay of the intensity inside the medium is obtained $I(z) = I_0 \exp(-\alpha z)$, with $\alpha = 2\omega\kappa(\omega)/c$ its absorption coefficient.

In the case of noble metals, the real and imaginary dielectric functions can be split in two contributions, corresponding to interaction of the field with electrons in the conduction band (Drude contribution) and to photoexcited transitions (interband contribution), yielding $\epsilon(\omega) = 1 + [\chi^D(\omega) + \chi^{ib}(\omega)] = \epsilon^D(\omega) + \epsilon^{ib}(\omega) - 1$. The dielectric functions of Ag and

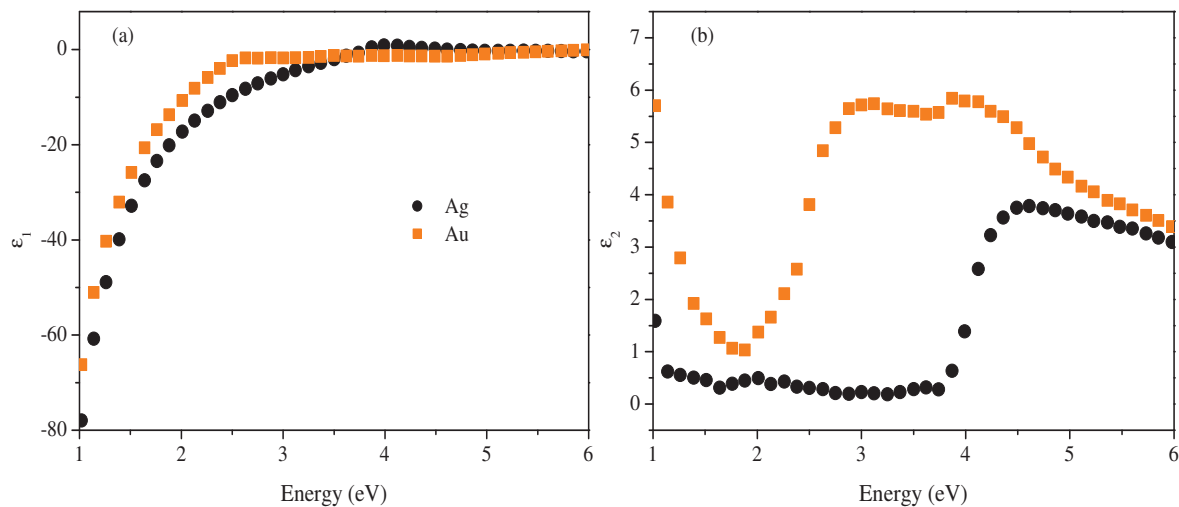


Figure 1.5: Experimentally measured (Johnson and Christy [25]) real (a) and imaginary (b) part of the dielectric function of Ag and Au.

Au have been measured experimentally by several authors [25–29]. In the case of Au, the most common dielectric constant table is the one measured by Johnson and Christy [25]. It is still widely adapted for modeling optical properties of Au nanosystems as it predicts their spectral characteristics (SPR position and width) reasonably well, which is also the case for more recently measured sets [27–29]. The experimental tables commonly used for

Ag are the ones of Johnson and Christy [25] and Palik [26], the latter better reproducing SPR positions (mainly determined by ϵ_1^{ib}), the former being more compatible for resonance widths (ϵ_2^{ib}) [30]. Recent experimental investigations failed to provide Ag dielectric constants better reproducing the nanoparticle SPR, probably because of their sensitivity to the quality and crystallinity of silver samples. ϵ_1 and ϵ_2 measured by Johnson and Christy will be used in the following. Figs. 1.5(a) and 1.5(b) show their evolution as a function of the incident photon energy.

1.1.3 Drude model

The Drude part of the dielectric function ϵ^D is associated to the absorption of light by electrons in the conduction band. In this picture, they are considered as a free gas, being described by the classical kinetic gas theory [22], with electron-electron and electron-ion scattering being introduced in a phenomenological way as a friction with characteristic time τ , or its counterpart in energy $\gamma = 1/\tau$. In an external electric field \vec{E} , motion of an electron of effective mass m^* and charge $-e$ is given by Newton's second law:

$$m^* \frac{d\vec{v}}{dt} = -\gamma m^* \vec{v} - e\vec{E}(t). \quad (1.20)$$

In equilibrium, the displacement of electrons induces a time-dependent dipole $\vec{p} = -e\vec{r}$ contributing to the macroscopic polarization of the medium $\vec{P} = n\vec{p} = \epsilon_0\chi^D(\omega)\vec{E}$. The expression of the Drude dielectric function is found to be:

$$\epsilon^D(\omega) = 1 + \chi^D(\omega) = 1 - \frac{\omega_p^2}{\omega(\omega + i\gamma)}, \quad (1.21)$$

with $\omega_p = \sqrt{ne^2/(\epsilon_0 m^*)}$ the plasma frequency. Isolating its real and imaginary parts, and assuming $\omega \gg \gamma$ (valid in the domain of optical frequencies), one obtains:

$$\begin{aligned} \epsilon_1^D(\omega) &= 1 - \frac{\omega_p^2}{\omega^2 + \gamma^2} \approx 1 - \frac{\omega_p^2}{\omega^2}, \\ \epsilon_2^D(\omega) &= \frac{\omega_p^2 \gamma}{\omega(\omega^2 + \gamma^2)} \approx \frac{\omega_p^2}{\omega^3} \gamma. \end{aligned} \quad (1.22)$$

Figures 1.6(a) and 1.6(b) illustrate the experimental dielectric functions of Ag (from Ref. [25]) and their fit by Eq. (1.22). The low-energy part of $\epsilon_{1,2}$ is very well reproduced, interband transitions being resonant only for higher energies. The fit in the infrared part of the spectrum allows thus extraction of the values of the plasma frequency and the damping rate, yielding $\hbar\omega_p = 8.98$ eV and $\hbar\gamma = 0.020$ eV for silver. A similar procedure can be made for gold.

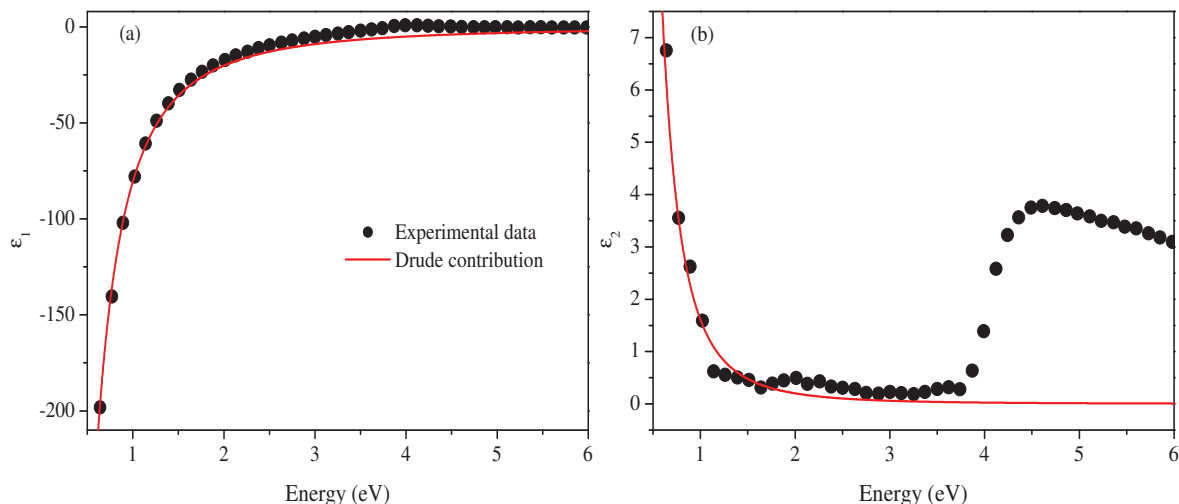


Figure 1.6: Fit of the experimental data of the Ag dielectric function [25] ϵ_1 (a) and ϵ_2 (b), by the Drude formula (Eq. (1.22)).

The imaginary part of the Drude term reflects photon absorption by conduction electrons, being described by the scattering rate γ . In a bulk-like picture, the momentum of a photon being negligibly small, absorption has to be assisted by a third particle (such as an auxiliary electron, a phonon of the ionic lattice or a defect) in order to satisfy energy and momentum conservation. Neglecting electron-defect scattering, γ can be split into two contributions, namely electron-electron and electron-phonon scattering which write:

$$\gamma(\omega, T_e, T_L) = \gamma_{e-ph}(\omega, T_e, T_L) + \gamma_{e-e}(\omega, T_e), \quad (1.23)$$

where the processes depend on the photon frequency ω , the electron gas temperature T_e and the lattice temperature T_L .

At room temperature, the dominant contribution to γ in bulk metals originates from the electron-phonon scattering term [31–35]. It has been computed modeling electron-phonon interaction via a deformation potential. Assuming a parabolic conduction band and an incident photon energy $\hbar\omega$ smaller than the Fermi energy E_F , a simplified expression is obtained [36]:

$$\gamma_{e-ph}(\omega, T_e, T_L) = \frac{G_{ph}}{\hbar\omega} \int_0^\infty \sqrt{E(E + \hbar\omega)} f(E) [1 - f(E + \hbar\omega)] dE, \quad (1.24)$$

where G_{ph} is the electron-phonon interaction constant, depending on the lattice temperature via the occupation number of phonon states. If the lattice temperature T_L is larger

1.1. Dielectric function of bulk and confined noble metals

than the Debye temperature, γ_{e-ph} is approximately linear with T_L while the dependence on T_e is included in the occupation factor $f(E)$.

Accordingly, γ_{e-e} describes the electron-electron scattering assisted photon-absorption rate, being affected only by *Umklapp* processes (electron-electron scattering by exchange of a vector in the reciprocal lattice). For thermalized conduction electrons it is given by [34, 37]:

$$\gamma_{e-e}(\omega, T_e) = \frac{\omega^2}{4\pi^2\omega_p} \left[1 + \left(\frac{2\pi k_B T_e}{\hbar\omega} \right)^2 \right]. \quad (1.25)$$

For optical frequencies ($\hbar\omega \gg k_B T_e$) the second term of the sum in Eq. (1.25) becomes negligible yielding a weak dependence of γ_{e-e} on the electronic temperature T_e .

For particles smaller than the electron mean free path (~ 30 nm in noble metals), effects of confinement must be considered. For not too small sizes ($D \geq 1$ nm) these effects can be taken into account by introducing a correction to the Drude model [1, 38]. This modification is described by an additional term in Eq. (1.23), the electron-surface scattering rate, which for spherical nanoparticles is given by:

$$\gamma_{e-S}(\omega, T_e, D) = 2g(\omega, T_e) \frac{v_F}{D}. \quad (1.26)$$

γ_{e-S} is a consequence of electron confinement and thus depends on the particle diameter D . In general, it can also be estimated for elongated particles where a shape-dependence is introduced, replacing $D/2$ in Eq. (1.26) by a surface term $\sqrt{S/\pi}$ [39]. In a classical picture γ_{e-S} describes absorption of a photon by a conduction electron assisted by electron-surface collisions in order to ensure momentum conservation. From a more correct quantum point of view it is associated to allowed optical transitions between confined states, the wave vector k being no longer a good quantum number [38]. The amplitude of this effect, defined “quantum confinement”, in contrast with the classical “dielectric confinement”, responsible for the surface plasmon resonance of metal nanoparticles (see Sec. 1.2) is given by [34, 40, 41]:

$$g(\omega, T_e) = \frac{1}{\hbar\omega E_F^2} \int_0^\infty E^{3/2} \sqrt{E + \hbar\omega} f(E) [1 - f(E + \hbar\omega)] dE, \quad (1.27)$$

where the electron temperature dependence is, again, included in the electron occupation number $f(E)$. For noble metals, a value $g \approx 0.7$ can be considered at room temperature in the optical domain. This value is consistent with recent experiments accounting for the explicit size dependence of γ_{e-S} and possible size-dependent modifications of γ_{e-ph} and γ_{e-e} [42–44] (their size dependence is not explicitly specified in Eq. (1.24) and Eq. (1.25)).

1.1.4 Interband dielectric function: Rosei model

The term ϵ^{ib} is associated to interband transitions of electrons from low energy bands (e.g. localized d-band) to bands of higher energy induced by absorption of an incoming photon [45, 46]. The interband transition contribution to the stationary absorption spectrum of Ag and Au can be computed through models developed to interpret thermo-modulation experiments on bulk noble metals accounting for the temperature-dependent optical response of a thin metal film under equilibrium conditions [47]. Rosei and collaborators explicitly established a model for computing the interband component of the imaginary dielectric function ϵ_2^{ib} for incident photon energies close to the interband transition threshold for noble metals like Ag [48] and Au [49]. Only vertical electron transitions are considered, thus locating the onsets of the possible optical transitions around few decisive points in the first Brillouin zone.

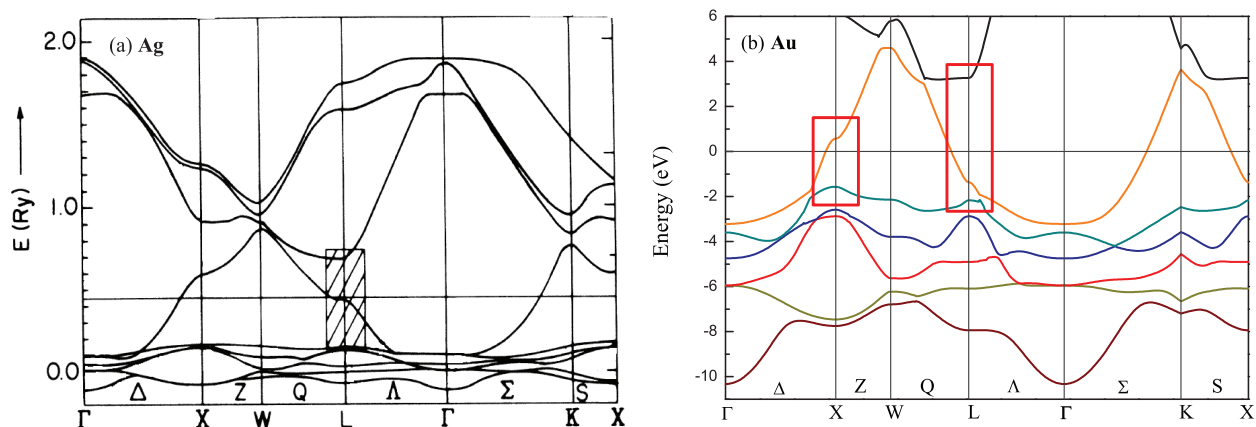


Figure 1.7: Band structure of Ag (a) and Au (b), taken from Refs. [50] and [51], respectively. The horizontal line indicates the position of the Fermi energy, which is shifted to 0 in (b). The indicated directions in k-space are shown in Fig. 1.3(c).

The bulk electron band structure, adopted from theoretical calculations, of Ag [50] and Au [51] is depicted in Figs. 1.7(a) and 1.7(b). The area in k-space where optical interband transitions mainly occur is highlighted by rectangles. Only three bands are considered, namely the fully occupied d-band (valence band), the partially occupied p-band (conduction band) and the empty s-band. In bulk silver, small energy transitions occur near the L point, whereas for gold the X point in the Brillouin zone has to be considered as well. The electron energy bands close to X and L can be assumed to depend quadratically on the distance from these high symmetry points. Figures 1.8(a), 1.8(b) and 1.8(c) illustrate an extract of the silver and gold band structures approximated by anisotropic parabolas. The considered zones correspond approximately to the boxes in Figs. 1.7(a) and 1.7(b).

1.1. Dielectric function of bulk and confined noble metals

In the following we present an outline of Rosei's calculations for Ag [48]. The same model is valid for Au with only few necessary adjustments [49].

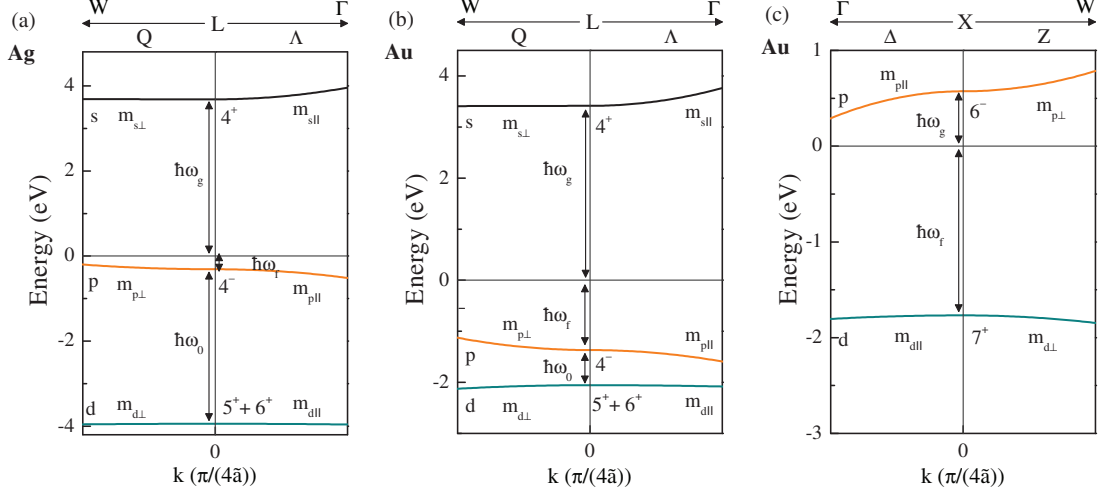


Figure 1.8: Electron band structure around high symmetry points in the Brillouin zone [50, 51], L for Ag (a) and L (b) and X (c) for Au, approximated by anisotropic parabolas. For the values of the parameters see Table 1.3. The origin of energies is taken at the Fermi level.

The electron wave vector along the $L - \Gamma$ direction is given by k_{\parallel} , the ones orthogonal to this axis by k_{\perp} , assuming rotational symmetry. The curvature of the parabolic bands can be described by the effective masses, for each particular band in the parallel and orthogonal direction of k (see labels in Fig. 1.8(a)). At L the separation of d and p-band corresponds to $\hbar\omega_0$ ($L_{5+6}^+ - L_4^-$), the distances of p band and s-band from the Fermi energy are called $\hbar\omega_f$ and $\hbar\omega_g$ respectively, the separation between the two bands being therefore given by $\hbar\omega_f + \hbar\omega_g$ ($L_4^- - L_4^+$). Note that the actual interband transition threshold is not equivalent to the minimal distance of the energy bands. As an optical transition can only occur from a filled to an empty electron state, the position of the Fermi energy must be taken into account. The electron energy dispersion around the L point of the reciprocal lattice for d, p and s-band with respect to E_F can be described by:

$$\begin{aligned}\hbar\omega_d &= -\hbar\omega_f - \hbar\omega_0 - \frac{\hbar^2}{2m_{d\perp}}k_{\perp}^2 - \frac{\hbar^2}{2m_{d\parallel}}k_{\parallel}^2, \\ \hbar\omega_p &= -\hbar\omega_f + \frac{\hbar^2}{2m_{p\perp}}k_{\perp}^2 - \frac{\hbar^2}{2m_{p\parallel}}k_{\parallel}^2, \\ \hbar\omega_s &= \hbar\omega_g + \frac{\hbar^2}{2m_{s\perp}}k_{\perp}^2 + \frac{\hbar^2}{2m_{s\parallel}}k_{\parallel}^2.\end{aligned}\tag{1.28}$$

Chapter 1. Linear and ultrafast properties of noble metal nanoparticles

The energy-dependent joint density of states (EDJDOS), which characterizes the probability for a transition from an initial electron state in band i of energy E to a final state in band f of energy $E + \hbar\omega$ (in $\text{J}^{-2}\text{m}^{-3}$), is defined as:

$$D_{i \rightarrow f}(E, \hbar\omega) = \frac{1}{(2\pi)^3} \int \delta \left[\Omega_{if}(\vec{k}) \right] \delta \left[E - E_i(\vec{k}) \right] d^3k. \quad (1.29)$$

The second delta function in Eq. (1.29) selects only transitions from an initial state with energy E while the first delta function picks out the transitions with energy gap $\hbar\omega$ between the initial and the final band [52]. Ω_{if} represents a surface of constant energy between the final and initial band described by:

$$\Omega_{if} = E_f(\vec{k}) - E_i(\vec{k}) - \hbar\omega = 0. \quad (1.30)$$

In practice, for the two transitions in Ag, $d \rightarrow p$ and $p \rightarrow s$ around L, the constant-energy-difference surfaces are given by

$$\begin{aligned} \Omega_{dp}(k) &= \hbar\omega_0 + \frac{\hbar^2}{2} \left(\frac{1}{m_{p\perp}} + \frac{1}{m_{d\perp}} \right) k_{\perp}^2 - \frac{\hbar^2}{2} \left(\frac{1}{m_{p\parallel}} - \frac{1}{m_{d\parallel}} \right) k_{\parallel}^2 - \hbar\omega = 0, \\ \Omega_{ps}(k) &= \hbar\omega_g + \hbar\omega_f + \frac{\hbar^2}{2} \left(\frac{1}{m_{s\perp}} - \frac{1}{m_{p\perp}} \right) k_{\perp}^2 + \frac{\hbar^2}{2} \left(\frac{1}{m_{s\parallel}} + \frac{1}{m_{p\parallel}} \right) k_{\parallel}^2 - \hbar\omega = 0. \end{aligned} \quad (1.31)$$

The EDJDOS can be rewritten as a line integral [45, 53]:

$$D_{i \rightarrow f}(E, \hbar\omega) = \frac{1}{(2\pi)^3} \int \frac{dl_{if}}{|\vec{\nabla}_{\vec{k}} E_f(\vec{k}) \times \vec{\nabla}_{\vec{k}} E_i(\vec{k})|}, \quad (1.32)$$

with integration along the intersection of the constant-energy surfaces $E_i = E$ and $E_f = E + \hbar\omega$. One obtains for the $d \rightarrow p$ and $p \rightarrow s$ [48]:

$$\begin{aligned} D_{d \rightarrow p}(E, \hbar\omega) &= \frac{F_{d \rightarrow p}}{16\pi^2 \hbar^3 \sqrt{[\hbar\omega - \hbar\omega_0 - \hbar\omega_f - (E - E_F)]/m_{p\perp} - [(E - E_F) + \hbar\omega_f]/m_{d\perp}}}, \\ D_{p \rightarrow s}(E, \hbar\omega) &= \frac{F_{p \rightarrow s}}{16\pi^2 \hbar^3 \sqrt{[(E - E_F) + \hbar\omega - \hbar\omega_g]/m_{p\perp} - [(E - E_F) + \hbar\omega_f]/m_{s\perp}}}. \end{aligned} \quad (1.33)$$

It should be noted that the two terms depend only on the energy difference $E - E_F$ and not on the absolute energy value. The energy-dependent joint density of states is weighted

1.1. Dielectric function of bulk and confined noble metals

by the geometrical factors $F_{i \rightarrow f}$ (in kg) given by:

$$F_{i \rightarrow f} = \sqrt{\frac{m_{i\parallel} m_{f\perp} m_{i\perp} m_{f\parallel}}{m_{i\parallel} m_{f\perp} + m_{i\perp} m_{f\parallel}}}. \quad (1.34)$$

It is now possible to calculate the joint density of states (JDOS) for a particular incident photon energy $\hbar\omega$, integrating the EDJDOS over all energies inducing transitions from i to f with a weight factor given by the occupation probability of the electron states:

$$J_{i \rightarrow f} = \int_{-\infty}^{\infty} D_{i \rightarrow f}(E, \hbar\omega) f(E) [1 - f(E + \hbar\omega)] dE, \quad (1.35)$$

where $f(E)$ is the Fermi distribution function (see Eq. (1.7)). If the bands d and s are completely filled and empty respectively, the equations for the JDOS of the dominating transitions in Ag can be simplified:

$$J_{d \rightarrow p}(\hbar\omega) = \int_{-\infty}^{E_{max}} D_{d \rightarrow p}(E, \hbar\omega) [1 - f(E)] dE, \quad (1.36)$$

$$J_{p \rightarrow s}(\hbar\omega) = \int_{E_{min}}^{\infty} D_{p \rightarrow s}(E, \hbar\omega) f(E) dE, \quad (1.37)$$

with the integration limits E_{max} and E_{min} given by [48]:

$$E_{max} = E_F - \hbar\omega_f + \begin{cases} \frac{m_{d\parallel}}{m_{d\parallel} - m_{p\parallel}} (\hbar\omega - \hbar\omega_0) & \text{for } \hbar\omega < \hbar\omega_0 \\ \frac{m_{d\perp}}{m_{d\perp} + m_{p\perp}} (\hbar\omega - \hbar\omega_0) & \text{for } \hbar\omega > \hbar\omega_0 \end{cases} \quad (1.38)$$

$$E_{min} = E_F - \hbar\omega_f + \begin{cases} \frac{m_{s\perp}}{m_{s\perp} - m_{p\perp}} (\hbar\omega_g + \hbar\omega_f - \hbar\omega) & \text{for } \hbar\omega < \hbar\omega_g + \hbar\omega_f \\ \frac{m_{s\parallel}}{m_{s\parallel} + m_{p\parallel}} (\hbar\omega_g + \hbar\omega_f - \hbar\omega) & \text{for } \hbar\omega > \hbar\omega_g + \hbar\omega_f \end{cases} \quad (1.39)$$

This relation can be derived from Fig. 1.8(a). It can also be observed that depending on the incoming photon energy, only electrons with parallel (k_{\parallel}) or orthogonal (k_{\perp}) wave vectors are excited. The lower and upper integration limit of Eq. (1.36) and Eq. (1.37) respectively is restricted by the occupation factors which vanish rapidly for energies far from E_F .

Starting from the analytical expression for the joint density of states for all considered transitions $J_{d \rightarrow p}(\hbar\omega)$ and $J_{p \rightarrow s}(\hbar\omega)$ it is possible to calculate the interband dielectric con-

stant given by [45, 46, 54]:

$$\epsilon_2^{ib}(\hbar\omega) = \frac{8\pi^2 e^2 \hbar^2}{\epsilon_0 m^2 (\hbar\omega)^2} \left(|\vec{P}_{d \rightarrow p}|^2 J_{d \rightarrow p}(\hbar\omega) + |\vec{P}_{p \rightarrow s}|^2 J_{p \rightarrow s}(\hbar\omega) \right). \quad (1.40)$$

Note that the equation is only valid for photon energies around the threshold of the considered interband transitions. The factor $|\vec{P}_{i \rightarrow f}|^2$ corresponds to the square of the momentum operator matrix element weighting each transition [45, 46, 54]. It couples electronic states with the same wave vector in the initial and final band and is given by [55]:

$$|\vec{P}_{i \rightarrow f}|^2 = |\langle f | \vec{p} | i \rangle|^2. \quad (1.41)$$

Its dependance with k has been omitted assuming small variations in the considered region. This assumption attributes constant weight to each optical transition [52] and is called the “constant-matrix-element approximation”.

The expression for ϵ_2^{ib} in Ag can be generalized to other noble metals e.g. Au or Cu, considering their specific electron band structures. In the case of Au, the sum in Eq. (1.40) has to contain a third term in order to include the transition at the point X from the d to the p-band. In Figs. 1.9(a) and 1.9(b) we show experimental [25] imaginary dielectric

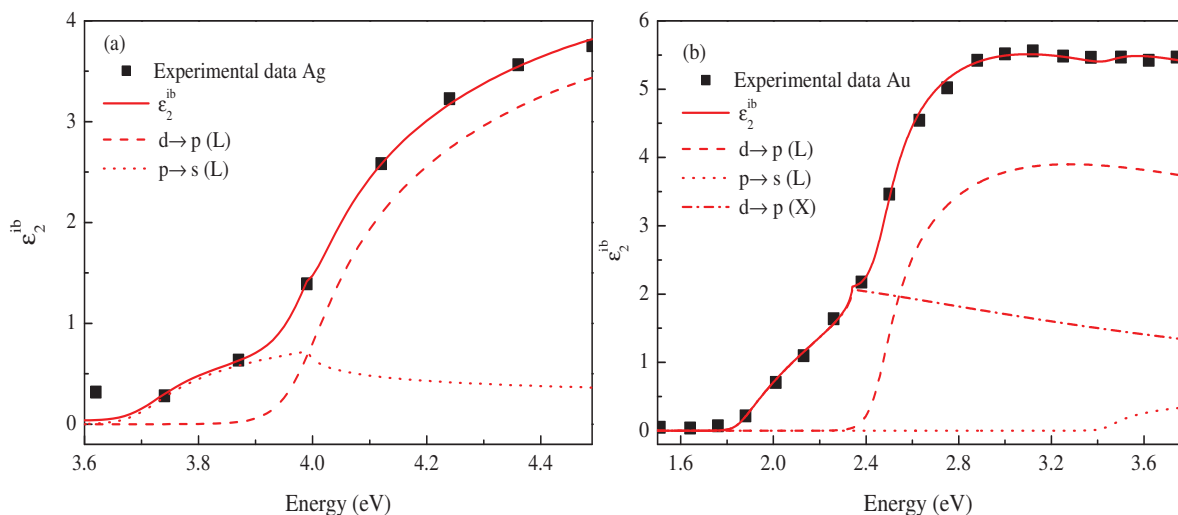


Figure 1.9: Fit of the interband imaginary part of the dielectric function deduced by Johnson and Christy [25] for Ag (a) and Au (b). The contributions to ϵ_2^{ib} corresponding to d→p and p→s transitions at the L point for both metals plus the d→p transition at the X point in Au, are also shown.

constants after subtraction of the Drude contribution for Ag and Au and the computed

1.1. Dielectric function of bulk and confined noble metals

contributions resulting from different interband transitions. The silver interband transition threshold is around 3.95 eV, being located at energies higher than the one of gold around 2.4 eV. In both cases we have defined the transition threshold as the onset of the $d \rightarrow p$ transition, this being the dominant contribution to ϵ_2^{ib} in both metals. However, as shown in Figs. 1.9(a) and 1.9(b), one should precisely define a threshold for every transition separately.

The corresponding ϵ_2^{ib} have been computed using Eq. (1.40), and the optical masses calculated from band curvatures (Table 1.3). The energy gaps between the bands varying between different computational methods (see e.g. Refs. [51] and [56]), we chose to keep this quantity as a fit parameter together with the dipole element determining the amplitude of each specific transition. The values obtained from the fit of the experimental data in 1.7(a) and 1.7(b) are shown in Table 1.3.

Table 1.3: Parabolic band parameters for optical transitions in Ag and Au near L and X points of the Brillouin zone. The optical gaps and momentum matrix element were free parameters while the optical masses result from parabolic fits to the theoretical band structure [50, 51].

Band	Mass (m_e)	⊥ Mass (m_e)	Energy (eV)	$ \vec{P}_{i \rightarrow f} ^2 (10^{11} m_e^2 \frac{m^2}{s^2})$
Ag L Point				
5 ⁺ + 6 ⁺ (d)	2.580	2.075	-3.942	d → p: 10.07 p → s: 4.83
4 ⁻ (p)	0.172	0.320	-0.310	
4 ⁺ (s)	0.128	5.160	3.648	
Au L Point				
5 ⁺ + 6 ⁺ (d)	1.326	0.499	-2.055	d → p: 17.80 p → s: 4.85
4 ⁻ (p)	0.157	0.146	-1.368	
4 ⁺ (s)	0.101	6.797	3.414	
Au X Point				
7 ⁺ (d)	0.944	0.446	-1.767	d → p: 5.70
6 ⁻ (p)	0.125	0.166	0.573	

The experimental data of Johnson and Christy [25] were chosen for the determination of interband transition parameters, the ratio between the dominating transitions in Ag and Au yielding:

$$\frac{|\vec{P}_{L:d \rightarrow p}^{Ag}|^2}{|\vec{P}_{L:p \rightarrow s}^{Ag}|^2} = 2.08 \quad \frac{|\vec{P}_{X:d \rightarrow p}^{Au}|^2}{|\vec{P}_{L:d \rightarrow p}^{Au}|^2} = 0.32,$$

which is in very good agreement with the fit by Rosei et al. (2.21 and 0.37) made on different sets of dielectric constants [49, 57].

1.2 Confinement effects on linear optical properties

The most remarkable effect of size reduction of noble metal systems is the appearance of the localized surface plasmon resonance (SPR), affecting the color of the nanoparticles [1, 3, 58, 59]. This resonance, associated to a collective electron motion, results in a strong enhancement and spatial localization of the electromagnetic fields inside and around metal nanoparticles.

Interaction of an incident electromagnetic wave and a spherical object characterized by its dielectric function ϵ in a dielectric environment is classically described by Maxwell's equations. An exact expression for the absorbed and scattered energy has been given by Mie, using a multipolar expansion [60].

For dimensions much smaller than the incident light wavelength (typically $D < 30$ nm), it is sufficient to consider only the dipolar terms (dipolar approximation). The response of a nanoparticle can thus be approximated by the one of a dipole $\vec{p}(\omega)$ at the center of the object aligned with the external oscillating electric field $\vec{E}(\omega)$, given by:

$$\vec{p}(\omega) = \epsilon_0 \epsilon_m \tilde{\alpha}(\omega) \vec{E}(\omega), \quad (1.42)$$

where $\tilde{\alpha}$ is the linear polarizability of the nano-object and ϵ_m the dimensionless, real and positive matrix dielectric constant. The polarizability of a nanosphere is given by [1, 21]:

$$\tilde{\alpha}(\omega) = 3V_{np} \frac{\epsilon(\omega) - \epsilon_m}{\epsilon(\omega) + 2\epsilon_m}, \quad (1.43)$$

where V_{np} is the nanoparticle volume. The scattering (σ_{sca}) and extinction ($\sigma_{ext} = \sigma_{sca} + \sigma_{abs}$) cross-sections can be analytically expressed as a function of the polarizability:

$$\sigma_{sca}(\omega) = \left(\frac{\omega}{c}\right)^4 \frac{\epsilon_m^2}{6\pi} |\tilde{\alpha}(\omega)|^2 = \frac{3\omega^4 V_{np}^2 \epsilon_m^2}{2\pi c^4} \left| \frac{\epsilon(\omega) - \epsilon_m}{\epsilon(\omega) + 2\epsilon_m} \right|^2, \quad (1.44)$$

$$\sigma_{ext}(\omega) = \frac{\omega}{c} \sqrt{\epsilon_m} \text{Im}[\tilde{\alpha}(\omega)] = 9V_{np} \epsilon_m^{3/2} \frac{\omega}{c} \frac{\epsilon_2(\omega)}{[\epsilon_1(\omega) + 2\epsilon_m]^2 + \epsilon_2^2(\omega)}. \quad (1.45)$$

It should be noted that the extinction cross-section is proportional to the particle volume while the scattering cross-section is linear to its square. The ratio of the two quantities is thus ruled by:

$$\frac{\sigma_{sca}}{\sigma_{ext}} \propto \left(\frac{D}{\lambda}\right)^3. \quad (1.46)$$

For small nanoobjects ($D \ll \lambda$) the scattering cross-section becomes negligible yielding to an extinction cross-section which is dominated by absorption, $\sigma_{ext} \approx \sigma_{abs}$.

1.2. Confinement effects on linear optical properties

For small and weakly dispersed values of ϵ_2 (which is the case in noble metals), vanishing of the first term in the denominator of Eq. (1.45) corresponds to a resonant enhancement of absorption. This surface plasmon resonance is a classical effect due to the presence of surfaces and thus of dielectric confinement. Combining Eq. (1.21) and Eq. (1.45), the resonant frequency can be expressed as [61, 62]:

$$\omega_{SPR} = \frac{\omega_p}{\sqrt{\epsilon_1^{ib}(\omega_{SPR}) + 2\epsilon_m}}. \quad (1.47)$$

If this frequency lies far from the interband transition threshold, as it is the case of Ag nanospheres, the shape of the SPR can be described by a quasi-Lorentzian profile, centered at ω_{SPR} with a full width at half maximum (FWHM) Γ :

$$\Gamma = \gamma(\omega_{SPR}) + \frac{\omega_{SPR}^3}{\omega_p^2} \epsilon_2^{ib}(\omega_{SPR}). \quad (1.48)$$

Position and shape of the SPR vary with the considered metal due to the dependencies on ω_p , ϵ_1^{ib} and ϵ_2^{ib} in Eq. (1.47) and Eq. (1.48). This is illustrated in Figs. 1.10(a) and 1.10(b), where we computed the extinction cross-section of $D = 30$ nm Ag and Au nanospheres in water in the dipolar approximation and using an exact multipolar solution [21] (black dotted and full lines, respectively). Conversely to silver, the gold SPR overlaps with interband transitions leading to an asymmetric shape.

Table 1.4: Plasma resonance $\hbar\omega_p$, surface plasmon resonance ($D = 30$ nm in water) $\hbar\omega_{SPR}$, interband transition threshold $\hbar\Omega_{ib}$, bulk Drude scattering term $\hbar\gamma_0$ and surface scattering correction g in Ag and Au.

metal	$\hbar\omega_p$ (eV)	$\hbar\omega_{SPR}$ (eV)	$\hbar\Omega_{ib}$ (eV)	$\hbar\gamma_0$ (eV)	g
Ag	8.98	3.2	3.95	0.020	0.7
Au	9.01	2.4	2.3	0.067	0.7

For computations, the experimental bulk dielectric functions of Johnson and Christy [25] were used. To take into account modifications to the dielectric functions resulting from quantum confinement (see Sec. 1.1.3), the bulk $\epsilon_2^D(\omega)$, derived from Eq. (1.21) with $\gamma(D = \infty)$ (Eq. (1.26)), is subtracted to the experimental values and replaced by its size-dependent expression $\gamma(D)$ (Eq. (1.26)) [63]. Some optical properties of Ag and Au nanospheres are summarized in Table 1.4.

For out-of-equilibrium investigations, the coefficients in Eq. (1.1), a_1 and a_2 (Figs. 1.10(a) and 1.10(b), dashed and dashed-dotted lines, respectively), can be computed by analytical (dipolar approximation) or numerical derivation (multipolar solution) of the Mie theory spectrum. They are visibly enhanced around the surface plasmon resonance, thus increasing the amplitude of the time-resolved transient optical signals $\Delta\sigma_{ext}$ around the SPR. The

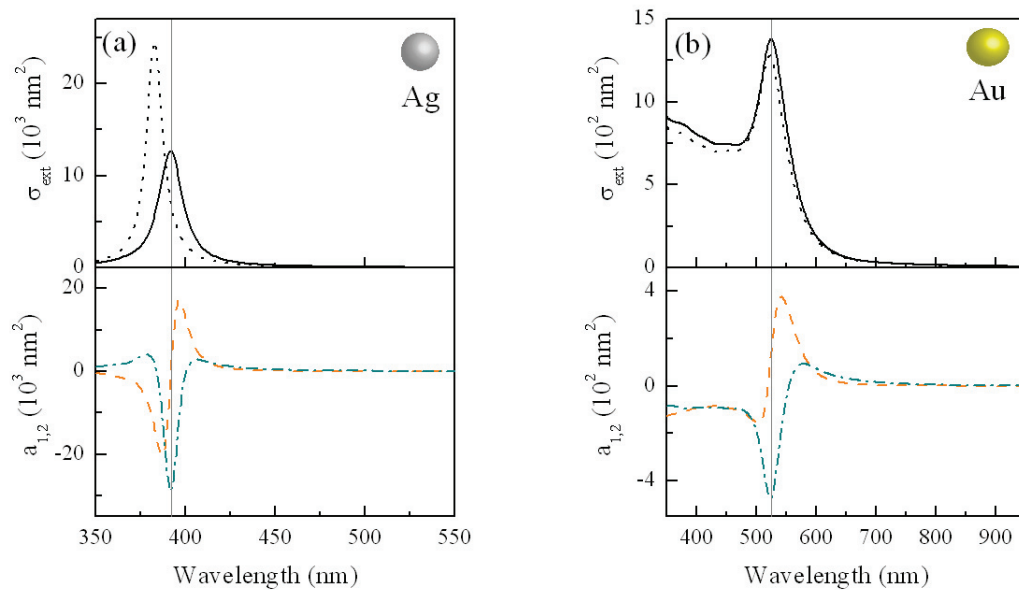


Figure 1.10: Computed extinction cross-sections and their a_1 and a_2 derivatives for a 30 nm diameter Ag (a) and Au (b) sphere in water ($n_m = 1.33$). The vertical gray lines indicate λ_{SPR} , full and dotted black lines correspond to σ_{ext} derived by exact calculations based on Mie theory and on the dipolar approximation (Eq. (1.45)), respectively. a_1 (dashed orange lines) and a_2 (dash-dotted green lines) terms were obtained by derivation of the exact expression of the extinction cross-section with respect to ϵ_1 and ϵ_2 .

SPR position depends sensitively on the matrix through ϵ_m . In Fig. 1.11 one can observe a red-shift for increasing values of $n_m = \sqrt{\epsilon_m}$ concomitantly with an amplitude increase due to the factor $\epsilon_m^{3/2}$ in Eq. (1.45). Eq. (1.45) can be extended to elongated particles [1] leading to a shift of the SPR with the aspect ratio of the elongated nanoobject [39, 58, 64–66].

1.3 Dynamic evolution of excited noble metals

Differential $\Delta\epsilon_{1,2}$ terms in Eq. (1.1) reflect the dynamics of a nanoobject i.e. its temporal response after initial ultrafast excitation by a pump pulse. In this section, after discussion of energy injection into the system and relaxation through electronic interactions we will consider how these kinetics affect the dielectric function of the metal nanoparticles, i.e. induces the transient $\Delta\epsilon_{1,2}(\omega_{pr}, t)$.

1.3.1 Excitation and time evolution of the free electron gas

Excitation of the metal nanoparticles is realized by absorption of the focused pump beam by the free electron gas. The amplitude of the perturbation of a single metal particle can be estimated assuming no dispersion in the ensemble and uniform heating of the sample. In

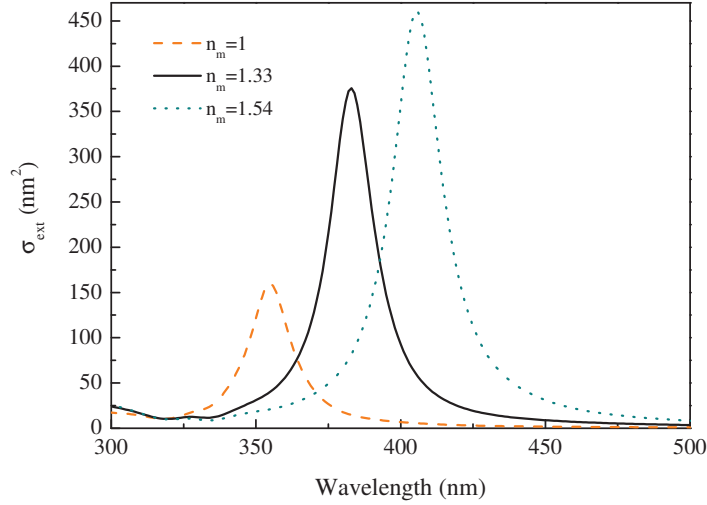


Figure 1.11: Calculated extinction cross-section for a silver nanoparticle ($D = 10$ nm) in vacuum ($n_m = 1$), water ($n_m = 1.33$) and silica ($n_m = 1.54$).

this case, the average energy density per unit volume that is absorbed by one nanoparticle is given by:

$$\Delta u_{exc} = A(\omega_p) \frac{P_p}{f_{rep}} \frac{1}{LpS_p}, \quad (1.49)$$

where P_p corresponds to the power of the pump pulse, $p = n_{np}V_{np}$ the volume fraction of the metal nanoparticles in the sample (V_{np} and n_{np} being their volume and number density respectively), f_{rep} the repetition rate of the ultrafast laser, A the fraction of energy absorbed by the sample and S_p the surface of the focal spot assuming a laser beam with homogenous light intensity in the sample plane. In our studies, all quantities in Eq. (1.49) can be measured experimentally and the average excitation amplitude of the nanoparticles Δu_{exc} can thus be estimated.

Even though an electron temperature cannot be defined briefly after excitation, as the electron gas is initially out-of-equilibrium, the amplitude of the perturbation can be quantified by an equivalent excited temperature, corresponding to the temperature of an electron gas in equilibrium with the same total energy as the excited system:

$$T_{exc} = \sqrt{T_0^2 + \frac{2\Delta u_{exc}}{a}}, \quad (1.50)$$

with T_0 the initial temperature of the system (typically ~ 300 K) and a the electronic heat capacity constant ($a \approx 63$ J/(m³ K²) for bulk Ag and Au [67]), defined in Eq. (1.9). Typically $\Delta T_{exc} = T_{exc} - T_0$ is in the 10-1000 K range.

The energy absorbed by the free electron gas is transferred to the lattice leading to a full thermalization of the nanoparticles. The interaction between electrons and lattice

following thermalization of the former (i.e. for timescales typically exceeding 300 fs [68]) can be described by a simplified approach according to the two temperature model (TTM). Here, the time evolution of the coupled system at temperatures T_e (electrons) and T_L (lattice) is given by a system of rate equations [32, 34, 69–71]:

$$\begin{aligned} c_e(T_e) \frac{\partial T_e}{\partial t} &= -G(T_e - T_L) \\ c \frac{\partial T_L}{\partial t} &= G(T_e - T_L), \end{aligned} \tag{1.51}$$

with $c_e(T_e) = aT_e$ and c the electronic and lattice specific heat per unit volume, respectively (see Eq. (1.9) and Eq. (1.15)). Here, a constant coupling term G has been assumed and the electron gas is initially characterized by its excitation temperature T_{exc} which depends exclusively on the total injected energy, with no memory of the pump photon energy. Other coupling channels, e.g. electron or lattice interaction with the environment have been neglected. Derivating the first term of Eq. (1.51) with respect to t and replacing $c(\partial T_L/\partial t) = -c(T_e)(\partial T_e/\partial t)$ one obtains:

$$T_e \frac{\partial^2 T_e}{\partial t^2} + \left(\frac{\partial T_e}{\partial t} \right)^2 + \frac{G}{a} \left(1 + \frac{a}{c} T_e \right) \frac{\partial T_e}{\partial t} = 0 \tag{1.52}$$

The analytical solution of Eq. (1.52) yields [71]:

$$-G \frac{\tilde{T} + T_{eq}}{2c} t = T_{eq} \ln \left[\frac{T_e - T_{eq}}{T_{exc} - T_{eq}} \right] + \tilde{T} \ln \left[\frac{T_e - \tilde{T}}{T_{exc} - \tilde{T}} \right], \tag{1.53}$$

with $\tilde{T} = T_{eq} + 2T_s$, $T_s = c/a$ and T_{eq} being the equilibrium temperature of the metal, i.e. the common temperature of electron gas and lattice after their thermalization:

$$T_{eq} = \sqrt{T_s^2 + T_{exc}^2 + 2T_s T_0} - T_s. \tag{1.54}$$

For weak electron heating ($\Delta T_{exc} = T_{exc} - T_0 \ll T_0$) one obtains $T_{eq} \approx T_0$. This assumption is equivalent to neglecting the temperature dependence of the electronic heat capacity, i.e. $c_e(T_e) \approx c_e(T_0)$. In this case both electron and lattice temperatures converge exponentially to T_{eq} [35]:

$$\begin{aligned} T_e(t) &= T_{eq} + (T_{exc} - T_{eq}) e^{-t/\tau_{e-ph}} \\ T_L(t) &= T_{eq} - (T_{eq} - T_0) e^{-t/\tau_{e-ph}}, \end{aligned} \tag{1.55}$$

1.3. Dynamic evolution of excited noble metals

where the decay rate $\tau_{e-ph}^{-1} = G/aT_0$ is proportional to the electron-phonon coupling constant G (see Fig. 1.12).

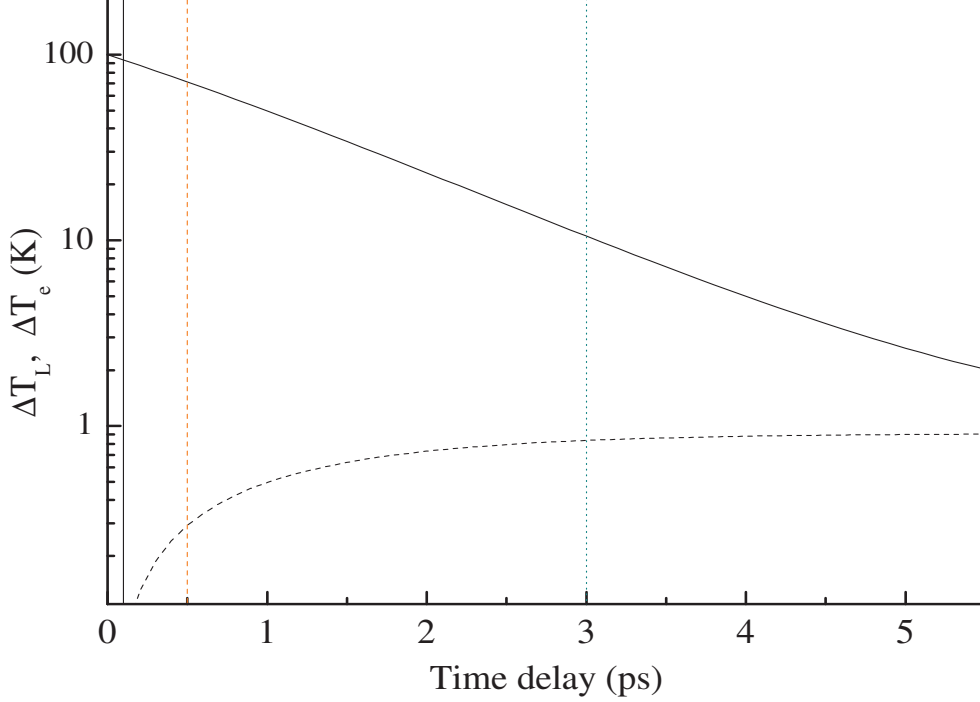


Figure 1.12: $\Delta T_e(t) = T_e(t) - T_0$ equal to 94 K, 71 K and 11 K for a delay of 100 fs (full black line), 500 fs (orange dashed line) and 3 ps (green dotted line), respectively and ΔT_L (0.06 K, 0.39 K and 0.82 K) calculated by the TTM.

For weak excitations, the specific heat per unit volume of the lattice being much higher than the electronic one $c \gg c_e(T_e)$, the equilibrium temperature of the lattice and thus of the whole nanoparticle is only slightly higher than T_0 (Fig. 1.12):

$$T_{eq} - T_0 = \Delta T_L^0 \approx \frac{\Delta u_{exc}}{c}. \quad (1.56)$$

For stronger excitations the T_e dependence of c_e leads to a non-exponential decay of the electron gas temperature, revealing slower dynamics and a strong dependence on T_{exc} [72]. An exponential decay is however obtained for longer times, the weak excitation regime being recovered when the electron gas has sufficiently cooled down [71].

1.3.2 Time-resolved electron distribution changes

Nanoparticles can be excited via intraband or interband transitions, depending on the pump pulse photon energy. In the first case the free electron gas of the conduction band is

excited, the number of conduction electrons being unchanged. Here, coupling of an incident electromagnetic field and electrons initially occurs via the excitation of coherent motion of the quasi-free electron gas. However, these excitations relax into quasi-particle pairs on the short timescale of the electron scattering time $\tau = \gamma^{-1}$ (~ 10 fs in nanoparticles [73–75]). Therefore, for perturbations both in and out of resonance with the SPR only single electron excitations are observed, their relaxation dynamics being described by the quasi-particle approach of the Fermi-liquid theory [22]. In the case of interband excitations ($\hbar\omega_p > \hbar\Omega_{ib}$) the created electron-hole pairs recombine within a few tens of femtoseconds via Auger processes [76, 77] and the electron kinetics can be described in the same way. The model that is presented here has basically been developed for bulk noble metals but it can be used for not too small nanoparticles ($D \geq 3$ nm) with only few modifications.

1.3.2.a The Boltzmann equation

The electron dynamics of an excited metal nanoparticle can thus be described in terms of its conduction electrons being characterized by the time and state-dependent distribution function $f(\vec{k}, t)$. As in bulk materials its variation is given by the Boltzmann equation [68, 78, 79]:

$$\frac{df(\vec{k})}{dt} = \left. \frac{df(\vec{k})}{dt} \right|_{exc} + \left. \frac{df(\vec{k})}{dt} \right|_{e-e} + \left. \frac{df(\vec{k})}{dt} \right|_{e-ph}, \quad (1.57)$$

where the different terms account for the electron occupation number evolution by initial pulse excitation, internal thermalization by electron-electron scattering and electron energy transfer to the lattice via electron-phonon coupling, respectively (Fig. 1.13). In the following, we assume an isotropic parabolic conduction band allowing to express Eq. (1.57) in terms of energies. Before absorption of the pump beam of photon energy $\hbar\omega_p$ the elec-

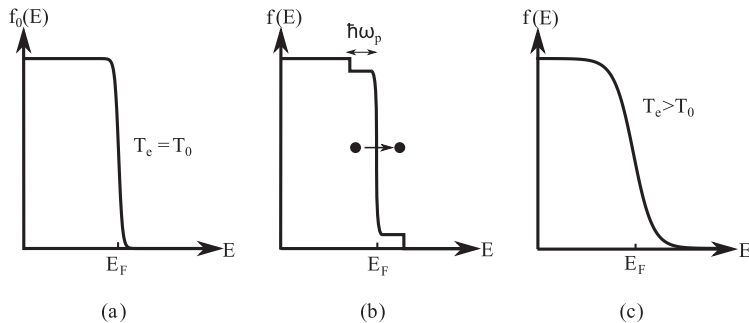


Figure 1.13: Schematic illustration of (a) an equilibrium electron distribution function before excitation, (b) a strongly athermal distribution in the case of instantaneous excitation and (c) a new Fermi distribution, after electron-electron interaction at a higher temperature than the initial one.

tron gas can be described by a thermalized Fermi-Dirac distribution at temperature T_0

1.3. Dynamic evolution of excited noble metals

(room temperature). At $t=0$ the electron gas is excited resulting in an athermal distribution, with a small fraction of electrons having absorbed a photon (typically $\sim 10^{-3}$) and being promoted to energies exceeding E_F whereas the majority still occupies unperturbed states. The electron gas internally thermalizes via electron-electron scattering and can then be described by its temperature $T_e = T_{exc}$ being considerably higher than the lattice temperature T_L . Internal thermalization in bulk materials and large nanoparticles are of the order of 350 fs and 500 fs in silver and gold respectively [68]. The electron excess energy is transferred from the electron gas to the ionic lattice via electron-phonon scattering. This process is typically in the picosecond range (~ 850 fs in Ag and ~ 1.15 ps in Au in the low perturbation regime [80]). Interaction of both electrons and phonons with the surrounding matrix or solvent and thus energy loss of the particle is not considered in Eq. (1.57).

1.3.2.b Electron excitation

The first term in the Boltzmann equation (Eq. (1.57)) accounts for the specific temporal dependence of the excitation pulse (typical durations from 20 to 100 fs). During this process electrons are transferred in the energy range from $E_F - \hbar\omega_p$ to $E_F + \hbar\omega_p$. In nanoparticles the excitation can be considered homogeneous and in the assumption of a parabolic conduction band all states \vec{k} can be described in terms of their energy $E = \hbar^2 k^2 / (2m^*)$. The electron occupation number variation of a state of energy E is given by the sum of the probabilities for electrons to be promoted to higher empty energy levels $E \rightarrow E' > E_F$ and electrons arriving in state E from lower energetic levels $E' < E_F \rightarrow E$:

$$\left. \frac{df(\vec{k})}{dt} \right|_{exc} = \left. \frac{df(E)}{dt} \right|_{exc} = \frac{A_{exc}(t)}{\rho(E)} (dN^+(E) - dN^-(E)), \quad (1.58)$$

with the density of states of the quasi-free electrons given by Eq. (1.5) and A_{exc} being a free parameter proportional to the intensity of the pump beam $I(t)$ which allows to take into account the injected energy into the electron gas of a single nanoparticle. The average number of electrons promoted to and excited from energy level E is given by [36, 68]:

$$\begin{aligned} dN^+(E) &= \rho(E - \hbar\omega_p) f_0(E - \hbar\omega_p) \rho(E) [1 - f_0(E)], \\ dN^-(E) &= \rho(E) f_0(E) \rho(E + \hbar\omega_p) [1 - f_0(E + \hbar\omega_p)], \end{aligned} \quad (1.59)$$

where f_0 is the unperturbed Fermi-Dirac distribution at initial temperature T_0 . Replacing Eq. (1.59) into Eq. (1.58) one obtains:

$$\left. \frac{df(E)}{dt} \right|_{exc} = AI(t) \frac{V}{2\pi^2} \left(\frac{2m^*}{\hbar^2} \right)^{3/2} \times \quad (1.60)$$

$$\left\{ \sqrt{E - \hbar\omega_p} f_0(E - \hbar\omega_p) [1 - f_0(E)] - \sqrt{E + \hbar\omega_p} f_0(E) [1 - f_0(E + \hbar\omega_p)] \right\},$$

where A is a parameter taking into account the electron gas excitation or analogously its equivalent excited temperature T_{exc} (see Eq. (1.50)).

1.3.2.c Electron-electron interaction

Energy redistribution intrinsic to the excited electron gas takes place via electron-electron interactions, being described by a screened Coulomb electromagnetic potential. Two electrons of wave vectors \vec{k} and \vec{k}_2 and energy $E_{\vec{k}}$ and $E_{\vec{k}_2}$ respectively, interact and scatter into states given by \vec{k}_3 and \vec{k}_4 of energy $E_{\vec{k}_3}$ and $E_{\vec{k}_4}$, schematically shown in Fig. 1.14.

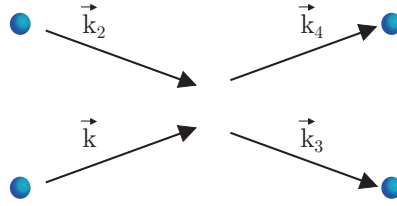


Figure 1.14: Schematic representation of scattering of states \vec{k} and \vec{k}_2 into states \vec{k}_3 and \vec{k}_4 .

The scattering rate of an electron in state \vec{k} can be described as the sum of two terms representing scattering in and out of \vec{k} [78]:

$$\left. \frac{df(\vec{k})}{dt} \right|_{e-e} = \frac{2\pi}{\hbar} \sum_{\vec{k}_2, \vec{k}_3, \vec{k}_4} |M_{e-e}(\vec{k} - \vec{k}_3)|^2 \delta(E_{\vec{k}} + E_{\vec{k}_2} - E_{\vec{k}_3} - E_{\vec{k}_4}) \quad (1.61)$$

$$\times \delta(\vec{k} + \vec{k}_2 - \vec{k}_3 - \vec{k}_4) \left\{ F^{in}(\vec{k}, \vec{k}_2, \vec{k}_3, \vec{k}_4) - F^{out}(\vec{k}, \vec{k}_2, \vec{k}_3, \vec{k}_4) \right\}.$$

The matrix element M_{e-e} describes interaction between initial and final Bloch states while $F^{in} = [1 - f(\vec{k})][1 - f(\vec{k}_2)]f(\vec{k}_3)f(\vec{k}_4)$ and $F^{out} = f(\vec{k})f(\vec{k}_2)[1 - f(\vec{k}_3)][1 - f(\vec{k}_4)]$ represent the Pauli principle for scattering in and out of the one electron states characterized by \vec{k} . Neglecting *Umklapp* processes and assuming a screened Coulomb potential, one gets:

$$|M_{e-e}(\vec{k} - \vec{k}_3)| = \frac{e^2}{V |\vec{k} - \vec{k}_3|^2 \epsilon_0 \left| \epsilon(\vec{k} - \vec{k}_3, E_{\vec{k}} - E_{\vec{k}_3}) \right|}. \quad (1.62)$$

1.3. Dynamic evolution of excited noble metals

Using Lindhard theory for screening in the static approximation ($\hbar\omega = E_{\vec{k}} - E_{\vec{k}_3} = 0$) and for small momentum exchange during collision ($\vec{q} = \vec{k} - \vec{k}_3$), the dielectric constant in Eq. (1.62) writes:

$$\epsilon(\vec{q}, \hbar\omega) \approx \epsilon(\vec{q}, 0) = \epsilon_0^{ib} \left(1 + \frac{q_S^2}{q^2} \right), \quad (1.63)$$

with ϵ_0^{ib} the interband constant due to screening by the core electrons (equal to 3.7 and 6.7 for Au and Ag, respectively [68]). The second term in Eq. (1.63) describes screening by the conduction electrons with q_{TF} the Thomas-Fermi wave vector, given by:

$$q_{TF}^2 = \frac{-e^2}{V\epsilon_0\epsilon_0^{ib}} \sum_{\vec{k}} \frac{\partial f}{\partial E}(\vec{k}). \quad (1.64)$$

The static approximation overestimates screening, and as a correction an adjustable parameter β , yielding $q_S = \beta q_{TF}$, has been used. For both silver and gold bulk and large nanoparticles the best reproduction of time-resolved pump-probe signals was found with $\beta=0.73$ in agreement with time-resolved two-photon photoemission measurements [68]. In the simulations in the context of this work β was fixed to this value.

As a consequence of the assumption of a parabolic conduction band the sum in Eq. (1.61) can be expressed as energy integral [36, 68]:

$$\begin{aligned} \left. \frac{df(E)}{dt} \right|_{e-e} &= \frac{e^4 m^*}{32\pi^3 \hbar^3 (\epsilon_0^2 \epsilon_0^{ib})^2 E_S \sqrt{E}} \int \int dE_2 dE_3 (F^{in}(E, E_2, E_3, E_4) - F^{out}(E, E_2, E_3, E_4)) \\ &\quad \times \left[\frac{\sqrt{\tilde{E}}}{\tilde{E} + E_S} + \frac{1}{\sqrt{E_S}} \arctan \sqrt{\frac{\tilde{E}}{E_S}} \right]_{\tilde{E}_{min}}^{\tilde{E}_{max}}, \end{aligned} \quad (1.65)$$

with $E_S = \hbar^2 q_S^2 / 2m^*$. The limits are determined by energy and momentum conservation, given by:

$$\begin{aligned} \tilde{E}_{max} &= \min \left\{ \left(\sqrt{E_2} + \sqrt{E_4} \right)^2, \left(\sqrt{E} + \sqrt{E_3} \right)^2 \right\}, \\ \tilde{E}_{min} &= \max \left\{ \left(\sqrt{E_2} - \sqrt{E_4} \right)^2, \left(\sqrt{E} - \sqrt{E_3} \right)^2 \right\}. \end{aligned} \quad (1.66)$$

This last equation is used in numerical simulations. β being fixed to the results on bulk Au and Ag [68], no free parameter is used to describe electron-electron interactions in noble metals.

1.3.2.d Electron-phonon interaction

Interaction between electrons and the lattice are included in the third term of the Boltzmann equation. Electrons can scatter from a particular state \vec{k} of energy $E_{\vec{k}}$ to another

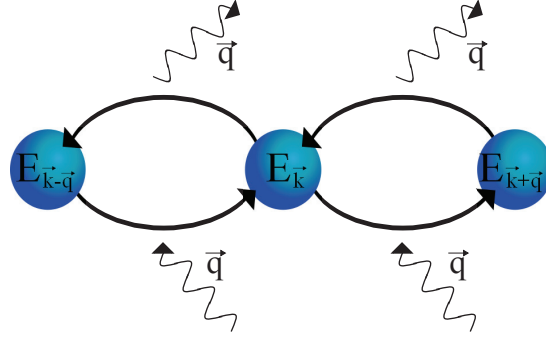


Figure 1.15: Scheme of phonon (\vec{q}) emission and absorption. Both processes can lead to scattering in or out of the electron state \vec{k} . Energy and wave vector conservation is assumed in the figure.

state \vec{k}' and $E_{\vec{k}'}$ by absorption or emission of a phonon with a scattering rate:

$$\left. \frac{df(\vec{k})}{dt} \right|_{e-ph} = \sum_{\vec{q}} \gamma_{\vec{q}}^{em}(\vec{k}) + \gamma_{\vec{q}}^{abs}(\vec{k}), \quad (1.67)$$

with $\gamma_{\vec{q}}^{em}$ and $\gamma_{\vec{q}}^{abs}$ corresponding to phonon emission and absorption rates. According to Fermi's golden rule one obtains:

$$\begin{aligned} \gamma_{\vec{q}}^{em}(\vec{k}) = \frac{2\pi}{\hbar} |M_{e-ph}(q)|^2 (1 + N_{\vec{q}}) & \left(-\delta(E_{\vec{k}} - \hbar\omega_{\vec{q}} - E_{\vec{k}-\vec{q}}) f(\vec{k}) [1 - f(\vec{k} - \vec{q})] \right. \\ & \left. + \delta(E_{\vec{k}+\vec{q}} - \hbar\omega_{\vec{q}} - E_{\vec{k}}) f(\vec{k} + \vec{q}) [1 - f(\vec{k})] \right), \end{aligned} \quad (1.68)$$

with $N_{\vec{q}}$ the Bose-Einstein statistics of a phonon of energy $\hbar\omega_{\vec{q}}$ (Eq. (1.14)), and $|M_{e-ph}(q)|$ the effective electron-phonon matrix element, which can be described by a deformation potential. In this picture the energy of the bottom of the electron conduction band changes linearly with lattice deformation and the matrix element can be expressed as [78]:

$$|M_{e-ph}(q)|^2 = \frac{\hbar^2 \Xi^2 q^2}{2\rho V \hbar\omega_{\vec{q}}}, \quad (1.69)$$

with ρ the metal mass density and Ξ a parameter determining the amplitude of the deformation potential.

1.3. Dynamic evolution of excited noble metals

Phonon absorption provides a term similar to emission but with a factor $N_{\vec{q}}$, yielding:

$$\begin{aligned} \gamma_{\vec{q}}^{abs}(\vec{k}) = \frac{2\pi}{\hbar} |M_{e-ph}(q)|^2 N_{\vec{q}} & \left(-\delta(E_{\vec{k}+\vec{q}} - \hbar\omega_{\vec{q}} - E_{\vec{k}}) f(\vec{k}) [1 - f(\vec{k} + \vec{q})] \right. \\ & \left. + \delta(E_{\vec{k}} - \hbar\omega_{\vec{q}} - E_{\vec{k}-\vec{q}}) f(\vec{k} - \vec{q}) [1 - f(\vec{k})] \right). \end{aligned} \quad (1.70)$$

The summation of \vec{q} can be replaced by an integral over a sphere of radius $q_D = \sqrt[3]{2}k_F$ (see Sec. 1.1.1). As it has been shown in the past [68], the electron-phonon coupling is at first order insensitive to the phonon band structure and we assume thus a sinusoidal dispersion relation $\hbar\omega_{\vec{q}} = \hbar\omega_q = \hbar\omega_M \sin(\pi q/(2q_D))$. Together with the parabolic dispersion for the electron conduction band Eq. (1.67) can be expressed by [36, 68]:

$$\left. \frac{df(E)}{dt} \right|_{e-ph} = \frac{\sqrt{m^*}\Xi^2}{4\sqrt{2}\pi\hbar\rho\sqrt{E}} \int_0^{\sqrt[3]{2}k_F} dq \frac{q^3}{\omega_M \sin\left(\frac{\pi q}{2q_D}\right)} [(1 + N_q)F_q^{em}(E) + N_q F_q^{abs}(E)], \quad (1.71)$$

where the factors F_q^{em} and F_q^{abs} are given by:

$$\begin{aligned} F_q^{em}(E) &= -f(E)[1 - f(E - \hbar\omega_q)] + f(E + \hbar\omega_q)[1 - f(E)], \\ F_q^{abs}(E) &= -f(E)[1 - f(E + \hbar\omega_q)] + f(E - \hbar\omega_q)[1 - f(E)]. \end{aligned} \quad (1.72)$$

The deformation potential method constitutes a simple and convenient model for the description of electron-phonon interactions in the Boltzmann equation. However, it should be kept in mind that this way of describing the electron-phonon matrix element is an approximation being only valid for emission or absorption of short wave vector phonons. Moreover we have neglected *Umklapp* processes and assumed a spherical Fermi surface. To account for these approximations, an effective value of the deformation potential parameter Ξ_{eff} is used instead of the theoretical one in order to reproduce the experimental relaxation value measured in noble metals. For bulk metals, this yields $\Xi_{eff} = 0.8\Xi$ [36, 68].

In small nanoparticles, size-dependent effects taking into account the experimentally measured modifications of electron-phonon coupling are introduced by using a size-dependent value of Ξ_{eff} .

1.3.2.e Numerical simulations

The numerical solution of the Boltzmann equation (Eq. (1.57)) yields the electronic variations after ultrafast optical excitation. Table 1.5 summarizes the parameters used for calculations in bulk systems. Size effect in nanoparticles can be taken into account via a modification of Ξ_{eff} (Sec. 1.3.2.d), which directly affects τ_{e-ph} .

Chapter 1. Linear and ultrafast properties of noble metal nanoparticles

Table 1.5: Parameters for bulk silver and gold used for the computations of the electron-electron and electron-phonon interaction terms of the Boltzmann equation.

metal	ϵ_0^{ib}	β	τ_{e-ph} (ps)
Ag	3.7	0.73	0.87
Au	6.7	0.73	1.15

As an example, the computed $\Delta f(E, t) = f(E, t) - f_0(E)$ relative to the Fermi energy E_F for bulk Au is depicted in Fig. 1.16 for different time delays $t = 100$ fs, 500 fs and 3 ps after an initial 50 fs (FWHM) pump pulse excitation at 850 nm and an equivalent electron temperature increase $\Delta T_{exc} = 100$ K. As expected, at short timescales, the pump pulse directly promotes electrons from occupied states with energies lower than the Fermi level to unoccupied states above, modifying the occupation number of states in a broad energy band ranging from $E_F - \hbar\omega_p$ to $E_F + \hbar\omega_p$ (full black line in Fig. 1.16, corresponding to $t = 100$ fs). Fast electron internal thermalization progressively leads to the build up of a narrower Δf distribution centered around E_F (orange dashed line, $t = 500$ fs) before electron energy loss by electron-phonon coupling dominates and Δf progressively vanishes (green dotted line, $t = 3$ ps).

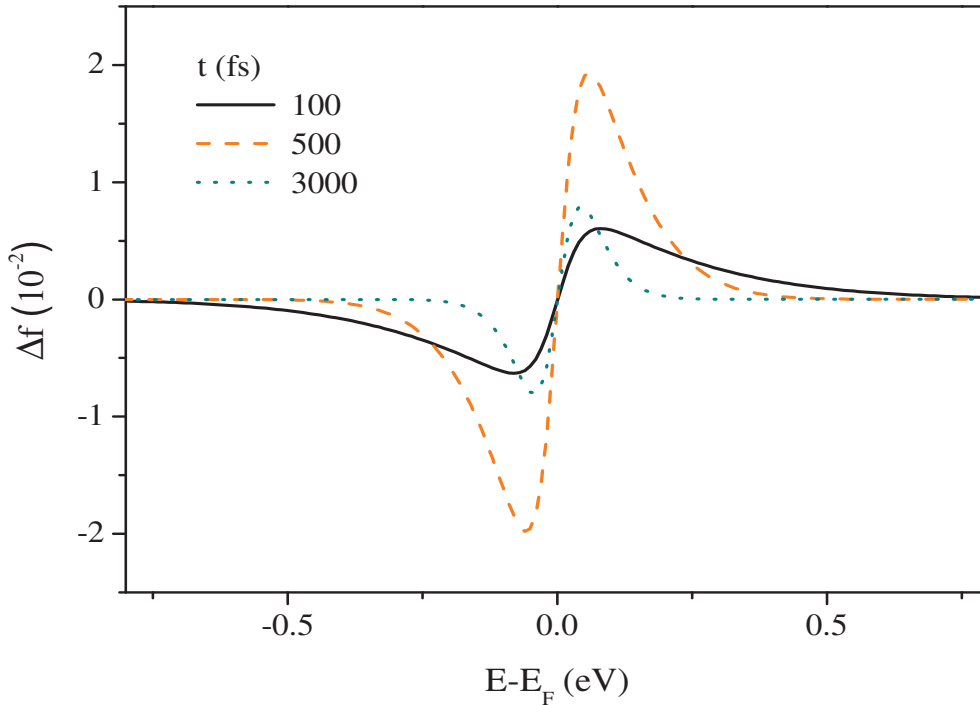


Figure 1.16: Computed electron gas distribution change in bulk silver for a 50 fs (FWHM) pump pulse excitation at 850 nm and an equivalent electron temperature increase of $\Delta T_{exc} = 100$ K.

1.4 Time-dependent metal dielectric function changes

The ultrafast optical response of a metal nanoparticle is ruled by the transient variations of its dielectric functions, $\Delta\epsilon_{1,2}$ (Eq. (1.1)). These are a consequence of the modification of the electron distribution, which induces a change in the interband term (dominant on the short timescale) and the Drude term, and of the concomitant heating of the lattice (this effect being more significant on a longer timescale).

1.4.1 Electronic contribution

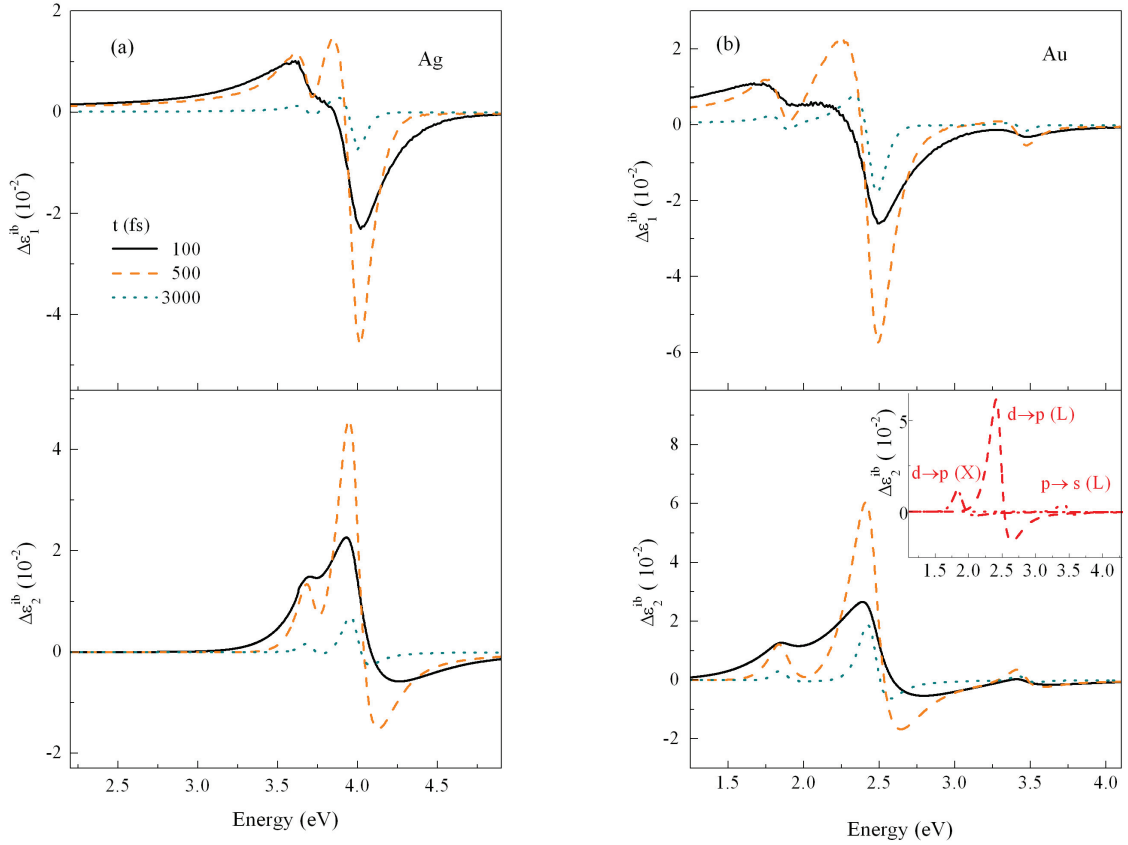


Figure 1.17: Computed changes of the imaginary and real part of the interband dielectric function $\epsilon_{1,2}$ of bulk gold (a) and silver (b) for different probe delays following excitation by a 50 fs pump pulse, electron temperature increase $\Delta T_{exc} = 100$ K and pump wavelength 850 nm. The inset in (b) shows the contribution of $d \rightarrow p$ (L), $p \rightarrow s$ (L) and $d \rightarrow p$ (X) to $\Delta\epsilon_2^{ib}$ for a probe delay of 500 fs.

Modifications of the electron occupation number Δf (see Eq. (1.57)) directly reflect into a change of the imaginary part of the metal interband dielectric function $\Delta\epsilon_2^{ib}(\omega_{pr}, t)$ (Eq. (1.36), Eq. (1.37) and Eq. (1.40), where $[1 - f(E)]$ and $f(E)$ are replaced by the time-dependent $\Delta f(E, t)$). The real part $\Delta\epsilon_1^{ib}(\omega_{pr}, t)$ can be subsequently deduced by

Kramers-Kronig transformation [1], given by:

$$\Delta\epsilon_1^{ib}(\omega_{pr}, t) = \frac{2}{\pi} P \int_0^\infty \frac{\omega' \Delta\epsilon_2^{ib}(\omega', t)}{\omega'^2 - \omega_{pr}^2} d\omega', \quad (1.73)$$

where P designs the Cauchy principal value of the integral. In contrast to the stationary dielectric function this integration is possible, the transient $\Delta\epsilon_2^{ib}$ being different from zero only around the interband threshold. The calculated transient $\Delta\epsilon_1^{ib}$ and $\Delta\epsilon_2^{ib}$ spectra are shown in Figs. 1.17(a) and 1.17(b) for both Ag and Au for a probe delay of 100 fs, 500 fs and 3 ps after ultrafast excitation by a 50 fs pump pulse. For both metals, the dynamical behavior of $\Delta\epsilon_{1,2}^{ib}$ follows the kinetics of the electron distribution change Δf . While the spectral shapes are flat for short time delays, they become sharper around the interband transition energies during internal thermalization, before decreasing. The peaks of $\Delta\epsilon_2^{ib}$ correspond to the distinct interband transitions of the metals (see Sec. 1.1.4). For Au the contributions of d \rightarrow p (L), p \rightarrow s (L) and d \rightarrow p (X) transitions are depicted in the inset of Fig. 1.17(b), the former having, as expected the largest amplitude.

Electron excitation also affects the Drude contribution of the dielectric function $\Delta\epsilon_{1,2}^D$, which is a consequence of the dependence of all scattering rates in the Drude formula on the electron temperature T_e (see Eq. (1.24), Eq. (1.25) and Eq. (1.26)). A change of the scattering rate mostly affects the imaginary part of the Drude dielectric constant (Eq. (1.22)), yielding:

$$\Delta\epsilon_2^D \approx \frac{\omega_p^2}{\omega^3} \Delta\gamma. \quad (1.74)$$

Variations of γ with electron temperature are dominated by the electron-electron scattering term $\Delta\gamma_{e-e}$, whose T_e dependence can be expressed as [34, 37]:

$$\frac{\Delta\gamma_{e-e}(T_e)}{\gamma_{e-e}} \approx \left(\frac{2\pi k_B}{\hbar\omega} \right)^2 (T_e^2 - T_0^2). \quad (1.75)$$

The temperature dependence of γ_{e-S} (Eq. (1.26)) is a consequence of the modification of the surface factor g (Eq. (1.27)) which is dependent on the variations of the electron occupation number Δf . $\Delta\epsilon_2^D$ for a 30 nm Au nanoparticle induced by modifications in γ_{e-e} (with $\hbar\gamma_{e-e} \approx 15$ meV, [31]) and γ_{e-S} are shown in Figs. 1.18(a) and 1.18(b), respectively. For smaller particles, the γ_{e-S} contribution to ϵ_1^{ib} can become more important for short time delays (see Eq. (1.26)).

1.4. Time-dependent metal dielectric function changes

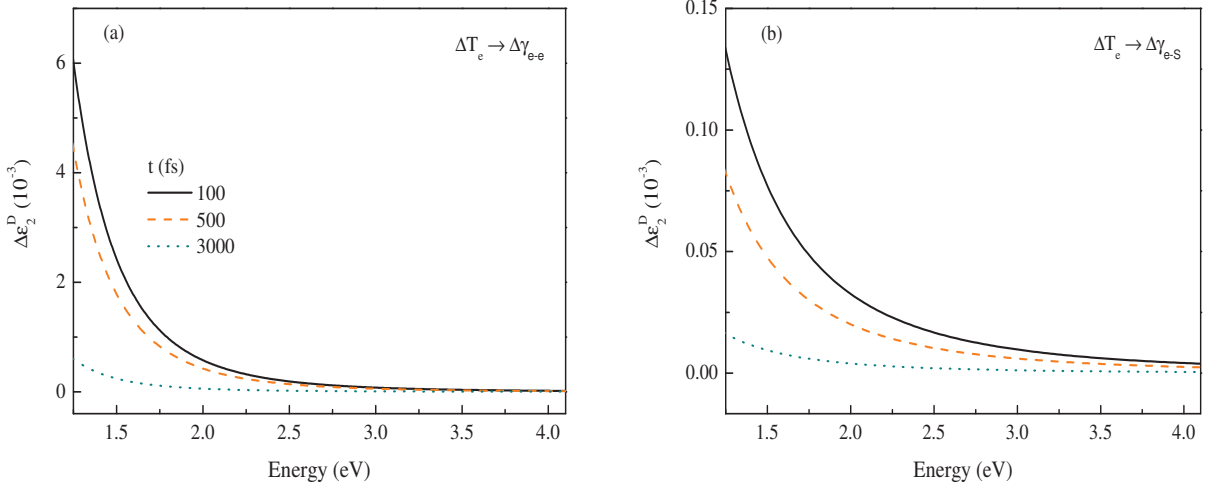


Figure 1.18: Computed changes of the Drude contribution to the dielectric function of Au (imaginary part) as a consequence of electron gas heating through modifications of γ_{e-e} (a) and γ_{e-S} (b) for a 30 nm nanosphere. Excitation conditions were the same as in Figs. 1.17(a) and 1.17(b) (50 fs pump pulse, electron temperature increase $\Delta T_{exc} = 100$ K and pump wavelength 850 nm).

1.4.2 Lattice contribution

After thermalization with the lattice (occurring within a few ps) the electron temperature has decreased to a new equilibrium value $T_e = T_L = T_{eq}$ and the direct contribution of excited electron dynamics to $\Delta\epsilon_{1,2}$ becomes negligible. Nevertheless the metal dielectric functions have not yet relaxed to their equilibrium values, due to their sensitivity to the lattice temperature rise and the concomitant metal dilation, both decaying with cooling by energy transfer to the environment. The change of the dielectric functions can be directly related to the lattice temperature rise by $\Delta\epsilon_{1,2} = (d\epsilon_{1,2}/dT_L)\Delta T_L$. In order to model the temperature dependence of the dielectric constants $d\epsilon_1/dT_L$ and $d\epsilon_2/dT_L$ one must have a closer look at the modifications of both interband and Drude contributions to $\epsilon_{1,2}$.

Particle dilation leads to an increase of the inter-atomic distance which translates into a shift of the Fermi level as well as a modification of the energy band structure. The effect on $\Delta\epsilon_{1,2}^{ib}$ can be estimated through the different $\epsilon_{2,l}^{ib}$ contributions (e.g. d \rightarrow p around the L point, Figs. 1.9(a) and 1.9(b)), by taking into account the displacement of the individual interband transition thresholds $\Omega_{ib,l}$, assuming a rigid band shift with dilation [34, 35]:

$$\Delta\epsilon_2^{ib}(\hbar\omega, t) = \sum_l \left(\frac{\partial\epsilon_{2,l}^{ib}}{\partial(\hbar\omega)} \frac{d(\hbar\Omega_{ib})}{dT_L} \right) \Delta T_L(t) = - \sum_l \left(\frac{\partial\epsilon_{2,l}^{ib}}{\partial(\hbar\omega)} \frac{d(\hbar\Omega_{ib})}{dT_L} \right) \Delta T_L(t). \quad (1.76)$$

The term $d(\hbar\Omega_{ib})/dT_L$ is estimated from temperature-dependent ellipsometric measurements on the bulk metals, yielding in the case of Au $d(\hbar\Omega_{ib})/dT_L \approx -1.7 \times 10^{-4}$ eV/K

and -3.2×10^{-4} eV/K for the d-band to Fermi energy transition around the L and X point of the Brillouin zone, respectively (the contribution of the transition from Fermi energy to the s-band around the L point is smaller and its dependence on T_L is neglected here) [81]. The derivatives $\partial\epsilon_{2,l}^{ib}/\partial(\hbar\omega)$ are numerically deduced from the fit of the experi-

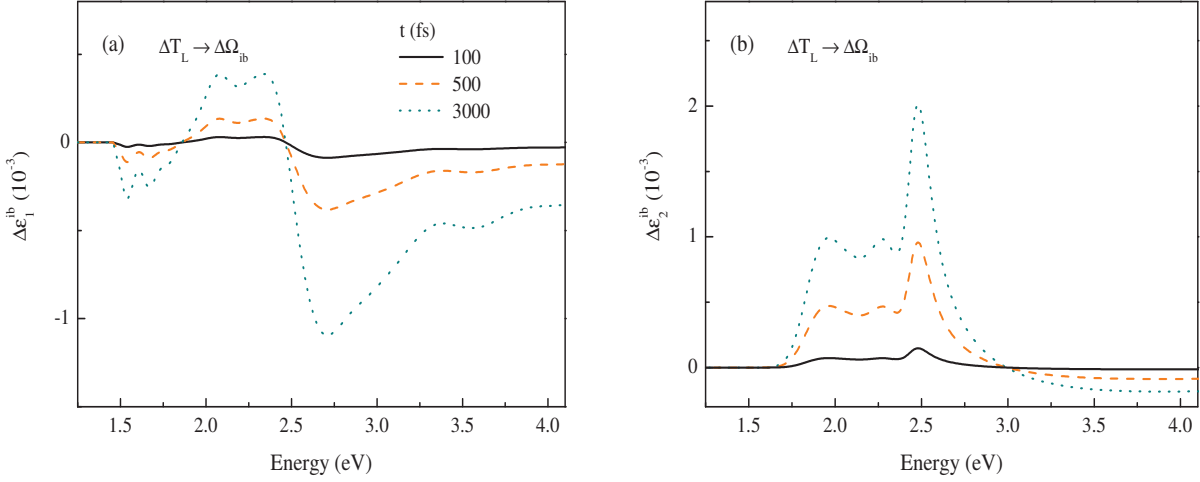


Figure 1.19: Computed changes of the interband dielectric function of Au induced by a rigid band shift due to lattice heating for different time delays after excitation in the same conditions as in Figs. 1.17(a) and 1.17(b) (50 fs pump pulse, electron temperature increase $\Delta T_{exc} = 100$ K and pump wavelength 850 nm).

mental bulk dielectric functions (Figs. 1.9(a) and 1.9(b)). In parallel, the ϵ_1^{ib} contribution is estimated by derivation of the Johnson and Christy bulk experimental data after subtraction of the Drude part [25]. The resulting changes $\Delta\epsilon_{1,2}^{ib}$ for gold are illustrated in Figs. 1.19(a) and 1.19(b). Real and imaginary interband parts of the dielectric function show some structures around the onset of the interband transitions, their contribution increasing with lattice temperature.

Lattice dilation does not only affect the metal interband transitions but also reduces the conduction electron density n (Fig. 1.20(a)). This has an impact on the real part of the intraband dielectric constant described by the Drude formula (Eq. (1.22)), leading to:

$$\Delta\epsilon_1^D \approx -\frac{\omega_p^2}{\omega^2} \frac{\Delta n}{n} \Delta T_L = \frac{\omega_p^2}{\omega^2} 3\alpha_L \Delta T_L, \quad (1.77)$$

with α_L the metal linear dilation coefficient ($1.42 \times 10^{-5}/\text{K}$ and $1.89 \times 10^{-5}/\text{K}$ for gold and silver respectively [22]). Additionally, lattice temperature increase changes $\Delta\epsilon_2^D$ via the scattering rate γ (Fig. 1.20(b)). In the thermalized particle this affects mainly γ_{e-ph} due to an increase of the phonon occupation number. Its variation with T_L can be expressed as $\Delta\gamma_{e-ph} = (\partial\gamma_{e-ph}/\partial T_L) \Delta T_L$, with $\partial(\hbar\gamma_{e-ph})/\partial T_L \approx 0.125$ meV/K and 0.057 meV/K

1.5. Ultrafast response of an ensemble of metal nanoobjects

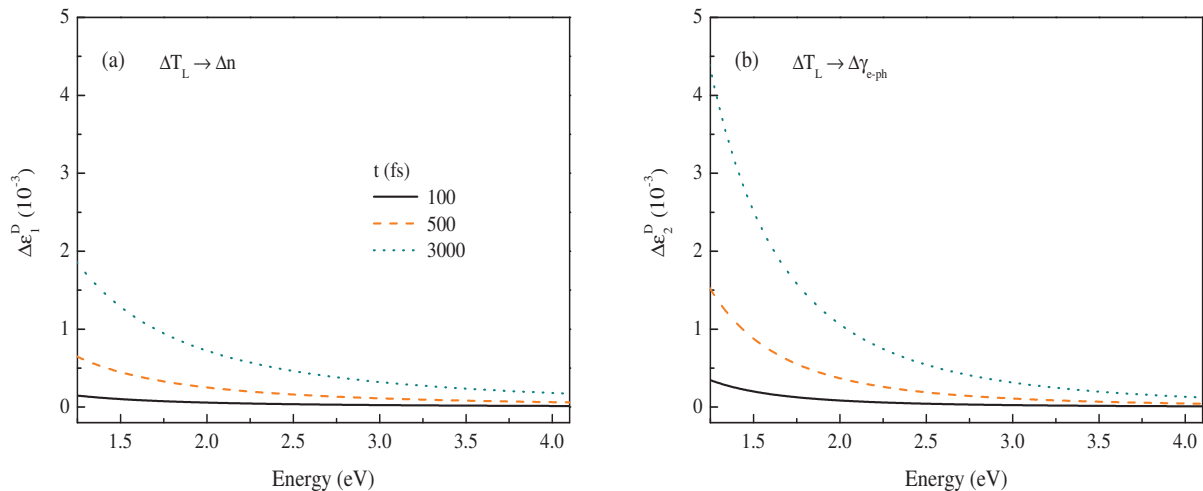


Figure 1.20: Computed modifications of the real and imaginary Drude contribution to the dielectric function due to changes in the density Δn (a) and in the electron-phonon scattering rate $\Delta \gamma_{e-ph}$ (b) as a consequence of lattice heating for different time delays after excitation by a 50 fs and 850 nm pump pulse with electron temperature increase $\Delta T_{exc} = 100$ K (similar to Figs. 1.17(a) and 1.17(b)).

for Au and Ag [82]. It is worth mentioning that lattice heating induces comparable modifications of both the interband (electron band shift) and intraband (change of electronic density and electron-phonon scattering) contributions (Figs. 1.19(a)-(b) and 1.20(a)-(b)). This sensitivity of $\epsilon_{1,2}^{ib}$ and ϵ_2^D to lattice temperature change is also responsible for the optical detection of acoustic vibrations of nano-objects (inducing periodic volume changes) [3, 17, 61, 83, 84]. Thermoreflectance experiments on thin gold films have been done in the past for determining the stationary $d\epsilon_{1,2}/dT_L$ variations [85–87]. Summing up interband and Drude-like contributions to $d\epsilon_{1,2}/dT_L$ (Figs. 1.19 and 1.20), a relatively good agreement with the experimental data was found (Fig. 1.21) [87]. The estimated and measured energy dispersions are very similar, the residual discrepancy in the absolute values of these derivatives being possibly due to uncertainties in the values of the parameters used in the previously estimated contributions or to possible modifications not taken into account in this model, such as changes in the electron effective mass [88].

1.5 Ultrafast response of an ensemble of metal nanoobjects

The transient modification of the extinction cross-section $\Delta \sigma_{ext}$ in the context of time-resolved experiments in Ag and Au are computed using Eq. (1.1) by multiplying the nanoparticle derivative coefficients $a_{1,2}(\hbar\omega_{pr})$, determined from their linear absorption

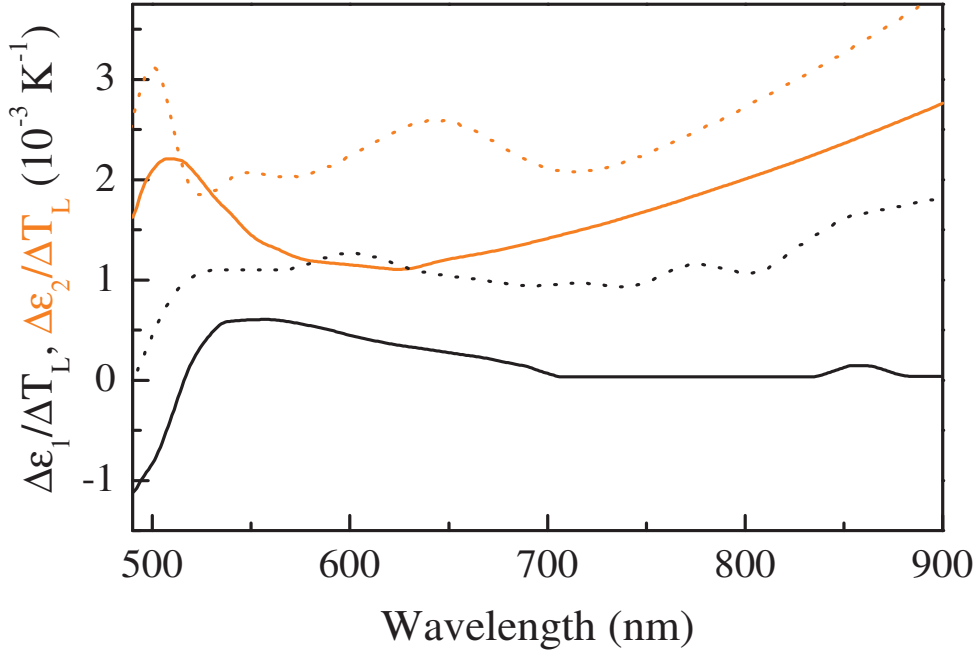


Figure 1.21: Theoretical (dotted lines) and experimental (full lines) temperature derivatives of the gold dielectric function. Theory is presented in the text as the sum of Drude and interband contributions of $\Delta\epsilon_{1,2}$. Experimental values have been deduced from Ref. [87].

spectrum (Sec. 1.2, Figs. 1.10(a) and (b)) with the dielectric function changes $\Delta\epsilon_{1,2}(\hbar\omega_{pr}, t)$, taking into account both interband and Drude contributions (Sec. 1.4).

In the case of silver nanospheres (Fig. 1.22(a)), transient spectral features are centered around two distinct positions, namely $\hbar\omega_{SPR}$ (~ 3.2 eV) and Ω_{ib} (~ 3.95 eV). The former highlights the enhancement of the time-resolved response by plasmonic effects (high $a_{1,2}$ derivatives near SPR, Fig. 1.10(a)). The latter is similar to that of bulk silver [68] and reflects modifications of the electron distribution around the Fermi energy and subsequent heating of the metal (Fig. 1.17(a)). In the spectral region around Ω_{ib} , a_1 and a_2 are small and undispersed and $\Delta\sigma_{ext}$ basically reflects the dispersion of $\Delta\epsilon_1^{ib}$ and $\Delta\epsilon_2^{ib}$, determined by electron internal thermalization and cooling (Fig. 1.17(a)). Around ω_{SPR} , spectrally separated from Ω_{ib} for Ag nanospheres, $\Delta\epsilon_2^{ib}$ vanishes except for very short time delays and the time behavior of $\Delta\sigma_{ext}$ essentially follows that of $\Delta\epsilon_1^{ib}$, which is approximately proportional to the particle electron excess energy density [17, 41, 89]. As a result, far from interband transitions, $\Delta\sigma_{ext}$ increases with energy injection in the electrons and decays with the electron energy loss to the lattice. For longer delays, during electron-lattice thermalization, the spectral shape of $\Delta\sigma_{ext}$ is modified. Interband $\Delta\epsilon_{1,2}^{ib}$ contributions, which mainly depend on the electron temperature T_e , become negligible and the strongest

1.5. Ultrafast response of an ensemble of metal nanoobjects

contributions result from the Drude terms $\Delta\epsilon_1^D$, proportional to lattice dilation, and $\Delta\epsilon_2^D$ reflecting the increase of the electron-phonon scattering rate. The latter being dominant, the $\Delta\sigma_{ext}$ spectral shape reflects that of a_2 (Figs. 1.10(a) and 1.22(a)).

In the case of a gold sphere, spectral overlap between the SPR and interband transitions (Figs. 1.10(b) and 1.17(b)) reflects for short time delays in a specific spectral shape of the $\Delta\sigma_{ext}$ response, characterized by a profile with two zero crossings (Fig. 1.22(b)). For longer delays, as before, interband terms $\Delta\epsilon_{1,2}^{ib}$ become negligible as compared to intraband ones and $\Delta\sigma_{ext}$ recovers a spectral dependence proportional to a_2 .

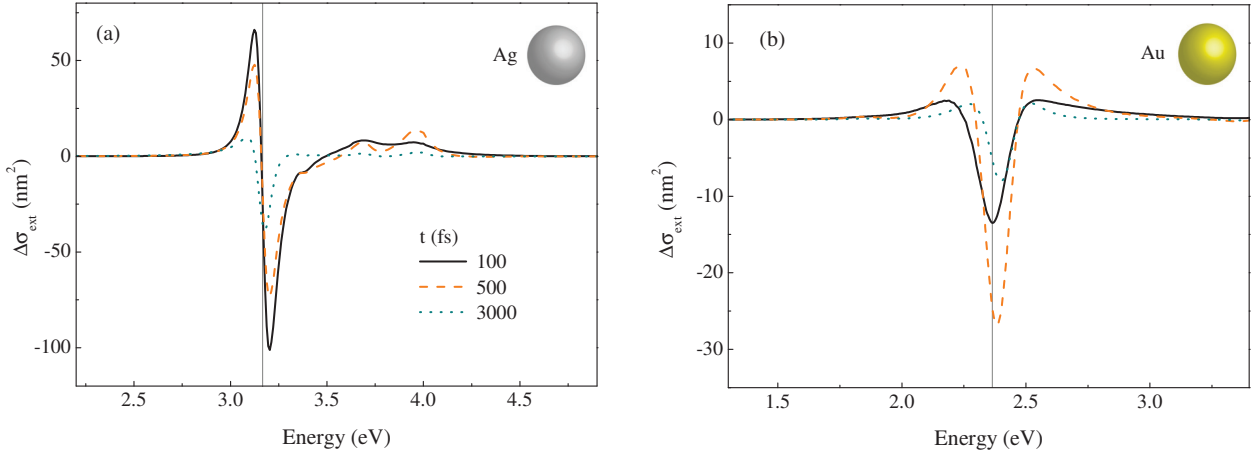


Figure 1.22: Computed extinction cross-section changes for the same Ag (a) and Au (b) nanospheres as in Figs. 1.10(a) and 1.10(b) for different delays after excitation by a 50 fs and 850 nm ultrafast pump pulse ($\Delta T_{exc} = 100$ K) using Eq. (1.1). The vertical gray lines correspond to ω_{SPR} .

The considerations developed in this section describe the transient behavior of a single nanoobject $\Delta\sigma_{ext}$, which is experimentally measurable [90]. They can be extended to investigations performed on nanoparticle ensembles, either glass-embedded or dispersed in a liquid. For small size and shape distributions and polarization-independent pump absorption (e.g. nanospheres), the transmitted power P_t of the probe beam can be expressed by $P_t(\omega_{pr}, t) = P_i \exp[-\alpha(\omega_{pr}, t)L]$, P_i being the incoming power, $\alpha(\omega_{pr}, t) = n_{np} \bar{\sigma}_{ext}(\omega_{pr}, t)$ the absorption coefficient, L the thickness of the sample (glass or cuvette), n_{np} the number density of the nanoparticles in the sample and $\bar{\sigma}_{ext}$ the mean value of their extinction cross-section. The experimentally measured relative differential transmission change can then be related to extinction cross-section changes by:

$$\frac{\Delta T}{T}(\omega_{pr}, t) = \frac{P_t(\omega_{pr}, t) - P_t(\omega_{pr}, -\infty)}{P_t(\omega_{pr}, -\infty)} \approx -\Delta\alpha(\omega_{pr}, t)L \approx -n_{np}L\Delta\bar{\sigma}_{ext}(\omega_{pr}, t), \quad (1.78)$$

Chapter 1. Linear and ultrafast properties of noble metal nanoparticles

where ΔT is defined as the sample transmission change at probe delay t , as compared to the unperturbed transmission.

Chapter 2

Size dependence of electronic interactions in metal clusters

Fundamental studies on different materials have allowed to determine both experimentally and theoretically by which mechanisms size reduction affects physical properties. In the case of metal nanoparticles, the most striking effect of spatial confinement is the appearance of the localized surface plasmon resonance (SPR) [1]. However, size reduction to the nanometric scale also impacts the internal ultrafast dynamic processes in the confined metal. In this context, femtosecond time-resolved optical pump-probe spectroscopy has been used to investigate the ultrafast transient electron dynamics in thin metal films [68, 79, 89] and nanoparticles [17, 41, 84]. Such pump-probe experiments constitute a far-field contact-free tool to investigate these processes with a very high temporal resolution.

The study of internal electron thermalization dynamics and electron-phonon coupling dynamics has been performed in the past on glass-embedded nanospheres of intermediate size range (3-30 nm diameter), modifications of both these dynamics being found to be mostly induced by classical effects of dielectric confinement and screening of electronic interactions close to the surfaces [5, 16–18]. The situation is expected to be different for even smaller sizes (below around 2 nm, ~ 250 atoms), where an increasing role of quantization is expected, leading to an evolution from a bulk-like behavior (quasi-continuum of electronic states in the conduction band) to a molecular-like one (discrete energy states). Small nanoparticles can be prepared by both physical and chemical means, leading to different surface conditions (e.g. with or without stabilizing surfactant molecules). Their investigation can be performed on matrix-embedded ensembles or a colloidal solution. While the static optical properties (e.g. optical linear absorption) of clusters with less than a few hundred atoms have been extensively studied [39, 42–44, 91], less investigations have been reported on their electronic dynamic interactions. Only recently, the

study of dynamic processes of functionalized metal clusters dispersed in organic solvents has been performed [92–98].

In this chapter we report experiments on silica-embedded surfactant-free small Ag nanospheres ($D \sim 1\text{-}3\text{ nm}$) and thiol-protected, atomically defined Au clusters in a solvent. They are based on time-resolved pump-probe investigations of their size-dependent electronic relaxation dynamics, monitoring both internal electronic interactions and electron-lattice coupling (see Secs. 1.3.2.c and 1.3.2.d). In the following we introduce the experimental setup used for these investigations (Sec. 2.1). We then present investigations of the electron-lattice energy transfer (Sec. 2.2) and electron-electron interactions (Sec. 2.3) in the Ag samples separately. The size-dependent dynamics are modeled with the theoretical description presented in Chapter 1 (Sec. 1.3.2), its deviations for small particles being experimentally studied. The last section of this chapter is devoted to Au cluster samples (Sec. 2.4), which constitute a slightly different system due to the presence of stabilizing surfactants and their extremely small sizes (from 25 to 144 atoms).

2.1 Two-colored pump-probe setup

Time-resolved optical pump-probe experiments allow the detection of nonequilibrium electron dynamics in metal systems. In this approach the metal free electron gas is selectively excited by a femtosecond pump pulse, while a time delayed probe pulse monitors the transient change of the samples optical properties (reflectivity or transmissivity).

For this work, two different experimental setups have been used, based on monochromatic pump and probe pulses (setup 1) or on a broadband probe pulse combined with high laser fluences (setup 2). In both cases, the transient relative transmission changes $\Delta T/T$ of an ensemble of noble metal nanospheres were investigated, in a transparent matrix or dispersed in a solvent. In the following, the characteristics of the two setups are presented, setup 1 being located in Lyon (FemtoNanoOptics Group) and being used on a daily basis while setup 2 was used for some specific studies in collaboration with G. Cerullo at the Center for Ultrafast Science and Biomedical Optics (CUSBO) facility of Politecnico di Milano, Italy.

2.1.1 Setup 1: Tunable femtosecond laser source

In this setup, tunable femtosecond pulses are provided by a commercial (Coherent: MIRA or Spectra-Physics: Mai-Tai, pulse duration $\sim 100\text{ fs}$) or homemade (pulse duration $\sim 60\text{ fs}$) mode-locked Ti:Sapphire laser with a 76 MHz repetition rate and a typical output power of $\sim 1\text{ W}$. Time-resolved spectroscopy is performed in a two-colored configuration (see Fig. 2.1), with different pump and probe wavelengths. For this purpose the infrared

2.1. Two-colored pump-probe setup

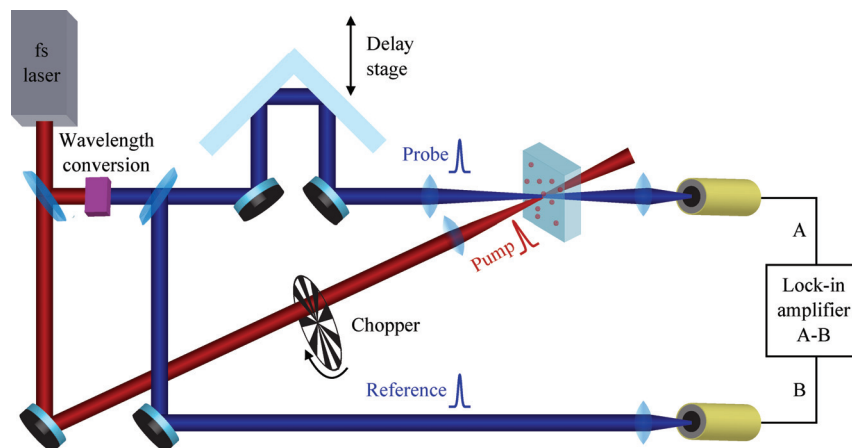


Figure 2.1: Schematic setup of a two-colored pump-probe experiment with synchronous and differential detection.

output of the Ti:Sapphire laser is split and wavelength conversion of one or both of the resulting beams is realized by different techniques. A very large spectrum of tunable wavelengths can be obtained by using the following tools:

- Infrared output of the Ti:Sapphire laser ($\sim 750\text{-}1000\text{ nm}$) and its second harmonic using a barium borate (BBO) crystal ($\sim 380\text{-}500\text{ nm}$), providing low pump fluences ($F \approx 100\ \mu\text{J}/\text{cm}^2$) at the sample position, necessary for investigations in a weak excitation regime.
- Optical parametric amplifier (OPA) in association with a regenerative amplifier (Coherent: REGA). Parametric amplification is a second order nonlinear optical effect yielding the conversion from a pump beam ω_p to a lower frequency signal beam ω_s and an additional third idler beam ω_i ($\omega_p = \omega_s + \omega_i$). The setup allows to create pulses in the visible range of the spectrum, $480\text{-}720\text{ nm}$, with a low repetition rate (250 kHz) and higher laser fluence ($F \approx 5\ \text{mJ}/\text{cm}^2$).
- Optical parametric oscillator (OPO), based on the same principle as the OPA, without the need of amplification due to the presence of an optical cavity around the nonlinear crystal. Visible light ($480\text{-}700\text{ nm}$) at low fluence ($F \approx 100\ \mu\text{J}/\text{cm}^2$) and high repetition rate is obtained.
- Third harmonic generation, covering wavelengths in the ultraviolet (UV, $\sim 250\text{-}330\text{ nm}$), was obtained by using two BBO crystals (type I) of $500\ \mu\text{m}$ (BBO 1) and $200\ \mu\text{m}$ (BBO 2) thickness, illustrated in Fig. 2.2 [36]. Shortly, BBO 1 generates the second harmonics (blue beam) of the IR beam ($\omega + \omega = 2\omega$) while BBO 2 creates the sum of the resulting frequencies ($\omega + 2\omega = 3\omega$), leading to ultraviolet light. After BBO 1, blue and IR beams are spatially separated and individually temporally compressed by a pair of fused silica prisms (P1 and P2 for ω , P1 and P3 for 2ω).

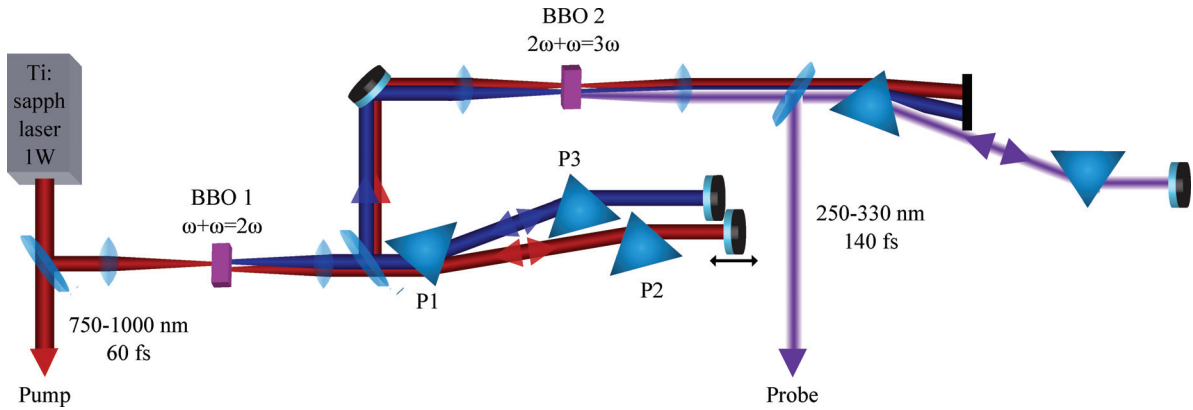


Figure 2.2: Scheme for third harmonic generation by two BBO crystals with pulse compression by two pairs of prisms (IR and blue beams are slightly shifted in the figure for clearness).

Their temporal overlap is adjusted via a mobile mirror in the optical path of the IR beam (ω). Harmonic (2ω) and fundamental beams (ω) are subsequently focused and overlapped on a second BBO (BBO 2) where their frequency sum is created ($\omega + 2\omega = 3\omega$). An additional pair of prisms compresses the duration of the resulting ultraviolet beam (3ω) and a beam block allows to cut off the IR and blue beams which are not utilized later on.

The analysis of the cross-correlation of the infrared and ultraviolet beam could be performed by generation of the frequency difference ($3\omega - \omega = 2\omega$) by another BBO crystal (200 μm thick), mounted at the position of the sample. A minimal cross-correlation of around 150 fs Full Width at Half Maximum (FWHM) was found (Fig. 2.3), providing the temporal resolution of the two-colored pump-probe experiment. Taking into account a duration of 60 fs for the IR pulse, this resolution corresponds to an UV pulse of around 140 fs.

Control of the delay between pump and probe pulses is achieved via a reflecting mirror mounted on a mechanical stage, with a spatial resolution of 0.125 μm corresponding to a temporal resolution of 0.83 fs (Fig. 2.1). Both beams are focused using achromatic lenses of 5 cm and 7 cm focal lengths, and overlapped on the sample. The average power of the probe beam after transmission through the sample is measured by a silica photodiode. Pump beam filtering is obtained by introduction of an important angle between pump and probe beam. Additionally, further rejection is achieved by inserting colored or dielectric filters before the photodiode, a procedure that is only possible due to the two-colored nature of the setup.

Typically the experimental relative transmission change $\Delta T/T$ is very weak, in the order of $10^{-4} - 10^{-7}$. In order to increase the sensitivity of the setup, synchronous and differential detection has been adopted. For synchronous detection, the pump pulse is chopped mechanically, typically with a frequency of $f_m = 100$ kHz. The probe signal detected by

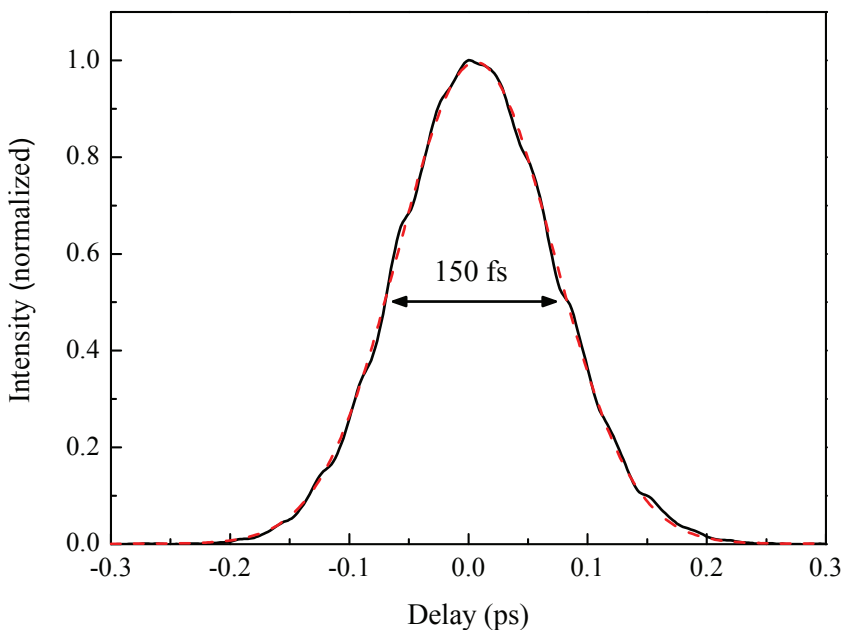


Figure 2.3: Cross-correlation measurement: Transient intensity (normalized to 1) of the frequency difference of the UV probe beam (303 nm) and the IR pump beam (910 nm). The red dashed line is a Gaussian fit with 150 fs FWHM.

the photodiode is demodulated at the same frequency by a Lock-in amplifier, filtering out all frequencies different than f_m . To further increase the signal to noise ratio at f_m , differential detection is performed by subtracting the transmitted beam and a reference one not interacting with the sample (denoted by A and B in Fig. 2.1). Samples sensitive to oxidation (Cu, Ag, Ni) were measured in vacuum using a special sample holder with transparent windows constructed to keep the samples at typically 10^{-5} mbar.

2.1.2 Setup 2: Broadband white light pump-probe experiment

This ultrafast spectroscopy system developed at CUSBO in Milan is based on two synchronized non-collinear optical parametric amplifiers [99–102], being pumped by a regeneratively amplified Ti:sapphire laser at 1 kHz. Here, the probe pulse is represented by a broadband white light continuum (WLC) while a narrowband pulse in the visible range of the spectrum is used to excite the samples (Fig. 2.4). Both beams are compressed by chirped mirrors leading to a sub-10 fs duration for the probe and 15 fs for the pump pulse. The pump beam is modulated at 500 Hz by a mechanical chopper, its frequency being locked to the laser pulse train. A spectrometer in combination with a photodiode array is used for simultaneous detection of all wavelengths in the probe spectrum. By recording pump-on and pump-off spectra, the differential transmission $\Delta T/T$ can thus be measured as a function of probe wavelength and pump-probe delay.

This equipment allows acquisition of two dimensional differential transmission maps on a broad spectral range, with extreme temporal resolution. However, as a consequence of low repetition rate and amplification, the samples are strongly excited, with pump fluences in the range of some hundred of mJ/cm^2 .

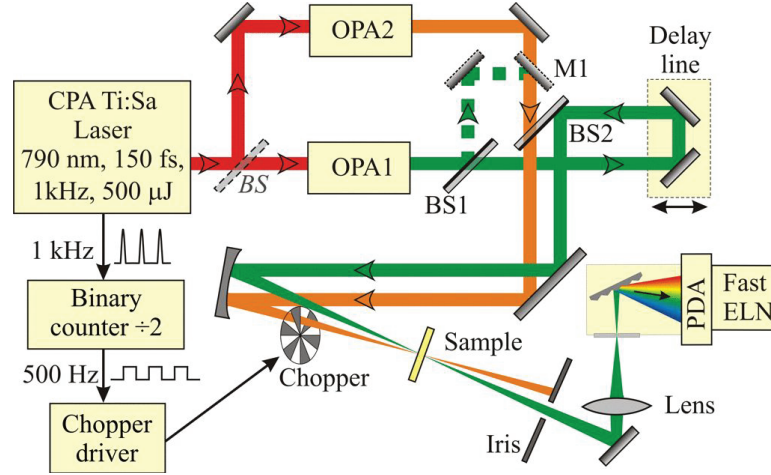


Figure 2.4: Schematic setup of the OPA/OPA pump-probe experiment. OPA 1 (probe) generates broadband white light, OPA 2 (pump) generates narrowband pulses in the visible (figure from Ref. [102]). PDA: Photodiode array.

2.2 Ultrafast electron-lattice interactions in Ag clusters

In bulk noble metals, electron-lattice coupling occurs typically at a picosecond timescale [68]. In the following we investigate its modification with size reduction on silver clusters synthesized by physical means by the Clusters and Nanostructures group of the Institut Lumière Matière in Lyon/ Plateforme Lyonnaise de Recherche sur les Agrégats (PLYRA) in collaboration with M. Pellarin and M. Hillenkamp.

2.2.1 Samples

Pump-probe measurements have been performed on silver nanospheres with mean diameters D varying between 1.1 and 3 nm (Table 2.1). The studied samples have been prepared by a physical technique based on cluster formation in gas phase, size selection and subsequent deposition on a substrate. To prevent oxidation, the particles were embedded in a silica matrix (SiO_2) which is transparent and permits good heat evacuation. Depending on particle sizes, different cluster sources were used. Particles of mean diameters between 1.8 nm and 3 nm were prepared by a laser vaporization cluster source and low energy cluster beam deposition (LECBD, Fig. 2.5). Here, a frequency-doubled Nd:YAG laser beam

2.2. Ultrafast electron-lattice interactions in Ag clusters

Table 2.1: List of the studied Ag samples obtained by LECBD and magnetron deposition technique (size dispersion indicated by the FWHM). A mean diameter D was calculated by weighting the original size distribution by the particle volume V_{np} (the optical response being proportional to V_{np}), D being the mean diameter corresponding to this weighted size distribution. In the case of large size dispersions, the resulting diameters were shifted to larger sizes as compared to the original ones D_0 , while for narrow size distributions D and D_0 are equal. n_{at} is the number of atoms in the particles.

D (nm)	ΔD_{FWHM} (%)	n_{at}	source	D_0
1.1	~ 70	40	magnetron	0.8
1.4	~ 65	85	magnetron	1.1
1.5	~ 50	100	magnetron	1.3
1.8	$\lesssim 10$	180	LECBD	1.8
1.9	~ 50	210	magnetron	1.6
2.2	$\lesssim 10$	330	LECBD	2.2
2.5	$\lesssim 10$	480	LECBD	2.5
2.8	$\lesssim 10$	670	LECBD	2.8
2.8	~ 15	670	magnetron	2.8
3	$\lesssim 10$	830	LECBD	3

is focused on a rod of a pure or alloy metal, creating a plasma by ablation. Before deposition, the charged particles are mass selected by an electrostatic deviator (quadrupole), on the basis of their kinetic energy [13, 14]. The resulting samples present thus a small size dispersion $\lesssim 10\%$ FWHM, which is measured by transmission electron microscopy (TEM). A drawback of this technique is the low intensity of cluster formation of small sizes resulting in a low particle density of the samples. Indeed, the metal volume fraction in the around 400 nm thick silica films is typically in the 10^{-4} to 10^{-2} range for particle mean diameters ranging from 1 to 3 nm. Fabrication of small size samples with an optical density convenient for pump-probe measurements is thus particularly challenging.

To circumvent this limitation, the smaller nanospheres were prepared by a magnetron cluster source [103]. The principle of the setup is shown in Fig. 2.6(a). In this technique, cluster generation is achieved by a homemade magnetron source, an incorporated time-of-flight mass spectrometer (TOF-MS) allowing to directly determine the cluster size distribution. In contrast to the previously presented technique, high cluster fluxes can be created and the preparation of optically dense samples with sub-nm sizes is possible. In principle, an additional size selection by a quadrupole deviator could be performed, which was not available due to experimental problems, resulting in a larger size distribution ($\sim 60\%$ FWHM, Fig. 2.6(b)). In both cases, direct measurement of the linear absorption spectrum of the samples was not possible because of their very low particle concentration.

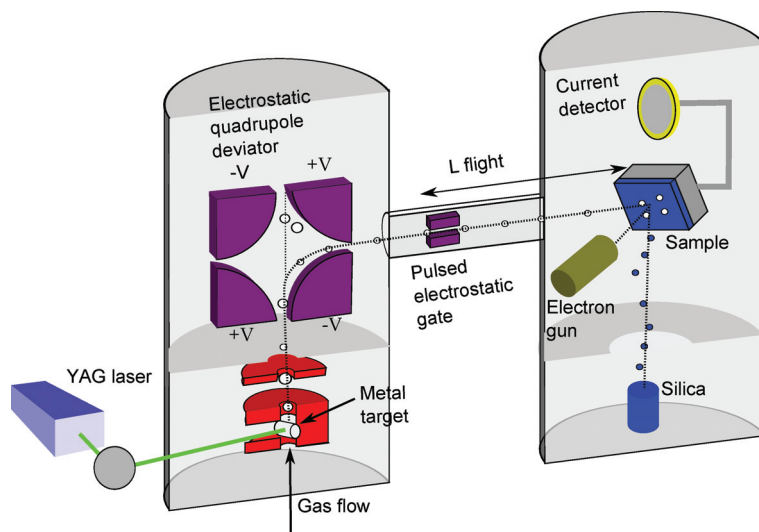


Figure 2.5: Schematic view on laser vaporization cluster source and low energy cluster beam deposition (LECBD) [13, 14].

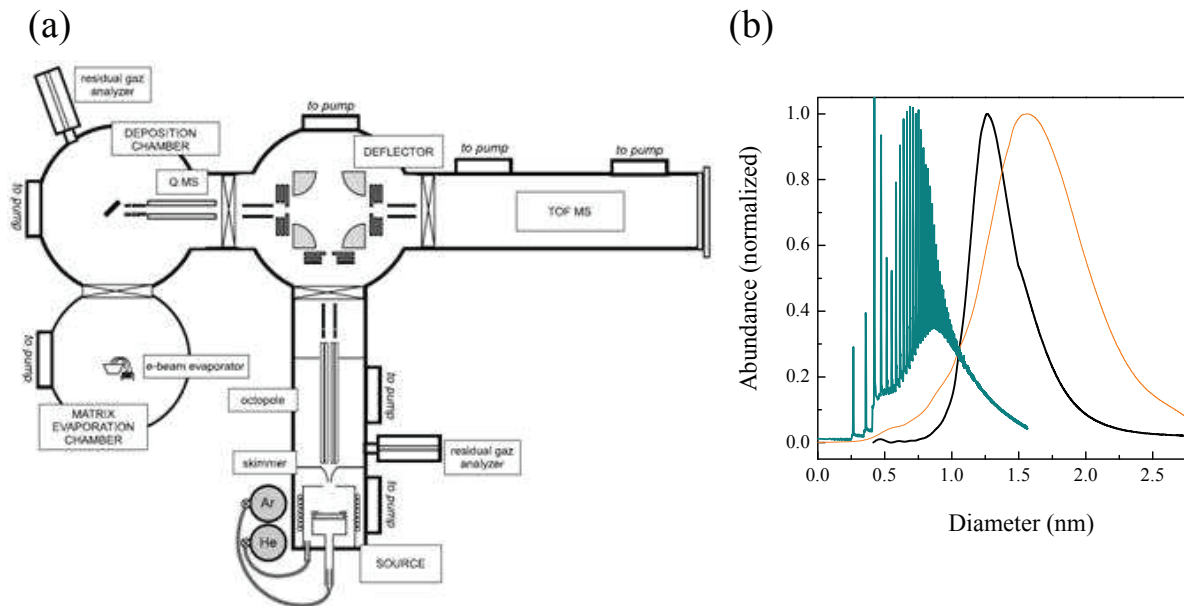


Figure 2.6: (a) Scheme of the principle of the magnetron cluster experiment [103]. (b) Size distribution of the samples measured by the TOF mass spectrometer (discrete peaks indicate the measurement of the number of atoms).

2.2.2 Optical detection of electron-phonon coupling

Optical time-resolved experiments on metal nanoparticles allow the measurement of the energy stored in the excited electron gas and of its dynamics $\Delta u_e(t)$. This energy is transferred to the lattice, or equivalently to the metal phonons. Monitoring of $\Delta u_e(t)$ gives thus access to the characteristic electron-lattice energy exchange time τ_{e-ph} (see Sec. 1.3.1) which is inversely proportional to the electron-phonon coupling constant G . In the following we discuss the optical detection mechanisms at the basis of these investigations.

For short probe delays ($t < 3$ ps after excitation by an ultrafast pump pulse), modifications of the interband parts of real and imaginary dielectric functions dominate over the Drude parts (see Sec. 1.4, Fig. 1.17) [35]. In this case $\Delta\epsilon_{1,2}^{ib}$ are determined by the change of the electron energy distribution function Δf , thus showing a strong dependence on the probe wavelength. Here, we are interested in the total excess energy of the electron gas and its dynamics, independently of its individual electronic state distribution changes. For this study, it is therefore convenient to choose a probe photon pulse of energy lower than the interband transition threshold Ω_{ib} . In these conditions, $\Delta\epsilon_2^{ib}$ is nonzero only for very short delays t , where the electron energy distribution is strongly out-of-equilibrium involving perturbed states far from the Fermi energy E_F . This makes interband transitions possible for probe photon energies far from the interband transition threshold with $\hbar\omega_{pr} + \hbar\omega_p = \hbar\Omega_{ib}$. However, perturbed states far from E_F scatter very quickly (less than 100 fs) to states closer to E_F , canceling $\Delta\epsilon_2^{ib}$ for $\hbar\omega_{pr} < \hbar\Omega_{ib}$. The optical response is thus dominated by $\Delta\epsilon_1^{ib}$, which is proportional to the electron gas excess energy density Δu_e [17, 68, 89].

The physical quantity monitored by a pump-probe experiment with $\hbar\omega_p < \hbar\Omega_{ib}$ and $\hbar\omega_{pr} < \hbar\Omega_{ib}$ is therefore the time-dependent electron excess energy:

$$\frac{\Delta T}{T}(t) \propto \Delta\epsilon_1^{ib}(t) \propto \Delta u_e(t) = \frac{1}{2}a [T_e(t)^2 - T_0^2], \quad (2.1)$$

with $T_e(t) = T_0 + \Delta T_e(t)$. Consequently, in the weak excitation regime, $\Delta u_e(t) \approx aT_0\Delta T_e(t)$, which leads to an exponentially decaying signal showing the same dynamics as the electron temperature, characterized by the relaxation time τ_{e-ph} (see Sec. 1.3.1). Pump-probe experiments were performed, if possible, in the weak perturbation regime, corresponding to electron gas heating $\Delta T_{exc} = T_{exc} - T_0 \lesssim 100$ K. For the smallest cluster sizes, however, a strong perturbation regime is reached, even for very low pump laser fluences, as will be discussed later. In this case, the temperature dynamics of the electron gas is more complex, requiring a numerical solution of Eq. (1.53). Additionally, the time-resolved signals must be considered to be proportional only to the electron gas excess

energy, the assumption of linearity with temperature not holding anymore. For the analysis of all signals we therefore introduce a characteristic experimental decay time $\tau_{1/e}$ defined by $\Delta u_e(\tau_{1/e}) = \Delta u_{exc}/e$, which corresponds to τ_{e-ph} in the case of weak electron excitation.

2.2.3 Experimental results

Time-resolved experiments have been performed on all samples presented in Table 2.1 using low energy pulses (setup 1, Sec. 2.1.1) and pump and probe wavelengths far from the interband transition threshold Ω_{ib} , which is around 3.95 eV in bulk silver (see Table 1.4). For this purpose, the direct output pulse of the oscillator (~ 800 nm, infrared) and its second harmonic (~ 400 nm, blue) were used for experiments.

2.2.3.a Analysis of time-resolved pump-probe signals

We systematically performed measurements in two different experimental conditions, with the pump pulse in the infrared (IR) and probe pulse in the blue and subsequently exchanging the two beams, thus using blue pump and IR probe pulses. Using a 500 μm thick BBO

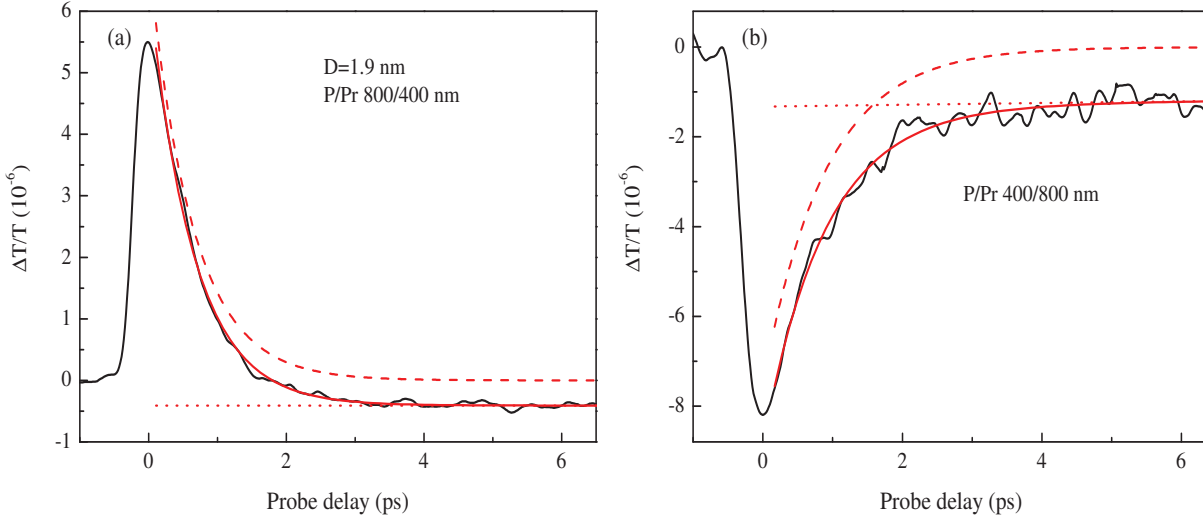


Figure 2.7: Experimental transient relative transmission change $\Delta T/T$ (full black line) for silver nanospheres of mean diameter $D = 1.9$ nm in the P/Pr configurations (a) 800/400 nm and (b) 400/800 nm and low pump powers (10 mW and 3 mW respectively). The pump power P_p can be connected to the pump fluence F by $F = 2P_p/(\pi\sigma^2 f_{rep})$ (with σ the pump beam waist and f_{rep} the laser repetition rate), yielding around 70 and 1 $\mu\text{J}/\text{cm}^2$ for the infrared and blue pump, respectively. Full red lines correspond to a fit by the sum of a fast and slower exponential function (red dashed and dotted lines).

crystal for the second harmonic generation, the cross-correlation between pump and probe

beam at the position of the sample was measured for this configuration to be around 200 fs FWHM, which yields a sufficient temporal resolution for the addressed electron-lattice dynamics.

Fig. 2.7(a) illustrates the transient relative transmission change $\Delta T/T$ obtained for the $D = 1.9$ nm sample in the pump-probe configuration P/Pr 800/400 nm, while Fig. 2.7(b) shows the same sample measured with interchanged pump and probe beams (P/Pr 400/800 nm). In both cases, after a fast rise of the signal amplitude (positive or negative), corresponding to energy injection into the electron gas by the pump pulse, a slower decay is observable. When probing far from the interband transition onset, as it is the case here, the characteristic time for the signal rise is basically determined by the pump-probe cross-correlation, its amplitude being proportional to the initially injected energy Δu_{exc} , whereas the decreasing part of the signal follows the dynamics of $\Delta \epsilon_1^{ib}$, reflecting electron energy loss to the lattice, with a small contribution of $\Delta \epsilon^D$ due to the concomitant lattice heating. The signal decay can thus be correctly fitted by the sum an exponential function and a constant or slowly decaying background (Figs. 2.7(a) and 2.7(b)). The former corresponds to electron gas cooling by electron-lattice interaction (the process which is studied here) while the latter is a weak contribution due to lattice heating which subsequently cools down by energy transfer to the environment on longer timescales.

2.2.3.b Effects of pump power and size reduction

To investigate the effect of initial electron gas excitation on the pump-probe signals, the pump power P_p was systematically varied. Linearity of the signals amplitude of silver clusters of a diameter $D = 1.9$ nm with the absorbed energy and thus P_p is shown in the inset of Fig. 2.8(a). In addition, for infrared pump pulses $\tau_{1/e}$ varied approximately linearly with pump power, before converging to a constant value for low excitations. These variations are consistent with the two temperature model in the regime of strong perturbation (see Sec. 1.3.1). No increase of $\tau_{1/e}$ with P_p could be observed with a blue pump beam, its intensity being typically ~ 50 times smaller than the infrared one and leading thus to weak excitations.

The weak excitation time constants are retained in the following discussion as the value describing the characteristic electron-phonon energy transfer dynamics. Size effects were subsequently investigated for different diameters in the two configurations (IR and blue pump) at low pump powers. Fig. 2.9 illustrates a comparison of the electron excess energy decay dynamics of the $D = 1.9$ nm sample for the two pump-probe configurations (P/Pr IR/Blue and P/Pr Blue/IR) after subtraction of the lattice contribution (to exclude an erroneous influence of lattice heating on the characteristic time $\tau_{1/e}$, signals were also acquired on a longer timescale where the lattice temperature-dependent contribution is

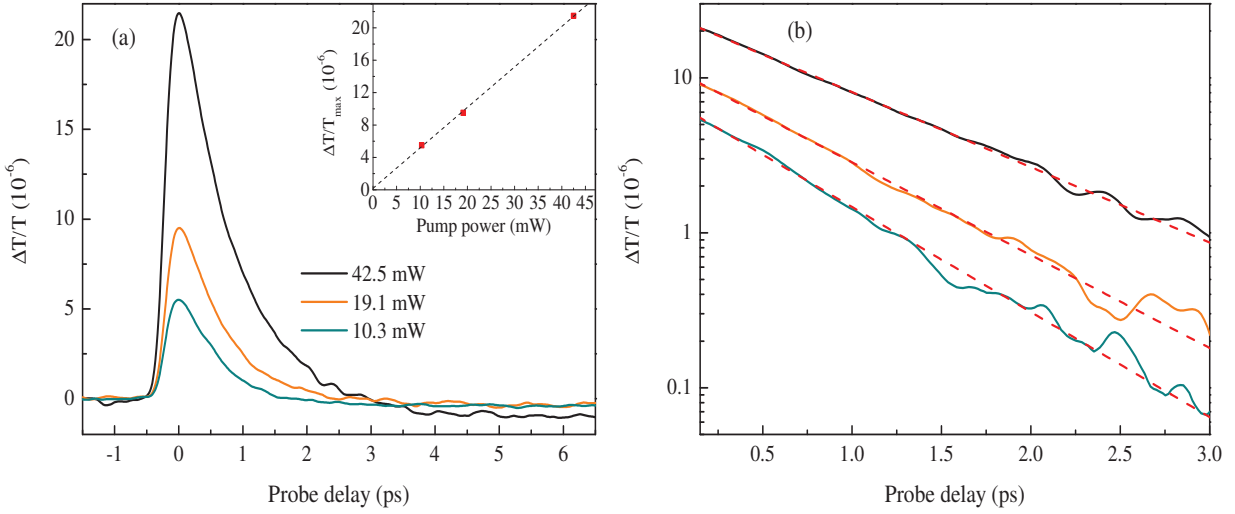


Figure 2.8: Experimental pump-probe signals (a) (P/Pr 800/400 nm) of $D = 1.9$ nm silver nanospheres for different pump powers P_p (42.5 mW, 19.1 mW and 10.3 mW, black, orange and green lines respectively). Inset: maximum signal amplitude as a function of pump power. (b) Mono-exponential fits are shown (red dashed line) after subtraction of a background associated to lattice heating. The deduced time constants $\tau_{1/e}$ were 0.89 ps, 0.73 ps and 0.64 ps for decreasing P_p .

dominant, allowing to fully take into account the long delay dynamics). A clear difference in the decay dynamics is observable, which has been shown to be independent of the probe wavelength [72]. This suggests a dependence of electron gas cooling on the pump photon energy, in stark contrast to previous measurements performed on larger gold and silver nanospheres ($D \geq 3$ nm), for which pump wavelength-independent timescales were obtained [18].

The decay dynamics of samples with different particle diameters can be compared, provided that the samples are excited under similar experimental conditions (pump wavelength and energy). Fig. 2.10 illustrates the decay dynamics of particles with mean diameters of 1.9 nm and 2.8 nm, excited by a blue laser beam around 400 nm and low power (~ 3 mW). An increase of the characteristic electron excess energy cooling time $\tau_{1/e}^B$ (the index B denotes the pump wavelength in the blue) with decreasing size can be observed with $\tau_{1/e}^B \approx 0.65$ ps and 0.8 ps for $D = 2.8$ nm and 1.9 nm, respectively. Similar results are obtained for IR pump pulses.

The principal experimental observations are summarized in Fig. 2.11 illustrating the characteristic decay time after excitation by an infrared ($\tau_{1/e}^{IR}$) or blue ($\tau_{1/e}^B$) laser beam at low power. The graph shows both recent experimental results obtained during this PhD thesis on silica-embedded clusters (1-3 nm, Table 2.1) and previous results on nanospheres of intermediate sizes (> 3 nm) embedded in different matrices [18]. The latter were syn-

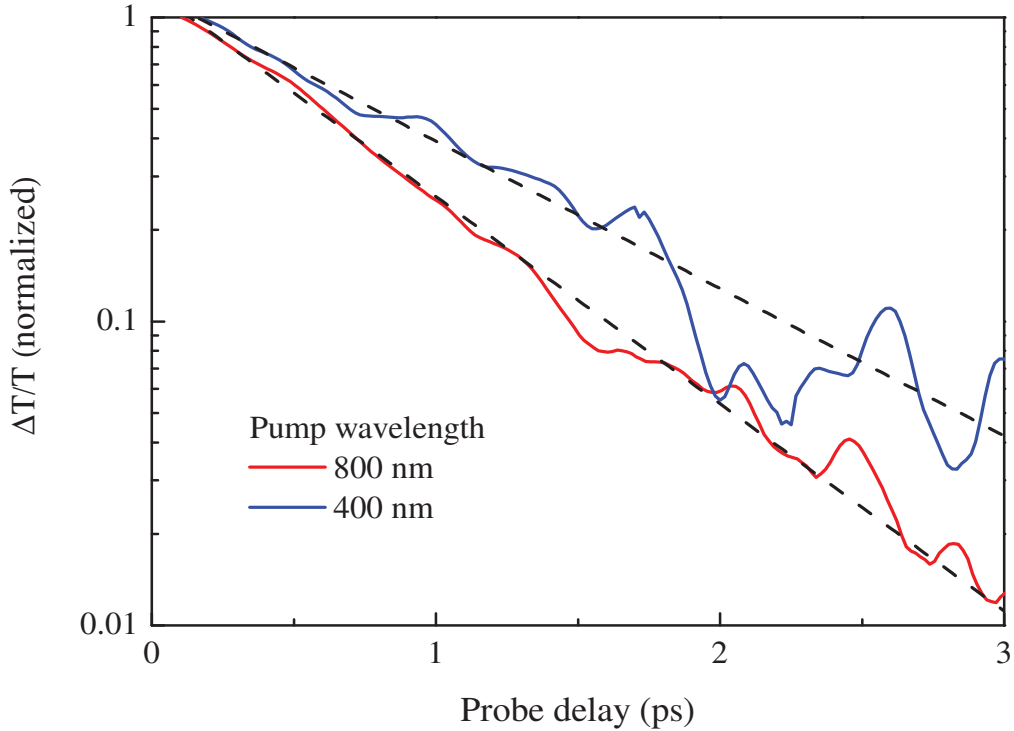


Figure 2.9: Normalized experimental signals after subtraction of the lattice heating contribution for $D = 1.9$ nm nanospheres with P/Pr 800/400 nm (full red line) and P/Pr 400/800 nm (full blue line) and corresponding exponential fits (black dashed lines) yielding $\tau_{1/e}^{IR} \approx 0.6$ ps and $\tau_{1/e}^B \approx 0.8$ ps for excitation at 800 nm and 400 nm, respectively. The samples were excited at low power with $P_p \approx 10$ mW and $P_p \approx 3$ mW for IR and blue pump beams.

thesized with a technique similar to LECBD with no mass selection or by a fusion and heat treatment technique [104]. For both pump colors, $\tau_{1/e}$ decreases with decreasing diameter in the intermediate size range ($D > 3$ nm) and increases for further size reduction. Additionally, experiments suggest a non-monotonic behavior in the very small size regime ($D < 3$ nm), as clearly shown for experiments with a blue excitation. Small particles also exhibit a clear dependence on the pump wavelength, showing a higher increase of $\tau_{1/e}$ with decreasing size for a blue pump pulse, while the larger nanospheres are insensitive to this parameter.

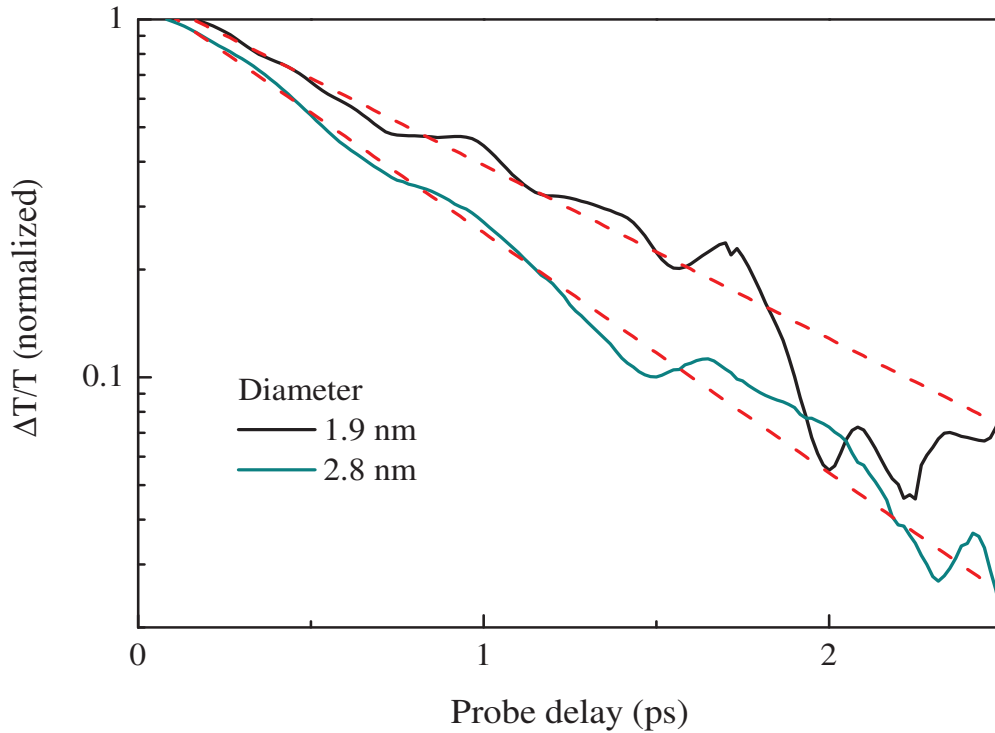


Figure 2.10: Normalized transient transmission for silver nanospheres of mean diameters 1.9 nm and 2.8 nm (full black and green line, respectively). The contribution due to lattice heating has been subtracted and the fits (red dashed lines) correspond to a monoexponential decay yielding $\tau_{1/e}^B \approx 0.8$ ps and 0.65 ps, respectively. The experimental conditions are very similar, with P/Pr Blue/IR and $P_p \approx 3$ mW.

2.2.4 Discussion

2.2.4.a Intermediate size range: size-dependent screening effects

Silver nanospheres in the intermediate size range from 3 to 30 nm have already been measured in the past [5, 18, 105]. Fig. 2.12 illustrates an overview of these results where the gray points in Fig. 2.11 have been replaced by colored points indicating the different matrices embedding the nanoparticles of the samples. These samples have been prepared by different techniques resulting in different surface conditions (surface roughness, attached molecules, ...). Nevertheless, the different matrices and preparation methods are shown not to influence the dynamics, suggesting that the signal decay in the pump-probe experiment reflects intrinsic electron-lattice interaction properties of the metal. It is also independent of different experimental conditions, as pump and probe wavelengths and power, as long as the system is probed far from the interband transitions (IR or blue) and in a low perturbation regime. The characteristic electron-phonon energy transfer time decreases with size reduction. This fast electronic relaxation has been attributed to an

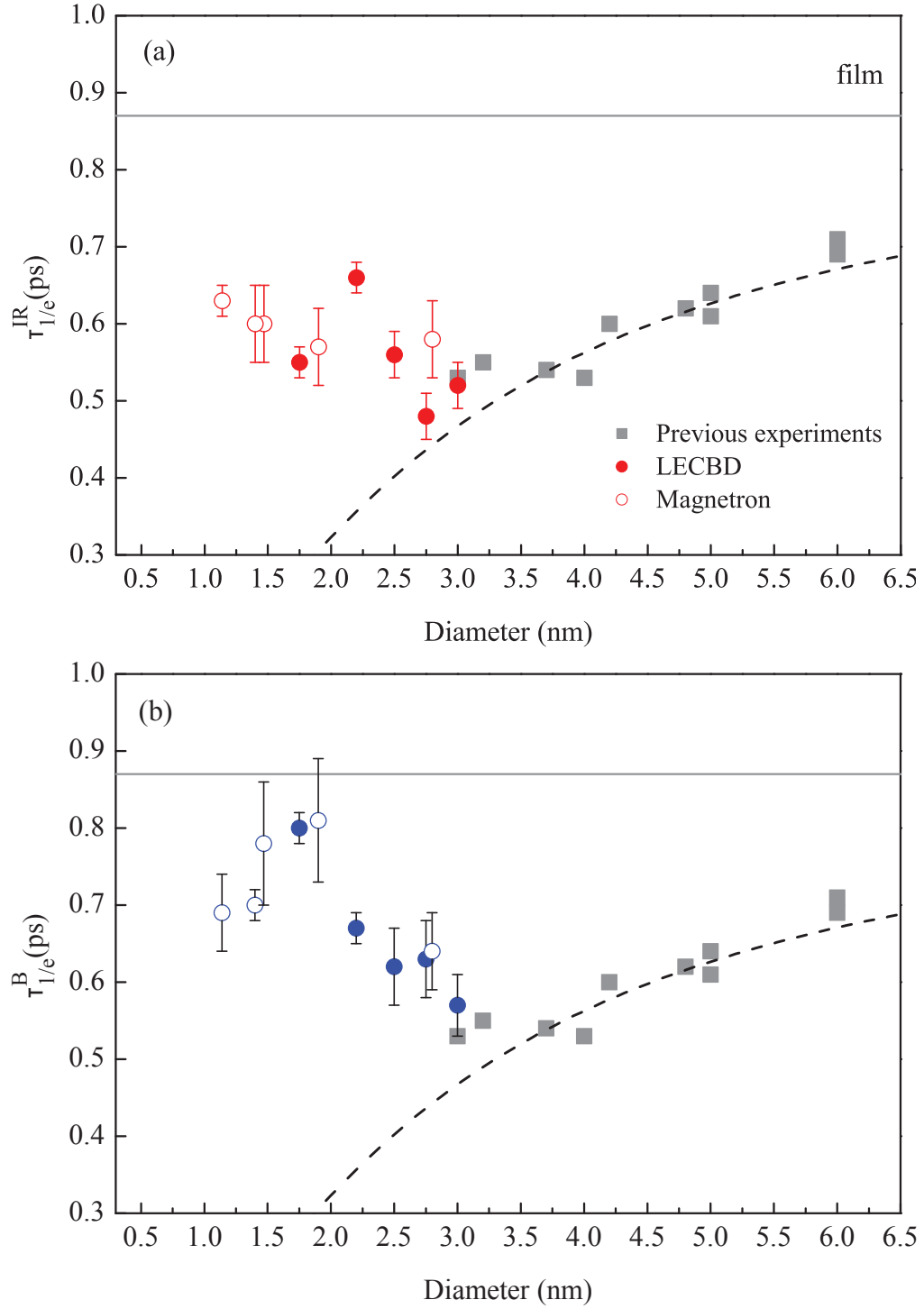


Figure 2.11: Overview of the measured electron-phonon energy exchange time as a function of the particle diameter at low excitations with a pump wavelength in the infrared (a) or in the blue (b). Ag clusters (silica matrix) have been fabricated by laser vaporization and magnetron cluster sources (red full and open circles respectively). Previously studied samples are illustrated by gray rectangles [18]. The gray line corresponds to $\tau_{\text{bulk}} = 0.87$ ps, the value of τ_{e-ph} in bulk silver (Table 1.5) [68]. The black dashed line is a phenomenological fit tracing the decay of $\tau_{1/e}$ in the intermediate size range (see text).

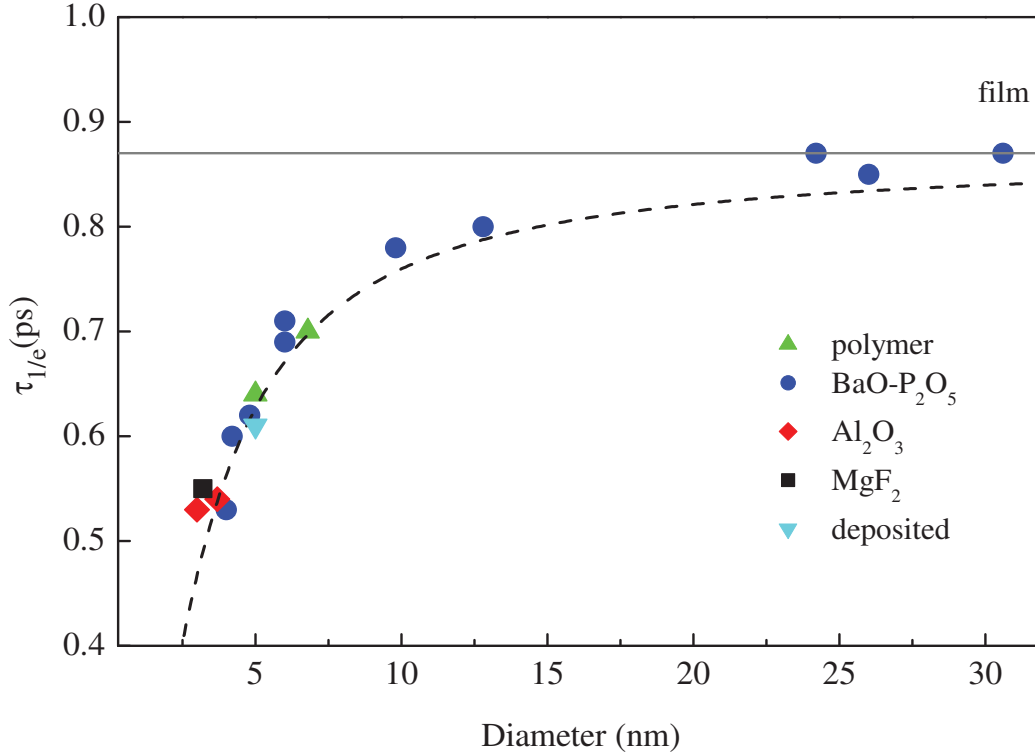


Figure 2.12: Previous measurements of the electron-phonon energy exchange time for $D > 3$ nm silver nanospheres (not mass-selected) embedded in different matrices or deposited on a substrate. The black dashed line is a phenomenological fit (see text).

enhanced electron-ion Coulomb interaction, due to the reduction of screening close to the surfaces [5, 18]. The experimental data can be phenomenologically reproduced by a function decreasing with the surface i.e. $1/\tau_{e-ph} = 1/\tau_{\text{bulk}}(1 + A/D^2)$, with A a free parameter and τ_{bulk} the bulk value of the electron-phonon energy transfer time in Ag (see Figs. 2.11 and 2.12). A quantitative description of this effect is difficult to obtain, as the simple deformation potential used to describe electron-phonon coupling in the model presented in Chapter 1 (Sec. 1.3.2.d) does not directly take Coulomb screening into account. However, a similar behavior has been observed for electron-electron interactions in silver and gold nanospheres in the same size range, where a quantitative model could be developed [5, 16].

2.2.4.b Small size range: pump excitation effect

The situation is different for the sizes investigated during this thesis. For clusters smaller than 3 nm, dependence of the signal dynamics on the pump wavelength is observed, $\tau_{1/e}$ being systematically larger for a blue photon excitation than for an infrared one. Conversely, previous experiments showed that the relaxation time is independent of the probe photon energy [72]. For small pump fluences and small cluster sizes, most of the particles

2.2. Ultrafast electron-lattice interactions in Ag clusters

contributing to the experimental signal have absorbed a single photon, the probability of two-photon absorption being negligibly small. The $\tau_{1/e}$ values obtained for this very small size range correspond therefore to absorption of only one pump photon. In this case, the electron excess energy density is given by:

$$\Delta u_{exc} = \frac{\hbar\omega_p}{V_{np}}. \quad (2.2)$$

As Δu_{exc} is inversely proportional to the particle volume (Eq. (2.2)), even the absorption of one photon can lead to very strong heating of the electron gas. Furthermore, Δu_{exc} is proportional to the incoming photon energy $\hbar\omega_p$, yielding a pump wavelength-dependent excitation. Fig. 2.13(a) illustrates the electron gas temperature increase (ob-

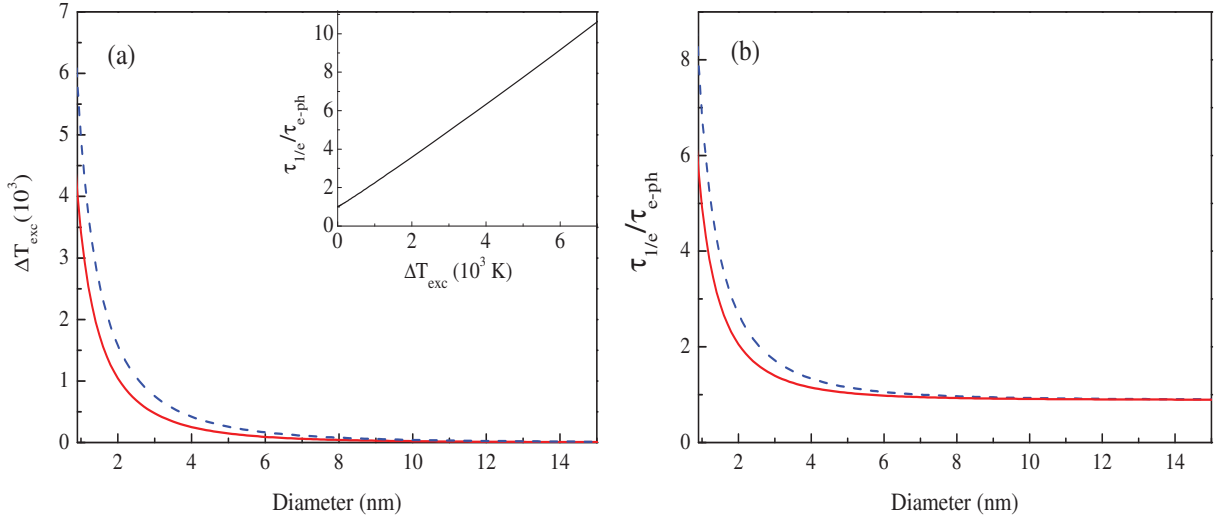


Figure 2.13: Initial excess temperature (a) after absorption of a single photon with a wavelength of 800 nm (full red line) and 400 nm (dashed blue line). Inset: Linear dependence of the decay time $\tau_{1/e}$ with ΔT_{exc} calculated by the TTM (Sec. 1.3.1). The corresponding $\tau_{1/e}$ for single-photon excitation is shown as a function of the particle diameter in (b).

tained by Eq. (1.50)) after absorption of a photon with $\lambda_p = 800$ nm (full red line) and 400 nm (dashed blue line) as a function of the particle diameter. A difference in the excitation temperature between the absorption of a single blue and infrared photon is already observable for diameters as large as 5 nm, this difference increasing for smaller sizes. By solving the TTM (Eq. (1.51)), in bulk Ag and large nanoparticles, one can show that $\tau_{1/e}$ depends linearly on ΔT_{exc} (see inset of Fig. 2.13(a)) [72], and converges to the low perturbation regime limit, $\tau_{bulk} = 0.87$ ps. The calculated $\tau_{1/e}$, normalized to this value (Fig. 2.13(b)), shows, as expected, a dependence on the pump photon energy and an increase for small particles, due to strong one photon excitation. Note that for a more

quantitative estimation of the electronic temperature increase, the size-dependent electron heat capacity should be introduced in the model (instead of using the bulk value $c_e = aT_e$, see Sec. 1.1.1), resulting in an even more important electron heating at small sizes.

2.2.4.c Small size range: quantum effects

To analyze the measured electron cooling time on the whole size range and reveal specific effects in the small size regime, we modeled both previous contributions (size and pump-wavelength dependence). Figs. 2.14(a) and 2.14(b) show a fit of the experimental data including both the increase of $\tau_{1/e}$ with size reduction (due to the strong excitation after absorption of a single photon) and its decrease as a consequence of reduced screening. While the mean $\tau_{1/e}$ rise is determined by ΔT_{exc} and depends on the pump photon energy (see Fig. 2.13(b)), the decaying behavior is independent of $\hbar\omega_p$ and was approximated by a phenomenological function. In this simple picture, assuming that these two effects are

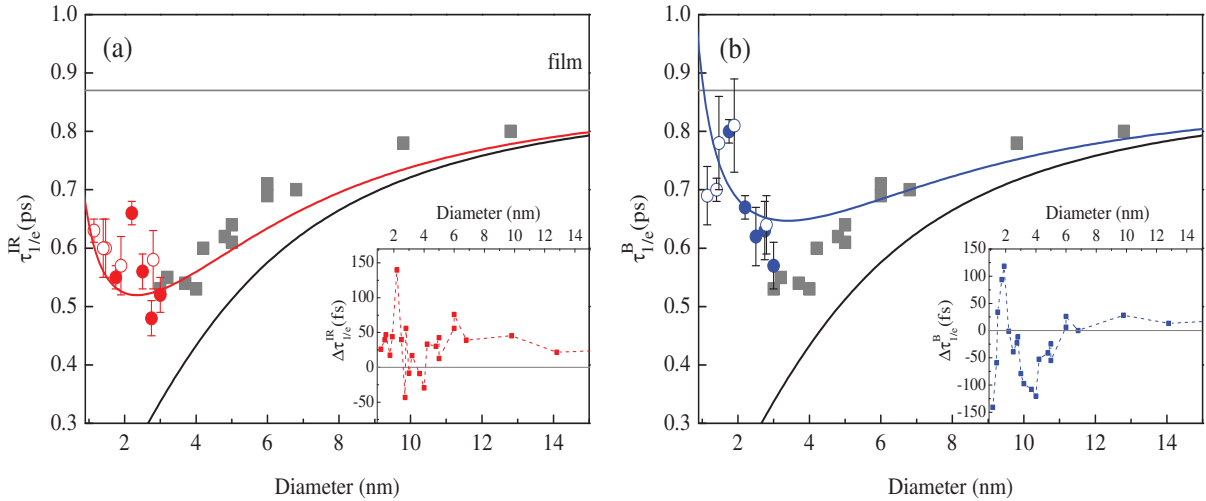


Figure 2.14: Fit of experimental $\tau_{1/e}$ for excitation by an infrared (a) or blue (b) pump pulse. For calculation of the red and blue lines in (a) and (b), respectively, the combination of the increase of $\tau_{1/e}$ and a decreasing function (black lines, free parameter) describing the reduction of screening was injected in the TTM. Insets: Deviations of the experimental points from the fit.

independent, we reproduced the tendency of the experimental data by their combination by solving the TTM model, with the phenomenological function used as a fit parameter, being the same one for both red and blue data (Figs. 2.14(a) and 2.14(b)). Here, we used $1/\tau_{e-ph} = 1/\tau_{bulk}(1 + B/(D + D_0)^2)$, with B a free parameter and $D_0 \approx 1$ nm, which retrieves the surface dependence previously measured in the intermediate size range ($D > 3$ nm) and reduces to a constant for $D \rightarrow 0$, when the previous “small solid” picture ($\sim 1/D^2$) is not expected to work anymore. The resulting fit is able to reproduce very

2.2. Ultrafast electron-lattice interactions in Ag clusters

well both the increase of $\tau_{1/e}$ as well as its sensitivity to $\hbar\omega_p$.

This indicates that one contribution to the increase of the electron-lattice energy exchange time can be interpreted as a consequence of strong initial heating for decreasing sizes after absorption of a single photon (Eq. (1.51)). Moreover, by subtracting the fit to the experimental results, the remaining size-dependent residuum of the electron-lattice relaxation time is revealed (inset in Figs. 2.14(a) and 2.14(b)). Experiments with both red and blue pump pulses illustrate that $\tau_{1/e}$ has a non-monotonic behavior with a sudden increase below ~ 2 nm, which cannot be explained by the simple approach based on the previous model. An oscillatory behavior of $\tau_{1/e}$ as a function of D is observable, suggesting a change in the electronic relaxation from a “small solid” regime to a molecular-like one. Although detailed explanation of these observations requires additional theoretical work, a general trend can be nonetheless understood with simple quantum mechanics arguments. For a qualitative characterization, the conduction electrons can be described by a simplified model system of free electrons in a cubic box (length $L_x = L_y = L_z = L$), with one electron states given by:

$$E_n = \frac{\hbar^2 \pi^2 n^2}{2mL^2}, \quad (2.3)$$

where the quantum numbers are described by $n^2 = n_x^2 + n_y^2 + n_z^2$. In order to be consistent with the case of a very large number of states and the transition to continuity, the states are supposed to be highly degenerated [106] with the degree of degeneracy of state n given by:

$$g_n = \rho(E_n) \cdot \Delta E_n, \quad (2.4)$$

where $\rho(E_n)$ is the density of states in the continuous limit (Eq. (1.5)). However, Kubo and coworkers [107] lifted this strong degeneracy, reasoning that realistic particles never form a perfect cube and that this deviation from symmetry leads to states that are only spin degenerated. Additionally, they assumed that eigenvalues with large quantum numbers (close to E_F) do not depend on the actual shape of the system nor on the boundary conditions. They obtained thus an average level spacing of

$$\Delta E = \frac{2}{\rho(E_F)} = \frac{4 E_F}{3 N}, \quad (2.5)$$

with N the number of conduction electrons in the particle. Insertion of E_F as a function of N and L [22] yields:

$$\Delta E = \frac{2\hbar^2 \pi^{4/3}}{3^{1/3} m^*} \frac{1}{N^{1/3} L^2}. \quad (2.6)$$

Chapter 2. Size dependence of electronic interactions in metal clusters

The noble metals gold and silver both supply one s-electron per atom to the conduction band and N is thus equal to the number of atoms in the particle, which can be expressed as a function of the diameter:

$$N = \frac{2\pi D^3}{3 \tilde{a}^3}, \quad (2.7)$$

with the lattice constant \tilde{a} which is, in the case of bulk silver 4.09 Å. Replacing furthermore L by the diameter D of a sphere with the same volume as the cube L^3 , one obtains for the level spacing of a small nanoparticle:

$$\Delta E = \frac{\hbar^2 2^{4/3} 3^{2/3} \pi^{1/3} \tilde{a}}{m^*} \frac{1}{D^3}. \quad (2.8)$$

The distance ΔE between consecutive levels increases with decreasing size and becomes

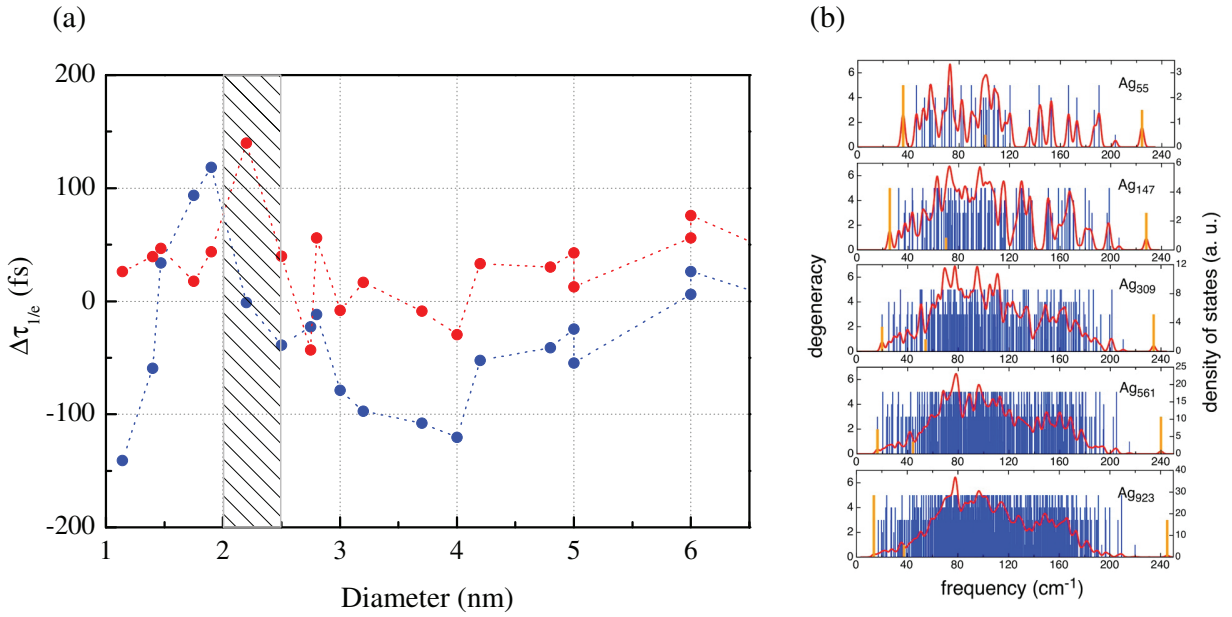


Figure 2.15: (a) Size-dependent residuum electron-lattice relaxation time after subtraction of the experimental points with the model (see text) for red (red points) and blue (blue points) pump pulses (zoom of inset in Figs. 2.14(a) and 2.14(b)). The patterned zone indicates a rise of $\Delta\tau_{1/e}$. For comparison the phonon density of states is shown from Ref. [108] (b).

comparable to thermal movement $k_B T_0$ at room temperature (300 K) for diameters around 2.1 nm. In this size range it also becomes comparable to the maximum phonon energy, $E_{ph,max}$, that can be exchanged by electron-lattice scattering. This value for acoustic phonons is not sensitively affected by size reduction, as demonstrated by molecular dynamics simulations [108], reproduced in Fig. 2.15(b), showing a cut-off phonon energy $E_{ph,max} \approx 200 \text{ cm}^{-1} \approx 25 \text{ meV}$ for small clusters, close to the one of bulk ($\sim 21 \text{ meV}$ in

Ag, see Sec. 1.1.1) [22]. If the electron energy spacing ΔE is larger than this maximum phonon energy, electron-lattice relaxation is expected to slow down, single phonon emission processes not being possible anymore. A blockage for electronic relaxation is expected for $\Delta E > E_{ph,max}$, corresponding to $D < 2.1$ nm. This is in very good quantitative agreement with the residual increase (after subtracting the effects of strong heating and reduced screening) of both characteristic relaxation times measured for red and blue pump pulses (see Fig. 2.15(a)). A quantum model which takes into account the electron-phonon interaction using the complete density of states for phonons is currently under investigation. Moreover, the further reduction of these times when the cluster sizes are even smaller remains to be interpreted.

2.3 Ultrafast electron-electron interactions in Ag clusters

In contrast to the former section where the interest was on the energy loss processes from the excited electron gas to the lattice, we focus here on the internal thermalization after excitation by a short pump pulse i.e. the buildup of thermalized (“hot”) electron distribution via electron-electron interactions. This takes place on a shorter timescale, typically hundred or few hundred of fs in noble metals and metal nanoparticles [5, 16, 68], the goal here being to extend former investigations to clusters of very small sizes ($D < 3$ nm).

2.3.1 Ultraviolet ultrafast spectroscopy

To observe the thermalization dynamics of the nanoparticle electron gas and its modification with size reduction, time-resolved optical spectroscopy has to provide information about the change of the electron distribution function, $\Delta f(E, t)$. This is actually possible when probing electron states close to the Fermi energy, by using wavelengths tuned around the interband transition threshold (see Sec. 1.5) [5, 17, 79]. For this purpose the infrared output of the femtosecond laser was used as pump pulse (see setup 1, Sec. 2.1.1), while for the probe beam the spectral range in the ultraviolet (UV) around 310 nm was exploited, the interband threshold of bulk silver being located at around 3.95 eV (see Table 1.4).

The power at the sample position was around 60 mW for the infrared and 10 μ W for the ultraviolet pulse. For measurements of the transient transmission, a special photodiode with a sensitivity extended to the UV, but with a low cutoff frequency, was used. The pump beam was thus chopped at 2 kHz which is lower than the frequency used for most experiments ($f_m = 100$ kHz, see Sec. 2.1.1). Also, as a consequence of the weak UV probe

power, differential detection could not be realized but a good signal to noise ratio was achieved as a consequence of a very stable laser output.

In order to compare the amplitude of the time-resolved signals at different probe wavelengths, they were carefully normalized to take into account variations of the pump power and pump and probe spot sizes. The following calculation was done to quantify the dependencies of the amplitudes of the time-dependent signals, assuming homogeneous particle distribution in a thin matrix. Radial symmetry and overlap of pump and probe beams in the sample plane were assumed, which reduces the discussion to a two-dimensional problem.

The contribution of a circle of radius ρ and width $d\rho$ to $\Delta T/T$, illuminated by the pump and probe beams both centered at $\rho = 0$, is proportional to $I_p(\rho)I_{pr}(\rho)/P_{pr}\rho d\rho$, with $I_p(\rho)$ and $I_{pr}(\rho)$ the intensities of the pump and probe beams at the sample position, respectively and P_{pr} the probe power, introduced due to the normalization by the transmission $\Delta T/T$. Assuming Gaussian shapes, the intensities can be described by:

$$\begin{aligned} I_p(\rho) &= \frac{2P_p}{\pi\sigma_p^2} e^{-2\rho^2/\sigma_p^2}, \\ I_{pr}(\rho) &= \frac{2P_{pr}}{\pi\sigma_{pr}^2} e^{-2\rho^2/\sigma_{pr}^2}, \end{aligned} \tag{2.9}$$

with $\sigma_{p,pr}$ the respective waists of pump and probe beams. The dependence of the signal amplitude on the beam spots can be obtained by integration over the entire plane (the sample being large with respect to the focused beams):

$$\left(\frac{\Delta T}{T}\right)_{exp} \propto \int_0^\infty \frac{I_p(\rho)I_{pr}(\rho)\rho}{P_{pr}} d\rho \propto \frac{A_p P_p}{\sigma_p^2 + \sigma_{pr}^2} \equiv K(P_p, A_p, \sigma_p, \sigma_{pr}). \tag{2.10}$$

The linearity on A_p , which is the absorption coefficient of the sample at the pump wavelength, and P_p , reflect proportionality to the absorbed energy, as has been shown for example in the inset of Fig. 2.8(a). The symmetric dependence on the waists of both beams $1/(\sigma_p^2 + \sigma_{pr}^2)$ takes into account not only the excitation of the nanoparticles via the focusing of the pump beam but also the detection of inhomogeneously heated particles via the width of σ_{pr} . Note that in the case of a probe spot size much smaller than the one of the pump ($\sigma_{pr} \ll \sigma_p$), the dependence on σ_{pr} can be omitted. In this situation, which is often preferred in experiments, only a small, homogeneously heated spot in the center of the pump beam is probed. For the present experiments, we could not purposely expand the pump beam to fulfill this condition, as this would yield a reduction of the amplitude of the signal.

The waists were measured by a CCD camera which was placed at the position of the sam-

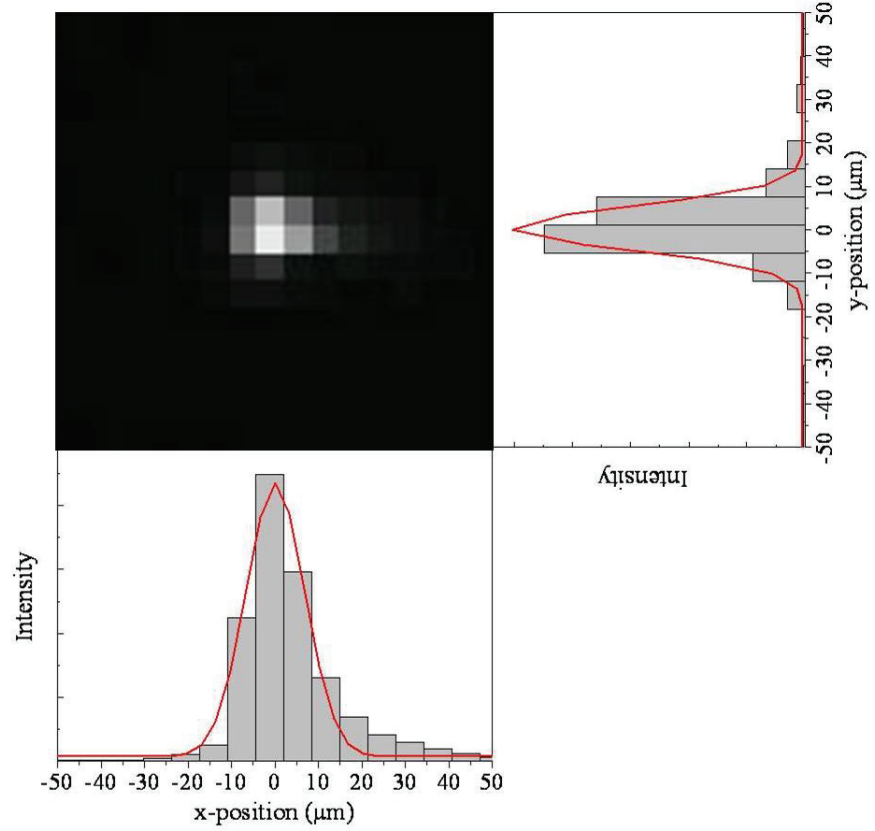


Figure 2.16: Pump beam ($\lambda_p = 980$ nm) at the sample plane, mapped by a CCD camera. Horizontal and vertical waists are deduced from this image by a Gaussian fit to the intensity in the x and y-plane.

ple. A typical image obtained by this type of measurement is shown in Fig. 2.16 yielding $\sigma_{p,pr}$ of the same order ($\sim 9 \times 13 \mu\text{m}$ and $\sim 8 \times 9 \mu\text{m}$ for IR and UV beam, respectively). For data analysis, all comparisons between the amplitudes of different transient signals of a sample for different probe wavelengths were done after normalization by reference values taking into account $\sigma_{p,pr}$ and P_p and A_p :

$$\left(\frac{\Delta T}{T}\right)_{norm} = \left(\frac{\Delta T}{T}\right)_{exp} \times \frac{K(P_{p0}, A_{p0}, \sigma_{p0}, \sigma_{pr0})}{K(P_p, A_p, \sigma_p, \sigma_{pr})} \quad (2.11)$$

2.3.2 Modeling of the optical detection of the electron thermalization

The principle of the experimental detection of the characteristic electron gas thermalization time is illustrated in Fig. 2.17(a). After intraband excitation by an IR pump pulse (solid red vertical arrow, Fig. 2.17(a)) and electron momentum conservation by inelastic scattering (red dashed horizontal arrow), the energy distribution of the electron gas in the

conduction band is strongly out-of-equilibrium (Fig. 2.17(b) and (c)). The optical detection of this distribution change can be realized via a probe pulse of photon energy close to the interband transition threshold ($\hbar\Omega_{ib}$), which is shown for the silver band structure near the L-point ($\hbar\Omega_{ib} \approx 3.95$ eV). At equilibrium, both transitions from the d-band to the conduction band (d \rightarrow p) and from the conduction band to the s-band (p \rightarrow s) contribute to the interband dielectric function. After ultrafast excitation, supplementary transitions are made possible (Fig. 2.17(a), full black arrows) whereas other transitions become less efficient due to the transiently modified electron distribution (Fig. 2.17(a), black dotted arrows). For photon energies close to $\hbar\Omega_{ib}$, the time delayed probe pulse is thus directly

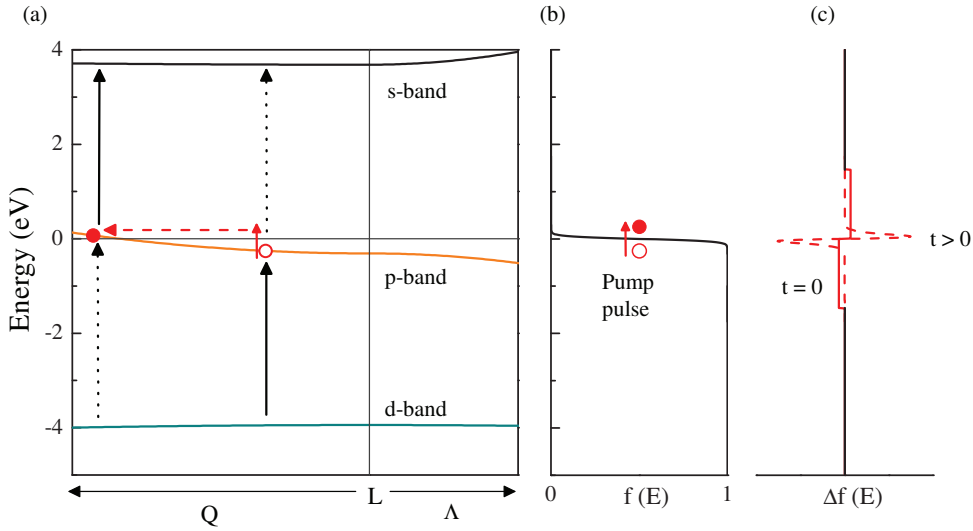


Figure 2.17: (a) Scheme of the experimental detection of the electron gas distribution change Δf (see text for details). (b) Electron distribution before excitation (energies are shown by their distance to the Fermi energy E_F). The pump pulse promotes electrons with energies below E_F to states above E_F . (c) Electron distribution change around E_F for $t = 0$ and $t > 0$ (full and dashed line, respectively).

sensitive to the electronic distribution change Δf (Fig. 2.17(c)) via the change of $\Delta\epsilon_1^{ib}$ and $\Delta\epsilon_2^{ib}$. For the short timescales of electron internal thermalization (few hundred fs), the modification of the interband term of the metal dielectric function indeed dominates over its Drude term [5, 17]. In the following, we thus concentrate on the analysis of $\Delta\epsilon_{1,2}^{ib}$ induced by Δf (see Secs. 1.3.2 and 1.4).

2.3.2.a Optical response of nanoparticles following electron distribution changes

Following the model presented in Chapter 1 (Secs. 1.3.2, 1.4 and 1.5), the transient modification of the extinction cross-section of a 30 nm silver sphere in a glassy matrix ($n_m=1.4$)

2.3. Ultrafast electron-electron interactions in Ag clusters

is computed (Fig.2.18(a)) for three different time delays and energies around the interband transition threshold of silver ($t = 0$ is defined as the moment when half of the energy of the pump pulse has been absorbed). The linear absorption spectrum σ_{ext} and its derivatives $a_{1,2}$ have already been commented in Sec. 1.2, Fig. 1.10(a). Fig. 2.18(b) shows the contributions of $a_1\Delta\epsilon_1^{ib}$ and $a_2\Delta\epsilon_2^{ib}$ to $\Delta\sigma_{ext}$ for a delay $t = 400$ fs. In the considered spectral region, the derivatives a_1 and a_2 being relatively undispersed (negative and positive, respectively), the contributions to $\Delta\sigma_{ext}$ follow the real and imaginary parts of the dielectric function $\Delta\epsilon_1^{ib}$ and $\Delta\epsilon_2^{ib}$ with a slight domination of $\Delta\epsilon_2^{ib}$ for most wavelengths (Fig. 2.18(b)).

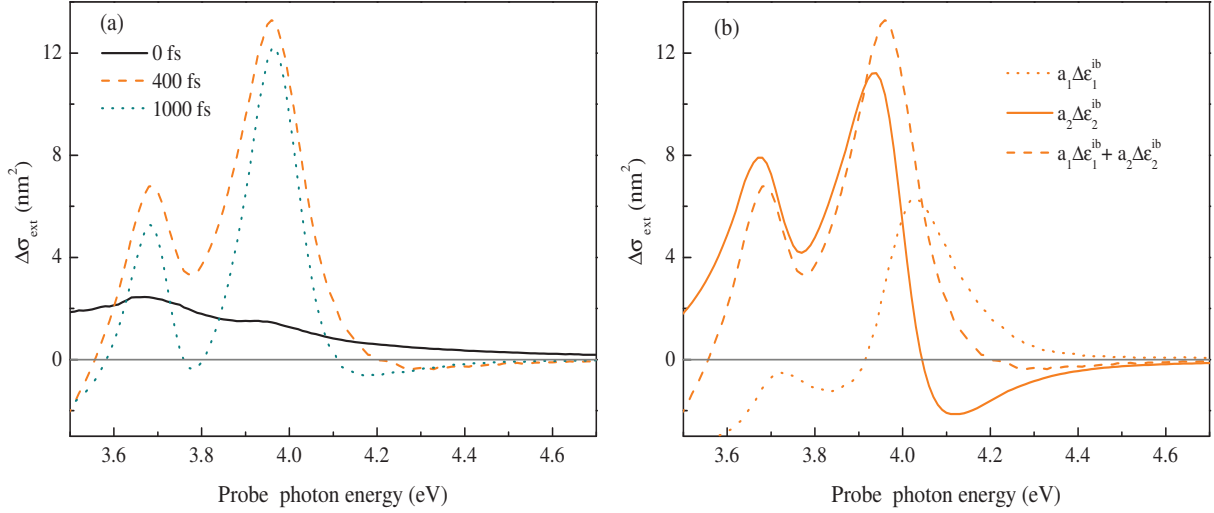


Figure 2.18: Computed extinction cross-section changes (a) for a $D = 30$ nm Ag nanosphere in glass ($n_m = 1.4$) at three different delays after excitation by a 850 nm and 60 fs pump pulse with $\Delta T_{exc} = 100$ K. For computation, the bulk dielectric function changes have been multiplied by the spectral derivatives of the calculated extinction cross-section (Sec. 1.5). (b) Contributions of the change of the real and imaginary parts of the interband dielectric functions for a delay of 400 fs.

Alternatively, $\Delta\sigma_{ext}$ can be plotted at fixed probe energy $\hbar\omega_{pr}$ as a function of the pump-probe time delay t (Fig. 2.19(a)). Comparing time-dependent signals of different probe photon energies around $\hbar\Omega_{ib}$ is very insightful. Close to the maximum amplitude (~ 4 eV) the transient behavior is characterized by a fast rise followed by an exponential decay. The delay necessary to reach the peak of the signal contains information on the electron-electron interaction dynamics, while its decay corresponds to the electron gas energy loss to the lattice [109]. Nonetheless the signal shape changes considerably for probe photon energies far from $\hbar\Omega_{ib}$ (> 4.2 eV), where the signals change sign with time evolution. Additionally, even for probe photon energies with no sign change (< 3.9 eV), the rise of $\Delta\sigma_{ext}$ is faster compared to the one at the maximum of the amplitude. Definition of a

characteristic internal electron gas thermalization time is thus less straightforward as the one of the electron-phonon interactions, where the dynamics are basically independent of the probe wavelength. Here, the signal dynamics is very sensitive to the probe photon energy due to the dependence of $\Delta\epsilon_{1,2}^{ib}$ on $\Delta f(E)$. For probe wavelengths far from $\hbar\Omega_{ib}$, a fast transitional response can thus be expected, due to fast electronic relaxation of energy states far from the Fermi level, as predicted by the Fermi-liquid theory [22] whereas close to $\hbar\Omega_{ib}$ slower electron kinetics are assumed.

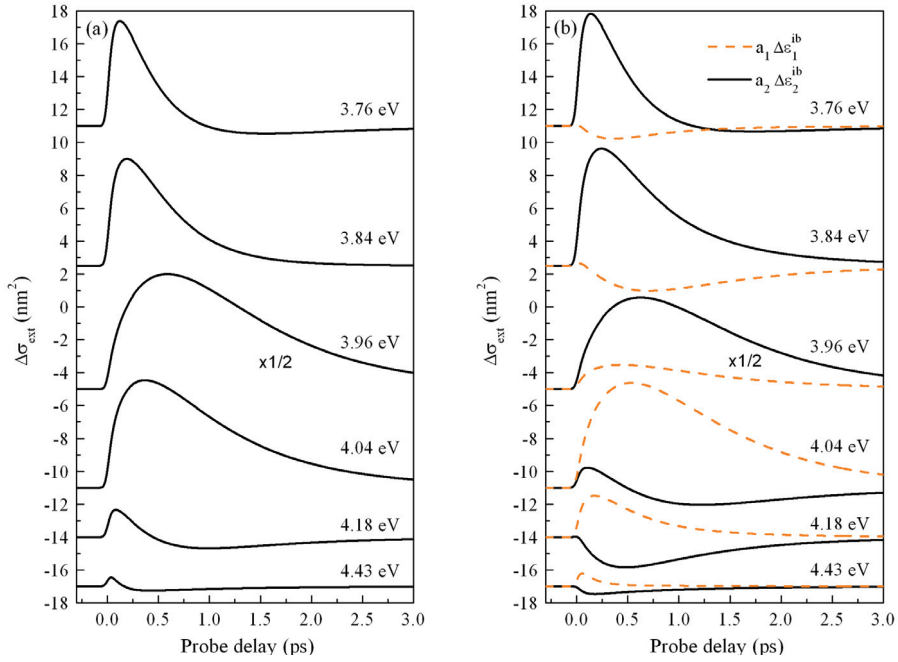


Figure 2.19: (a) Same as in 2.18(a) plotted as a function of probe delay for different probe photon energies. In (b) the contribution to $\Delta\sigma_{exc}$ of the real and imaginary part of the change of the interband dielectric functions are shown. Signals are vertically shifted for clarity.

However, close to the signal maximum the dynamics are unchanged over a small spectral range (3.9 eV to 4.1 eV), the rise of $\Delta\sigma_{ext}$ reflecting the occupation change of electronic states close to the Fermi energy. Electron scattering in and out of those states is the slowest process during the thermalization of the electron gas and a measure of their occupation change reflects thus the characteristic thermalization dynamics of the entire free electron gas.

In this section we will study modifications due to nanoparticle size reduction of both the spectral features of $\Delta\sigma_{ext}$ around the interband transition threshold (see e.g. Fig. 2.18(a)) and of the characteristic electron gas thermalization time τ_{th} , defined as the rise of the time-dependent $\Delta\sigma_{ext}$ at its maximal amplitude.

2.3.2.b Testing the model: Ag film

The quantitative modeling described here and in Chapter 1 (Secs. 1.3.2, 1.4 and 1.5) provides the absolute value of the transmission changes $\Delta T/T$. As a test for the different parameters used in the Boltzmann equation (screening β , bulk τ_{e-ph} , see Table 1.5), as well as the ones in the model for the interband dielectric function (electronic band gaps and momentum matrix element, see Sec. 1.1.4), which we chose differently than in previous studies (e.g. Refs. [5, 17, 68]), we compare the simulated dynamics to that measured in an optically thin ($L = 23$ nm) polycrystalline silver film. Measurements on the Ag film were realized in parallel to the actual samples, thus also serving as a test of the experimental conditions and of the normalization of the signal amplitudes.

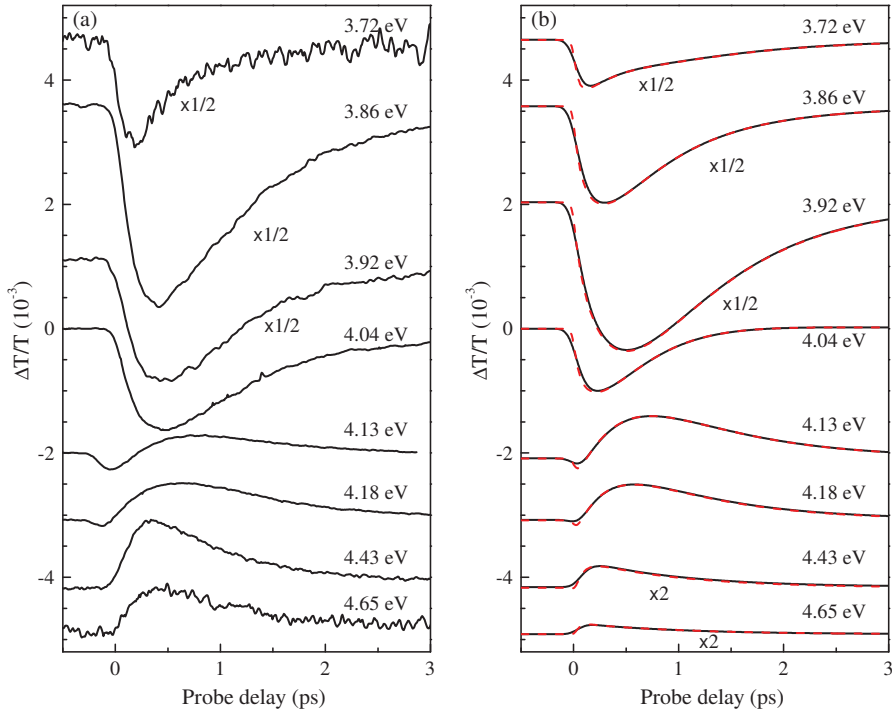


Figure 2.20: Experimental (a, $\lambda_p = 3\lambda_{pr}$) and simulated (b, $\lambda_p = 850$ nm) pump-probe transient transmission for a $L = 23$ nm silver film for different probe photon energies. The amplitudes of the experimental signals were normalized to $\Delta T_{exc} = 100$ K. For the calculated signals a 850 nm and 60 fs pump pulse with $\Delta T_{exc} = 100$ K was used. The red dashed lines in (b) correspond to an infinitely short temporal resolution, the black full lines illustrate the same signals convoluted by a Gaussian function of 140 fs FWHM, corresponding to the temporal width of the experimental probe pulses.

The experimental results of the relative transmission change $\Delta T/T$ for different probe photon energies are shown in Fig. 2.20(a). The sample has been excited by the direct output of the Ti:Sapphire laser and the signals have been normalized to an equivalent electron excess temperature $\Delta T_{exc} \approx 100$ K. The experimental signals can be compared to the simulated ones (Fig. 2.20(b)), where $\Delta\epsilon_{1,2}^{ib}$ has been calculated with the same pa-

rameters as before (850 nm and 60 fs pump pulse with $\Delta T_{exc} = 100$ K). The transmission of the film and its derivatives with respect to $\epsilon_{1,2}$ were introduced by using the theoretical transmission formula for thin films [36, 110].

Shape and amplitude of the signals are in very good agreement, except for small discrepancies in amplitude for high probe photon energies, which could be ascribed to uncertainties in film thickness or excitation. The good quantitative agreement is underlined by Fig. 2.21, where the amplitudes of the experimental, time-dependent $-\Delta T/T$ signal for probe delays of 0 fs, 400 fs, 1 ps have been plotted as a function of probe photon energy and compared to simulations. For a better visibility both signals have been normalized at the spectral maximum for a delay of 400 fs. The simulated $-\Delta T/T(\hbar\omega_{pr})$ (Fig. 2.21) have been convoluted by a Gaussian function of 0.2 eV FWHM in order to take into account the energy width of the probe pulse (Fig. 2.21, inset) while the simulated time-dependent signals have been convoluted with a 140 fs probe pulse duration (Fig. 2.20(b)).

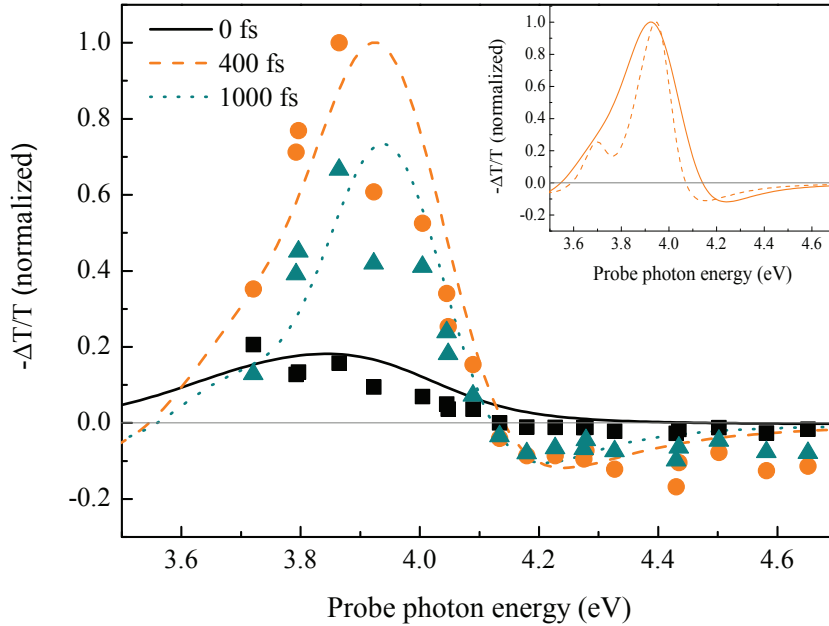


Figure 2.21: Experimental transient spectra of the $L = 23$ nm Ag film for probe delays of 0 fs (black rectangles), 400 fs (orange dots) and 1 ps (green triangles) with the same conditions as in Fig. 2.20(a). Simulations have been performed with the same parameters as in Fig. 2.20(b), the results being convoluted by a Gaussian function of 0.2 eV FWHM. For easier comparison, experimental and simulated signals have been normalized, setting the maximum of the curve of a probe delay of 400 fs to unity. Inset: Simulated transient absorption for $t = 400$ fs before (orange dashed line) and after convolution (full orange line).

As in the case of Ag nanoparticles, the slowest dynamics occurs for probe wavelengths yielding signals of maximal amplitude. It can be fitted using a phenomenological response function, assuming a monoexponential rise with an internal thermalization time constant

2.3. Ultrafast electron-electron interactions in Ag clusters

τ_{th} and exponential decay with the relaxation time $\tau_{1/e}$:

$$f(t) = H(t) [B(1 - e^{-t/\tau_{th}})e^{-t/\tau_{1/e}}], \quad (2.12)$$

with $H(t)$ the Heaviside function. The first term represents the exponential rise due to electron-electron scattering, while the second one describes the decay provoked by electron-phonon interactions. If necessary, an additional background y_0 taking into account lattice heating and heat transfer to the matrix can be introduced. A fit of the experimental results is obtained by convolution of the response function $f(t)$ and the pump-probe cross-correlation function, described by a Gaussian function with 150 fs FWHM (see Sec. 2.1.1). The experimental signal at probe photon energy $\hbar\omega_{pr} = 3.92$ eV (Fig. 2.22(a)) yields the characteristic times $\tau_{th} = 300$ fs and $\tau_{1/e} \approx \tau_{e-ph} = 0.9$ ps which are in very good agreement with literature values [68]. The phenomenological function can also be used to reproduce the simulated signal yielding similar values (Fig. 2.22(b)). This comparison between model and experiments in an Ag film confirms that the chosen parameters are correct for the ultrafast spectroscopy investigations of bulk silver and that the normalization procedure we introduced in Sec. 2.3.1 is adapted for analysis of signals with variable pump-probe parameters (e.g. absorption, pump power, waists).

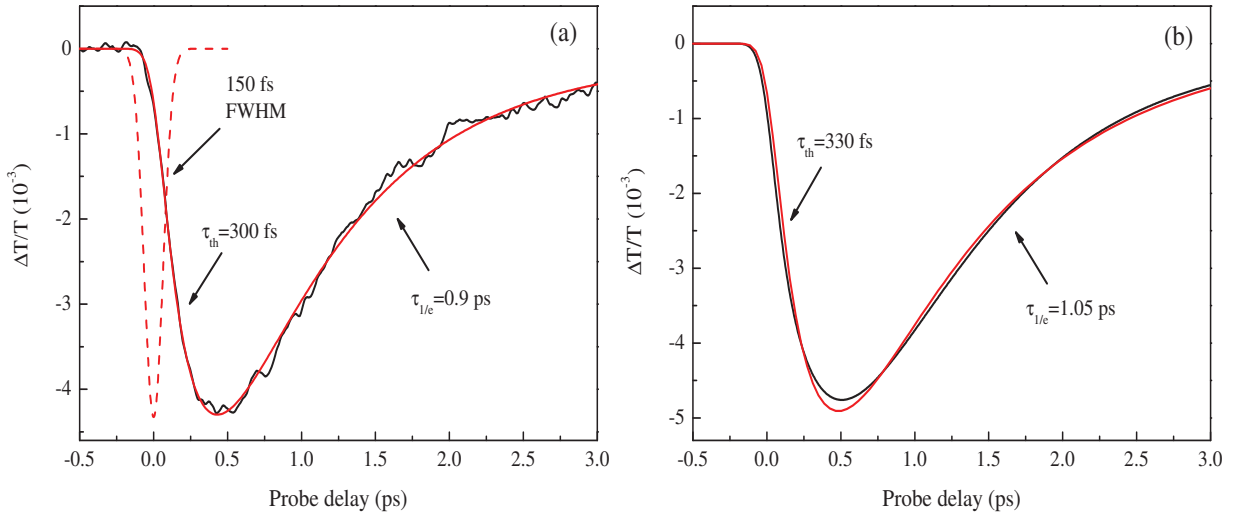


Figure 2.22: (a) Experimental pump-probe signal of a silver film with P/Pr 1.31/3.92 eV (full black line, same as in Fig. 2.20(a)) and fit using the phenomenological function f (full red line), convoluted by a Gaussian function of 150 fs FWHM (red dashed line) corresponding to the temporal resolution of the experiment. (b) Simulated signal for the same probe photon energy and by taking into account the 140 fs temporal duration of the probe pulse (full black line, same as in Fig. 2.20(b)) and its fit (full red line).

2.3.3 Experimental results for small particle sizes

2.3.3.a Transient time-resolved signals

Pump-probe signals have been recorded for several Ag cluster samples of Table 2.1 obtained by magnetron ($D = 1.1, 1.5$ and 1.9 nm) and LECBD ($D = 2.2$ and 2.8 nm) synthesis. In

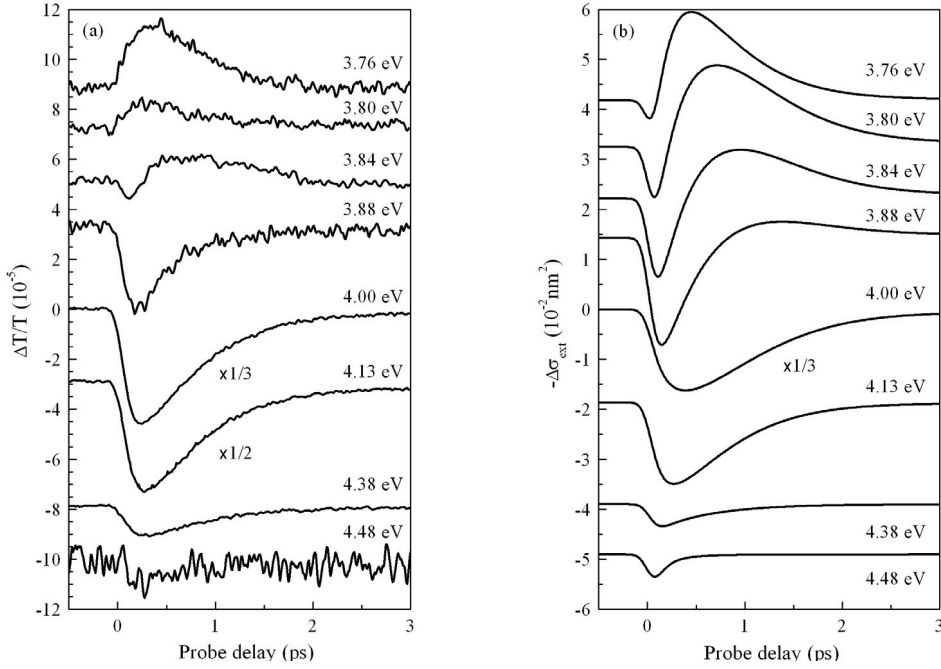


Figure 2.23: Experimental pump-probe signals (a) and simulated transient extinction cross-section (b) for $D = 2.8$ nm Ag nanospheres in silica at different probe photon energies. Simulations have been performed with a 60 fs and 850 nm pump pulse with $\Delta T_{exc} = 580$ K (absorption of one photon) and convoluted with the 140 fs probe pulse. The bulk model has been adapted to stronger electron-phonon coupling due to size reduction ($\tau_{e-ph} = 0.48$ ps).

Fig. 2.23(a) the time-dependent $\Delta T/T$ for different probe photon energies for the largest studied sample is reported, consisting of Ag nanospheres with an average diameter of $D = 2.8$ nm. A maximal signal is obtained for $\hbar\omega_{pr} = 4$ eV and a sign change is observable for low photon energies (< 3.88 eV). The short delay dynamics behave in the same way as predicted for larger particles (see Sec. 2.3.2). The change of the extinction spectra $\Delta\sigma_{ext}$ (proportional to $-\Delta T/T$) has been modeled by solving the Boltzmann equation with a 60 fs and 850 nm pump pulse and equivalent electron gas heating of $\Delta T_{exc} = 580$ K, corresponding to absorption of a single IR photon. Furthermore the electron-phonon intrinsic time was fixed to $\tau_{e-ph} = 0.48$ ps which corresponds to the experimentally measured value of $\tau_{1/e}$ for this size (see Sec. 2.2.3.b). The experimental extinction spectrum of the samples not being available because of their very low density, the derivatives a_1 and a_2 have been calculated from the simulated spectrum as explained in Chapter 1 (Sec. 1.2) using the refractive index n_m of the porous silica matrix as a free parameter. To properly

2.3. Ultrafast electron-electron interactions in Ag clusters

reproduce the spectral features, an effective value $n_m \approx 1$ was used compensating for uncertainties in the dielectric functions measured by Johnson and Christy [25], which are known not to correctly reproduce the SPR position in silver (Sec. 1.2) [30].

Agreement of the shape of experimental and simulated signals is still very good for particles in this size range. Moreover, the thermalization time τ_{th} (given by the characteristic time of the amplitude rise at 4 eV) is visibly shorter for the experimental signal than for the simulated one. This is a consequence of particle size reduction which will be discussed in Sec. 2.3.3.d.

2.3.3.b Excitation-dependent dynamics

We have seen above (Sec. 2.2.4.b) that for very small nanospheres ($D < 3$ nm), excitation is most often induced by absorption of a single photon and the equivalent temperature of the electron gas is very high. This strong temperature rise ΔT_{exc} also affects τ_{th} , which then strongly depends on the energy injected in the electron gas [68, 109]. Indeed, for strong excitation the rise of the signals becomes faster, yielding reduction of τ_{th} . The increase of electron-electron scattering rates can be quantitatively understood by basic considerations on the perturbed electron gas. For weak energy injection, only a small fraction of the conduction electrons are implicated in the scattering processes, most of them still occupying initial unperturbed states. However, for stronger excitation a greater number of electrons is perturbed which leads to a decrease of occupied states around the Fermi energy. As a consequence of the Pauli exclusion principle the unoccupied states constitute an increasing number of final scattering states and thus lead to more efficient electron-electron scattering processes [109].

In the same way as in Sec. 2.2.4.b, effects of strong excitation are observed for infrared pump pulses by varying their power, due to the absorption of more than one photon by a part of the nanoparticles. Fig. 2.24(a) illustrates the transient transmission signals of $D = 1.1$ nm particles in the pump and probe configuration P/Pr 910/303 nm (4.09 eV). The pump power has been increased from 7 mW (green line) to 68 mW (black line), the signals being fitted following the procedure of Sec. 2.3.2.b (dashed red lines). As expected, for the stronger excitation the signals show a faster electron scattering dynamics ($\tau_{th} = 130$ fs vs. $\tau_{th} = 250$ fs) and a slower electron-phonon dynamics ($\tau_{1/e} = 1.95$ ps vs. $\tau_{1/e} = 0.84$ ps), the second quantity being in good agreement with the two-temperature model and experiments in the configuration IR/Blue (compare Fig. 2.11). To simulate the increase of τ_{th} , in Fig. 2.24(b) we modeled the signal by solving the bulk Boltzmann equation for different electron gas excitations corresponding to absorption of one and two 850 nm photons ($\Delta T_{exc} \approx 2800$ K and 4400 K, respectively). The experimentally measured trend is confirmed.

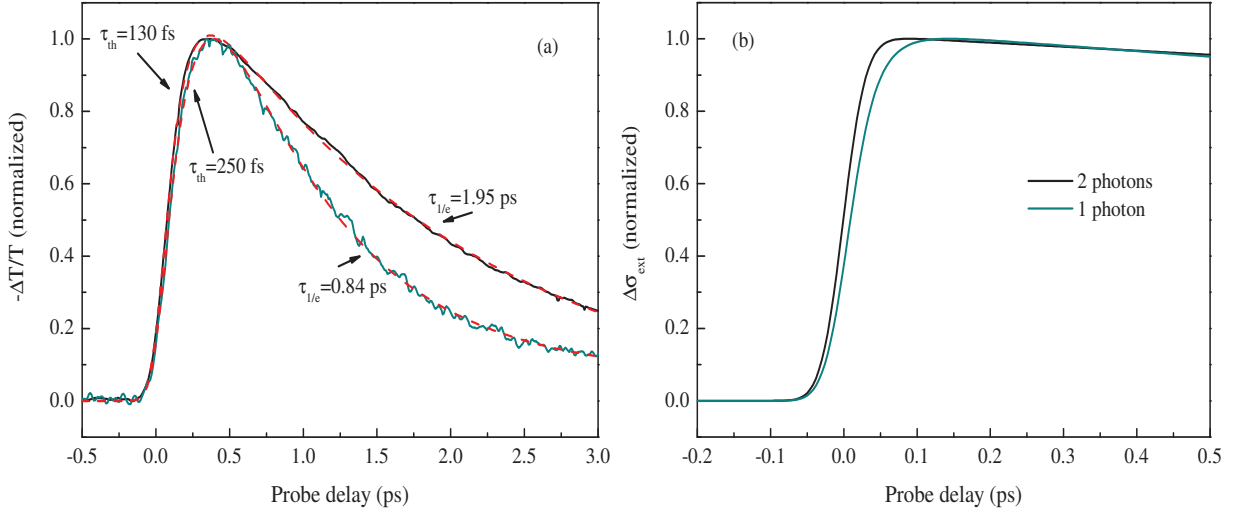


Figure 2.24: Experimental transient transmission (a) and simulated transient extinction cross-section (b) for $D = 1.1$ nm silver nanospheres for $\hbar\omega_{pr} = 4.09$ eV. For the pump pulse of the experimental signal a 910 nm beam of 7 mW (full green line) and 68 mW (full black line) was used. Experimental signals were fitted by $f(t)$ (Eq. (2.12)), convoluted by the pump-probe cross-correlation of 150 nm FWHM (dashed red line). For the simulated signals in (b), bulk parameters were used and the free electrons were excited by a 60 fs and 850 nm pump pulse with $\Delta T_{exc} = 2800$ K (full green line) and $\Delta T_{exc} = 4400$ K (full black line). In order to take into account the duration of the probe pulse, the simulated signals were convoluted by a 140 fs FWHM Gaussian function.

When comparing τ_{th} in samples of different sizes it must be kept in mind that, as in the case of electron-phonon interactions, in this size range particles are excited by a single photon for low pump fluences. As a consequence, the excitation of the particles is size-dependent, their dynamics for these strong perturbations being sensitive to ΔT_{exc} . The experimental values obtained for τ_{th} should thus be considered as a lower limit (τ_{th} decreases for strong excitation). For further investigation on the impact of single photon absorption on the thermalization dynamics of Ag clusters in the very small size range, similarly to the observations for $\tau_{1/e}$ (Sec. 2.2.4.b), the dependence of τ_{th} on the pump photon energy (e.g. blue pump wavelength) should be studied in future experiments.

2.3.3.c Ultrafast transient absorption spectra: size dependence

The $-\Delta T/T$ spectra at a fixed probe delay (e.g. 400 fs) for different diameters have been experimentally investigated and theoretically simulated. In simulations the intrinsic coupling time $\tau_{e-ph} = 0.87$ ps of bulk silver was kept constant with particle size, as it does not influence the signal at short probe delays. Additionally we checked that the transient spectra were not considerably modified for slightly changing electron thermalization dynamics, using therefore a weak excitation $\Delta T_{exc} = 100$ K for all particle sizes (for a complete re-

2.3. Ultrafast electron-electron interactions in Ag clusters

production of the time-dependent signal shapes, both modifications of the size-dependent ΔT_{exc} and the adjustment of the electron-electron kinetics via the screening parameter β with particle size would be needed. However, small excitation signals reproduce well the shape of the experimental signals, a small change of their dynamics being negligible for the comparison of size-dependent transient absorption spectra). In Figs. 2.25(a)

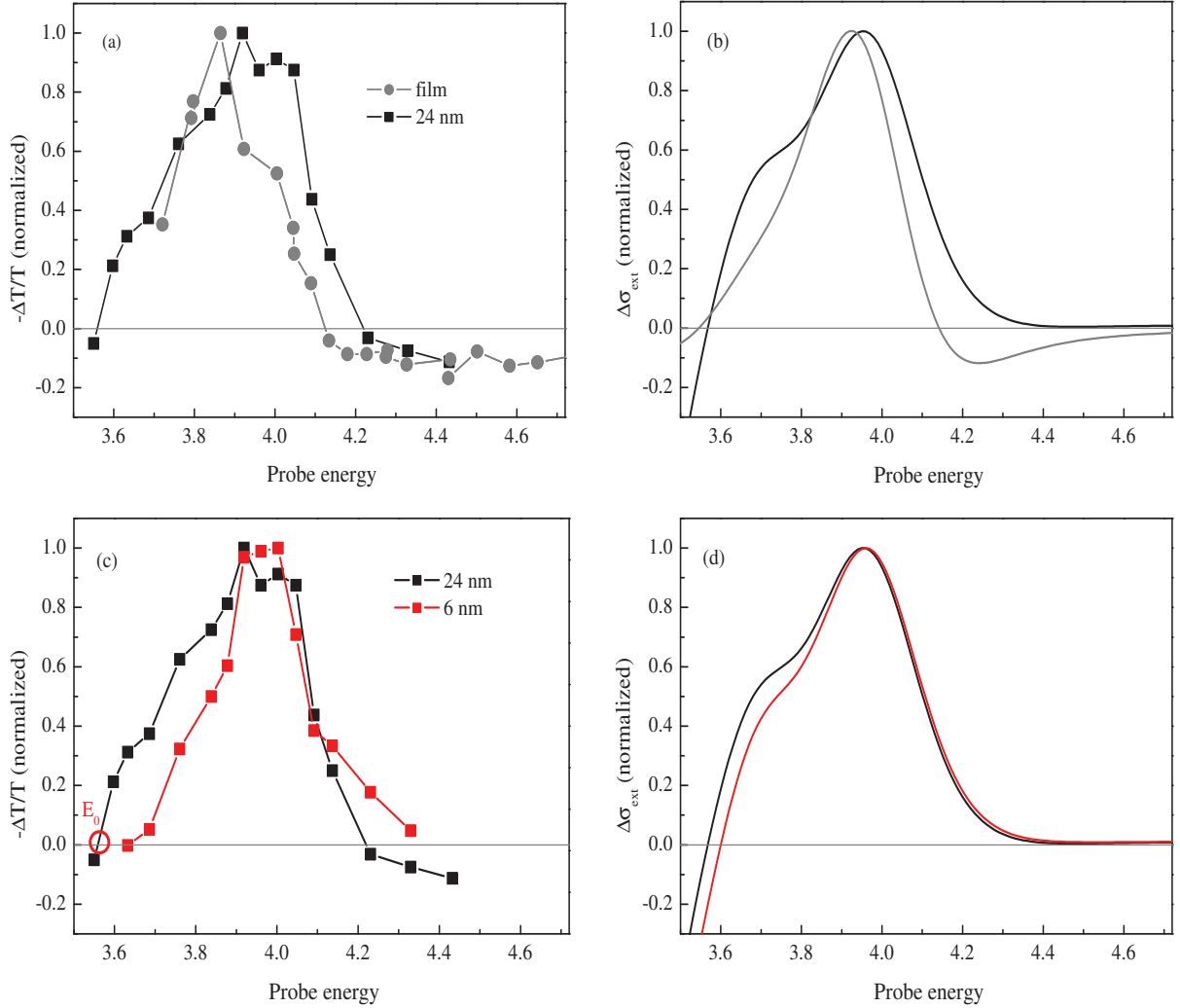


Figure 2.25: Experimental (a,c) and simulated (b,c) transient spectra at pump-probe delay $t = 400$ fs for Ag nanoparticles of different diameters and for the Ag film. All spectra were normalized at their maximum. The simulated ones were convoluted by a Gaussian function of 0.2 eV FWHM. Excitation in the experimental transient spectra was made by an IR beam ($\lambda_p = 3\lambda_{pr}$) with a power around 60 mW. Simulations were performed using bulk parameters and a 60 fs and 850 nm pump beam with $\Delta T_{exc} = 100$ K.

and 2.25(c) we show the experimental transient absorption spectra for the Ag film and for large nanospheres investigated in the past ($D \geq 6$ nm in glass [104]). For computations (Figs. 2.25(b) and 2.25(d)), an effective value of the glass optical constant $n_m = 1.4$ was used yielding the best reproduction of the spectral positions for metal nanoparticles.

Chapter 2. Size dependence of electronic interactions in metal clusters

When comparing the transient spectrum of the largest nanoparticles ($D = 24$ nm) to the one of bulk Ag (Fig. 2.25(a)), its width is considerably larger and the sign change is shifted to higher energies (blue shift). The size decrease of the glass-embedded nanospheres ($D = 6$ nm, Fig. 2.25(c)) induces a further blue shift of their transient spectra, with a clear sign change at low probe photon energies and a tail in amplitude towards high energies. This is also reproduced by simulations (Fig. 2.25(d)), where size effects are exclusively in-

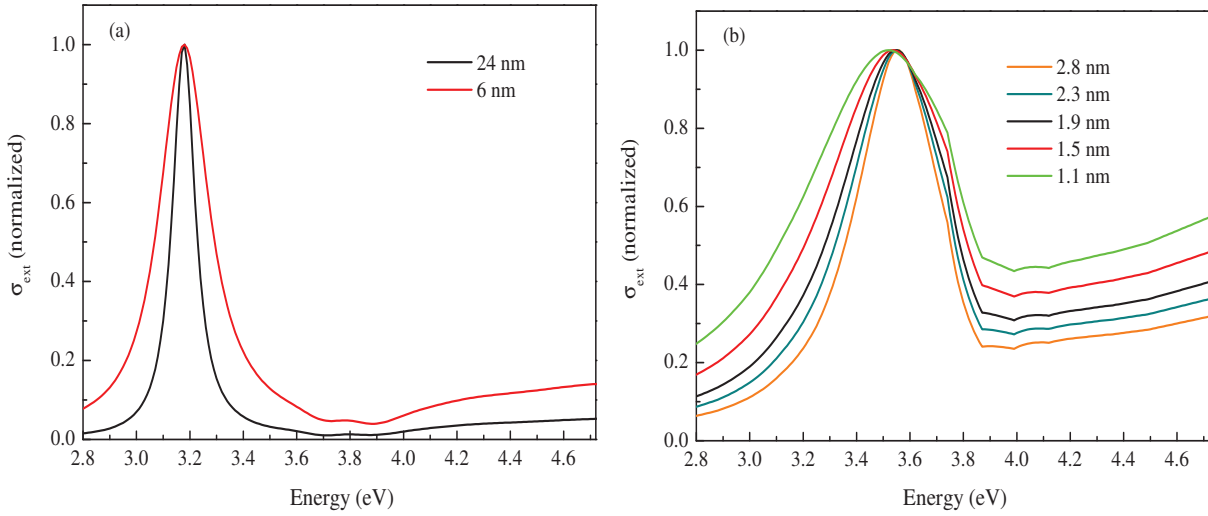


Figure 2.26: Computed extinction cross-section for silver nanospheres of different diameters in glass (a) and silica (b).

troduced in the linear extinction spectra of the particles, via the surface broadening term $2gv_F/D$ (with $g=0.7$) in ϵ_2 (see Sec. 1.1.3, Eq. (1.26)). The associated extinction spectra, calculated by Mie theory (Sec. 1.2) are shown in Fig. 2.26(a). This has a consequence in the derivative coefficients a_1 and a_2 (Sec. 1.2) which become size-dependent. This pure plasmonic effect is able to explain the $\Delta T/T$ spectral shape modifications in $D = 24$ nm and $D = 6$ nm samples being precisely reproduced with no adjustment of the bulk parameters in the Boltzmann equation and the model for optical transitions of Rosei et al. (see Secs. 1.1.4 and 1.3.2, Figs. 2.25(b) and (d)).

In the small size regime investigated in this work, transient absorption behaviors are different. Fig. 2.27(a) shows the transient absorption spectra obtained for $1.1 \leq D \leq 2.8$ nm nanospheres (Table 2.1). Here, the samples below $D = 2.8$ nm show non-monotonic shifts with reducing diameter. At the same time the width reduces and the curves lose their long energy tail. This behavior does not seem to be predicted by the present model (Fig. 2.27(b)), based on bulk considerations for the dynamic processes via $\Delta f(t)$, and dielectric plasmonic modifications for the extinction spectra. In this “small solid” picture,

2.3. Ultrafast electron-electron interactions in Ag clusters

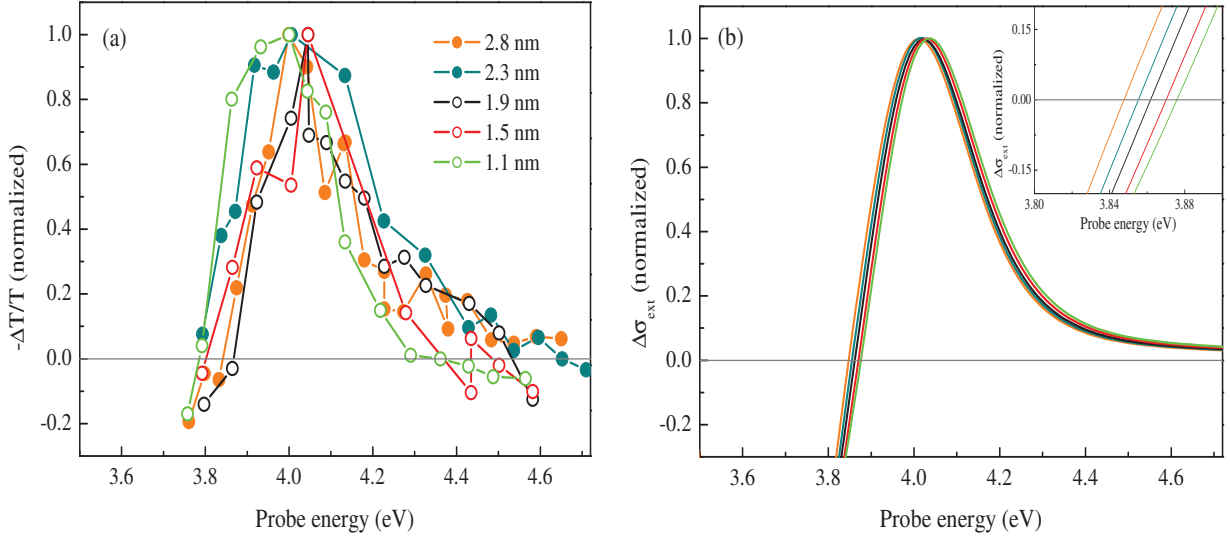


Figure 2.27: Experimental (a) and simulated (b) transient spectra for Ag clusters in the very small size range (full dots: LEBCD, open dots: magnetron source) in the same conditions as in Fig. 2.25. All spectra were normalized at their maximum, the simulated ones were convoluted by a Gaussian function of 0.2 eV FWHM.

the SPR broadening with size reduction (Fig. 2.26(b)) would as for the larger sizes induce a blue shift of the transient absorption spectra (see Fig. 2.27(b)).

Fig. 2.28 summarizes the size dependence of a characteristic property of the transient $-\Delta T/T$ spectra ($t = 400$ fs, Figs. 2.25(a), 2.25(c) and 2.27(a)), namely the energy position of the sign change at low energies (E_0 , see Fig. 2.25(c)). The energy E_0 is a reliable parameter with a very small uncertainty as it is independent of the amplitude normalization. Fig. 2.28 shows a continuous blue shift of the experimental transient absorption spectra with size reduction for nanospheres larger than 2.3 nm, while for smaller sizes the position of the peak ceases to vary continuously and shows an oscillating behavior around a constant red-shifted value (blue dots), this being not predicted by simulations.

An interpretation for the modified behavior of the size-dependent transient absorption spectra in the small size regime can be given by interband transition modifications, and for small sizes, by electron energy discretization effects. In linear spectroscopy investigations on gold nanoparticles, a change in the interband transition spectrum was already observed in the past for sizes constituting the transition from bulk-like to molecular-like systems and attributed to lattice parameter modifications [111]. This can lead to modifications of the interband onsets for $d \rightarrow p(L)$ and $p \rightarrow s(L)$ transitions in Ag, or even enable supplementary transitions. Also, the momentum matrix element can be altered, thus changing the ratio between the different interband transitions (Sec. 1.1.4, Fig. 1.9(a)). As for the

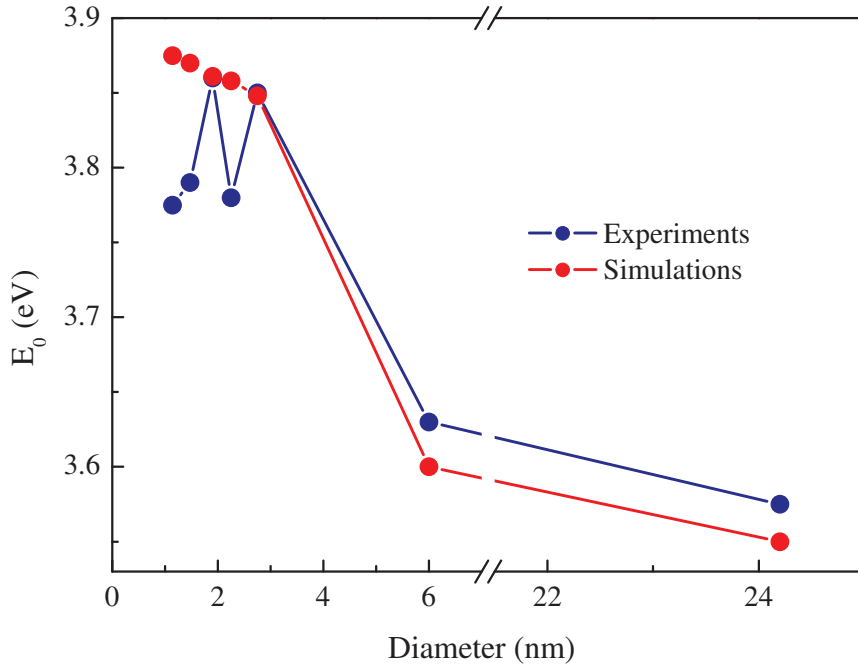


Figure 2.28: Position of the sign changes at low energies E_0 of the experimental (blue dots) and simulated (red dots) transient spectra obtained from Figs. 2.25(c)-(d) and 2.27(a)-(b) as a function of the particle diameter.

electron-lattice relaxation, this small size regime is characterized by specific dependencies which are not in continuity with the “small solid” regime.

2.3.3.d Electron internal thermalization: size dependence

To study electron gas thermalization kinetics, the internal thermalization time τ_{th} of the samples with different particle sizes has been measured. The experimental short delay transient transmission signals of particles with diameters of 2.3 nm, 1.5 nm and 1.1 nm (normalized to unity) are illustrated in Fig. 2.29. They have been fitted using the phenomenological function $f(t)$ (Eq. (2.12)), convoluted by the cross-correlation of pump and probe pulses. The rise of the signals clearly slows down for smaller particles. This phenomenon cannot be explained by the “small solid” model describing the dynamics by Δf , with a size-dependent excitation ΔT_{exc} (see Sec. 2.3.3.b). A stronger excitation for smaller nanospheres would lead to the acceleration of the electron gas thermalization, which is in contrast to the experimental observations. The “small solid” model is thus not sufficient for the reproduction of the observed increase of τ_{th} .

The characteristic electron gas thermalization times are plotted in Fig. 2.30. They decrease continuously from the bulk value $\tau_{th} \approx 340$ fs [68] to $\tau_{th} \approx 150$ fs for nanospheres of a diam-

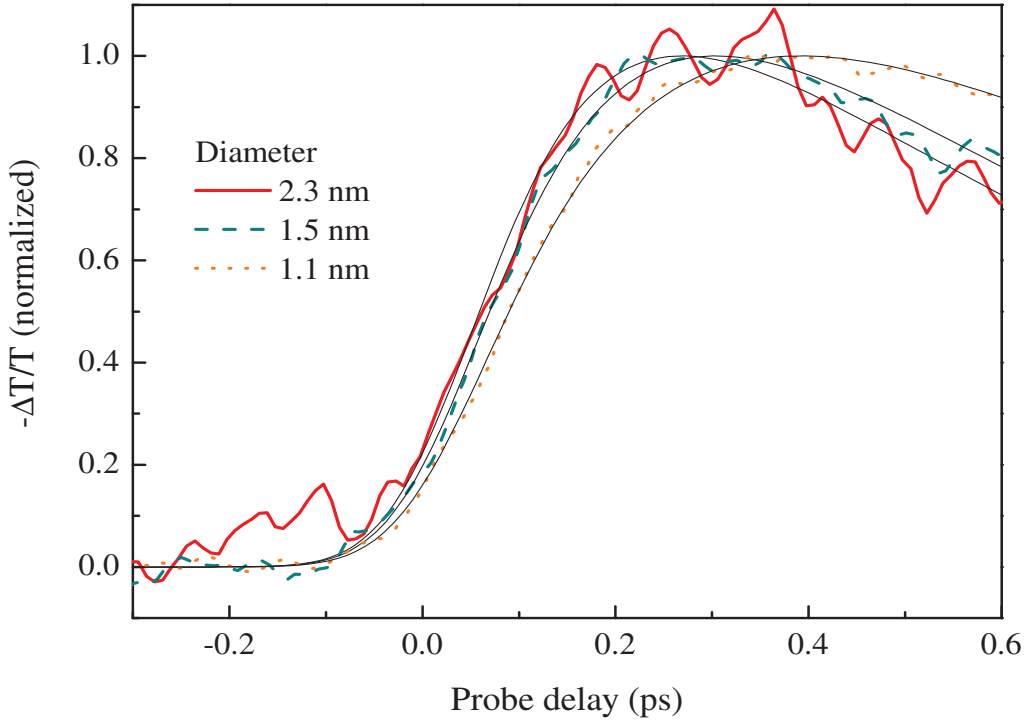


Figure 2.29: Experimental transient transmission signals for $D = 2.3$ nm (full red line), 1.5 nm (dashed green line) and 1.1 nm (dotted orange line) silver nanospheres and their respective fits (full black lines). The samples were excited at low pump powers (~ 10 mW) and probe photon energies were around 4 eV. The fits yield $\tau_{th} = 150$ fs, 200 fs and 250 fs for decreasing sizes. One photon absorption corresponds to $\Delta T_{exc} \approx 850$ K, 1800 K and 2800 K for the samples of decreasing size.

eter $D = 2.8$ nm. As for the electron-phonon coupling time, the measured modifications result from an intrinsic effect of the metal and are not affected by the embedding matrix or the sample preparation technique [5, 16, 17]. The decrease of τ_{th} has been quantitatively studied and interpreted in the past [5, 16, 17]. It has been experimentally shown that this effect is independent of the pump photon energy and is thus not uniquely provoked by a stronger excitation with decreasing nanosphere diameter. The more efficient electronic interaction responsible for decreasing τ_{th} has been explained by modifications of electronic Coulomb screening close to the surfaces. Using Eq. (1.65) and assuming weak excitation, the dependence of the scattering rate of an electron out of its state can be approximated by [112]:

$$\gamma_e \propto n^{-5/6} (\epsilon_0^{ib})^{-1/2}, \quad (2.13)$$

with ϵ_0^{ib} the d-electron contribution to the static metal dielectric function and n the metal free electron density. The thermalization time τ_{th} is a consequence of many scattering

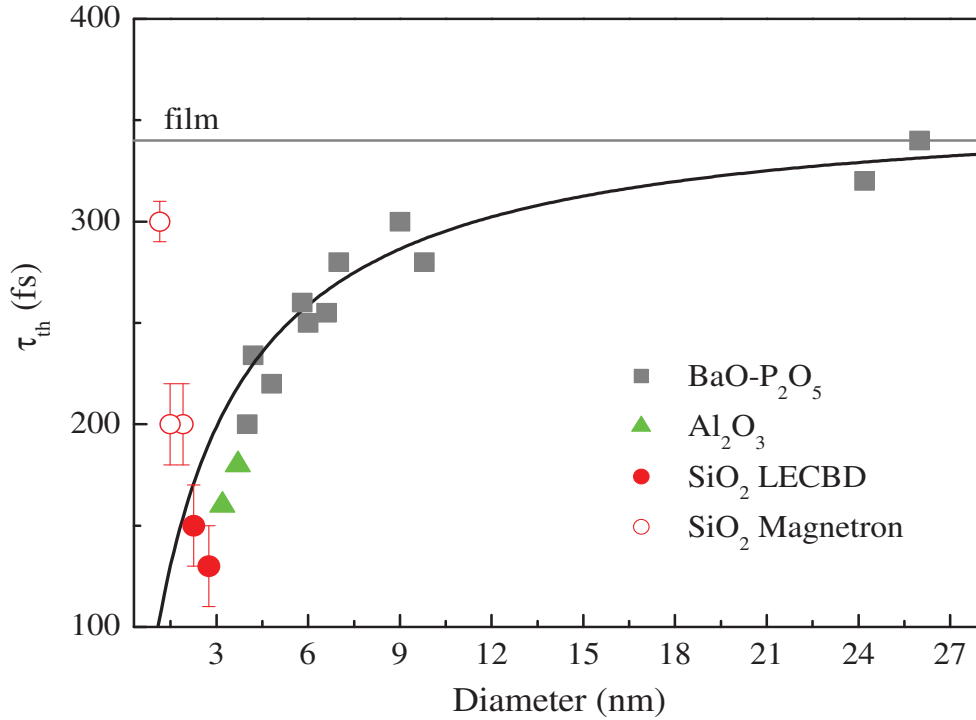


Figure 2.30: Characteristic electron gas thermalization time as a function of the silver nanoparticle diameter and for several matrices. The horizontal gray line corresponds to literature value for a thin silver film. The full black line is obtained by computations of electron scattering with reduced screening, described in the text.

events whose characteristic times vary with γ_e^{-1} . Both parameters in Eq. (2.13) are modified with particle size due to the increasing impact of surfaces. First, the electron density has been shown to be non zero for a region exceeding the classical particle radius, which is the so-called electron spillover effect [113]. Furthermore, screening by d-electrons is less efficient in the outer layers of the particles [114, 115]. Both effects contribute to an increase of γ_e for increasing surface-to-volume ratios (hence for small particles). Using this “small solid” approach, the modifications of τ_{th} in the intermediate size range were quantitatively reproduced (Fig. 2.30).

However this correction to the bulk model begins to fail for particles smaller than about 2.3 nm, being the same size range as the observed deviations from the bulk description of the transient absorption spectra (Sec. 2.3.3.c). In this range the measured thermalization time increases with decreasing diameter, and becomes even comparable to the bulk value for the smallest samples ($\tau_{th} \approx 300$ fs). This is not explainable by including reduced screening due to surfaces, nor by strong heating as a consequence of one photon absorption. It could be another manifestation of discretization of electronic states (Sec. 2.2.4.c),

a quantum model remaining to be developed.

2.3.4 Electronic interactions in Ag clusters: summary

Time-resolved pump-probe measurements were performed on surfactant-free silica-embedded silver clusters with diameters from 1.1 to 3 nm. This demonstrated modifications of different physical processes for sizes smaller than about $D = 2.3$ nm, corresponding to few hundred atoms.

The electron-phonon interactions optically investigated far from resonances showed pump photon-dependent dynamics which could be quantitatively explained by the excitation following the absorption of a single photon, inducing an average increase of the electron-lattice energy exchange time $\tau_{1/e}$ with size reduction. However, for $D < 2.3$ nm, a non-monotonic behavior of $\tau_{1/e}$ demonstrated a change of “regime”, where the discretization of electronic energy states plays an important role.

Close to the interband transitions, the transient absorption spectra $-\Delta T/T$ could be reproduced for particles with diameters larger than 2.3 nm while the transient spectra of the smaller sizes showed characteristics that could not be described by the “small solid” model. A change in the transient absorption spectra can be induced by the modification of the electronic band structure which can also be a consequence of discretization effects. The observed increase of the characteristic electron gas thermalization time τ_{th} with particle size reduction occurred in the same size range (~ 2 nm). In a simple picture this rise can be explained by the increasing distance of discrete electronic levels leading to weaker interactions due to fewer possible final electronic states (reduced phase space).

Modifications in dynamics and spectral features could not be explained by describing the metal nanoparticles as a “small solid” modified by surface effects. The onset of these modifications in Ag clusters was found to be a diameter of $D = 2.3$ nm. Here, quantum confinement effects begin to become dominant, yielding the expected transition from a bulk-like to a molecular-like behavior. This transition for diameters around 2 nm is in good agreement with former measurements on the electrochemical [116] and linear optical properties of metal nanoparticles [111], and correspond to energy level spacing larger than the thermal energy and the maximum phonon energy.

2.4 Electron dynamics in thiol-stabilized Au clusters

Various modifications of optical and electrochemical properties of gold due to size reduction have been reported in the past: gold nanoparticles have been found to be particularly active in catalysis although bulk gold is totally inactive, the origin of this phenomenon still being unclear [10, 11]. The linear optical absorption spectra of gold clusters show a local-

ized surface plasmon resonance down to a diameter of 2 nm, signature of a metallic state, and exhibit molecular states for smaller sizes with specific optical absorption characteristics depending on their structure and environment [117–119]. Furthermore, fluorescence with a high quantum yield was detected in the visible and in the infrared range of the spectrum, also in contrast to bulk gold [95, 120, 121].

In this context, thiol-protected gold clusters present the key advantage of being atomically well defined in the very small size range (0.5 to 2 nm), opening an excellent possibility for time-resolved investigations [92–98, 120]. In this section we investigate the ultrafast dynamics of these model gold nanoparticles, the objective of these studies being the characterization of electronic interactions in a size range where transitions from a “small solid” to a molecular-like behavior will occur.

2.4.1 Samples

Thiol-stabilized Au clusters were synthesized by the “Functional and Nanostructured Materials” team (A. Demessence) at the Institut de Recherches sur la Catalyse de l’Environnement de Lyon (IRCELYon) in Lyon. These nanosystems are precisely defined by n gold atoms and m surrounding thiolate ligands, formulated as $\text{Au}_n(\text{SR})_m$. Only few n, m combinations are stable, giving rise to “magic numbers”. For the synthesis, ligands and metal salts are kept in a strong reducing environment (NaBH_4), the ligands serving to regular and stabilize cluster formation. Using appropriate synthesis parameters, size and thiolate ligands at the surface can be controlled [15, 122–126]. In this work, the neutral atomically defined clusters Au_{25} , Au_{102} and Au_{144} , as well as a larger nanoparticle sample of mean diameter of $D = 3.5 \text{ nm}$ ($\text{Au}_{D=3.5\text{nm}}$) are studied. The samples, their surfactants, solubility, corresponding diameters (in the approximation of a homogeneous gold sphere with the same number of atoms as in the clusters) and reported preparation methods are provided in Table 2.2, the different ligand molecules being shown in Fig. 2.31.

Table 2.2: Presentation of the investigated samples, different stabilizing ligands, solubility, equivalent mean diameters and references for the preparation method.

gold atoms (n)	ligands	(m)	solubility	D (nm)	reference
25	$\text{SCH}_2\text{CH}_2\text{Ph}$	(18)	CH_2Cl_2 , toluene, DMF	0.9	[15]
102	SPhCOOH	(44)	water, DMF	1.5	[123]
144	$\text{SCH}_2\text{CH}_2\text{Ph}$	(60)	CH_2Cl_2 , toluene, DMF	1.7	[122, 124]
1400	$\text{SCH}_2\text{CH}_2\text{Ph}$		CH_2Cl_2 , toluene, DMF	3.5	[125, 126]

2.4. Electron dynamics in thiol-stabilized Au clusters

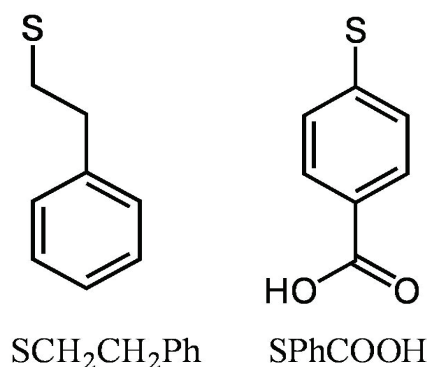


Figure 2.31: Ligands used for stabilizing the gold clusters. The sulfur atoms are bound to the gold ones.

The complete cluster structure could be resolved for Au_{25} [127, 128] and Au_{102} [129, 130] by X-ray crystallography, the one for Au_{144} [131] was deduced from theoretical computations, recently confirmed by STEM-measurements [132]. The smallest cluster, Au_{25} , is constituted by an icosahedral Au_{13} core capped by an exterior shell composed of the remaining twelve Au atoms, the whole cluster being encapsulated by the eighteen thiolate ligands (see Fig. 2.32(a)). Similar structures are observed for Au_{102} and Au_{144} , where a core of gold atoms is surrounded by a quasi-shell of gold atoms bound to the sulfur atoms of the ligands, leading to “monolayer protected clusters (MPCs)” [133].

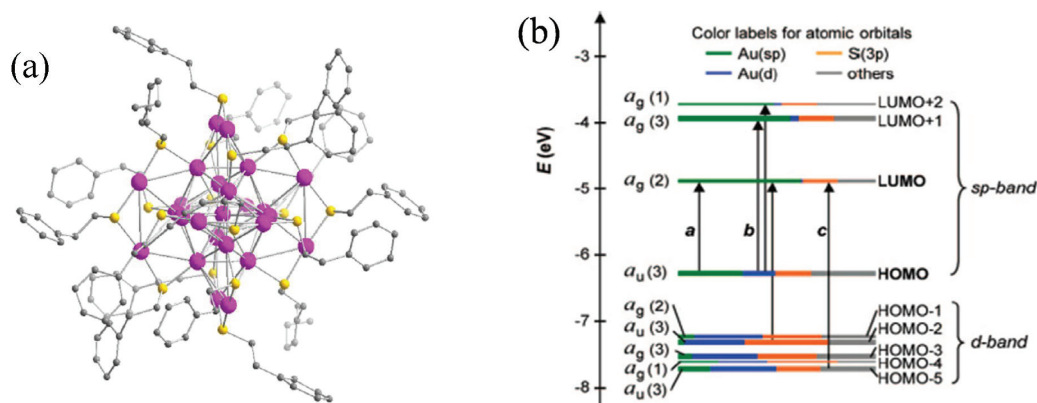


Figure 2.32: Geometric structure (a) of Au_{25} , formed by an Au_{13} icosahedral gold core encapsulated by 6 $\text{Au}_2(\text{SCH}_2\text{CH}_2\text{Ph})_3$ semirings [127, 128]. Electronic energy structure calculated by Zhu et al. [127] (b), showing HOMO-LUMO separation.

The structure of metal clusters and their electronic and optical properties are directly related [117–119]. In general the electronic energy states of small clusters reflect a hybridization between the gold and ligand electronic levels [117]. For Au_{25} , discrete electronic energy levels could be computed [127] yielding a quite large gap (1.3 eV) between the highest occupied and lowest unoccupied molecular states (HOMO and LUMO, respectively,

Fig. 2.32(b)). A HOMO-LUMO separation is still predicted for Au_{102} with a smaller value of around 0.5 eV and smearing out of the energy levels [134, 135], and becomes smaller in the case of Au_{144} [131].

The measured absorption spectra of the different samples is shown in Figs. 2.33(a) and (b). The largest sample presents a surface plasmon resonance at around 520 nm, in agreement with Mie calculations for nanospheres in an aqueous solution (red line). This resonance is

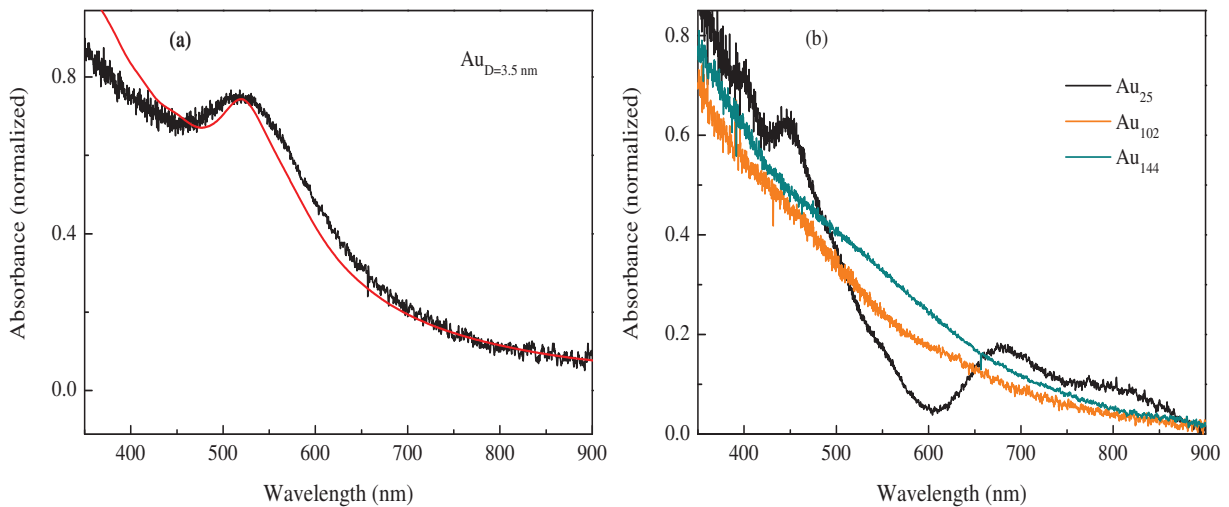


Figure 2.33: Experimental (black line) and simulated (red line) absorption spectra of the $D = 3.5$ nm sample in DMF. Simulation were obtained by Mie theory and considering quantum confinement and inhomogeneous broadening by the factor $g = 1.5$ (Eq. (1.26)). (b) Experimental spectra of small Au clusters in DMF.

smearred out in Au_{144} and Au_{102} due to size reduction as a consequence of electron-surface broadening (see Sec. 1.1.3) and quantum confinement effects. In Au_{25} three distinct features are observed, at 680 nm, 450 nm and 400 nm and can be explained by electronic transitions between the calculated electron energy levels [127]. In particular, the peak at 680 nm in the linear absorption spectrum is attributed to the HOMO-LUMO transition (Fig. 2.32(b), see transition a), dominated by the quantized sp states of the gold atoms. The small shoulder at around 800 nm has previously been attributed to a negatively charged sample [136]. However, as we observed a similar shoulder in our neutral samples, increasing with solution aging, it could also be associated to impurities in the solution. Moreover, after several days, the spectra of the clusters in solution lose their characteristic features, especially Au_{25} , probably due to aggregation or their separation into atoms. The absorption spectra were thus carefully monitored during experiments to guarantee the sample stability.

In order to check the quality of the synthesis, the smallest clusters were characterized by

2.4. Electron dynamics in thiol-stabilized Au clusters

electrospray ionization mass spectrometric analyses (ESI-MS), X-ray crystallography and thermal gravimetric analysis (TGA). For the bigger Au₁₄₄ sample Matrix-Assisted Laser Desorption/Ionization (MALDI) TOF measurements were performed instead of ESI-MS. The size of the largest $D = 3.5$ nm particles was measured by TEM, this sample being polydisperse conversely to smaller clusters (Fig. 2.34).

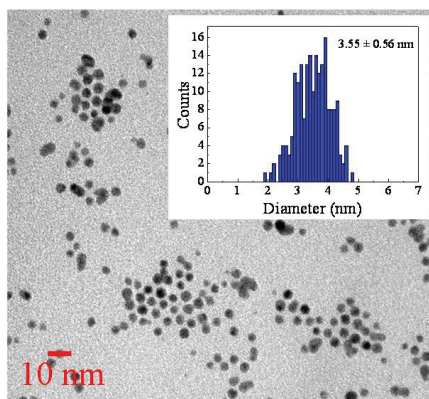


Figure 2.34: TEM image of $D = 3.5$ nm sample and its size distribution.

2.4.2 Experiments

Time-resolved, low excitation experiments have been performed using setup 1 (Sec. 2.1.1) both in the configuration P/Pr IR/Blue and P/Pr Blue/IR by frequency doubling the IR beam (see Sec. 2.2), and with a visible probe light using the optical parametric oscillator (OPO). The OPO emitting light in the visible range 480-700 nm, it was thus possible to probe the samples close to the bulk gold interband transition threshold, centered around 520 nm. In configurations including the OPO, the temporal resolution of the experiment, namely the pump-probe cross-correlation FWHM, was determined to be ~ 350 fs, processes considerably faster than this resolution could thus not be precisely characterized. All measurements were performed on solutions in 1 mm-thick quartz cuvettes, and low particle concentration. The samples were kept in powder form, under refrigeration and were dissolved in Dimethylformamide (DMF) before each experimental series. Measurements in a strong perturbation regime with a white light probe (setup 2, Sec. 2.1.2) were performed to confirm the experimental results.

2.4.2.a Transient absorption spectra

The transient absorption spectra $-\Delta T/T$ for low excitations (pump fluence $F \approx 100 \mu\text{J}/\text{cm}^2$) at a pump wavelength of 820 nm and a time delay of 1 ps for Au₂₅, Au₁₀₂, Au₁₄₄ and for the largest sample ($D = 3.5$ nm) are shown in Fig. 2.35. They have been obtained by

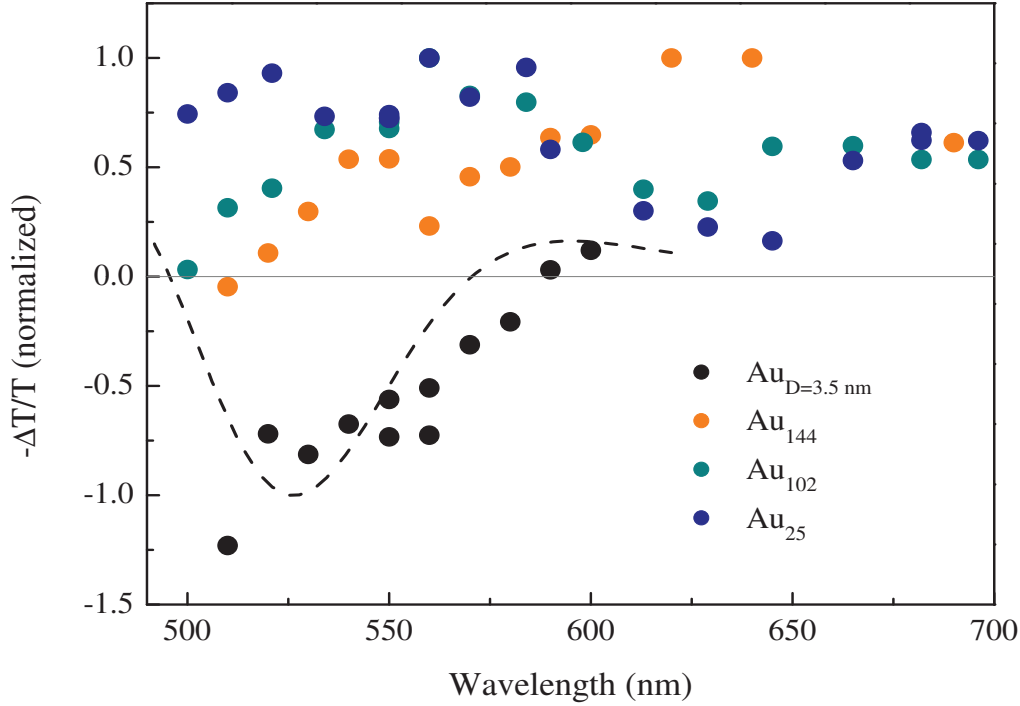


Figure 2.35: Experimental transient absorption spectra at a time delay of $t = 1$ ps for the samples $\text{Au}_{D=3.5 \text{ nm}}$, Au_{144} , Au_{102} and Au_{25} . The theoretical transient spectra for $\text{Au}_{D=3.5 \text{ nm}}$ (black dashed line) has been computed using the derivatives $a_{1,2}$ from the linear spectrum shown in Fig. 2.33(a), and the computed $\Delta\epsilon_{1,2}^{ib}$ for bulk Au (see Secs. 1.3.2, 1.4 and 1.5).

repeating the time-resolved acquisition for different probe wavelengths and comparing the signals using the same normalization procedure as presented in Sec. 2.3.1. The transient absorption of the largest sample (black dots) is characterized by a minimum (bleaching) around the SPR (~ 520 nm) and a zero crossing at larger wavelengths. It is well described by the model presented in Chapter 1 (Sec. 1.5) and in the previous chapter (Sec. 2.3, dashed line in Fig. 2.35). One can thus conclude that in this size range no significant modification of the transient absorption spectrum due to quantum confinement or the stabilizing ligands at the surfaces occur. This is in agreement with the samples linear absorption spectrum (see Fig. 2.33(a)) and measurements on silver particles of similar sizes embedded in glass [5]. Conversely, the shapes of the transient absorption spectra of the smaller clusters are modified, none of the samples displaying the strong bleaching around 520 nm. For the investigated wavelength range, the clusters transient absorption $-\Delta T/T$ basically becomes positive with size reduction, with the appearance of some structures around 550 nm and 630 nm.

Measuring the transient spectra with a monochromatic probe pulse (setup 1, Sec. 2.1.1)

is quite cumbersome and induces systematic errors due to the necessary normalization of each pump-probe signal (see Sec. 2.3.1). However, the systems being excited with weak pump fluences, non-linear absorption processes like multi-photon absorption are limited and interpretation of the observed time-dependent measurements is more accessible. In Fig. 2.36 the transient absorption spectra ($t = 1$ ps) obtained with setup 1 (Sec. 2.1.1) with infrared pump pulses and with setup 2 (Sec. 2.1.2) with visible pump pulses are compared. Probing with white light allowed to record smooth spectra between 530 nm and 730 nm, with stronger excitations ($F \approx 200$ mJ/cm²) resulting in larger signals and short acquisition times. The spectral features for weak and strong excitations are comparable for all samples. The signals signs and the positions of local minima and maxima agree well in the case of Au_{D=3.5nm}, Au₁₄₄ and Au₁₀₂ (Fig. 2.36(a)-(c)). The minima of the transient spectra of Au₂₅ are slightly shifted and a transient bleaching is found for the measurements by setup 2 close to 650 nm, which can be explained by a larger excitation as compared to the non-amplified setup.

The radical change of the shapes of the transient absorption spectra with size reduction are a consequence of the modification of electronic energy states, which also affects the linear spectra, as shown before (Fig. 2.33(b)). In particular, the transient absorption of Au₂₅ can be compared to its ground state absorption (linear spectrum), as shown in Fig. 2.37(a). The linear absorption presents a peak at 680 nm and a small shoulder at 550 nm. Close to these wavelengths, spectral features also show up in the transient absorption, presenting a clear minimum at 630 nm and a weaker one around 530 nm, the linear and transient spectral features being correlated.

The transient absorption spectrum of Au₂₅ has been studied before and similar results have been obtained [93, 94, 97]. The spectral features have been attributed to two effects:

- Excited states absorption (ESA): depopulation of the HOMO by the pump pulse resulting in additional transitions from lower electronic states (HOMO- n), and population of the LUMO leading to LUMO \rightarrow LUMO+ n transitions. ESA gives a positive contribution to the transient absorption spectrum.
- Ground state bleaching (GSB): decreasing probability of transitions from the HOMO state due to its depopulation by the pump pulse, yielding a negative sign in $-\Delta T/T$.

The measured transient spectrum remains positive over the whole studied range, which demonstrates an important contribution from ESA (see Fig. 2.37(a)). Indeed, low-energy states are very densely distributed (see Fig. 2.37(b)) and a broad ESA can thus be expected. The minimum in the transient absorption spectrum around 630 nm can be associated to GSB, after excitation from the pump beam (Fig. 2.37(b), transition a). We can associate the shoulder in the linear spectrum and the resulting minimum in the transient

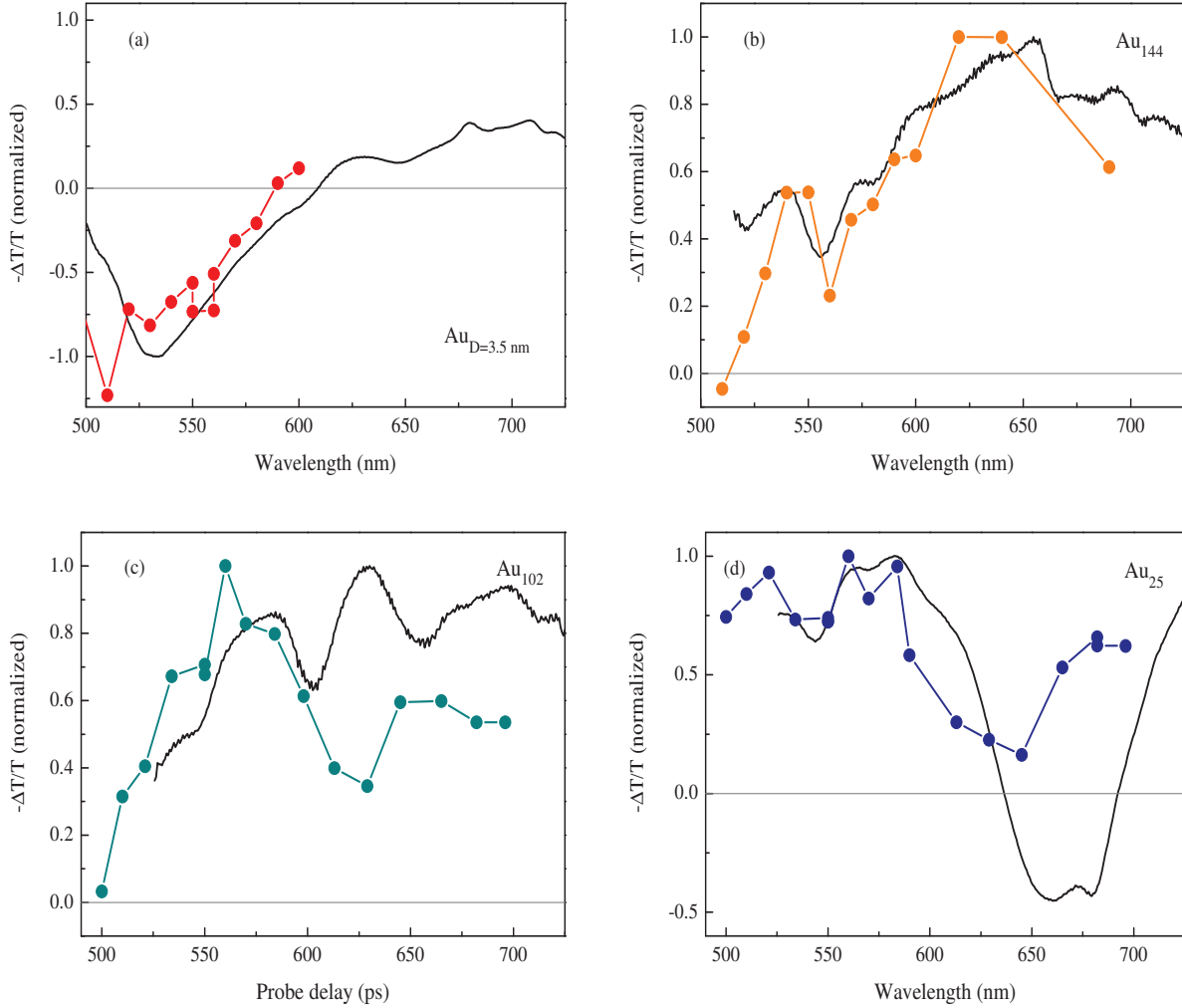


Figure 2.36: Transient absorption spectra using setup 1 (dots, monochromatic probe, IR pump with $F \approx 100 \mu\text{J}/\text{cm}^2$) and setup 2 (full lines, broad white light probe, visible pump with $F \approx 200 \text{ mJ}/\text{cm}^2$).

one to similar effects, even though a resonance for this wavelength is not explicitly predicted in Fig. 2.37(b).

A correlation between linear and transient absorption spectra can also be observed for Au_{102} , where a small shoulder in the linear spectrum appears concomitantly with a bleach of the transient spectrum (Fig. 2.37(c)). This small shoulder has been predicted by Ref. [135] as a consequence of electronic transitions from the ground state, inducing GSB, as in the case of the Au_{25} sample. The complex spectral features for all studied samples and moreover, the transition between the Au_{144} and $\text{Au}_{D=3.5 \text{ nm}}$ optical response, requires however further investigations, both from an experimental and theoretical point of view.

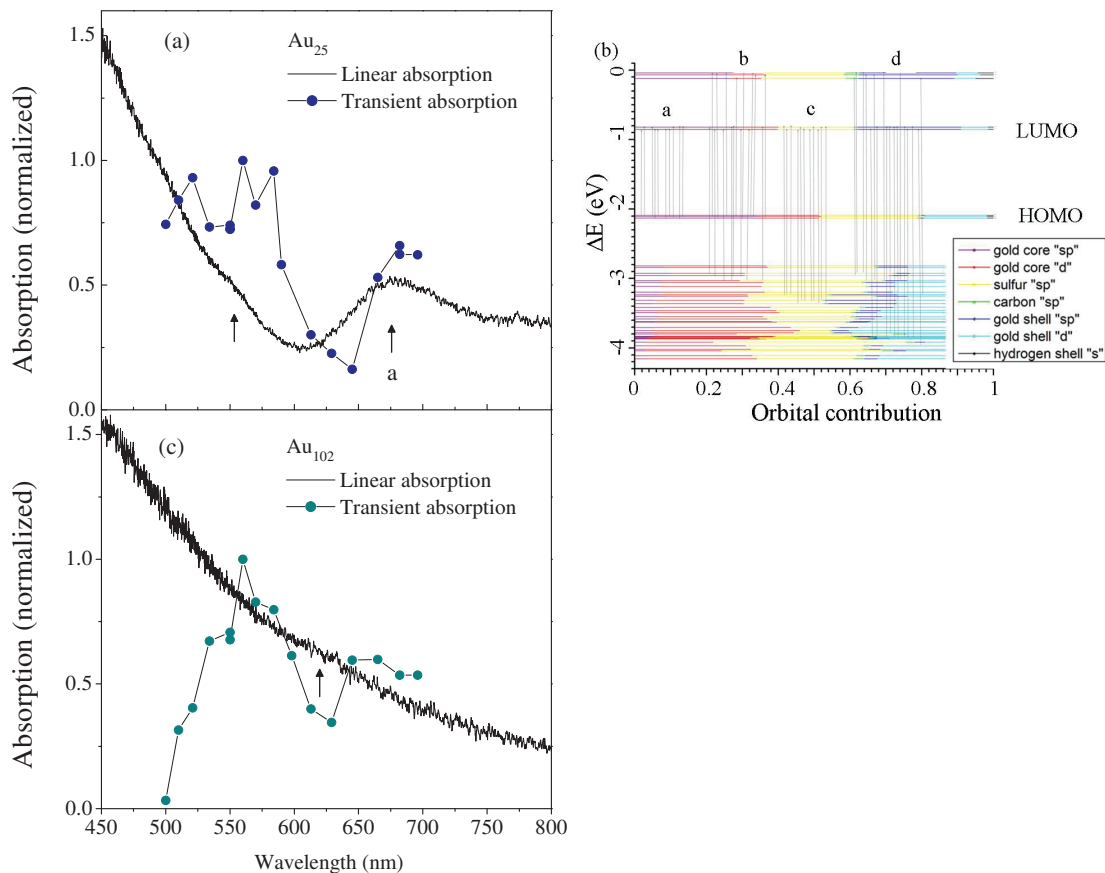


Figure 2.37: Normalized linear and transient absorption spectra of Au₂₅ (a) and its electronic energy structure (b) computed by I. Garzon (UNAM, Institute of Physics, Mexico City). (c) Normalized linear and transient absorption spectra of Au₁₀₂. The transient spectra are the ones obtained with setup 1 (monochromatic probe, IR pump with $F \approx 100 \mu\text{J}/\text{cm}^2$). Arrows indicate characteristics in the linear absorption spectra.

2.4.2.b Relaxation dynamics

The time evolution of the pump-probe signals whose amplitudes are shown at a fixed time delay in Fig. 2.35 were studied in the weak excitation regime as a function of the probe wavelength. Figs. 2.38(a)-(d) illustrate some time-dependent signals of the four samples. After excitation by a pump pulse, the electron dynamics of not too small metal nanoparticles ($> 2 \text{ nm}$) is ruled by electron gas internal thermalization via electron-electron interactions and its subsequent energy loss by coupling to the lattice (see Sec. 2.2) [17, 68, 71]. When probing close to the metal interband transition, the two effects are characterized by a signal rise and an exponential decay which is the case for the Au_{D=3.5nm} sample, shown in Fig. 2.38(a) (green dotted line). By fitting the decaying part of the signal by an exponential function and a constant background, accounting for the electron-phonon

Chapter 2. Size dependence of electronic interactions in metal clusters

coupling and lattice heating (see Secs. 2.2 and 1.4), we obtained $\tau_{1/e} \approx \tau_{e-ph} \approx 0.75$ ps (Fig. 2.38(b)). As expected, this value is lower than the bulk one $\tau_{e-ph} = 1.15$ ps, and in agreement with size reduction effects observed in silver and gold nanoparticles in the same size range [18]. In the low excitation regime, this characteristic time is independent of the pump power and, as for the investigated silver samples (see Sec. 2.2), of the probe wavelength.

Independence of the pump power (for weak excitations) was also observed for the smaller clusters, however the signal decay dynamics of Au₁₄₄, Au₁₀₂ and Au₂₅ illustrate a dependence on the probe wavelength (Figs. 2.38(c) and 2.38(d)). The signals are characterized by the combination of a fast decay and a constant (or slowly decaying) background, their relative contributions depending on the probe wavelength. The background can have contributions resulting from thermal heating of the clusters and from their environment (see Chapter 4), but has also been associated in the case of Au₂₅ and Au₁₄₄ to electronic states localized in the ligand shells, which induce fluorescence in the IR [93, 95, 98]. Moreover, for some probe wavelengths signal oscillations are observable (Fig. 2.38(d)), an effect ascribed to particle vibrations which will be discussed in Chapter 3.

The characteristic times of the faster relaxation are in the ps timescale and vary between 1 ps and 3.5 ps for Au₂₅, 1 ps and 1.5 ps for Au₁₀₂ and 1 ps and 4 ps for Au₁₄₄. Note that all signals in Figs. 2.38(a)-(d) have been obtained with an infrared pump pulse under similar conditions except one signal of the Au₁₄₄ sample which was obtained with a blue pump pulse (Fig. 2.38(c), green dotted line). We therefore attribute the variations in the fast relaxation time to a dependence on the probe wavelength, even though experiments should be done in the future in order to confirm this assumption. For the larger samples, a non-monotonic behavior with size reduction is observed (Fig.2.38(b)), similar to observations in small silver clusters (see Sec. 2.2). A comparison with the Au₂₅ sample is not possible due to its strong probe wavelength-dependent dynamics for visible probe pulses. In analogy with the analysis of the transient absorption spectra we interpret the short delay signal decay as the size and probe wavelength-dependent monitoring of the population and depopulation of different electronic states having different characteristic dynamics.

The measured time constants and probe wavelength dependencies of this decay in Au₂₅ fluctuate between different experiments reported in the literature, probably due to the different excitation conditions [93, 94, 97, 120]. It has most often been associated to one or more internal transitions from LUMO+n states to states close to LUMO [93, 94, 120]. A slightly different explanation for different fast contributions to the pump-probe signal decay was proposed for Au₁₄₄, where a ~ 1 ps timescale was assigned to an electron resonance in the Au core while a slower relaxation ~ 3 ps was characterized by bulk-like interband transitions [98]. To our knowledge electron relaxation has not been studied in

2.4. Electron dynamics in thiol-stabilized Au clusters

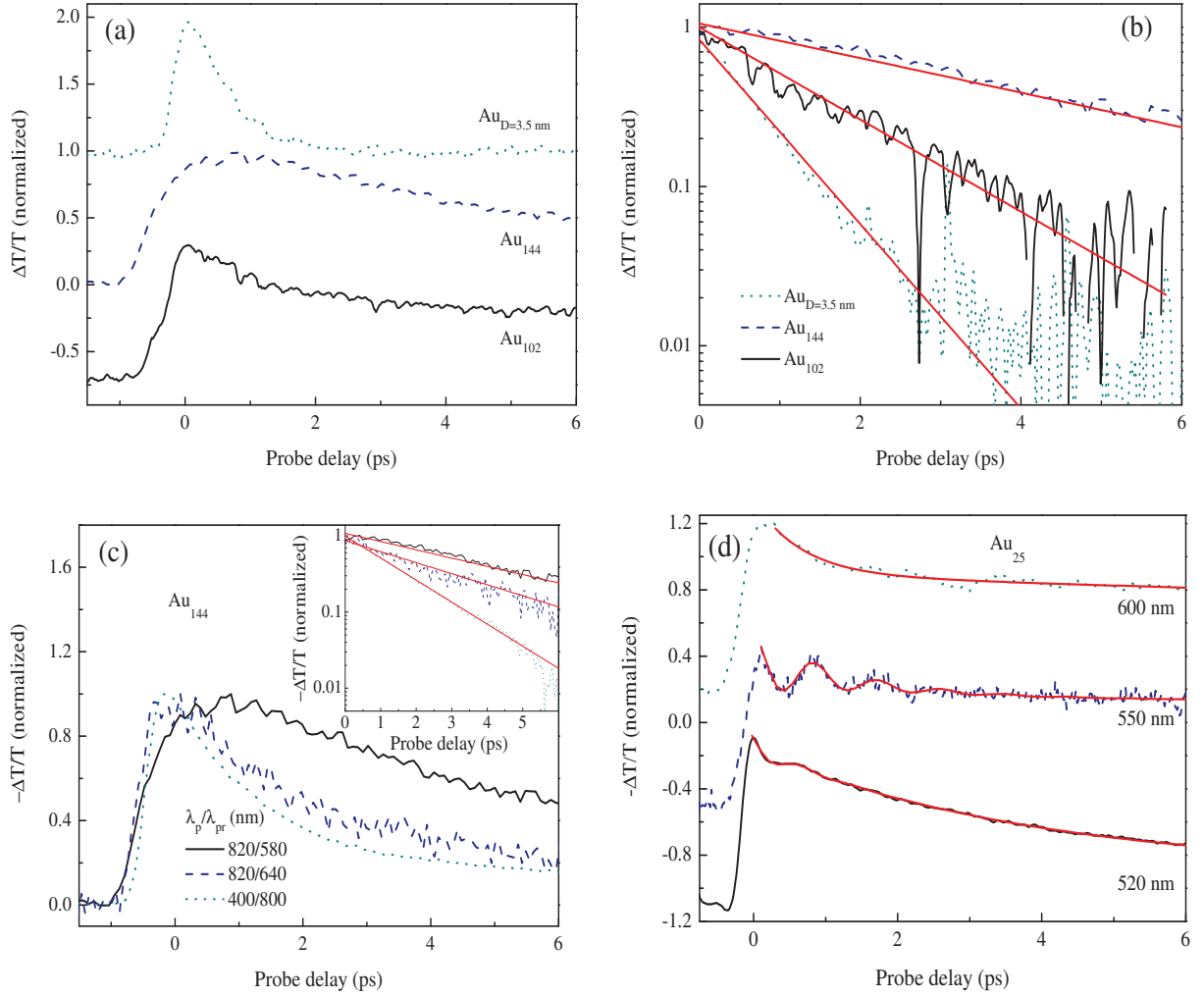


Figure 2.38: Experimental time-resolved normalized transient transmission signals using setup 1 and weak excitations $F \approx 100 \mu\text{J}/\text{cm}^2$. (a) Comparison of the dynamics of the Au_{102} , Au_{144} and $\text{Au}_{D=3.5\text{nm}}$ samples using an infrared pump (820 nm) and a visible probe pulse (~ 550 nm). (b) Same signals after subtraction of a constant background and with a monoexponential fit yielding 0.75 ps, 1.5 ps and 4 ps for the Au_{102} , Au_{144} and $\text{Au}_{D=3.5\text{nm}}$ samples, respectively. The effect of the probe wavelength for Au_{144} and Au_{25} are shown in (c) and (d), respectively (IR pump wavelength except of green dotted line in (c), where a blue pump pulse was used). Inset in (c): Exponential fits (red lines) of the signals after subtraction of a constant background yielding 4 ps, 3 ps and 1.5 ps for $\lambda_{pr} = 580$ nm, 640 nm and 800 nm, respectively. Full red lines in (c) correspond to fits by the combination of a fast and a slow decaying exponential function and a cosine function for the oscillating signals.

Au₁₀₂ before. For a more quantitative description of the complex dynamics observed in these clusters, theoretical modeling should be done in the future. Furthermore systematic experimental investigations of the role of stabilizing ligands, the solvent and the pump wavelength should be performed.

2.4.2.c Signal rise dynamics

As shown in Sec. 2.3, the signal rise can provide insight on the intrinsic thermalization processes of nanoparticles. In Figs. 2.38(a)-(d) one can already observe that the dynamics of the amplitude rise differs for different clusters. For more precise characterization we recorded signals on a shorter timescale in the low excitation IR/visible experimental configuration. At short timescales, the nonlinear response of the pure DMF solvent was also measured and subtracted from the original signal (an example of this procedure is shown in Fig. 2.39, where the initial signal, the DMF signal and their difference can be observed). Fig. 2.40(a) illustrates the signal rise of the four samples at probe wavelengths around

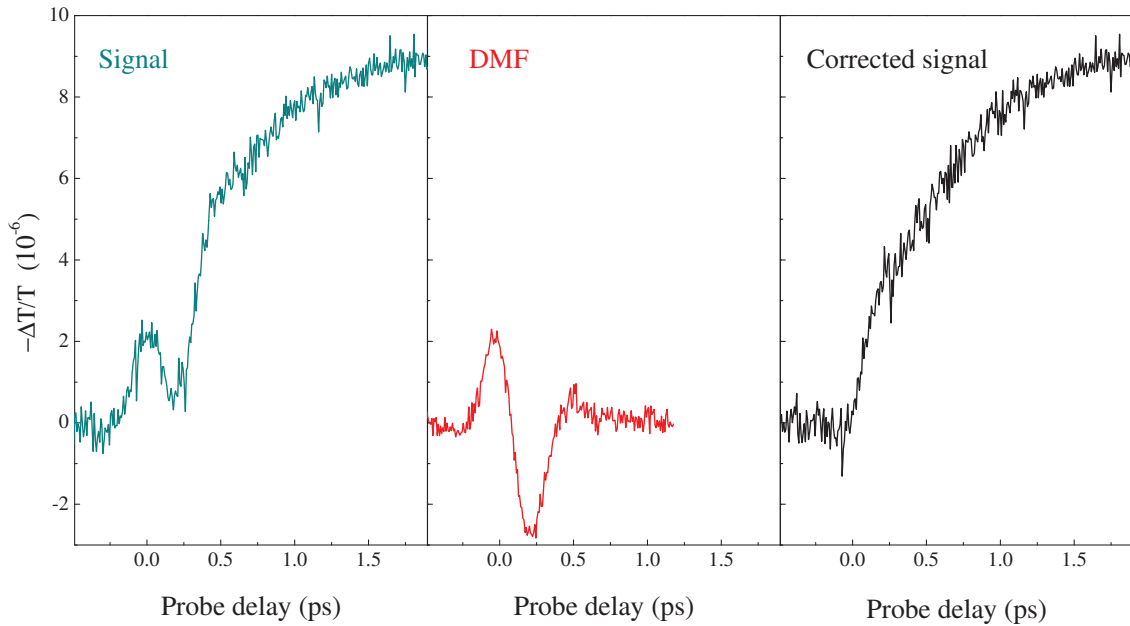


Figure 2.39: Time-resolved signal of Au₁₄₄ in solution, of the solvent (DMF) and their difference. No parameter has been used to adjust the amplitudes.

520 nm for low excitations after solvent subtraction. While the two smallest clusters Au₂₅ and Au₁₀₂ present a very fast rise dynamics, the one of Au₁₄₄ is extremely slow. The fits of the signals by Eq. (2.12), convoluted by the pump-probe cross-correlation of ~ 350 fs for the Au_{D=3.5nm} and Au₁₄₄ samples are shown in Fig. 2.40(b), while the signal rise of

2.4. Electron dynamics in thiol-stabilized Au clusters

the two smallest clusters were too fast to be resolved in the experiment (< 100 fs). For

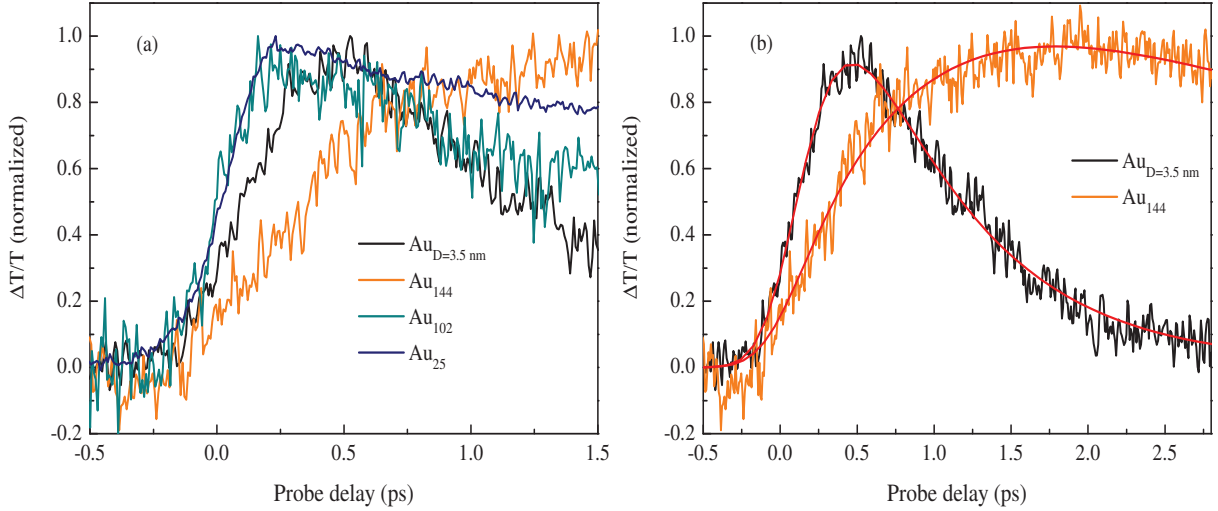


Figure 2.40: Short delay pump-probe signals (P/Pr 820/520 nm) of the samples (a) and the respective fits for the samples $D = 3.5$ nm and Au_{144} (b) using Eq. (2.12), convoluted by a Gaussian function of ~ 350 fs FWHM (red lines). The resulting characteristic rise time was 330 fs and 1.1 ps for $D = 3.5$ nm and Au_{144} , respectively.

the $\text{Au}_{D=3.5 \text{ nm}}$ sample the fit yields $\tau_{th} = 330$ fs. For this size the characteristic time can be associated to the electron thermalization time τ_{th} presented in more detail in Sec. 2.3. As for silver particles in this size range (see Sec. 2.3), this value is slightly smaller than the bulk value (~ 500 fs) [79] and is in very good agreement with former measurements on gold nanoparticles [5, 16]. Conversely, the signal rise of Au_{144} is very slow ~ 1.1 ps, a value that corresponds to about twice the bulk value. The dynamics apparently presents a non-monotonic behavior with size reduction. It first slows down due to the introduction of electron energy quantization, and then decreases with further size reduction, the two remaining samples Au_{102} and Au_{25} being characterized by a signal rise faster than the temporal resolution of the experimental setup. Similar to silver clusters, as a consequence of increasing energy level spacing, the “small solid” picture of a free electron gas is no more adapted, and further quantum modeling would be necessary to precisely interpret the kinetics in these thiolated clusters, taking into account not only the effect of gold atoms, but also the presence of surfactant molecules, the whole system constituting a molecular-like entity.

2.4.3 Summary of observations in Au clusters

A transition from bulk-like to molecular-like electronic properties could be observed for the studied thiol-protected Au clusters. While the transient absorption spectrum of $D = 3.5$ nm Au nanoparticles showed the expected features characterized by the overlap of interband transitions and surface plasmon resonance around a probe wavelength of 520 nm, the transient spectra (between 500 nm and 700 nm) of the smaller thiol-protected, atomically defined gold clusters, changed drastically, starting from the Au₁₄₄ sample. In the case of Au₁₀₂ and Au₂₅, these specific characteristics can be correlated to the linear absorption spectrum and its modeling, suggesting a monitoring of different discrete electronic energy states. All transient absorption spectra were studied for weak and strong excitation regimes (setup 1 and 2) with infrared and visible pump pulses, respectively, and a qualitative agreement within the spectral features was obtained. Agreement was also found with former measurements on Au₂₅ [93–95, 97] and Au₁₄₄ [98] where the pump fluence was comparable to setup 2 in either the IR or the visible spectral range.

The observed decay dynamics of the largest ($D = 3.5$ nm) nanoparticles could be ascribed to electron-phonon coupling with a time constant consistent with former measurements, independent of pump and probe wavelengths. The observations for the smaller clusters were more complex, showing for probe wavelengths between 500 nm and 700 nm a probe-dependent characteristic time in the ps range.

The rise time of the low excitation signals was also investigated. As expected, the rise time of the Au_{D=3.5nm} sample can be described by free electron gas thermalization dynamics, with an accelerated characteristic time compared to bulk due to reduced electron screening at the surfaces (see Sec. 2.3). The signal rise of Au₁₄₄ was slower than bulk, possibly as a first evidence of electron energy discretization, an effect that has also been observed in silver for particles of similar sizes (Sec. 2.3). The bulk model breaks down for Au₁₀₂ and Au₂₅ where the rise time was found to be much faster (faster than the pump-probe time resolution), which we interpret as a signature of a molecular-like behavior, as in the case of discrete electronic transitions excitation is instantaneous.

From these experiments, a transition from a “small solid” to a molecular-like behavior can already be defined for Au₁₄₄, in agreement with the conclusions of Refs. [98, 137]. This is characterized by the disappearance of the typical Au SPR signature in the linear and transient absorption spectra. Molecular-like effects are observable in the wavelength-dependent pump-probe decay dynamics and modifications to the finite signal rise time can be interpreted as the appearance of electron energy discretization effects. In the future, sizes between Au₁₄₄ (~ 1.7 nm) and 3.5 nm should be studied in detail in order to define more precisely the onset of molecular-like behavior in thiol-protected gold clusters.

2.5 Conclusion

In this chapter we reported studies on the transition from a bulk-like to a molecular-like behavior in small Ag and Au nanoparticles by investigations of their electron dynamics in combination with their transient absorption spectra by time-resolved spectroscopy. In this context, the effect of size reduction on the electronic properties of surfactant-free, silica embedded Ag nanoparticles and thiol-protected Au clusters immersed in DMF has been investigated. For both systems, samples in the intermediate size range ($D > 3$ nm) evidenced no significant modification of their electron dynamics or their transient absorption spectra due to electronic level quantization. First signatures of this effect could be observed in Ag clusters of diameters between 2.3 and 1.1 nm. Similar signatures were observed in the thiol-protected Au₁₄₄ clusters. In the case of the even smaller clusters, Au₁₀₂ and Au₂₅, clear evidence of a molecular-like behavior was shown.

The effect of size reduction was more striking in Au samples than in Ag. This could be an effect of the different nature of their synthesis (chemical vs. physical), yielding in the first case to strong surface effects induced by the presence of ligand molecules. It could also result from the different electronic properties of the two metals, e.g. the interplay between interband transitions and the SPR (the two being overlapped in Au nanospheres while in Ag nanospheres the interband transitions are far from the SPR, corresponding more to a “free” electron collective excitation in this case), or from the different vibrational properties [108].

In the future, electronic interactions (i.e. electron-lattice coupling and electron-electron interactions) should be investigated theoretically in order to quantitatively interpret the experimental observations. From an experimental point of view, extensions of ultrafast relaxation measurements to samples of gold clusters prepared by the magnetron cluster source, or to thiol-protected silver clusters [138], would allow to discriminate the role of the metal and the particles surface conditions.

Chapter 3

Acoustic response of bimetallic nanoparticles and metal clusters

The vibrational properties of nanometric size objects have raised a large technological and fundamental interest during the last decade. They have been motivated by the creation of high frequency electrically or optically driven oscillators scaling down the object size [139, 140], fundamental analysis of acoustic energy transfer at the nanoscale [3, 4, 61, 84, 141–145] and investigation of the vibrational response of objects of a few tens of atoms as compared to the bulk material one [61, 84, 108, 146–150]. In the case of metal nanoparticles, studies performed either in the spectral or temporal domains mostly focused on nanoobjects formed by a single material, with various shapes and sizes down to about one nanometer [3, 84]. The experimentally observed vibrational mode frequencies were found to be in excellent agreement with a macroscopic acoustic model, i.e. describing nanoobject vibrations with continuum mechanics and using the elastic constants of the bulk material forming the object [61, 148, 151].

The impact of size reduction on the acoustic modes of nanomaterials can yield important information about geometry, electronic and phononic structure and interactions with the environment. A theoretical approach for calculating vibrational modes in the small size range is the use of atomistic calculations, describing interatomic interactions by many-body model potentials. The resulting vibrational modes of small gold nanospheres (> 1 nm) were found to be in excellent agreement with continuum mechanics predictions and experiments [108]. From the experimental point of view, only few investigations on small clusters have been done in the past. Time-resolved experiments on small thiol-protected gold clusters lead to contradictory results [93, 94, 152, 153], possibly due to very different excitation and probing conditions.

In this chapter we present investigations on the impact of morphology and size on the acoustic vibrations of metal nanoparticles. Bimetallic alloyed and segregated (i.e. with

separation of the two metals) core-shell nanoobjects were chosen to study the impact of combining two metals in the small size range. The transition from bulk-like systems to molecule-like ones was investigated via the study of the vibrational modes of thiol-stabilized gold clusters over a broad size range.

Sec. 3.1 describes the basics of the computation of vibrational modes of spherical particles by classical continuum mechanics. The study of breathing mode vibrations in bimetallic nanoobjects is presented in Sec. 3.2, while the last part of this chapter (Sec. 3.3) focuses on the time-resolved investigation of the acoustic response of surfactant-stabilized gold clusters.

3.1 Macroscopic elastic model

The periods of mechanical oscillations can be predicted by elasticity theory from bulk objects down to nanoobjects of few hundred atoms. In this picture metals are described as homogeneous continuous media, their discrete atomic structure being neglected. The principles describing deformation of continuous objects are ruled by the laws of classical physics, namely Hooke's and Newton's laws, which lead to Navier's equation [154, 155]:

$$\rho \frac{d^2 \vec{u}}{dt^2} = (\lambda + 2\mu) \vec{\nabla}(\nabla \cdot \vec{u}) - \mu \vec{\nabla} \times (\vec{\nabla} \times \vec{u}), \quad (3.1)$$

relating the temporal and spatial variations of the displacement vector \vec{u} to the Lamé constants λ and μ and the density ρ of the homogeneous isotropic material. The vibrational eigenmodes of Eq. (3.1) correspond to harmonic solutions $\vec{u}(\vec{r}, t) = \vec{u}(\vec{r}) \exp(i\tilde{\omega}t)$, $\tilde{\omega}$ being a complex frequency in the most general case. In the case of a sphere, this solution is given in terms of spherical Bessel functions, with angular momentum number l , azimuthal number m ($-l \leq m \leq l$) and radial number n . The resulting vibrational modes frequencies $\tilde{\omega}_{n,l}$ do not depend on m , their angular dependence being given by l . An important subset is formed by radial modes, corresponding to $l = m = 0$, for which the displacement takes place only in the radial direction. In optical pump-probe experiments the excitation of nanospheres is isotropic with no preferred directions and only radial modes are launched [3, 156]. Definition of the boundary contributions is necessary to solve Navier's equation (Eq. (3.1)). This was first done for free spheres (no radial stress at the interface), yielding [154]:

$$\tan(x_R) = \frac{4x_R}{4 - x_R^2/\zeta^2}, \quad (3.2)$$

where x_R is the normalized frequency $x_R = \omega_{n,0}R/v_l$, $\zeta = v_l/v_{tr}$ and $v_{l,tr}$ the longitudinal and transverse speed of sound in the nanosphere. Here, the frequency is real (no damping),

as energy cannot be evacuated to the outside. Introduction of a matrix by imposing continuity of displacement and of the radial stress component at the particle interface [157] has a weak impact on radial vibrational periods, which can still be approximated with:

$$T_n \approx \frac{D}{(n+1)v_l}, \quad (3.3)$$

illustrating a scaling law of periods with the particle diameter D . Note that this dependency has been proved to be valid for metal particles down to a diameter of 1 nm, corresponding to less than 100 atoms [148]. The damping time due to mechanical energy transfer to the environment for matrix-embedded particles follows the same scaling law with diameter and is almost independent of the mode number n . It is mainly determined by the acoustic impedance mismatch of the two materials Z_p/Z_m , with $Z_{p,m}$ the acoustic impedances of particle and matrix, given by $\rho_{p,m}v_l^{p,m}$. An additional contribution to the damping may come from internal processes (e.g. defect scattering, energy coupling between different phonon modes, ...) [3] and is more difficult to model. The computation of vibrational eigenmodes can be analytically generalized to spherical composite nanoobjects, composed by a metal core and an arbitrary number of metal or dielectric concentric layers. Here, a matrix formalism is used for solving Eq. (3.1) [4, 158, 159].

Nanoparticle vibrations can be impulsively launched by an ultrafast laser pulse via two possible mechanisms, namely hot electron pressure and thermoelasticity [3, 141]. The former leads to the direct excitation of vibrations by the excited electrons while in the latter the oscillating modes are indirectly excited. Here, the lattice heating induced by electron-phonon energy transfer (~ 1 ps) leads to a fast increase of the equilibrium particle size (lattice dilation), launching volume oscillations around its new equilibrium diameter. For a spherical particle, the fundamental breathing mode ($l = n = 0$) is the one which is excited with the largest amplitude as its displacement field best matches the dilation field induced by heating [159].

Acoustic vibrations induce modifications of the nanoparticle dielectric constant $\epsilon_{1,2}$ (see Sec. 1.4) via the periodic modulation of its volume. In this context, the fundamental breathing mode is again favorably detected, its displacement field yielding the strongest volume change. Yet, experimentally both the fundamental ($n = 0$) and the first harmonic ($n = 1$) radial modes have been observed by time-resolved spectroscopy, either directly [160] or with an appropriate experimental setup enhancing the detection of the first harmonic mode [161] by coherent suppression of the fundamental one.

3.2 Ultrafast acoustic response of bimetallic nanoparticles

Nanoobjects composed of two or more materials have rarely been investigated in the past, though information on the size reduction effects on the acoustic properties and on the spatial distribution and mechanical interaction of the forming materials can be obtained by studying their acoustic response. In this context, results obtained in heterogeneous metal based nanospheres, i.e. metal/insulator [159, 162] or insulator/metal [163, 164] core/shell nanoparticles show a large impact of the non-metallic component on the measured time domain vibrational responses, and yield information about the material coupling in the particles.

In the case of bimetallic particles, few alloyed and segregated core-shell systems were investigated [165–169]. In the former case, acoustic vibrations of Au-Ag alloyed particles were studied by Raman spectroscopy in 2 nm clusters [170] and 25 nm nanospheres [171], and by time-resolved spectroscopy for larger sizes, from 40 to 90 nm nanoboxes and nanocages [172]. As for monometallic particles, the results were interpreted using the continuum mechanics model presented in Sec. 3.1 combined with linearly averaged Au and Ag densities and sound velocities [170, 171] or fundamental elastic constants (e.g. C_{11} , C_{12} and C_{44}) [172]. Experimental results and continuum mechanics calculations were in agreement with atomistic modeling for Au-Ag alloyed 0.5 to 4 nm nanospheres [173, 174]. In the case of particles formed by two segregated materials, spatial distribution and mechanical interaction of the constituents is expected to translate into their vibrational response. For bimetallic systems, both metal parts are excited and vibration of the full particle has been detected using time-resolved pump-probe experiments in chemically synthesized Au/Pb spheres, Au/Pd rods and Au/Ag bipyramids [165, 166, 169, 175]. The results show excellent mechanical coupling of the metallic components and constitute a signature of the metal distribution [169]. In contrast, Raman study of matrix-embedded Ni/Ag core/shell nanospheres fabricated by deposition of laser sputtered clusters (low energy cluster beam deposition, see Sec. 2.2.1) indicates vibration of only the Ag shell [167]. This was ascribed to weak component coupling and to a larger Raman response of the Ag part due to SPR enhanced coupling. These results suggest significant influence of both the particle fabrication technique, leading to different contacts between the material components, and of the optical investigation method, involving different optical interactions with the metal components.

To further analyze the acoustic properties of multi-metallic nanosystems, we investigated in this section the vibrational response of alloyed or segregated Au-Ag nanospheres synthesized by either chemical or physical means using a time-resolved pump-probe technique (see Sec. 2.1.1). Effects of segregation and alloying were investigated in colloidal solutions

3.2. Ultrafast acoustic response of bimetallic nanoparticles

with sizes in the 20-45 nm range and different compositions, the results being interpreted in terms of the macroscopic acoustic model which is fully applicable in this size range. The possible modification of the acoustic response with size reduction was investigated in the case of small size (2-3 nm) core/shell Pt/Au and Ni/Ag nanospheres fabricated by LECBD (see Sec. 2.2.1). In this size range, depending on the composition, the shell is either incomplete or formed by a monoatomic layer, offering the unique possibility of experimentally investigating the acoustic properties of such small systems.

3.2.1 Samples

Measurements were performed in different alloyed and segregated bimetallic nanospheres whose compositions, morphology, diameters, size dispersions and embedding environment are summarized in Table 3.1.

Table 3.1: Characteristics of different samples: Nanoparticle composition (atomic fraction), surrounding matrix, internal morphology, external diameter D_0 . Uncertainties correspond to available standard deviations of the size distribution. For core/shell nanoparticles, the element in the core is Au (samples d and e), Pt (samples f to h) and Ni (sample i).

name	composition	matrix	morphology	D_0 (nm)
a	Au _{0.25} Ag _{0.75}	water	alloy	44.5 ± 3.0
b	Au _{0.50} Ag _{0.50}	water	alloy	36.0 ± 10.0
c	Au _{0.75} Ag _{0.25}	water	alloy	33.0 ± 3.0
d	Au _{0.36} Ag _{0.64}	water	core/shell	21.0
e	Au _{0.10} Ag _{0.90}	water	core/shell	33.0
f	Pt _{0.20} Au _{0.80}	silica	core/shell	2.5 ± 0.1
g	Pt _{0.50} Au _{0.50}	silica	core/shell	2.5 ± 0.1
h	Pt _{0.80} Au _{0.20}	silica	core/shell	2.3 ± 0.1
i	Ni _{0.50} Ag _{0.50}	silica	core/shell	2.75 ± 0.1

Au-Ag nanospheres in water were synthesized both in an alloy configuration (samples a to c) and in a core/shell geometry (d and e) by the chemistry group of L.M. Liz-Marzán (University of Vigo, Spain). In the case of Au-Ag nanoalloys (Au_{0.25}Ag_{0.75}, Au_{0.50}Ag_{0.50} and Au_{0.75}Ag_{0.25}, samples a to c respectively), synthesis was obtained by the methods described by Link et al. [176] and Rodríguez-González et al. [177]. Absorption spectra of Au-Ag alloy nanospheres (diameters ranging from 33 to 45 nm) with the three different compositions are shown in Fig. 3.1(a). As expected, their surface plasmon resonance [1] shifts to longer wavelengths with increasing gold fraction [176, 178–182], its central position varying linearly with composition. Au/Ag core/shell samples (samples d and e) with a gold core diameter of 15 nm and two different silver shell thicknesses (3 and 9 nm, corre-

Chapter 3. Acoustic response of bimetallic nanoparticles and metal clusters

sponding to $\text{Au}_{0.36}\text{Ag}_{0.64}$ and $\text{Au}_{0.10}\text{Ag}_{0.90}$ respectively, see Fig. 3.1(c)) were also obtained by chemical synthesis. The values of shell thickness and particle diameters were measured by High Resolution Transmission Electron Microscopy. Sample d (Fig. 3.1(d)), which contains a smaller amount of silver, shows a SPR similar to the one of gold [183, 184], while the absorption spectrum of sample e, having a thick silver shell and a very small amount of gold in the core, is similar to the spectrum of a silver monometallic sphere, characterized by a SPR around 400 nm [42] (Fig. 3.1(c)).

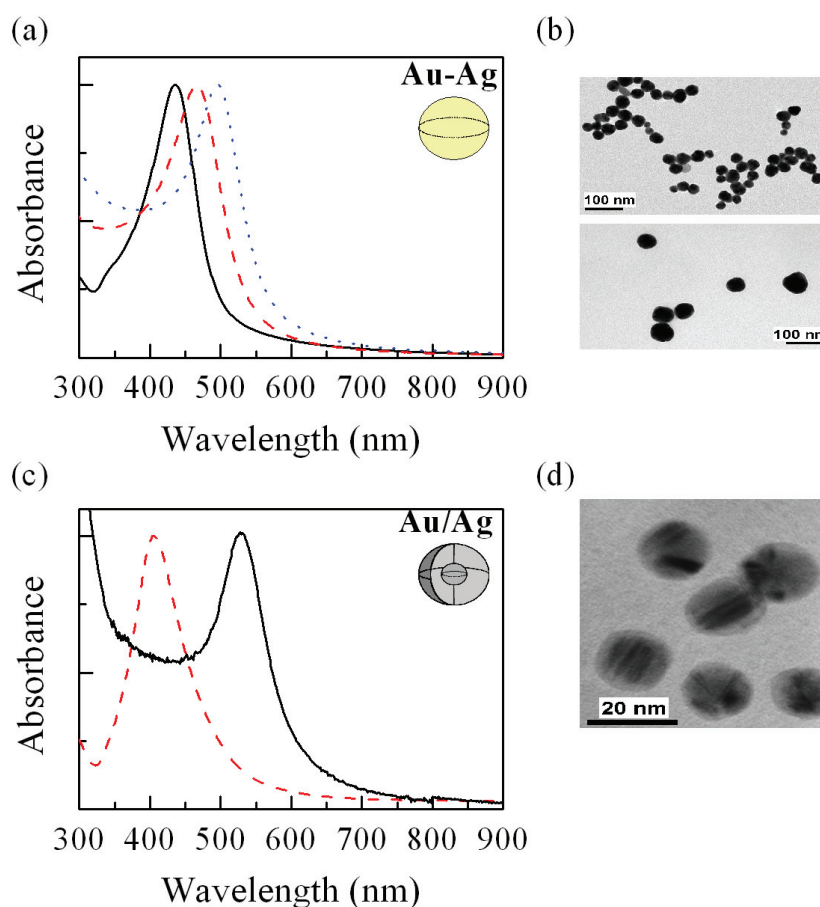


Figure 3.1: (a) Normalized absorption spectra of water-dispersed Au-Ag nanoalloys (full, dashed and dotted lines for samples a, b, and c, respectively) and (b) transmission electron microscope (TEM) images of $\text{Au}_{0.75}\text{Ag}_{0.25}$ (sample c, top) and $\text{Au}_{0.50}\text{Ag}_{0.50}$ (sample b, bottom). (c) Absorption spectra of Au/Ag core/shell samples (full and dashed line for sample d and e, respectively) and (d) TEM image of $\text{Au}_{0.36}\text{Ag}_{0.64}$ (sample d).

Four samples of spherical nanoparticles ($\text{Pt}_{0.20}\text{Au}_{0.80}$, $\text{Pt}_{0.50}\text{Au}_{0.50}$, $\text{Pt}_{0.80}\text{Au}_{0.20}$ and $\text{Ni}_{0.50}\text{Ag}_{0.50}$, from f to i respectively) with small sizes (external diameter ranging from 2.3 to 2.75 nm) embedded in a silica matrix were synthesized with the LECBD technique (see Sec. 2.2.1) at PLYRA (Plateforme Lyonnaise de Recherche sur les Agrégats by M. Pelarín). Here, electrostatic mass selection guarantees a very narrow size selection, resulting in a $\pm 4\%$ (see Table 3.1) size distribution width [13]. The clusters have a quasi-spherical

3.2. Ultrafast acoustic response of bimetallic nanoparticles

shape and their surfaces are free from contaminant molecules. This aspect is particularly important for small nanoparticles as, for the size considered here (around 2.5 nm), more than 50 % of the atoms lie close to the surfaces [148] and investigated properties can thus be sensitively affected by molecules attached to the external shell. During the synthesis by LECBD, the silica embedded bimetallic clusters have the same average stoichiometric composition as the alloy bulk target. However, between cluster formation and their stabilization on the substrate, their chemical configuration may evolve (atomic interdiffusion). Depending on kinetic and thermodynamic constraints, nanoparticles with different structures can be formed, e.g. more or less ordered alloys, segregated systems like concentric core/shell or side separated (Janus) geometries [185]. In the case of Pt-Au and Ni-Ag mixtures, the high miscibility gap in the respective alloy bulk phases and the larger surface tension of Ni and Pt as compared to Ag and Au are in favor of the formation of Pt/Au and Ni/Ag core/shell structures, with Pt and Ni in the core, respectively [186]. A phase segregation in the Ni-Ag system with the most probable core-shell symmetry has been evidenced in previous optical studies [167, 187, 188]. The Pt-Au system is more debated and its structure proves to be dependent on preparation conditions, composition and environment [189]. For instance, colloidal chemistry has shown the possibility of producing both Pt/Au and Au/Pt core/shell particles ($D > 10$ nm) [190]. However, a Pt/Au core/shell formation is predicted to be favored in the small size range [191], even if the growth of side separated clusters (Janus) cannot be totally ruled out when surface effects are dominating as is the case for the investigated clusters ($D < 5$ nm).

For samples f to i the nanoparticle concentration is too low to detect their absorption spectra. These are however still expected to show a SPR peak, in spite of the small size of the nanoparticles (from 2.3 to 2.75 nm), as observed in denser systems and predicted both on monometallic nanoparticles of similar dimensions [192] and on bimetallic segregated Pt-Au [179, 193] and Ni-Ag systems [187, 194–196].

3.2.2 Experimental methods

The elastic behavior of the different nanosystems was measured using a time-resolved two-colored femtosecond pump-probe setup based on a Ti:Sapphire cavity oscillator. The choice of the probe wavelength is determined by the nanoparticle SPR, optical detections of oscillations being enhanced close to its position [61]. For this purpose, two different configurations of setup 1, described in Sec. 2.1.1, were alternatively employed. The first is based on the output of the Ti:Sapphire laser ($\lambda \approx 800$ nm) and its second harmonic ($\lambda \approx 400$ nm). This setup generates weak excitations (pump pulse energy ~ 10 nJ) and allows to achieve a relative transmission change $\Delta T/T$ signal with a sensitivity in the 10^{-7} range. The second configuration is based on the Ti:Sapphire regenerative amplified

system. In this case [162, 169], the infrared beam is amplified yielding a pulse duration of approximately 120 fs, with a 250 kHz repetition rate and pulse energy of a few μJ . By combining the amplified system with an Optical Parametric Amplifier (OPA), the full visible range from 500 to 700 nm can be generated. In this configuration, part of the amplified beam before the OPA is used as pump, after frequency doubling. This second configuration thus allows a better wavelength tunability in the visible range and time-resolved signals with a bigger contrast, due to stronger excitation, at the price of a higher noise ($\Delta T/T$ noise level around 10^{-5}).

3.2.2.a Time-resolved ultrafast oscillations

A pump-probe signal of the $\text{Au}_{50}\text{Ag}_{50}$ sample (sample b) obtained with the regenerative amplified system (pump wavelength $\lambda_p = 400$ nm and probe wavelength $\lambda_{pr} = 500$ nm) is shown in Fig. 3.2(a) (blue line). The probe relative transmission change $\Delta T/T$ being essentially proportional to the excess energy in the metal quasi-free electron gas (Sec. 1.5) [17, 35, 89], its fast rise and fall reflects heating of the electrons by the pump pulse and their subsequent cooling by electron to lattice energy transfer. The latter results in a thermal dilation of the nanoparticle lattice equilibrium diameter [3, 61], which launches acoustic vibrations, the fundamental breathing mode being as expected preferentially excited and detected for metallic nanoparticles [4, 159]. The resulting modulation of the nanoparticle volume affects the optical response through a periodic variation of the dielectric constant, which is at the origin of the oscillation in the $\Delta T/T$ signal (see Sec. 1.4). Frequency and damping of oscillations in the time-resolved signal thus directly reflect the breathing mode vibrational period and its energy loss. On longer pump-probe delays (on a few tens of ps timescale) a slowly varying background signal reflects cooling of the nanoparticles by heat transfer to the environment [19]. To focus on the acoustic vibrations, the oscillating contribution (black solid line in Fig. 3.2(a)) is first singled-out by subtracting from the decaying part of the raw signal (blue full line) its fit by a two exponential function (red dashed line), which reflects electron cooling and heat transfer to the environment. Period and decaying time can then be obtained by fitting the oscillating part (black full line) with a damped oscillating function. Fourier transforming the oscillating contribution (Fig. 3.2(a), inset) alternatively leads to the same frequency.

Time-resolved pump-probe characterizations were repeated for all samples, measured signals having different amplitudes depending on the excitation pulse energy (oscillator or amplified laser system), concentration of nanoparticles in the sample, and wavelength-dependent laser absorption. Transient signals obtained on sample $\text{Au}_{0.10}\text{Ag}_{0.90}$ (sample e, oscillator with $\lambda_p = 860$ nm and $\lambda_{pr} = 430$ nm) and $\text{Pt}_{0.20}\text{Au}_{0.80}$ (sample f with $\lambda_p = 810$ nm and $\lambda_{pr} = 405$ nm) and extraction of their oscillating parts are shown in Figs. 3.2(b)

3.2. Ultrafast acoustic response of bimetallic nanoparticles

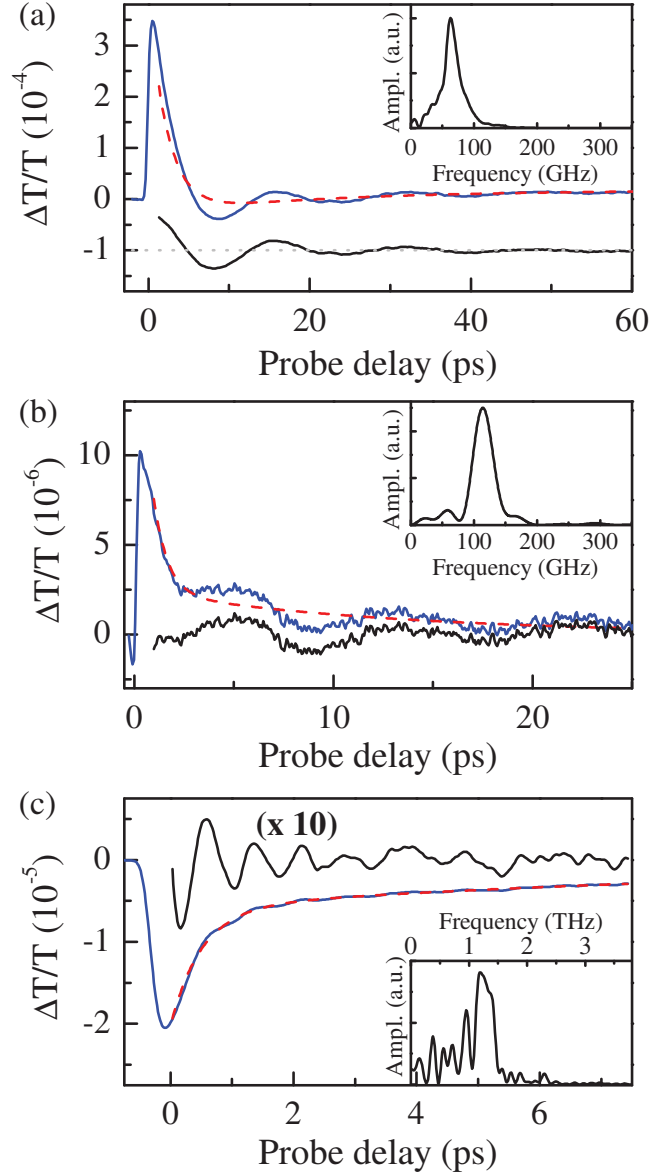


Figure 3.2: (a) Time-resolved pump-probe signal of sample $\text{Au}_{0.50}\text{Ag}_{0.50}$ (sample b), measured at $\lambda_p = 400$ nm, $\lambda_{pr} = 500$ nm and pump fluence $F = 5$ mJ/cm². Blue full line: raw signal. Red dashed line: two-exponential fit of the decay. Black full line: oscillating contribution after subtraction of the exponential decay (downshifted for clarity). Inset: Fourier transform of the oscillating contribution. (b) Same as (a) for sample $\text{Au}_{0.10}\text{Ag}_{0.90}$ (sample e, $\lambda_p = 860$ nm, $\lambda_{pr} = 430$ nm and $F = 30$ $\mu\text{J}/\text{cm}^2$) and (c) $\text{Pt}_{0.20}\text{Au}_{0.80}$ (sample f, $\lambda_p = 810$ nm, $\lambda_{pr} = 405$ nm and $F = 50$ $\mu\text{J}/\text{cm}^2$).

and 3.2(c), respectively.

3.2.2.b Analysis including size dispersion

According to the macroscopic elasticity theory, the breathing mode period is proportional to particle diameters (Eq. (3.2)) [154, 157]. The analysis of the elastic properties of bimetallic systems is thus carried out by comparing the variation of the periods normalized over the particle diameter as a function of composition. In the case of mass-selected silica-embedded samples (samples f to i), having a very small size dispersion ($\pm 4\%$), the normalized period is simply given by the measured period over mean diameter ratio $T_0^{\text{norm}} = T_{\text{exp}}/D_0$.

A more accurate analysis is required in the case of a broader size distribution, as in the case of colloidal Au-Ag samples (samples a to c), which induces both an inhomogeneous damping and a central frequency shift, both these effects being a consequence of the linear dependence of the period on the nanoparticle diameter [3, 61, 108, 148, 157]. For the calculation of the normalized period, size distribution is accounted for by a simple model. As, for a metal nanoparticle with a spherical shape and for the size range considered here, the amplitude of the ultrafast transient response is proportional to its volume $V(D) = \pi D^3/6$, through its linear absorption cross-section [21] (see Eq. (1.45)), its contribution to the oscillating part of the transient absorption signal is given by [61, 143, 151, 197]:

$$s(D, t) = s_0 V(D) e^{-t/\tau_h(D)} \cos\left(\frac{2\pi t}{T(D)} - \phi_0\right), \quad (3.4)$$

where $T(D) = T_0^{\text{norm}} \cdot D$ and $\tau_h(D) = \tau_{h,0}^{\text{norm}} \cdot D$ are the breathing mode period and homogeneous damping time, respectively, s_0 is an amplitude factor and ϕ_0 is the oscillation phase, considered in a first approximation as a fit parameter independent of D [3, 61, 141, 151]. The normalized period T_0^{norm} and homogeneous damping time $\tau_{h,0}^{\text{norm}}$ can be extracted for each sample. By assuming a Gaussian size distribution $P(D)$ with standard deviation ΔD :

$$P(D) = P_0 \exp\left[-\frac{1}{2} \frac{(D - D_0)^2}{\Delta D^2}\right], \quad (3.5)$$

with $\int P(D) dD = 1$, the oscillating part of the transient absorption signal resulting from the sum of all particle sizes in the sample is given by:

$$\frac{\Delta T}{T}(t) = \int_0^\infty P(D) s(D, t) dD. \quad (3.6)$$

For a given size distribution (fixed D_0 and standard deviation ΔD , see Table 3.1 and Fig. 3.3(a) for samples a and b), Eq. (3.6) thus reproduces the experimental transient

3.2. Ultrafast acoustic response of bimetallic nanoparticles

signal with amplitude s_0 , normalized period T_0^{norm} , normalized damping time $\tau_{h,0}^{\text{norm}}$ and phase ϕ_0 as free parameters, determination of T_0^{norm} being the main goal of this analysis. T_0^{norm} values obtained by fitting the $\Delta T/T$ signal with Eq. (3.6) (Fig. 3.3(b), red lines) are plotted in Fig. 3.3(c) (full circles, samples a to c) as a function of nanoparticle composition. Black crosses in Fig. 3.3(c) represent the normalized breathing periods obtained by a direct fit of the oscillating part of the transient signal by a simple sinusoidal function (or by its Fourier transform), dividing its period by the mean diameter D_0 (see Fig. 3.2), without taking size dispersion into account. As expected, direct fitting leads to a negligible discrepancy in the case of a small size dispersion (as for $\text{Au}_{0.25}\text{Ag}_{0.75}$, sample a), the error being more important for broader distributions ($\text{Au}_{0.50}\text{Ag}_{0.50}$, sample b). In the latter case, omitting to take size dispersion into account yields a value for the normalized period considerably larger (Fig. 3.3(c)), since the dominant contribution to the signal comes from vibrations of larger particles (absorption being proportional to nanoparticle volume), an effect that systematically shifts the resulting breathing oscillations to longer periods. Homogeneous damping is introduced in the classical elastic model (Sec. 3.1) as the relaxation of the breathing mode through energy transfer to the surrounding matrix [141, 143, 144, 197–199]. Furthermore, damping can also be provoked by anharmonic interactions with other vibrational modes [200] or interactions with crystalline defects [142, 197]. For ensemble measurements an additional inhomogeneous contribution to damping of the oscillating signal results from the different particle sizes in the sample, each of them having a different oscillating period, their sum inducing a decay of the total acoustic signal. For broader size distributions ($\text{Au}_{0.50}\text{Ag}_{0.50}$, Fig. 3.3(a), sample b, right column), the dominant contribution to the experimental damping time arises from inhomogeneous effects. This prevents extraction of a reliable $\tau_{h,0}^{\text{norm}}$ value by the analysis above, a fit with no homogeneous contribution ($\tau_{h,0}^{\text{norm}} \rightarrow \infty$) correctly reproducing the $\Delta T/T$ signal (Fig. 3.3(b), right column). In the case of a narrower size distribution (Figs. 3.3(a) and 3.3(b), sample a, left column), both inhomogeneous and homogeneous contributions play a role in the observed acoustic damping, even if the former is still dominant. The $\tau_{h,0}^{\text{norm}}$ value deduced by the fit of sample $\text{Au}_{0.25}\text{Ag}_{0.75}$ (sample a) by Eq. (3.6) is equal to $(0.9 \pm 0.4)\text{ps/nm}$. This value is smaller than the one expected from continuum mechanics calculations for particle to environment energy transfer (in the case of water-immersed bare Ag or Au spheres this would correspond to 2.8 and 5.7 ps/nm respectively [61, 157], with negligible contribution from solvent viscosity [144, 199]). Indeed, the fit of the transient absorption signal by Eq. (3.6) (Fig. 3.3(b), left column, green dotted line) with $\tau_{h,0}^{\text{norm}}$ fixed to the Ag value shows a longer oscillation damping time. The difference between the values expected for monometallic systems and the one deduced experimentally for the bimetallic spheres could arise from uncertainties in the knowledge of the size distribution, which affect the value of the inhomogeneous damping time. It could also be due to an intrinsic effect,

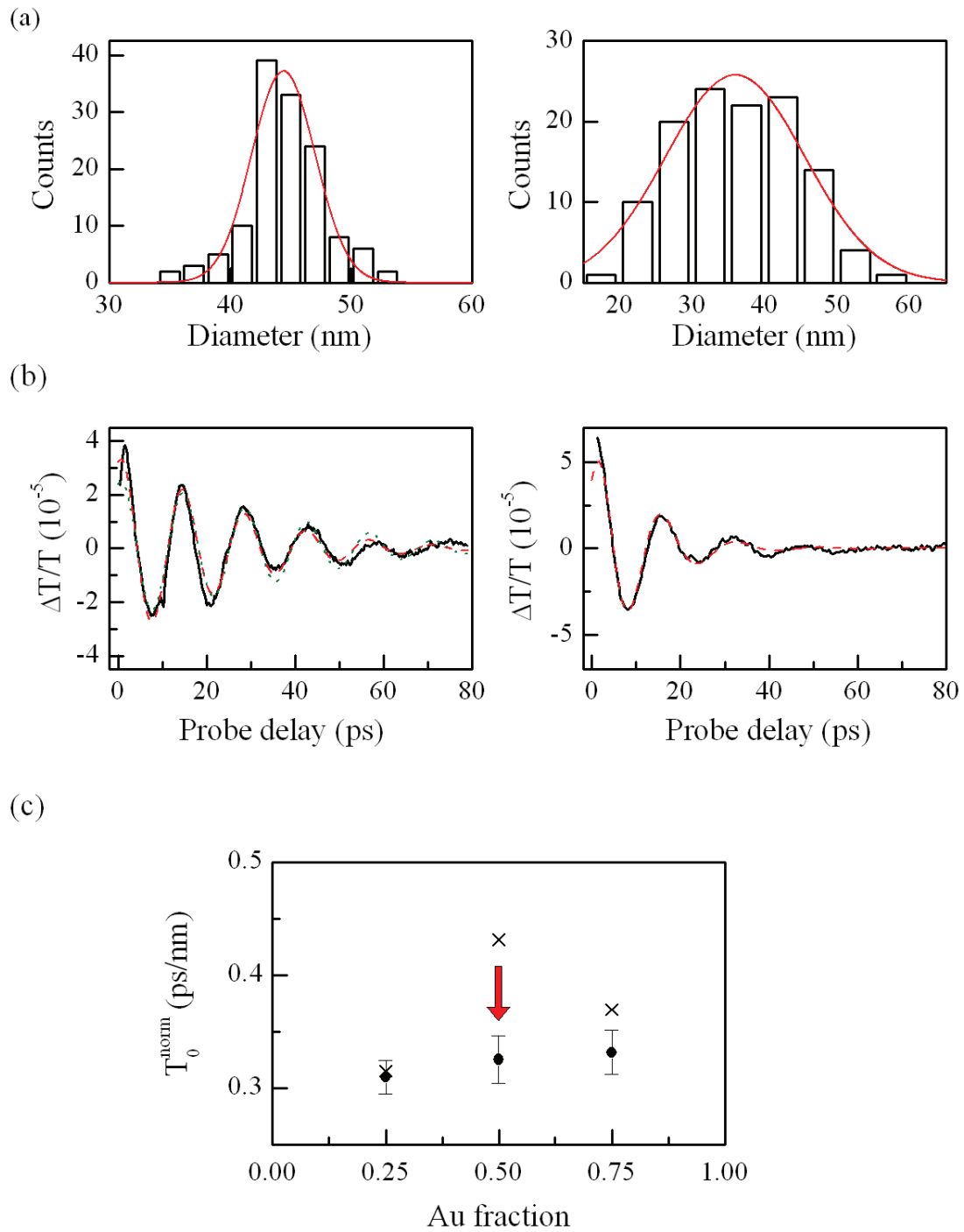


Figure 3.3: (a) Size distribution of sample $\text{Au}_{0.25}\text{Ag}_{0.75}$ (left, sample a) and sample $\text{Au}_{0.50}\text{Ag}_{0.50}$ (right, sample b). Red lines are fits to the distributions, yielding mean values and standard deviations shown in Table 3.1. (b) Oscillating parts of the time-resolved signals (black lines) for the two samples. Red dashed lines are fits using Eq. (3.6) with s_0 , T_0^{norm} , $\tau_{h,0}^{\text{norm}}$ and ϕ_0 as free parameters. The green dotted line represents a fit with $\tau_{h,0}^{\text{norm}}$ set to the expected value for Ag nanoparticles in water. (c) Normalized breathing mode periods T_0^{norm} obtained by a simple direct fit (crosses) and after analysis of inhomogeneous broadening (full circles, see text).

3.2. Ultrafast acoustic response of bimetallic nanoparticles

alloying of Ag and Au leading to a shorter homogeneous $\tau_{h,0}^{\text{norm}}$, possibly due to additional mechanisms of relaxation of the breathing mode energy in the bimetallic samples. Further investigations on samples with a size distribution in which the homogeneous damping time dominates would provide useful information on the effects responsible for damping of acoustic vibrations in alloyed systems. Nonetheless, it should be noted that deduced T_0^{norm} values are negligibly affected by the values of the considered $\tau_{h,0}^{\text{norm}}$.

As its variations with size are expected to be small [61, 141, 151], the oscillation phase ϕ_0 has been considered constant throughout the analysis. The values deduced for samples a and b ($\phi_0 = 0.58 \pm 0.10$ and 0.40 ± 0.10 respectively) are consistent with the sample sizes, assuming indirect excitation of the breathing mode by lattice heating [3, 141]. Using the complete size-dependent expression for ϕ_0 also results in a fit (not shown) similar to the one obtained with constant ϕ_0 within error bars.

3.2.3 Analysis of the breathing mode periods

Normalized periods for water-immersed Au-Ag alloyed nanoparticles (samples a to c) deduced by the analysis above are reported in Fig. 3.4(a) (full dots) as a function of gold composition. Periods of Au/Ag core/shell nanoparticles are also reported (samples d and e, empty squares). As a consequence of a complex dispersion in the core shape and diameter and in the shell thickness, large error bars have to be introduced and the analysis of the normalized periods taking size distribution into account (Sec. 3.2.2.b) could not be performed. Values for Pt/Au and Ni/Ag core/shell clusters (samples f to i) are reported in Figs. 3.4(b) and 3.4(c), respectively. Due to the very small size dispersions, analysis of inhomogeneous broadening was not necessary for these mass-selected samples, as in this case the apparent breathing mode period (Fig. 3.2) can be directly normalized by the average diameter. When available, normalized breathing mode periods for monometallic nanospheres were taken from experiments in the literature on nanoparticles within the same matrix (water or transparent solid matrix) and shown as reference. This is the case for water-immersed Au (Fig. 3.4(a), red circle) [151], silica-embedded Au (Fig. 3.4(b), red circle) [108] and Pt (Fig. 3.4(b), gray circle) [148], and glass-embedded Ag (Fig. 3.4(c), yellow circle) [61] nanospheres. Note that by changing the gold particle environment from water to silica, a decrease in period of the order of 4% is expected [61, 141, 148].

The theoretical normalized periods of nanospheres with core/shell configurations are reported in Figs. 3.4(a)-(c). Periods were calculated by solving Navier's equation (Eq. (3.1)) of a core/shell system in a homogeneous surrounding matrix after imposing, as boundary conditions, continuity of the displacement and of the radial component of the stress tensor at the intermediate interface and at the nanoparticle/matrix interface [4, 158, 159]. Full (dashed) lines correspond to core/shell Au/Ag (Ag/Au), Pt/Au (Au/Pt) and Ni/Ag

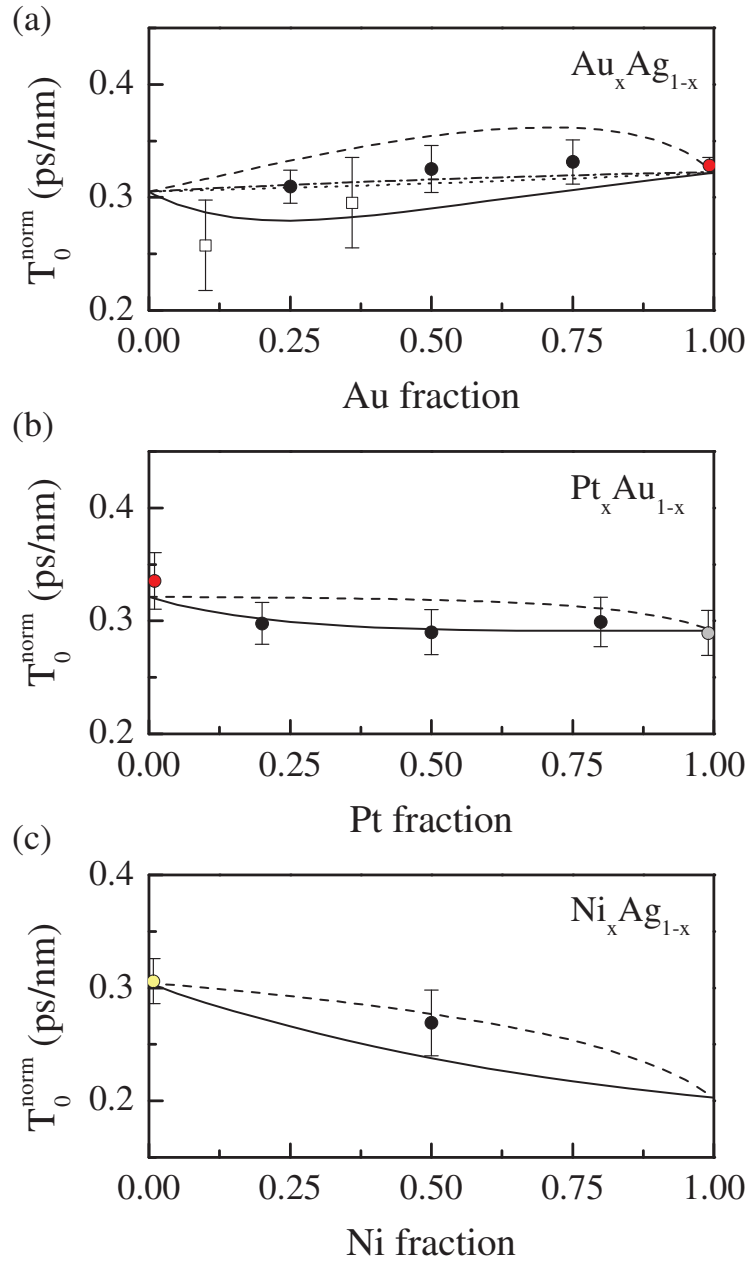


Figure 3.4: Normalized breathing mode periods T_0^{norm} as a function of sample composition for Au-Ag (a, samples a-c and d-e in black dots and empty squares, respectively), Pt-Au (b, samples f-h) and Ni-Ag (c, sample i). Black full (dashed) line corresponds to expected values calculated by continuous elasticity theory and bulk elastic constants of Ref. [201] (except for Pt [202]) for a core/shell configuration with Au (Ag), Pt (Au) and Ni (Ag) in the core. Colored points are experimental reference values for monoatomic nanospheres. Dotted and dash-dotted lines in (a) show periods predicted for Au-Ag alloyed nanospheres obtained by a weighted average of either sound velocities or fundamental elastic constants C_{11} , C_{12} and C_{44} .

3.2. Ultrafast acoustic response of bimetallic nanoparticles

(Ag/Ni) from Figs. 3.4(a) to 3.4(c), respectively. The theoretical values of normalized periods in the case of monometallic nanospheres (values in Figs. 3.4(a) to 3.4(c) corresponding to a variable metal fraction of 0.0 or 1.0) match those calculated by continuous elasticity equations [155, 157] starting with the same bulk polycrystalline elastic constants. Note that in the case of monometallic Au and Pt nanospheres, a variation in the estimation of the breathing mode periods as large as 10% is obtained depending on the set of elastic constants [108, 201, 202], while this is not the case for Ag and Ni. For the calculations of Fig. 3.4, the set of elastic constants best matching experimental reference values for each monometallic constituent has thus been retained, this being Ref. [201] for all metals except Pt (Fig. 3.4(b)), for which Ref. [202] was used. Values of density, longitudinal and transverse sound velocity for water (Fig. 3.4(a)) are $\rho = 1000 \text{ kg/m}^3$, $v_l = 1482 \text{ m/s}$ and $v_{tr} = 0 \text{ m/s}$. In the case of silica-embedded nanoparticles (samples f to i, Figs. 3.4(b) and 3.4(c)), calculations were made assuming a vacuum environment, as the silica matrix is highly porous (see also Ref. [108]).

For Au-Ag alloyed nanospheres (Fig. 3.4(a)), the effect of alloying on the normalized periods has been computed by applying the same macroscopic acoustic approach based on continuous mechanics elasticity equations (Sec. 3.1) [157] as for monometallic nanospheres, using as material parameters a weighted average of the densities of the two metals, and either of their sound velocities (Fig. 3.4(a), dotted line) or their C_{11} , C_{12} and C_{44} fundamental elastic constants used for the calculation of the alloy sound velocities (dash-dotted lines) [172, 203, 204]. Although there is no ultimate conclusion in the literature on the dependence of the elastic properties of bimetallic bulk alloys on composition, different investigations reporting either linear averaging of the fundamental elastic constants upon alloying [204–206] or a slight deviation from linearity [207, 208], we indeed expect breathing mode periods to lie in the range between the ones of their individual components. This is confirmed, in the 1-4 nm range, by molecular dynamics calculations on Au-Ag nanoalloys [173, 174].

Experimental normalized periods of Au-Ag nanoalloys (full dots in Fig. 3.4(a)) show values consistent with the individual ones for both Au and Ag, and with the values corresponding to the two different averages of elastic parameters (dotted and dash-dotted lines). No unexpected signature of alloying on the breathing mode frequencies is observed experimentally. These values deviate from the periods expected for core/shell configurations (full and dashed lines). On the other hand, breathing mode periods of Au/Ag core/shell nanoparticles (with Au core, empty squares in Fig. 3.4(a)) are consistent with values expected for the corresponding core/shell structure (full line). It should be underlined that no corrections to the expected values have been made taking crystallinity of the samples into account as in the case of nanoparticles with a radial symmetry the variation of the breathing mode frequencies with different crystal orientations is very small [3, 156, 209], in contrast to

quadrupolar modes which are sensitively affected by crystalline anisotropy [210].

In the case of Pt/Au nanospheres (Fig. 3.4(b)), the computed breathing mode periods for the monometallic and core/shell configurations are very close. Nonetheless, experimental normalized values lie close to the theoretical line (Fig. 3.4(b), full line) corresponding to the expected configuration (Pt/Au core/shell with platinum in the core), predictions for Au/Pt (dashed line) deviating from experimental values. Computations in the core/shell configuration have been reported so far in the model configuration of a homogeneous and radially symmetrical core/shell structure. This morphology is not realistic for all samples, as for instance the size and composition of samples g and h (2.5 nm Pt_{0.50}Au_{0.50} and 2.3 nm Pt_{0.80}Au_{0.20}, respectively) estimated by purely geometrical considerations would lead to a homogenous gold shell with a thickness smaller than the one of a monoatomic layer. Bimetallic nanoparticles of these sizes are more likely characterized by an asymmetric morphology with a monoatomic thin shell only partially covering the core, forming a Janus-like structure. For this more realistic geometry, we computed the breathing modes by Finite Element Modeling [4, 156]. The breathing mode periods deduced by this modeling match the ones computed for homogeneous radially symmetrical core/shell nanospheres, confirming the validity of the predictions regardless of the exact amount of covering (partially extended or complete shell).

The period measured for the Ni_{0.50}Ag_{0.50} 2.75 nm nanospheres (sample i) (Fig. 3.4(c)) proves the existence of a breathing mode for this composition and the possibility of an ultrafast time-resolved pump-probe apparatus to detect it. This extends previous results by Raman spectroscopy on samples with the same structures [167], for which only the mode corresponding to the isolated Ag shell breathing was detected. The experimental value (Fig. 3.4(c)) lies closer to the predictions for a Ag/Ni core/shell configuration (dashed line), while Ni atoms are expected to be in the core of the nanospheres thus forming Ni/Ag structures (full line). This discrepancy can be due to incorrect modeling of the breathing mode periods by the continuous elasticity approach (Sec. 3.1) for this very small size range in the case of bimetallic core/shell nanospheres with two metals having very different elastic constants, as for Ni-Ag systems (elastic constants of Au-Ag and Pt-Au being more similar). By providing additional information on the precise core-shell structure, supplementary morphological investigations of these small clusters could also bring further insights for interpretation of these results.

3.2.4 Conclusion on the acoustic vibrations of bimetallic nanosystems

Time-resolved ultrafast spectroscopy was used to investigate the vibrational dynamics of bimetallic alloyed and core/shell nanoparticles, in order to elucidate the impact of combin-

3.2. Ultrafast acoustic response of bimetallic nanoparticles

ing two different metals on their acoustic response. The experiments were performed on water-immersed chemically-synthesized Au-Ag nanospheres with alloyed composition in the 33-45 nm range, Au-Ag core/shell nanoparticles of 21 and 33 nm, and on small silica-embedded 2.3-2.75 nm segregated Pt-Au and Ni-Ag clusters. The time-resolved optical evolution corresponding to the radial fundamental vibration mode (breathing mode) was observed for all of them, allowing to determine their breathing mode periods.

In the case of Au-Ag systems, the measured normalized periods were different for alloyed and segregated Au/Ag core/shell nanospheres. In both cases, experiments were in quantitative agreement with predictions based on continuous elastic theory (Sec. 3.1). In the former case, periods were calculated as for monomaterial spheres with sound velocities computed by averaging the two metals elastic properties. Different averaging (sound velocities or fundamental elastic constants) gave very similar predictions, all in agreement with experiments. No unexpected effect of gold and silver alloying on the acoustic vibration periods was observed. For the core/shell nanostructures, predictions are based on a two material continuous elastic mechanics approach [4, 158, 159], whose application to a metal-dielectric systems [162] has been extended to bimetallic Au-Ag nanoobjects. Experiments and theoretical predictions on alloyed and core/shell Au-Ag nanosystems are in good quantitative agreement, measuring their breathing mode periods can thus be used as a discriminating approach to sensitively probe their internal structures.

The same model was used for analyzing breathing mode periods of the small glass-embedded Pt/Au core/shell nanospheres. The measured periods were also in agreement with the predictions for the expected Pt/Au configuration. This confirms (as for the case of monometallic clusters [19]) that a macroscopic acoustic model based on the physical continuous elasticity equations, coupled with bulk material elastic constants, is valid for predicting the acoustic response of particles with sizes down to the nanometer size range. The breathing mode period of small Ni-Ag core/shell nanoparticles, even if measured with less precision, was found to be more compatible with the Ag/Ni core/shell structure, in contrast with the suggested morphological structure (see Sec. 3.2.1). This could be ascribed to the higher difference in the elastic properties of Ni and Ag, which could yield deviations in the acoustic properties of the combined system in this small size range. For this purpose, an interesting perspective would be to extend ultrafast investigations to other bimetallic clusters made by materials with higher differences in their elastic constants as for instance Au-Pb [151], both with a segregated core/shell and alloyed composition, concomitant with a precise morphological characterization.

Combination of two metals (or more generally, hybrid systems) at the nanoscale is an important field of research and the study of its effect on other ultrafast properties through investigation of their time-resolved dynamics could lead to a better understanding of mixed systems. In this context, more detailed analysis of the damping of acoustic vibrations could

provide useful information. Higher order harmonic modes of such systems could also be detected and characterized [141, 160]. The effect of the shape of small bimetallic nanoobjects on the acoustic dynamics would deserve further investigations, through the analysis for instance of fundamental breathing and extensional modes of alloyed nanorods. Finally, study of other dynamical properties as electron-electron and electron-lattice thermalization (Chapter 2) of bimetallic systems could also yield insight into composition-dependent modifications [84, 194, 211].

3.3 Ultrafast vibrational spectroscopy of thiol-protected Au clusters

Understanding at which size a macroscopic model based on continuum mechanics (Sec. 3.1) breaks down in the description of vibrational modes of metal nanoparticles is of fundamental interest and can give insight into the metal electronic and phononic properties in the small size limit. Theoretically, acoustic modes of small nanoparticles (< 4 nm) have been computed using atomistic simulations [108, 149, 150, 212]. Free Au, Ag and Pt nanospheres in the size range of 0.4-4 nm and for different cluster shapes have been studied by Saucedo et al [108]. In order to determine the mode which is preferentially observed in time-resolved optical experiments, a quasi-breathing mode (QBM) was defined, being the computed mode with the highest analogy in displacement with the fundamental radial mode obtained within continuum mechanics. A QBM period linear to the particle diameter was obtained for the considered size range, which is in excellent agreement with experiments performed on small Pt clusters ($D > 1$ nm) prepared by physical means, and classical mechanics calculations (Sec. 3.1) [19, 157].

In the case of surfactant-stabilized clusters, the surface molecules are expected to have a strong impact on the vibrational modes. Accordingly, the computation of the normal modes of very small thiol-protected clusters (4-25 atoms) [150, 212] shows a QBM of the Au core approximately independent of size. Additionally, various modes assigned to the interaction of gold with the attached sulfur molecules (Au-S) were determined. Experimentally, the mechanical vibrations of such small nanoparticles represent a quite unexplored domain. As a consequence of the loss of spherical symmetry and discretization of electronic states, the question of the excitation and detection mechanisms in optical pump-probe spectroscopy remains open. In the past, mainly Au₂₅ clusters have been studied and a single period [93, 152, 153] or two periods have been detected [94]. Other investigations suggested independence of the frequency with size for oscillations measured on Au₂₅, Au₁₄₄ and Au₃₀₉ [133, 152, 153], which is in contrast to the predictions of the macroscopic model. Here, time-resolved pump-probe investigations of the vibrational behavior of thiol-stabilized

3.3. Ultrafast vibrational spectroscopy of thiol-protected Au clusters

Au clusters as a function of their size are presented. For this purpose, four samples ranging from particles consisting of only 25 gold atoms to a diameter of $D = 3.5$ nm were studied (same samples as in Sec. 2.4.1). These experiments on particles of a broad size range may allow further insights into the role of surfactant molecules, the impact of quantum confinement and the possibility of acoustic mode detection at small sizes.

3.3.1 Experimental methods

Time-resolved experiments have been performed on Au_{25} , Au_{102} , Au_{144} and $\text{Au}_{D=3.5\text{nm}}$ clusters in a solution (dimethylformamide (DMF) or water). Synthesis, optical properties and characterization of the samples have been described in Sec. 2.4.1. The pump-probe measurements were performed with either a monochromatic (setup 1, Sec. 2.1.1) or a broadband (setup 2 in collaboration with the CUSBO facility of Politecnico di Milano, Sec. 2.1.2) white light probe beam. The two setups differ in pump wavelength and energy, laser repetition rate and time resolution. In the first case, the clusters are excited by a blue beam, obtained as the second harmonic of an amplified Ti:Sapphire laser, ($\lambda_p = 400$ nm, $F \approx 5$ mJ/cm², $f_m = 250$ kHz) and probed by a monochromatic OPA output (Sec. 2.1.1, 500-700 nm). Here, the pump-probe cross-correlation (~ 180 fs FWHM) only allows a limited temporal resolution. Experiments were therefore extended using setup 2 (Sec. 2.1.1), where both pump and probe beams are characterized by a duration of less than 20 fs, the clusters being excited using visible light ($\lambda_p \approx 590$ nm, $F \approx 200$ mJ/cm², $f_m = 1$ kHz).

Fig. 3.5 shows a typical two dimensional map of the differential transmission $\Delta T/T$ of the Au_{25} sample as a function of probe wavelength and time delay, obtained by white light probing. The horizontal axis shows the pump-probe time delay, while the vertical axis reports the probe wavelength, obtained by dispersion of the white laser light by a spectrometer, the color code representing the corresponding $\Delta T/T$ value. Analyzing $\Delta T/T$ as a function of probe delay, oscillations in the signals are observable. Three different periods can be retained. A very fast one (~ 50 fs), corresponding to solvent vibrations (DMF) [213], characterized by the fine fringes visible throughout the map. Two slower periods ($T_0 \approx 450$ fs and $T_1 \approx 1$ ps), associated to the thiol-protected gold clusters, are the main focus of this section. Both periods are detected close to characteristic features of the samples linear absorption spectrum (see arrows in Fig. 3.5). While the shorter one, T_0 , is particularly visible for probe wavelengths close to the pronounced peak at ~ 680 nm, assigned to the HOMO-LUMO molecular transition (see transition *a* in Fig. 2.37(b) and Ref. [127]), the slower mode, T_1 , is more visible close to a small bump at ~ 550 nm which has not been associated to any molecular transition in electron energy calculations [127]. The choice of wavelengths close to spectral features in the sample absorption spectrum for

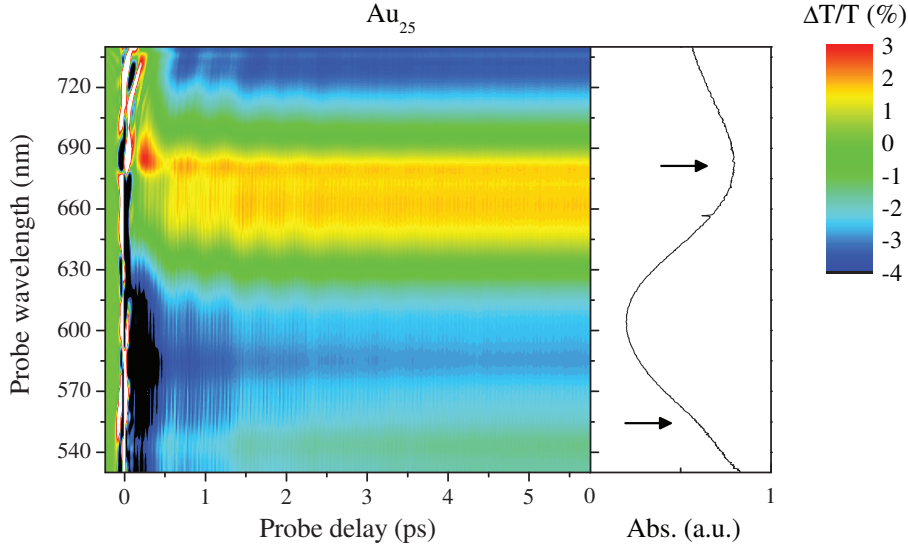


Figure 3.5: Differential transmission map of Au_{25} in DMF for excitation by a visible $\lambda_p = 590$ nm, ~ 15 fs pump pulse ($F \approx 200$ mJ/cm²) and probing by broadband ultrafast ~ 5 fs white light. For comparison, the normalized absorption spectrum of the sample is shown in the same scale (arrows indicate characteristic spectral features).

the detection of vibrational modes has previously been exploited in larger metal nanoparticles, where breathing mode oscillations were mainly observed for probe wavelengths close to the surface plasmon resonance [61].

To adequately characterize the vibrational dynamics, multiple $\Delta T/T(t)$ profiles at fixed λ_{pr} of the 2D map in Fig. 3.5 were analyzed. Fig. 3.6(a) illustrates the time-resolved signal for $\lambda_{pr} = 630$ nm. Due to the high fluence and short time duration of pump and probe pulses of setup 2, a strong non-linear response is observed at delay $t = 0$ with a large contribution from the solvent. The subsequent decay of the negative signal, reminiscent of the electron-lattice thermalization in larger nanoparticles, is overlapped to an oscillating contribution which was studied in detail by subtracting a two-exponential fit from the signal (red line in Fig. 3.6(a)). The resulting oscillating contribution (Fig. 3.6(b)) is fitted by two damped oscillating functions (red line) and Fourier transformed (Fig. 3.6(b), inset). The two low-frequency periods ($T_0 = 450$ fs and $T_1 = 1.1$ ps) and the fast solvent oscillations appear as distinct peaks in the frequency spectrum.

Time-resolved pump-probe investigations with a broadband white light probe beam were systematically performed on all samples (Table 2.2). Note that all of them were diluted in DMF except Au_{102} which was diluted in water. Figs. 3.7(a) and 3.7(c) illustrate time-resolved signals of the Au_{102} and Au_{144} samples at probe wavelengths $\lambda_{pr} = 620$ nm and $\lambda_{pr} = 630$ nm, respectively. The fit of the oscillating part of the time-resolved signals (3.7(b) and 3.7(d)) and the Fourier transform (3.7(b), inset) yield two low-frequency vi-

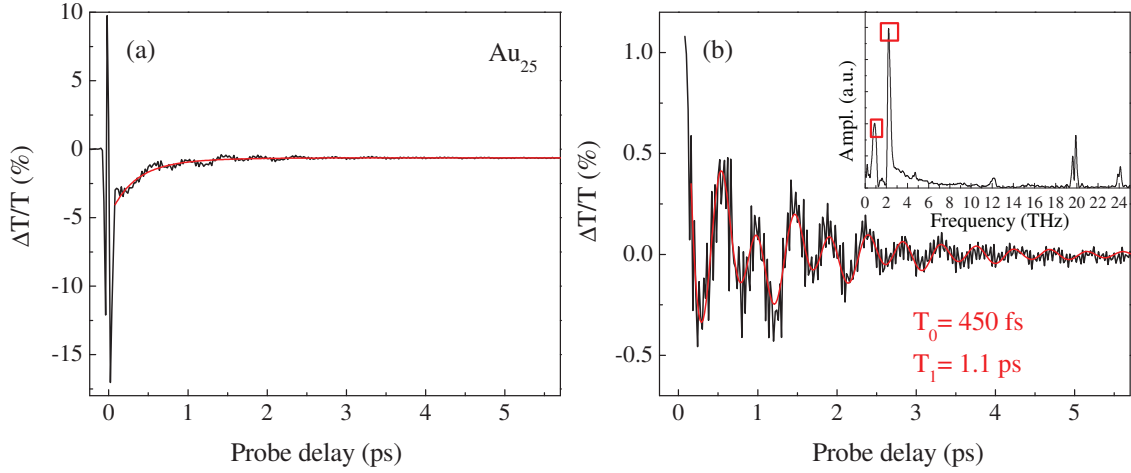


Figure 3.6: (a) Time-resolved transient transmission signal of the Au_{25} sample (same as in Fig. 3.5) for $\lambda_{pr} = 630$ nm (black line) and two-exponential fit of the signal decay (red line). (b) Oscillating contribution (black line) and fit by two damped oscillating functions (red line). The Fourier transform of the oscillating contribution is shown in the inset (red boxes indicate low frequency oscillations of the cluster).

brational periods for the two samples (note that oscillations of the DMF solvent are not observable for the Au_{102} sample, this being diluted in water). Similar to the Au_{25} sample, T_0 and T_1 are in the 0.5 ps and one ps range (see Figs. 3.7(b) and 3.7(d)). In the case of Au_{102} the detection amplitude of T_0 is maximum close to a specific small peak in its the linear absorption spectrum around 620 nm, which has been assigned to transitions from HOMO to higher electron energy states [135]. The amplitude of the oscillating part of the Au_{144} sample was very weak and an optimal probe wavelength for the detection of oscillations could not be determined. This is related to its linear absorption spectrum which does not show any distinctive structure (Fig. 3.7(c), inset).

Pump-probe experiments on all samples were also repeated using the monochromatic source of setup 1 (Sec. 2.1.1). In this case, as a consequence of the lower temporal resolution of the system, only the longer period T_1 could be detected, T_0 and the fast solvent oscillations being not visible. Here, the amplitude of the signals is smaller due to a weaker pump fluence, but the setup is more sensitive. The periods obtained by using two different experimental systems were in good agreement.

In the case of the largest studied particles $\text{Au}_{D=3.5\text{nm}}$, a single oscillating period was detected. In Fig. 3.8(a) the time-resolved pump-probe signal in the configuration P/Pr 400/545 nm (setup 1) is illustrated. The signal shows the typical rise and decay due to energy injection into the free electron gas of the metal, electron-electron and electron-phonon interactions, respectively (see Sec. 2.2.2). Subtracting a two-exponential fit (red line in Fig. 3.8(a)), and fitting the oscillating contribution by taking into account the size

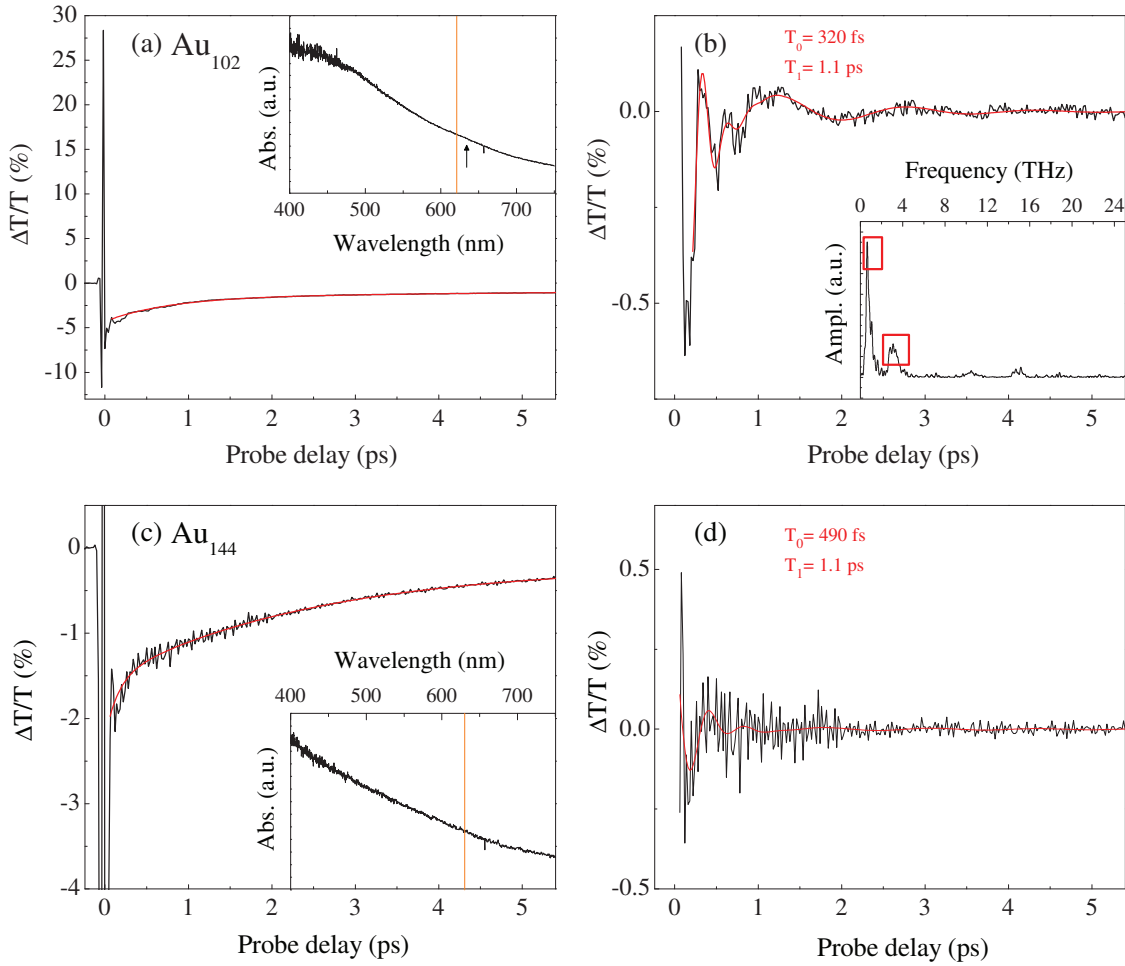


Figure 3.7: (a) Time-resolved transient transmission signal of the Au_{102} sample with $\lambda_p = 590$ nm, $\lambda_{pr} = 620$ nm and $F \approx 200$ mJ/cm² (black line) and two-exponential fit of the signal decay (red line). Inset: linear absorption spectrum of the sample (black line) and spectral position of the selected probe wavelength (orange vertical line). Arrow indicates the position of a small bump in the absorption spectrum. (b) Oscillating contribution (black line), its fit by two damped oscillating functions (red line) and Fourier transform (inset). (c) and (d) Same as (a) for the Au_{144} sample ($\lambda_p = 590$ nm, $\lambda_{pr} = 630$ nm and $F \approx 200$ mJ/cm²), with its linear spectrum and probe wavelength shown in the inset.

3.3. Ultrafast vibrational spectroscopy of thiol-protected Au clusters

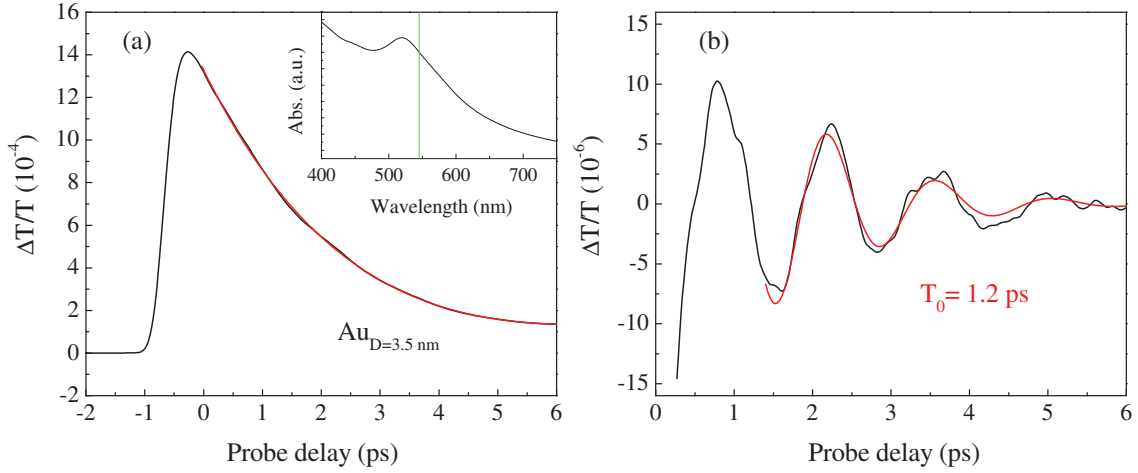


Figure 3.8: (a) Time-resolved pump-probe signal of sample $\text{Au}_{D=3.5\text{nm}}$ with $\lambda_p = 400$ nm, $\lambda_{pr} = 545$ nm and $F \approx 3$ mJ/cm² (black line) and two-exponential fit of the signal decay (red line). Inset: linear absorption spectrum (black line) and probe wavelength (green vertical line). (b) Oscillating contribution (black line) and its fit (red line) using the detailed analysis presented in Sec. 3.2.2.b taking into account the size distribution of the sample with a standard deviation $\Delta D = 0.6$ nm (Eq. (3.6)).

distribution of the sample (standard deviation $\Delta D = 0.6$ nm) as presented in Sec. 3.2.2.b, a period of around of 1.2 ps can be observed (Fig. 3.8(a)). As expected, the maximal detection amplitude of these vibrations is located close to the SPR of the sample (Fig. 3.8(a), inset). The detected mode corresponds to the breathing mode of the Au core which can be reproduced using elasticity theory (Sec. 3.1), as it has been shown in former experiments on metal nanoparticles in this size range [3, 17, 61, 84].

3.3.2 Analysis of the Au cluster vibrational frequencies

The periods experimentally detected for small thiol-protected clusters are reported in Fig. 3.9 as a function of the cluster diameter, defined as the diameter of a homogeneous gold sphere with the same number of atoms. The black dashed line illustrates the classical computation of the breathing mode period of Au nanospheres in water using elasticity theory (Sec. 3.1).

The detected period of the largest sample ($\text{Au}_{D=3.5\text{nm}}$) can be attributed to the classical breathing mode of the gold core, corresponding to radial volume oscillations of the nanospheres [108]. After the size dispersion analysis presented in Sec. 3.2.2.b, the period is in perfect agreement with the theoretically obtained one. Smaller clusters are characterized by two vibrational periods. In the case of Au_{25} , the shorter period T_0 was best detected for wavelengths close to the HOMO-LUMO gap. The HOMO-LUMO levels being mainly located in the gold core, this indicates that this period can be attributed to

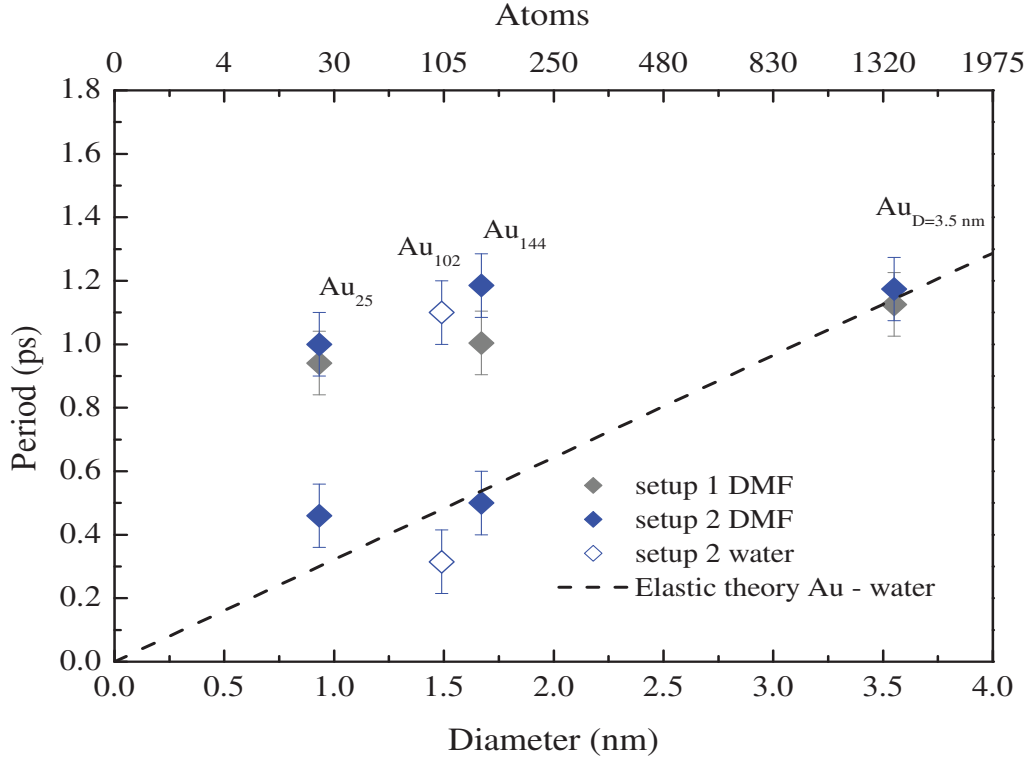


Figure 3.9: Experimentally measured periods of the oscillating pump-probe signals as a function of particle size (number of atoms or equivalent particle diameter) obtained by setup 1 (gray diamonds) and setup 2 (full and open blue diamonds for samples in DMF and water, respectively). The black dashed line illustrates the breathing mode period of Au nanospheres in water obtained by the classical model (Sec. 3.1).

the QBM of the icosahedral Au₁₃ core of the cluster. In this context, the measured value of T_0 is in qualitative agreement with molecular calculations of the QBM for surfactant-stabilized Au₂₅ clusters, predicting a period of 320 fs [150, 212]. T_0 shows a nearly constant value for the Au₂₅, Au₁₀₂ and Au₁₄₄ samples (400 ± 100 fs) in agreement with Goodson et al. [133, 152, 153] observing a similar periods for the vibrational modes of Au₂₅, Au₁₄₄ and Au₃₀₉. However, by taking into account the full investigated size range (Au₂₅-Au_{D=3.5nm}), the observed periods also lie very close to the classical continuum mechanics predictions (Fig. 3.9). Investigation of even smaller clusters, as Au_{x=4-25}, would provide an experimental evidence that could be compared to atomistic predictions [150, 212].

The longer period $T_1 \approx 1$ ps in the Au₂₅ sample was best detected using probe wavelengths in the visible (~ 550 nm), corresponding to photon energies higher than the HOMO-LUMO band gap. Sensitivity to the detection wavelengths and the observed period are in good agreement with previous results [94]. Detection of this longer oscillation could be induced by periodic modifications of electron energy states associated to the presence of surfactant molecules. Comparing the period with atomistic computations, this lower frequency

mode is close to values calculated for Au-S-Au bending modes [150, 212]. These modes describe interaction of the Au₁₃ core with the ligand shell and induce thus modifications of lower-lying electronic states (HOMO-n), where orbitals from the Au-ligand shell contribute more to the molecular orbital states. However, in a classical picture, the longer period T_1 can also be attributed to the quadrupolar mode ($n = 0, l = 2, m = 0$) of the Au₁₃ gold core. It has been observed in previous experiments on larger nanoparticles that this mode can be excited in optical pump-probe experiments in samples deviating from spherical symmetry [156]. For the larger samples, Au₁₀₂ and Au₁₄₄, T_1 increases slightly with increasing diameters, which supports the classical picture of excitation and probing of the quadrupolar mode of the Au core atoms.

3.3.3 Summary of experiments on small thiol-protected Au clusters

The effect of size reduction on the vibrational dynamics of small thiol-protected Au clusters was investigated by time-resolved ultrafast spectroscopy. Here, two different pump-probe setups were used, with white light or monochromatic probe beams. The setups also differed in pump wavelength, energy and temporal resolution. The periods which could be detected using both experimental systems were in very good agreement.

A high-frequency mode was detected in a size range from only 25 Au atom clusters to diameters of 3.5 nm (Au₂₅, Au₁₀₂, Au₁₄₄ and Au_{D=3.5nm}). By analyzing its evolution with size and probe wavelength sensitivity, this mode could be associated to the radial volume oscillation of the Au core of the clusters, the measured periods being in agreement with atomistic computations in the case of the smallest Au₂₅ sample [150, 212]. Additionally, a lower frequency oscillation in the signals of Au₂₅, Au₁₀₂ and Au₁₄₄ was detected. Its period agrees with the classical picture of the quadrupolar mode of the Au core. An Au-S-Au bending mode with a period similar to experiments has been theoretically predicted by calculations for Au₂₅ [150, 212]. However, more experimental and theoretical work should be done for the identification of the measured T_1 mode in Au₂₅, Au₁₀₂ and Au₁₄₄. In this context, systematic measurements as a function of surfactant molecules and solvent could give further insight.

3.4 Conclusion

Time-resolved spectroscopy allowed the observation of a radial fundamental vibration mode (breathing mode) for both bimetallic nanospheres and small Au clusters. The determination of the breathing mode periods was in good agreement with calculations based on classical elasticity theory, using bulk material elastic constants. In the case of

Chapter 3. Acoustic response of bimetallic nanoparticles and metal clusters

bimetallic nanoparticles, the internal structure (core-shell, alloy) of the samples could be discriminated using pump-probe spectroscopy. No unexpected modification of the breathing modes due to the combination of two different metals was observed, even when in some core/shell configurations the shell was formed by a monoatomic metal layer. The breathing modes could also be observed in the case of thiol-protected Au clusters, down to particles consisting of only 25 metal atoms. The validity of the classical continuum mechanics model already reported for small Pt nanospheres (> 1 nm) [19] can thus be extended to the sub-nanometer size range and to bimetallic core/shell nanometric size structures. This is in stark contrast to other dynamical properties (e.g. electron-electron and electron-phonon interactions, see Chapter 2), where significant modifications to the bulk model were observable for particles smaller than ~ 2 nm.

Chapter 4

Thermal relaxation of colloidal gold and gold-silica nanospheres

With the development of devices in the nanometric size range, understanding and modeling thermal transport at the nanoscale and the underlying fundamental processes are becoming key technological issues [20]. In particular, much attention is currently devoted to the increased role of interfaces, characterized by their Kapitza resistance, defined as the ratio between temperature jump and heat flux at boundaries [214].

A lot of experimental and theoretical works are currently devoted to the understanding of the Kapitza resistance, in particular at room temperature where current agreement between experiments and models is poor [20, 215]. In practice, measurements of this resistance have most frequently been performed for both solid-solid and solid-liquid interfaces on nanofilms, superlattices and nanoparticle samples using optical pump-probe spectroscopy, which enable monitoring of thermal kinetics on picosecond timescales [19, 215–224]. Pump-probe experiments on metal nanoparticles in liquid or dielectric media involve their selective heating by a pump pulse and subsequent cooling governed by heat flow at the interfaces and heat diffusion in the environment, monitored by a probe pulse. In such experiments, pump and probe beams are thus used as heater and thermometer, respectively.

The thermal interface conductance, defined as the inverse of the Kapitza resistance, at metal-liquid interfaces has been subject to a large number of time-resolved experiments based on bare metal nanoparticles in solution. These investigations have addressed the sensitivity of nanoparticle cooling dynamics to the composition of the metal, of the solvent and of the surfactant molecules stabilizing the nanoparticles [217–220, 222–225], yielding interface conductances G typically between 20–300 MW/(m² K). For instance, Plech et al. [226] measured a conductance of 105 MW/(m² K) for citrate-stabilized gold particles in water, while Wilson et al. [217] obtained $G = 130$ MW/(m² K) for citrate-stabilized

platinum spheres. Solid-dielectric interfaces have also been considered and values in the same range as for the metal-liquid case were obtained [216, 221, 227, 228]. Stoner and Maris [216] reported in a pioneering work the measurement of G for various solid plane interfaces, with $40 \text{ MW}/(\text{m}^2 \text{ K})$ for Au-sapphire, Au-BaF₂ and Au-diamond. An earlier study of our group considered metal nanoparticles in different glasses, leading to an interface conductance of $100 \text{ MW}/(\text{m}^2 \text{ K})$ between Au and a glass with 53 % silica content [19]. Pump-probe studies have been more rarely performed on core-shell nanoparticles, whose cooling requires heat propagation through two interfaces (those between the core and shell components, and between the shell and the nanoparticle surroundings). Despite the presence of such an additional interface, Hu et al. [220] observed an acceleration in the pump-probe signal dynamics with addition of a silica shell to gold nanoparticles in water or ethanol. In another context, Emelianov et al. [229, 230] have shown that silica encapsulation of gold nanorods in water yields an amplification of the amplitude of their photoacoustic signal, pointing to significant modification of their thermal dynamics.

Most previous time-resolved experiments have analyzed the resulting signals in a simplified way. Heat diffusion in nanoparticle environment was sometimes omitted in thermal modeling assuming cooling dynamics is mostly governed by interface resistances [231]. Moreover, most studies have assumed a direct proportionality between pump-probe signals and the metal nanoparticle temperature [218–220, 222]. However, this hypothesis is not necessarily valid, as environment heating leads to a modification of its optical properties, susceptible to affect signals. Such simplified analysis may lead to incorrect determination of interface conductances, possibly accounting for the large dispersion of values reported in literature. Here, we report a quantitative approach to analyze pump-probe experiments, based on both a complete description of thermal dynamics (yielding spatial and temporal variations of temperature as a function of the thermal parameters of the nanoparticles and their environment) and modeling of their effect on the optical properties of the sample. This methodology is applied to analyze experiments performed on both bare and silica-encapsulated gold nanospheres in water or ethanol, enabling determination of thermal conductances at gold-liquid, gold-silica and silica-liquid interfaces. Additionally, a large contribution of the environment to pump-probe signals acquired on gold nanoparticles in ethanol is demonstrated through systematic variation of the probe beam wavelength.

4.1 Experiments

4.1.1 Nanoparticle samples

Experiments have been performed on gold nanospheres, bare or coated with silica of varying thickness, diluted in both water and ethanol with a particle volume fraction p

around 10^{-5} . All samples have been synthesized by the the Liz-Marzán group in Vigo, Spain.

The bare gold spheres present a mean diameter of $D = 18.5$ nm and are stabilized by citrate groups and thiol modified Polyethyleneglycol (mPEG-SH) for dilution in water and ethanol, respectively. Gold-silica core-shell samples were synthesized from the initial solution of gold nanospheres in water, with silica growth by Stöber method [232], using variable growth time for the realization of different shell thicknesses which are in this case given by: $a_1 = 3.4$ nm, $a_2 = 12.4$ nm, $a_3 = 18.5$ nm, $a_4 = 25.7$ nm. Mean diameter and shell thickness were deduced by transmission electron microscopy (TEM), shown in Figs. 4.1(a) and 4.1(b) for bare gold and gold-silica core-shell nanoparticles (a_4). Their gold core size dispersion was found to be around 15 % (inset in Fig. 4.1(a)). All samples

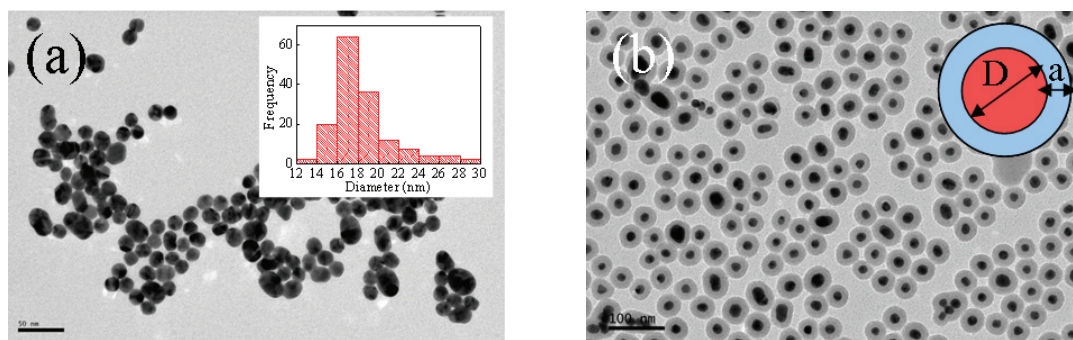


Figure 4.1: TEM images for (a) bare gold nanospheres of mean diameter $D = 18.5$ nm and (b) same particles coated with silica, with shell thickness $a_4 = 25.7$ nm. Inset in (a): Size distribution of gold spheres.

show a surface plasmon resonance (see Sec. 1.2) around 530 nm, with a position at slightly larger wavelengths for particles in ethanol than in water and slightly shifting to the red with increasing silica loading (Fig. 4.2, inset). The experimental absorption coefficient αL (see Sec. 1.5) for bare gold nanoparticles in water is shown in Fig. 4.2. For the purpose of further experimental analysis, it is reproduced using the dipolar approximation of Mie theory applied to nanospheres in a homogeneous environment ($n_m = 1.33$, see Eq. (1.45)). The bulk gold dielectric function was adopted from Ref. [25]. The position of the resonance peak of the computed absorption spectrum agrees very well with the experimental one. Its width was phenomenologically adjusted to incorporate inhomogeneous and homogeneous broadening due to quantum confinement [42, 43] (see Sec. 1.2 and Eq. (1.26), with an effective parameter $g = 1.5$).

The small deviation still remaining between the experimental and the simulated SPR profile can be explained by inhomogeneous effects resulting from size and morphology dispersion in the sample (e.g. deviation from perfect sphericity). Table 4.1 summarizes the thermal parameters at room temperature of the materials involved in the studies.

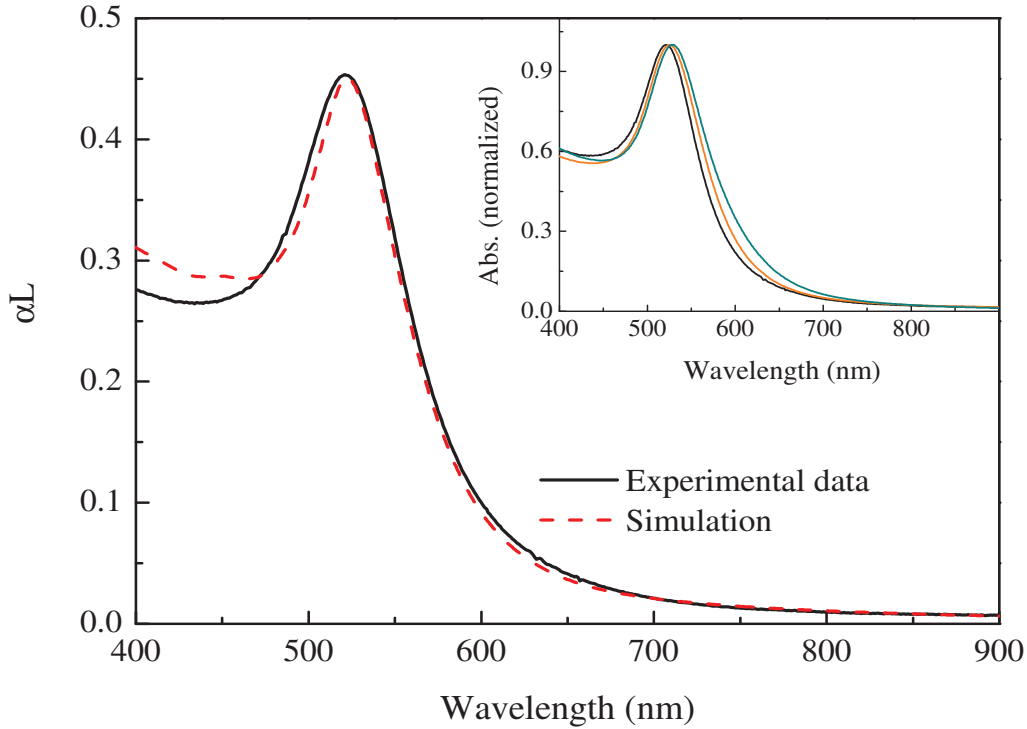


Figure 4.2: Experimental (full black line) and simulated (red dotted line) absorption coefficient αL for $D = 18.5$ nm Au nanospheres in water ($n_m = 1.33$). Absorption was calculated using Mie theory in the dipolar approximation (Eq. (1.45)). Inset: normalized absorption spectra for bare Au nanoparticles in water (black line), ethanol (orange line) and core-shell nanoparticles of shell thickness $a_4 = 25.7$ nm in ethanol (green line).

4.1.2 Pump-probe experiments

Thermal cooling of the presented nanoparticles in solvent is investigated by ultrafast pump-probe spectroscopy. Time-dependent transmission measurements were performed with a two-color pump-probe setup in the weak excitation regime (setup 1, Sec. 2.1.1) using the direct (820 nm) or frequency-doubled (410 nm) output of a Ti-sapphire oscillator and the output of an Optical Parametric Oscillator (OPO). The latter emits light in the visible range of the spectrum (500-700 nm) and is pumped by part of the output of the Ti-sapphire oscillator. For more detail on this setup, see Sec. 2.1.1. Solutions were inserted in a quartz cuvette of $L = 1$ mm thickness which was mounted on a metal ring serving as sample holder and heat sink at the same time.

The two-colored beams (IR or blue on one branch, the OPO output on the other one) were both used as pump (P) or probe (Pr). While the pump wavelength only affects the amplitude of the signals, depending on the amount of excitation after pump beam absorption, the probe wavelength dependence was systematically investigated during this work. The focal spot size σ of the pump beam was ~ 10 μm while the one of the probe beam was 20 μm . A larger probe beam as compared to the pump one reduces the sensitivity to slight

Table 4.1: Density ρ , specific heat capacity C , volumetric heat capacity c and thermal conductivity Λ [22, 233, 234]

material	ρ (kg/m ³)	C (J/(kg·K))	c (10 ⁶ J/(m ³ ·K))	Λ (W/(m·K))
gold	19320	129	2.5	317
fused silica	2200	703	1.5	1.38
water	1000	4180	4.18	0.6
ethanol	800	2400	1.92	0.179

P/Pr misalignments upon movement of the mechanical stage for the long paths necessary to obtain a pump-probe delay of some hundreds of ps [221]. Knowledge of the spot sizes, measured by a CCD camera, allows evaluation of the initial temperature increase of the gold part of the particles by pump beam absorption. All experiments were performed in the low perturbation regime, with a pump fluence of typically $\sim 100 \mu\text{J}/\text{cm}^2$ yielding a temperature increase $\Delta T_L^0 \approx 3 \text{ K}$. For this weak excitation, being well below the onset of particle melting ($\sim 1000 \text{ K}$ for gold nanoparticles in the same size range [235]), a linear dependence of pump/probe (P/Pr) signals with temperature can be safely assumed. This linearity with heating was methodically verified on all samples by varying the pump laser fluence.

Fig. 4.3(a) illustrates the relative transient transmission signal $\Delta T/T = -\Delta\alpha L$ (Sec. 1.5) for bare gold particles in ethanol. The sample has been excited by an infrared beam (820 nm) and transmission changes have been probed at 530 nm. Like in former pump-probe measurements the signal is characterized by a strong peak corresponding to the particle excitation and internal thermalization, followed by a slow decaying signal due to lattice cooling (see inset in Fig. 4.3(a)). Here, we concentrate on the dynamics of the latter, typically occurring on a timescale of several hundred ps. For the purpose of analysis, time zero $t = 0$ was defined in all signals as the moment just after the metal internal thermalization (few ps after pump excitation), hence the instant the gold core has reached maximum temperature $T_L^0 = T_0 + \Delta T_L^0$ (with almost no heat transferred to the surrounding yet, see Fig. 4.5(a)). In practice $t = 0$ is characterized by a break in the signal's slope (compare Fig. 4.3(a)), which changes from a steep decay to slow-decaying dynamics.

In Figs. 4.3(b), 4.4(a) and 4.4(b), the effects of solvent, probe wavelength and silica shell on those long timescale dynamics are observable. Fig. 4.3(b) illustrates the long delay time-resolved signals of gold particles in water and ethanol, obtained in the same experimental conditions. For easier comparison the two signals have been normalized at their temporal origin. In ethanol the signal decay is slower than in water, which can be qualitatively explained by its smaller heat conductivity (Table 4.1). Ethanol evacuates heat more slowly, which leads to slower cooling in the metal particle as well. Still, this explanation

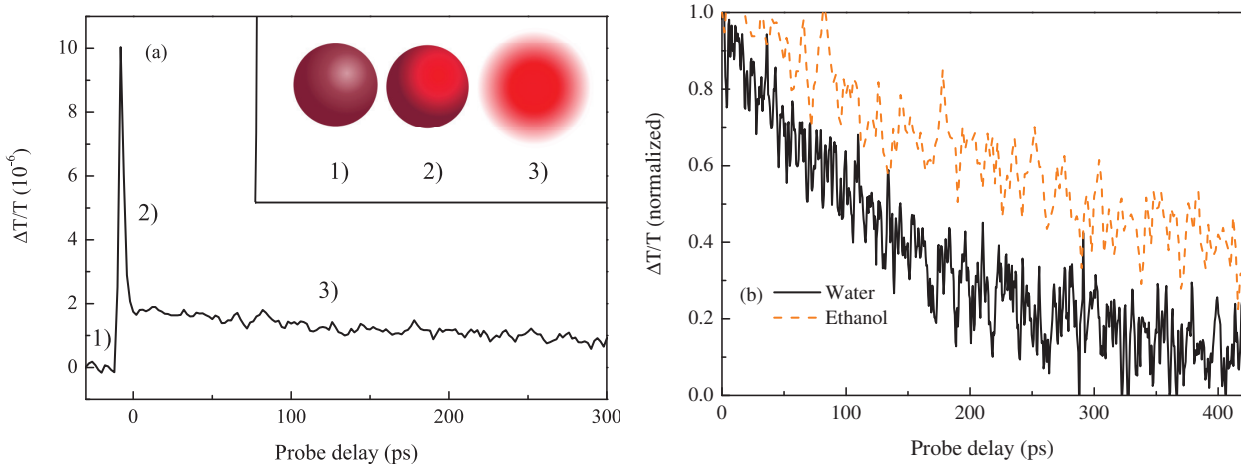


Figure 4.3: (a) Time-resolved signals of bare gold nanospheres in ethanol for a pump beam of $\lambda_p = 820$ nm, pump fluence $F \approx 200 \mu\text{J}/\text{cm}^2$ and probe beam $\lambda_{pr} = 530$ nm. The inset schematically describes the processes observable in the experiment, corresponding to a flat signal before excitation (1), a pronounced peak during particle internal electronic thermalization (2) and a slower decay due to its subsequent cooling (3). (b) Same signal normalized to unity at $t=0$ (orange dashed line). Also shown is the pump-probe signal in the same configuration for gold nanoparticles in water, also normalized at $t=0$ (black solid line).

remains approximate, not taking into account a possible change of the thermal interface resistance with solvent exchange.

Fig. 4.4(a) depicts transient transmission signals of bare gold particles in ethanol for different probe wavelengths close to the surface plasmon resonance of the sample (see inset). Excitation was identical for these measurements, the frequency-doubled laser output (410 nm) being used to generate the pump beam whose fluence was not modified. Close to the surface plasmon resonance the signals feature strong sensitivity to the probe wavelength, not only in their amplitudes but also concerning their dynamics. The signal sign changes from negative to positive with decreasing probe wavelength, while for intermediate wavelengths the transient signals change sign with pump and probe delay. This clearly demonstrates the absence of proportionality between P/Pr signals, and the nanoparticle temperature and highlights the requirement of a rigorous analysis of the detection mechanism, connecting the experimental signal to the physical processes in the sample.

The effect of the addition of a silica shell is shown in Fig. 4.4(b). For the particles in water (P/Pr 820/530 nm), an increasing silica shell accelerates the decay dynamics, an effect that has been observed before [220]. A naive way to explain this evolution would, again, be the higher thermal conductivity of silica compared to water (Table 4.1). However, as discussed above, the transient signals must be carefully analyzed, considering both heat diffusion in the system and heat transfer at interfaces. Also, the signals do not necessarily reflect the evolution of the gold temperature, due to possible contributions of the thermal dynamics of their environment.

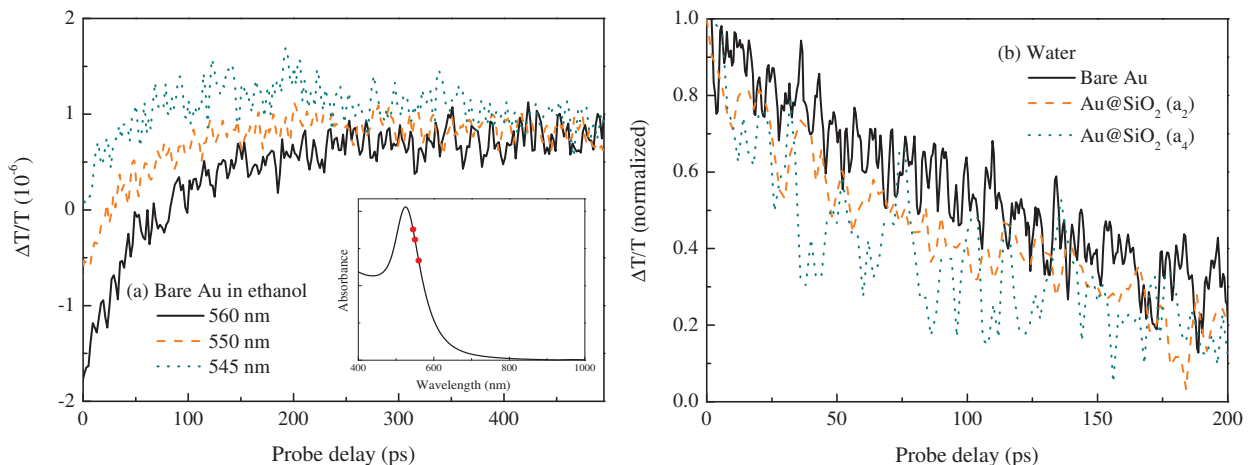


Figure 4.4: (a) Transient long delay signals of bare gold spheres in water excited by a blue pump pulse (410 nm) of similar fluences $F \approx 20 \mu\text{J}/\text{cm}^2$ for all signals and a probe pulse of different wavelengths. Inset: Position of the probe wavelength with respect to the sample absorbance. (b) Comparison of the pump-probe signals (P/Pr 820/530 nm, $F \approx 200 \mu\text{J}/\text{cm}^2$) of bare gold and core-shell particles with different silica shells in water. The signals have been normalized to unity at $t=0$.

In the following sections we develop an analytic model for computing the temperature dynamics in all parts of the studied systems, considering both heat diffusion and thermal resistances at the interfaces. We then connect the temperature changes in gold core ΔT_p and environment ΔT_m to the absorption change $\Delta\alpha$ of the sample in a similar approach to Eq. (1.1), where the change of the dielectric functions ($\Delta\epsilon_1, \Delta\epsilon_2, \Delta\epsilon_m$) can be connected linearly to the temperature excess of particle and environment.

4.2 Modeling heat transfer dynamics

In order to model the successive heat evacuation of the initially heated metal particle to the dielectric shell and to the solution, two distinct processes are considered (see Figs. 4.5(a) and 4.5(b)). Heat evacuation in the shell and in the surrounding medium is taken into account in a classical diffusive model for heat transfer (neglecting confinement effects like ballistic transport) whereas the particle temperature is considered to be homogeneous due to its high thermal conductivity compared to dielectric materials ($\Lambda_{\text{metal}} \gg \Lambda_{\text{dielectric}}$, see Table 4.1). Furthermore, a thermal interface resistance, the Kapitza resistance (see Sec. 4.2.1), is introduced at all interfaces. In former experiments an analytic model for the temperature of bare metal particles in solution or deposited on a glass matrix [19, 217, 218] has been presented, taking into account these two contributions. We expand this model introducing a second material with an additional interface and describe not only the particle temperature, but also the position-dependent temperature of the surrounding

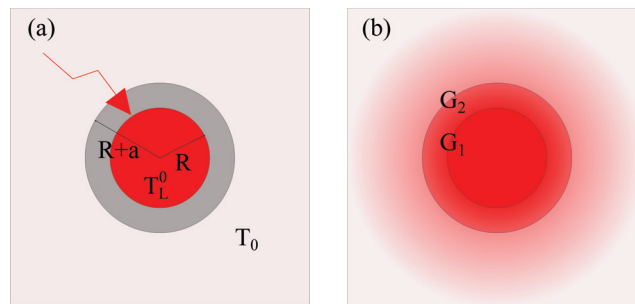


Figure 4.5: Schematic view of a core shell-particle of core radius $R = D/2$ and shell thickness a in a solvent. (a) Initial heating of the metal core ($t = 0$) to temperature increase while silica shell and solvent are still at room temperature T_0 . (b) Heat diffusion in shell and solvent, thermal interfaces are present at the core surface ($r = R, G_1$) and the shell surface ($r = R + a, G_2$).

shell and solvent. Here, thermal parameters are taken from bulk tables, assuming no modification for the given particle sizes (Table 4.1).

4.2.1 The Kapitza resistance

A temperature discontinuity ΔT at the boundary of two materials is introduced by a thermal resistance (Kapitza resistance R_K) or its inverse, the thermal interface conductance G , which is defined as follows:

$$J = G\Delta T, \quad (4.1)$$

where J describes the heat flow per unit area across the interface [214]. A temperature jump at the interface is present because of the change in the characteristics of the phonons (being primarily responsible for heat transfer) from one material to another. A complete description of their transmission at the boundary demands extensive studies about the exact nature of the interface and on the materials on both sides. In the past years, mainly two assumptions have been made to simplify the problem: The acoustic mismatch model (AMM) and the diffuse mismatch model (DMM) [214].

In the picture of the AMM, phonons are treated as plane waves and the materials they are propagating in are described by classical continuum mechanics. Here, scattering of phonons at the interfaces is completely neglected and their transmission probabilities can be determined by the acoustic analog of the Fresnel equations. Assuming additionally normal phonon incidence and independence of the transmission to the phonon frequency, one can find a simplified equation for the energy transmission coefficient from side 1 to

side 2 [216]:

$$t_{1 \rightarrow 2} = \frac{4Z_1 Z_2}{(Z_1 + Z_2)^2}, \quad (4.2)$$

where $Z_{1,2}$ describe the acoustic impedances, given by the product of mass density ρ and sound velocity v_l of the materials.

The DMM, in contrast to the AMM, assumes all phonons to be diffusely scattered at the boundary, losing thus all memory of their original state. In this case the probability of being scattered from one side to the other side of the interface is simply proportional to the corresponding density of phonon states. In a rude approximation, one can assume that phonons can only scatter into identical states. If the corresponding phonon states available on side 1 are close to the one on side 2, a good transmission coefficient can thus be expected. A simple parameter to characterize similarity of the phonon density of states is given by the ratio of the Debye temperatures Θ_1/Θ_2 of the two materials [216, 227].

While these two models are in agreement with measurements performed at low temperatures on plane interfaces [214], at room temperature they are too simplified to describe the thermal interface conductance, for reasons remaining an issue in nanoscale thermal transfer.

4.2.2 Bare gold nanospheres

In the present section we introduce the equations governing heat transfer and their analytic solution for bare nanospheres in a solid or liquid environment. Extension to the more complex core-shell system will be done afterward.

In the given spherical geometry all governing equations can be written in spherical coordinates, the physical quantities depending only on the distance r from the particle center. Moreover, the samples under study are sufficiently dilute to assume an infinite environment and no interaction between the different metal particles in solution. For particles with a radius $R = D/2$ we can thus write three equations describing heat evacuation at the particle interface ($r = R$), heat diffusion in the environment and the boundary condition for continuous heat flux at the interface [236].

$$\frac{dT_p(t)}{dt} = -\frac{3G}{Rc_p} [T_p(t) - T_m(R, t)], \quad (4.3)$$

$$\frac{\partial T_m(r, t)}{\partial t} = \frac{\Lambda_m}{c_m} \frac{1}{r} \frac{\partial^2}{\partial r^2} [rT_m(r, t)], \quad (4.4)$$

$$\left. \frac{\partial T_m(r, t)}{\partial r} \right|_{r=R} = -\frac{G}{\Lambda_m} [T_p(t) - T_m(R, t)], \quad (4.5)$$

Chapter 4. Thermal relaxation of colloidal gold and gold-silica nanospheres

with the temperatures of particle and environment T_p and T_m respectively, c_p and c_m their specific heat per unit volume, Λ_m the thermal conductivity of the matrix and G the thermal interface conductance.

To solve this system of equations it is helpful to describe the temperature in the matrix by the reduced variable $F_m(r, t)$, which is defined as:

$$F_m(r, t) = r (T_m(r, t) - T_{m,i}), \quad (4.6)$$

with $T_{m,i}$ the initial temperature of the matrix.

An appropriate way to find an exact solution for the temperature in both materials is to operate in the Laplace domain [237] defined by the transformation:

$$\tilde{h}(r, s) = \int_0^\infty e^{-st} h(r, t) dt \quad (4.7)$$

Eq. (4.4) in Laplace space and using $F_m(r, t)$ then becomes:

$$s\tilde{F}_m(r, s) = \kappa \frac{\partial^2}{\partial r^2} \tilde{F}_m(r, s), \quad (4.8)$$

with $\kappa = \Lambda_m/c_m$ corresponding to the thermal diffusivity of the environment. The solution of this equation is a decaying exponential function, as we impose the temperature increase far from the particle to be zero:

$$\tilde{F}_m(r, s) = \tilde{F}_m(R, s) e^{-q(r-R)}, \quad (4.9)$$

where q is the thermal wavelength, $q^2 = s/\kappa$.

It is then relatively straightforward to derive the solution of the system in Laplace space for the metal particle and the dielectric environment. We obtain [19, 236]:

$$\tilde{T}_p(s) = -\frac{\alpha_p \left[1 - \frac{Rg}{1+R(q+g)} \right]}{s + \alpha_p \left[1 - \frac{Rg}{1+R(q+g)} \right]} \frac{T_{m,i}}{s}, \quad (4.10)$$

$$\tilde{F}_m(r, s) = \frac{-gR^2 \left[\frac{1}{1+R(q+g)} \right]}{s + \alpha_p \left[\frac{1+Rq}{1+R(q+g)} \right]} e^{-q(r-R)} T_{m,i}, \quad (4.11)$$

with $\alpha_p = 3G/(Rc_p)$ and $g = G/\Lambda_m$ corresponding to the inverse Kapitza length l_K [238]. In order to obtain the temperature dynamics in direct space, the inverse Laplace transform of Eq. (4.10) and Eq. (4.11) has to be executed. For the temperature excess of particle

$\Delta T_p(t)$ and matrix $\Delta T_m(r, t)$ with regard to their temperature before heating we obtain:

$$\Delta T_p(t) = \frac{2}{\pi} k(Rg)^2 \Delta T_L^0 \int_0^\infty \frac{u^2 e^{-\frac{\kappa u^2}{R^2} t}}{[u^2(1+Rg) - kRg]^2 + (u^3 - kRgu)^2} du, \quad (4.12)$$

$$\Delta T_m(r, t) = \frac{2}{\pi} k(Rg)^2 \frac{R}{r} \Delta T_L^0 \int_0^\infty \frac{u e^{-\frac{\kappa u^2}{R^2} t}}{[u^2(1+Rg) - kRg]^2 + (u^3 - kRgu)^2} \times \quad (4.13)$$

$$\left[u \left(1 - \frac{u^2}{kRg} \right) \cos \left(\frac{u}{R} (r - R) \right) + \left(1 - \frac{u^2}{kRg} (1 + Rg) \right) \sin \left(\frac{u}{R} (r - R) \right) \right] du,$$

with $k = 3c_m/c_p$. It is thus possible to monitor the heat evacuation of particle and matrix in an exact way. Instead of using the definition of the inverse Laplace transform to express Eq. (4.10) and Eq. (4.11) in direct space, it is also possible to factorize these two equations and to use tabulated Laplace transforms to get an analytical expression of the temperature dynamics [236]. These expressions are more complicated but demand less calculating time, which is why we chose to use them for simulations.

Discussion and extreme limits There are two limiting cases for heat dissipation of the particle depending on the interface thermal conductance, characterized by the parameter gR .

- For high thermal conductance at the interface or large particles, $gR \rightarrow \infty$ and the decay of the nanoparticle temperature is limited by diffusion of heat in the surrounding environment. In this case Eq. (4.4) is the governing equation and a non-exponential decay of the particle excess temperature ΔT_p is expected. A characteristic cooling time τ_D can be estimated by equating the heat capacity of the metal particle $4/3\pi R^3 c_p$ and the heat capacity of a surrounding layer with thickness of the thermal diffusion length, given by $4\pi R^2 c_m \sqrt{\Lambda_m/c_m \tau_D}$ [218]:

$$\tau_D = \frac{R^2 c_p^2}{9c_m \Lambda_m}. \quad (4.14)$$

- For $gR \rightarrow 0$, heat evacuation of the metal nanoparticle is ruled by the thermal interface resistance. The particle cooling is then described by Eq. (4.3) with a fixed matrix temperature $T_m(R, t)$ and the temperature exponentially decays with a characteristic time τ_G given by:

$$\tau_G = \frac{Rc_p}{3G}. \quad (4.15)$$

Chapter 4. Thermal relaxation of colloidal gold and gold-silica nanospheres

The times differ in their dependence on the particle radius R . Characteristic times associated to a diffusion-limited process alone vary quadratically with particle radius while the decay time in the case of low interface conductance varies linearly with size. In general, the kinetics of big particles is controlled by the diffusive process, whereas for very small sizes the impact of low interface conductance overtakes. Previous time-resolved studies on metal nanoparticles have often been analyzed considering one of these extreme cases ([218–220, 239] → Diffusion, [231] → Interface). However, for intermediate sizes such simplifications are not valid and both processes must be considered. In this case, the temperature decay of the particles is dominated by the surface process on shorter timescales after initial excitation and by heat diffusion in the matrix on a longer timescale.

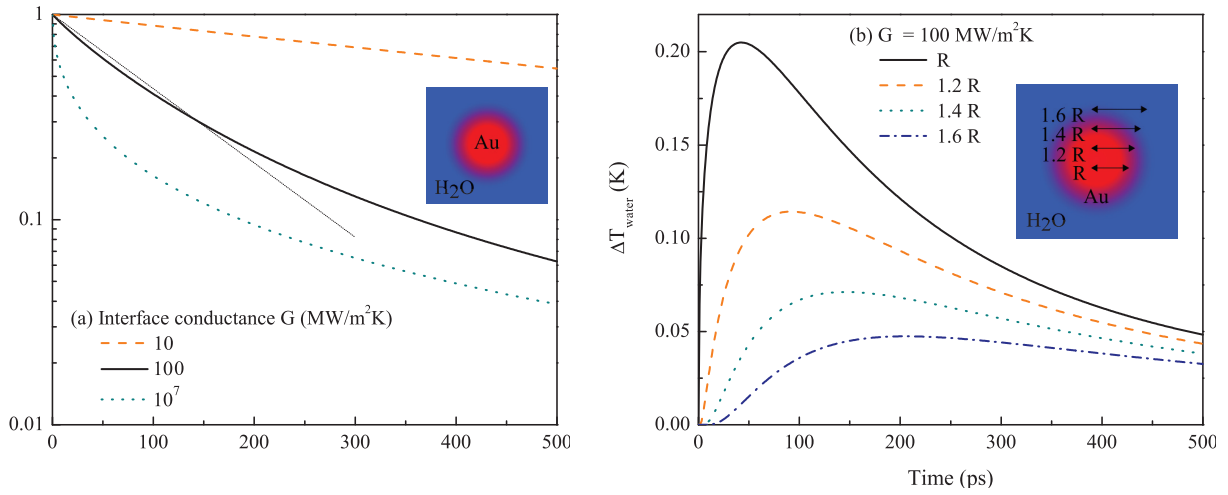


Figure 4.6: Simulated temperature dynamics for gold nanospheres in water with initial metal heating of 1 K. (a) Excess temperature of gold for varying thermal interface conductances, $G = 10$ MW/(m² K) (orange dashed line), $G = 100$ MW/(m² K) (full black line), and $G = 10^7$ MW/(m² K) (green dotted line). (b) Excess temperature of water for $G = 100$ MW/(m² K) at varying positions r .

Fig. 4.6(a) depicts the metal excess temperature ΔT_p of gold particles in water and initial heating of $\Delta T_L^0 = 1$ K for a realistic thermal interface conductance $G = 100$ MW/(m² K), as well as the two extreme limits of very small and very large conductances. For the dynamics plotted in a semi-logarithmic graph, one can notice an almost exponential behavior for a small conductance as expected from Eq. (4.12) and Eq. (4.15), whereas for an increasing thermal conductance the decaying curves become more and more concave corresponding to dynamics controlled by Eq. (4.14).

The matrix temperature dynamics (Fig. 4.6(b)) are characterized by a rise followed by a decay corresponding to heat transfer from the particle and the subsequent cooling by radial energy propagation, with amplitudes and timescales depending on the considered position. The water excess temperature of the same system as presented above is shown in Fig. 4.6(b). The thermal interface conductance is fixed to the value $G = 100$ MW/(m² K) and the dynamics at different positions r are depicted. Moving away from the surface the temperature

rise is slower and the maximum value decreases due to heat diffusion in water.

4.2.3 Addition of a dielectric shell

The proposed model can be generalized in order to describe metal particles with a dielectric shell (see Sec. 4.1.1). Eq. (4.3), Eq. (4.4) and Eq. (4.5) stay valid for heat transport from the metal particle to the adjacent material m_1 (in this case the silica shell), diffusion in this material and continuity of heat flux at the first interface. To adapt the equations to the new situation we add the index 1 for the first (metal-dielectric) interface and heat propagation in the shell e.g. $G \rightarrow G_1$ and $\Lambda \rightarrow \Lambda_1$. In contrast to the previous system the extension of m_1 is not infinite, the shell having a thickness a , and we have to introduce a second interface between the shell and the environment m_2 with thermal interface conductance G_2 . It follows the addition of three equations to describe heat diffusion in the environment, heat transport at the second interface and heat flux conservation at this interface:

$$\frac{\partial T_{m_2}(r, t)}{\partial t} = \frac{\Lambda_2}{c_2} \frac{1}{r} \frac{\partial^2}{\partial r^2} [r T_{m_2}(r, t)], \quad (4.16)$$

$$\left. \frac{\partial T_{m_2}(r, t)}{\partial r} \right|_{r=R+a} = -\frac{G_2}{\Lambda_2} [T_{m_1}(R+a, t) - T_{m_2}(R+a, t)], \quad (4.17)$$

$$\Lambda_1 \left. \frac{\partial T_{m_1}(r, t)}{\partial r} \right|_{r=R+a} = \Lambda_2 \left. \frac{\partial T_{m_2}(r, t)}{\partial r} \right|_{r=R+a}. \quad (4.18)$$

The new system of equations can still be solved in Laplace space using the normalized variables \tilde{F}_{m_1} and \tilde{F}_{m_2} of Eq. (4.6), with $T_{m_1, i} = T_{m_2, i} = T_{m, i}$. The shell-matrix thermal interface involves both energy transmission and reflection. Therefore heat propagation in the shell can be defined by the sum of a rising and a decaying exponential. On the other hand the matrix is considered to be infinite which leads to a decaying exponential behavior for \tilde{F}_{m_2} as before in Eq. (4.9):

$$\tilde{F}_{m_1}(r, s) = A_1(s)e^{-q_1 r} + B_1(s)e^{q_1 r}, \quad (4.19)$$

$$\tilde{F}_{m_2}(r, s) = A_2(s)e^{-q_2 r}, \quad (4.20)$$

with $q_{1,2}^2 = s/\kappa_{1,2}$ the thermal wavelength of shell and matrix and $A_{1,2}$ and B_1 parameters to be determined by the system of equations. We eventually obtain an analytical solution of the temperature dynamics in Laplace space for all involved parts of the composite

system $T_p(s)$, $T_{m_1}(r, s)$ and $T_{m_2}(r, s)$:

$$\tilde{T}_p(s) = \frac{\alpha_p \left[1 - \frac{Rg_1(1-u)}{(1+Rg_1)(1-u)+Rq_1(1+u)} \right]}{s + \alpha_p \left[1 - \frac{Rg_1(1-u)}{(1+Rg_1)(1-u)+Rq_1(1+u)} \right]} \frac{T_{m,i}}{s}, \quad (4.21)$$

$$\tilde{F}_{m_1}(r, s) = \frac{-g_1 R^2 \left[\frac{1}{(1+Rg_1)(1-u)+Rq_1(1+u)} \right]}{s + \alpha_p \left[1 - \frac{Rg_1(1-u)}{(1+Rg_1)(1-u)+Rq_1(1+u)} \right]} \left(e^{-q_1(r-R)} - u e^{q_1(r-R)} \right) T_{m,i}, \quad (4.22)$$

$$\tilde{F}_{m_2}(r, s) = \frac{-g_1 R^2 \left[\frac{1}{(1+Rg_1)(1-u)+Rq_1(1+u)} \right]}{s + \alpha_p \left[1 - \frac{Rg_1(1-u)}{(1+Rg_1)(1-u)+Rq_1(1+u)} \right]} \tilde{g}_2 e^{-q_1 a} (1 - e^{2q_1 a} u) e^{-q_2(r-(R+a))} T_{m,i}, \quad (4.23)$$

with $\alpha_p = 3G_1/(Rc_p)$ and $g_{1,2} = G_{1,2}/\Lambda_{1,2}$. The variable $\tilde{g}_2 = \frac{g_2(R+a)}{1+(R+a)(q_2+g_2)}$ can be interpreted as a normalized inverse Kapitza length for the shell-matrix interface which depends not only on thermal interface conductance and conductivity but also on particle radius, shell thickness and the thermal wavelength of the environment. The parameter u illustrates the amplitude of heat reflection at the shell-matrix interface which can be seen in Eq. (4.22). It is given by $u = e^{-2q_1 a} \frac{(1-\lambda\tilde{g}_2)+(R+a)(q_1-\lambda\tilde{g}_2q_2)}{(1-\lambda\tilde{g}_2)-(R+a)(q_1+\lambda\tilde{g}_2q_2)}$ with λ the ratio of the thermal conductivities of environment and shell $\lambda = \Lambda_2/\Lambda_1$.

The temperature evolution of excess temperatures in metal, shell and solvent, are obtained from the inverse Laplace transform. This yields an integral expression for the temperature dynamics in each part of the system, which can be solved numerically.

Discussion and extreme limits For some limiting cases Eq. (4.21), Eq. (4.22) and Eq. (4.23) describe the former system with a single interface between bare gold nanoparticles and their environment (Sec. 4.2.2), as in the two following situations:

- If $a \rightarrow \infty$ (infinite shell) then $u \rightarrow 0$ (no heat reflection) and the system is well described by Eq. (4.21) and Eq. (4.22) corresponding in this case to Eq. (4.10) and Eq. (4.11), respectively.
- If $G_2 \rightarrow \infty$, $\lambda = 1$ and $q_1 = q_2 = q$. This corresponds to eliminating the second interface by setting an infinite conductance and identical materials for shell and matrix. In this case $\tilde{g}_2 \rightarrow 1$ and $u \rightarrow 0$ and both Eq. (4.22) and Eq. (4.23) describe heat transfer in the matrix of a system with a single interface. The equations in Laplace space describing temperature in particle and matrix again correspond to Eq. (4.10) and Eq. (4.11).

Heat evacuation from the metal particle is determined by the thermal interface conductance at both interfaces as well as the thermal parameters of both surrounding materials.

In general this leads to a complex dynamics, the effects of different parameters being not necessarily decorrelated. In this context, one can show that e.g. lowering the heat conductivity of the shell has the same effect on the metal particle thermal dynamics as a decrease of the thermal conductance at the shell-solvent interface.

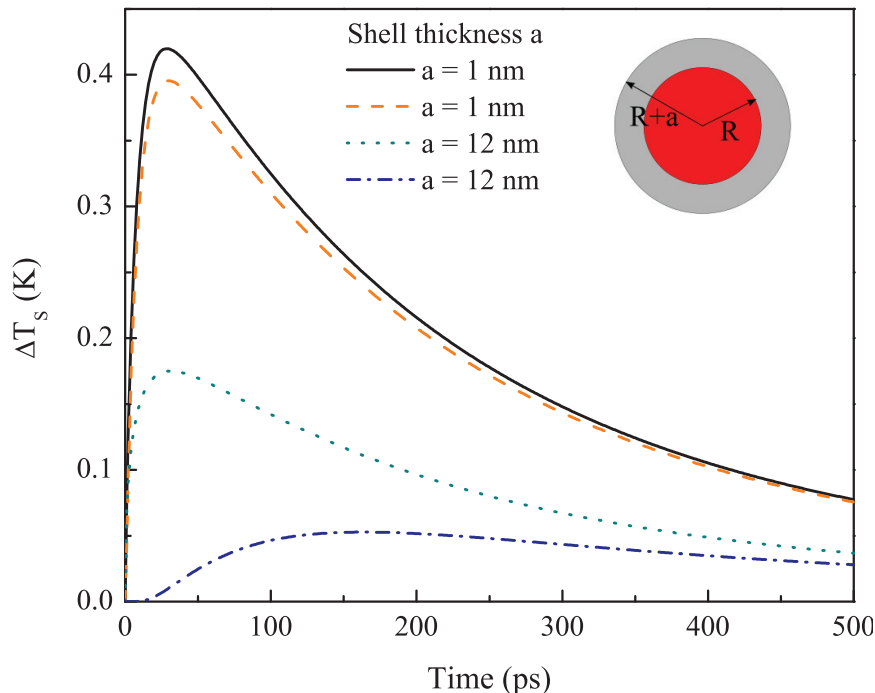


Figure 4.7: Simulated excess temperature of the shell for gold-silica core-shell particles in water, for initial metal heating of 1 K and equal thermal conductance at the two interfaces ($100 \text{ MW}/(\text{m}^2 \text{ K})$). The full black and dashed orange lines describe the silica excess temperature for $a = 1 \text{ nm}$ at $r = R$ (gold-silica interface) and $R + a$ (silica-water interface), respectively. The green dotted and blue dash-dotted lines show the temperature excess at the same positions for $a = 12 \text{ nm}$.

Fig. 4.7 illustrates a comparison of the temperature dynamics of the shell for core-shell gold-silica nanoparticles in water computed for two different shell thicknesses. For this purpose the time-dependent silica excess temperature $\Delta T_{m_1} = \Delta T_S$ is plotted at the gold-silica interface $r = R$ and at the silica-water interface $r = R + a$ (see inset of Fig. 4.7). For the same thermal interface conductances $G_1 = G_2 = 100 \text{ MW}/(\text{m}^2 \text{ K})$, temperature increase of a 1 nm shell is distinctively higher than the one of a 12 nm shell. This is a result of the overlap of heat transferred from the metal particle and reflected from the shell external surface. Although heat reflection at the external interface occurs in both systems, this effect is moderate in the thicker shell due to heat diffusion within silica.

The presented model provides a description of the temperature dynamics of all implicated materials of a spherical metal-dielectric core-shell system in a transparent environment. However, for more complex systems (e.g. involving supplementary shells, or non-spherical geometry) it is more convenient to make use of numerical simulations. Here, we performed

finite element modeling (FEM) [4] in order to confirm the validity of our analytical approach, obtaining excellent agreement between the two methods.

4.3 Optical detection of heat transfer

The thermal properties of the described samples, especially the role of thermal interface resistances, were investigated by time-resolved pump-probe spectroscopy. In contrast to steady-state measurements on the thermo-optical response of gold or silver nanoparticles in a glass matrix, where heating of both the metal and the substrate was considered [86, 88, 240, 241], in most previous time-resolved optical experiments, signal proportionality to the temperature of the metal particle was assumed [218–220, 222]. Only rarely temperature increase in the environment was discussed in ultrafast optical spectroscopy experiments, e.g. on colloidal gold nanorods [224], substrate deposited gold nanorods [223] or metal nanospheres in different glasses [19], where a contribution of the environment to the signal was estimated and assumed to be negligible for certain probe wavelengths. However, the knowledge of the contribution to the transient signal from the heated environment is essential to precisely interpret optical experiments and extract values for the thermal boundary conductance G . Here we develop a model for the quantitative analysis of time-resolved pump-probe signals, taking into account temperature dynamics in both metal particles and their environment.

The absorption coefficient α of the composite system is correlated to the dielectric functions of the constituting materials, being complex for the absorbing metal ($\epsilon = \epsilon_1 + i\epsilon_2$) and real for the transparent shell (ϵ_S) and solvent (ϵ_{sol}). For particles much smaller than the incident light wavelength, absorption of the composite system of spherical core-shell particles in solvent $\alpha_{c-s} = n_{np}\bar{\sigma}_{ext}$ (see Sec. 1.5) can be written using Mie theory in the dipolar approximation [21]:

$$\alpha_{c-s}(\lambda) = \frac{6\pi p\sqrt{\epsilon_{sol}}}{\lambda} \times \text{Im} \left[\frac{(\epsilon_S - \epsilon_{sol})(\epsilon(\lambda) + 2\epsilon_S) + f_\nu(\epsilon(\lambda) - \epsilon_S)(\epsilon_{sol} + 2\epsilon_S)}{(\epsilon_S + 2\epsilon_{sol})(\epsilon(\lambda) + 2\epsilon_S) + 2f_\nu(\epsilon(\lambda) - \epsilon_S)(\epsilon_S - \epsilon_{sol})} \right], \quad (4.24)$$

with $p = n_{np}V_{np}$ the metal volume fraction (Sec. 1.3.1) and $f_\nu = \frac{R^3}{(R+a)^3}$ the ratio between the core and the total volumes of the core-shell particle.

After heating of the gold core of the nanoparticle by pump pulse absorption, both real ϵ_1 and imaginary parts ϵ_2 of the metal dielectric function change (see Sec. 1.4.2). Additionally, heat transfer to the shell and to the solvent induces a change in ϵ_S and ϵ_{sol} .

For weak heating by the pump pulse one can estimate at first order the absorption change

4.3. Optical detection of heat transfer

of the sample $\Delta\alpha_{c-s}$, which is directly connected to the excess temperatures of metal core, silica shell and solvent (extension of Eq. (1.1)):

$$\begin{aligned}\Delta\alpha_{c-s}(\lambda_{pr}, t) &= \left(\frac{\partial\alpha_{c-s}}{\partial\epsilon_1} \frac{d\epsilon_1}{dT_p} \Big|_{\lambda_{pr}} + \frac{\partial\alpha_{c-s}}{\partial\epsilon_2} \frac{d\epsilon_2}{dT_p} \Big|_{\lambda_{pr}} \right) \Delta T_p(t) \\ &+ \frac{\partial\alpha_{c-s}}{\partial\epsilon_S} \frac{d\epsilon_S}{dT_S} \Big|_{\lambda_{pr}} \Delta T_S(t) + \frac{\partial\alpha_{c-s}}{\partial\epsilon_{sol}} \frac{d\epsilon_{sol}}{dT_{sol}} \Big|_{\lambda_{pr}} \Delta T_{sol}(t). \quad (4.25) \\ &= A_p \Delta T_p(t) + A_S \Delta T_S(t) + A_{sol} \Delta T_{sol}(t)\end{aligned}$$

Note that we have replaced T_{m_1} by T_S and T_{m_2} by T_{sol} , considering from now on a precise system of gold core, silica shell and solvent. For simplicity, in Eq. (4.25) the spatial variations of the temperatures of silica shell and solvent are initially omitted. As a first approximation, shell and solvent temperatures at R and $R + a$, respectively, can be considered in this simplified equation. However, as the response of a metal nanoparticle is sensitive to the dielectric constant of its environment over a distance of the order of the particle radius [242], this assumption is not quite realistic and Eq. (4.25) will be used only for estimations of the amplitudes A_p , A_S and A_{sol} of the different materials to the pump-probe signal.

For a quantitative computation of the optical response, a more complete way to describe shell and particle temperatures is to decompose both materials into a large number of subshells, in order to account for their temperature gradient. The following equation is valid for an arbitrary number of shells [243, 244]:

$$\Delta\alpha_{multi}(\lambda_{pr}, t) = A_p \Delta T_p(t) + \sum_{i=1}^{N_S} A_{S_i} \Delta T_S(R + a_{S_i}, t) + \sum_{i=1}^{N_{sol}} A_{sol_i} \Delta T_{sol}(R + a + a_{sol_i}, t), \quad (4.26)$$

where the linear absorption coefficient α_{multi} is explicitly given in Refs. [243, 244]. The metal contribution to $\Delta\alpha$ does not change in comparison to Eq. (4.25), the temperature in the metal part of the nanospheres being uniform. The environment has now been divided in N_S subshells for the silica shell (total thickness a) and N_{sol} subshells for the solvent (on a large enough distance at least of the order of the particle diameter), with spacings a_{S_i} and a_{sol_i} respectively.

The amplitude associated to the temperature variation of each subshell is given in the same way as for the core-shell system in Eq. (4.25), by $A_{S_i} = \partial\alpha_{multi}/(\partial\epsilon_{S_i})d\epsilon_S/dT_S$ and $A_{sol_i} = \partial\alpha_{multi}/(\partial\epsilon_{sol_i})d\epsilon_{sol}/dT_{sol}$, with here $\epsilon_{S_i} = \epsilon_S$ and $\epsilon_{sol_i} = \epsilon_{sol}$. Typically, division of the immediate surrounding on a distance of the diameter of the gold particle into 100 subshells with a quadratically increasing thickness for increasing r is enough to obtain

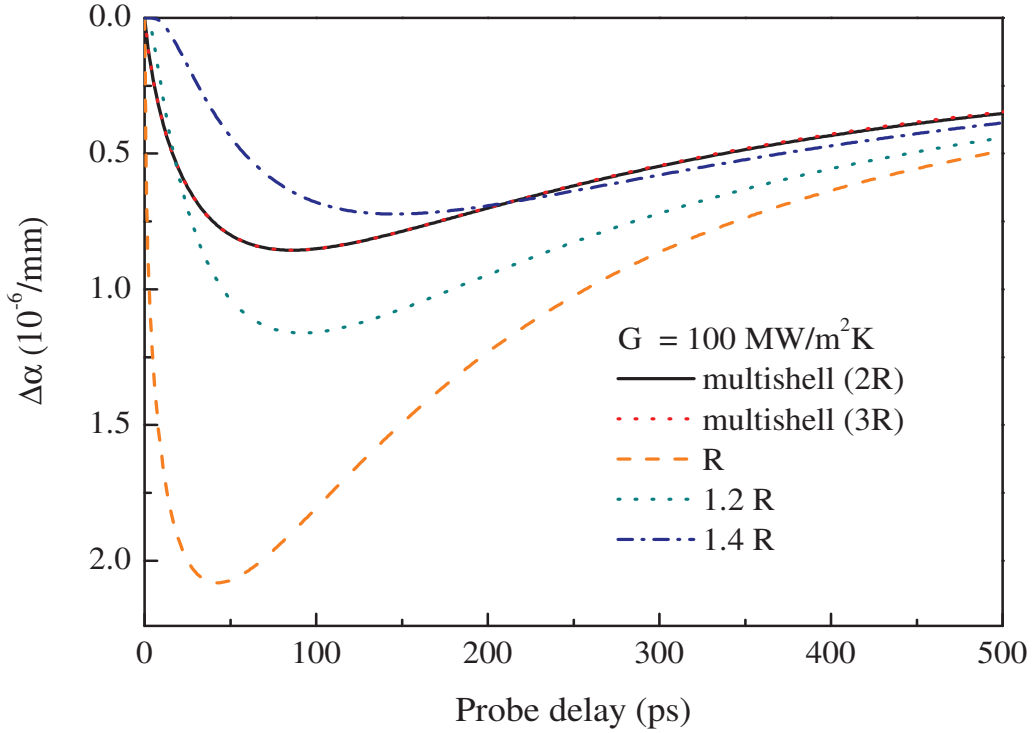


Figure 4.8: Simulated time-dependent contribution of water heating to the absorption change of bare gold particles in water, with interface conductance $G = 100 \text{ MW}/(\text{m}^2 \text{K})$ and $\Delta T_L^0 = 1 \text{ K}$. Solid line: Multishell model (Eq. (4.26)) with shell spacings $a_{sol_i} = 2R \cdot (i/100)^2$ for i from 1 to 100 (distance $2R$ from the particle surface, full black line), and for i from 1 to 122 (distance $3R$ from the particle surface, red dotted line). For comparison contributions using the simplified model (Eq. (4.25)) imposing an effective water temperature corresponding to that of the particle surface $r = R$ (dashed line), or at the positions $r = 1.2R$ (dotted line) and $r = 1.4R$ (dash-dotted line).

convergence of the sum in Eq. (4.26) (see Fig. 4.8). We therefore used this configuration for our investigations.

Fig. 4.8 illustrates the importance of such a decomposition in the case of bare gold particles in water. The contribution of water heating to the optical signal described by Eq. (4.26) and Eq. (4.25) with solvent temperatures $\Delta T_{sol}(R)$, $\Delta T_{sol}(1.2R)$ and $\Delta T_{sol}(1.4R)$ are compared. One can see that even though the amplitude is reproduced for some conditions, the temporal evolution of the multishell response cannot be accurately modeled by simply using a uniform solvent temperature.

4.3.1 Derivatives of the absorption spectra

In Eq. (4.25) we described the simplified out-of-equilibrium response of the composite system of gold-silica core-shell nanoparticles in a transparent solution. The amplitudes A_p , A_S and A_{sol} depend on the derivatives of the linear absorption spectrum $\partial\alpha_{c-s}/(\partial\epsilon_i)$. This can be calculated using Eq. (4.24) and the dielectric constants of gold, fused silica,

and the solvent (water or ethanol) from literature [25, 245–247]. Fig. 4.9 illustrates the

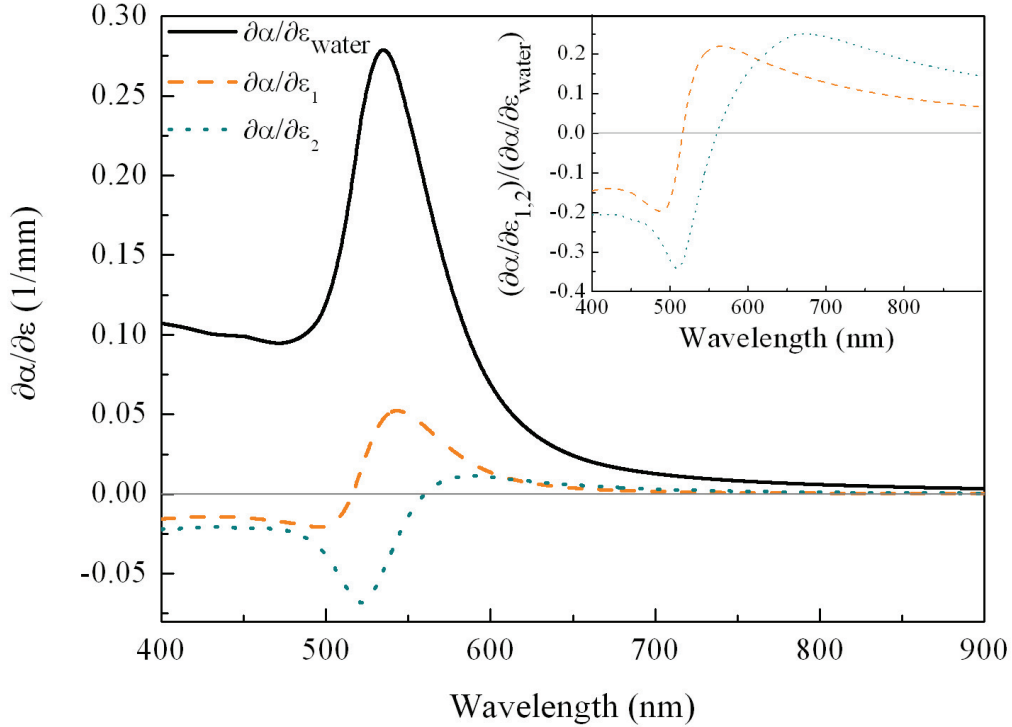


Figure 4.9: Derivatives of the absorption coefficient α with respect to ϵ_{water} (full black line), ϵ_1 (orange dashed line) and ϵ_2 (green dotted line) for $D = 18.5$ nm Au nanospheres in water. Inset: Ratios $(\partial\alpha/\partial\epsilon_1)/(\partial\alpha/\partial\epsilon_{water})$ (orange dashed line) and $(\partial\alpha/\partial\epsilon_2)/(\partial\alpha/\partial\epsilon_{water})$ (green dotted line).

derivatives of the absorption coefficient of bare $D = 18.5$ nm Au nanospheres in water, computed with respect to the real and imaginary parts of the metal dielectric function and the dielectric constant of water. The derivative with respect to ϵ_{water} is strongly enhanced at the position of the surface plasmon resonance of the system (~ 530 nm, see Fig. 4.2), while the derivatives with respect to $\epsilon_{1,2}$ show, as expected [35], a sign change close to the SPR. For more visibility, the ratios of the two quantities are illustrated in the inset of Fig. 4.9. Close to the resonance both ratios are characterized by a minimum while increasing in the red part of the spectrum, where they are less dispersed. This behavior, yielding an important contribution of the solvent to the time-resolved signals at probe wavelengths close to the SPR, is almost independent of the nature of the liquid.

4.3.2 Temperature dependence of the dielectric constants

The temperature variations of the dielectric constants of silica, ethanol and water have been measured in literature [245, 246, 248]. They exhibit an almost undispersed behavior with respect to wavelengths in the visible and IR range, with mean values of $d\epsilon_{silica}/dT_{silica} = 2.9 \times 10^{-5}/\text{K}$, $d\epsilon_{water}/dT_{water} = -2.4 \times 10^{-4}/\text{K}$ and $d\epsilon_{ethanol}/dT_{ethanol} =$

$-1.1 \times 10^{-3}/\text{K}$. This highlights the very different sensitivities of the optical properties of these media to temperature changes, with a stronger optical response for liquids than for solid matrices. The temperature dependence of the gold dielectric function $d\epsilon_1/dT_p$ and $d\epsilon_2/dT_p$ was discussed in detail in Sec. 1.4.2 and the presented experimental results by Cahill et al. (Fig. 1.21) [87] were used for computations.

4.3.3 Contributions of metal, shell and solution to the observed signal

In the simplified picture of Eq. (4.25) the time-resolved response of the different samples can be interpreted in terms of a combination between the distinct responses of gold, silica shell and solvent, the amplitudes A_p , A_S and A_{sol} being deduced from the product of the coefficients $\partial\alpha/\partial\epsilon_i$ and $d\epsilon_i/dT_i$, described in the previous sections. We display in Fig. 4.10

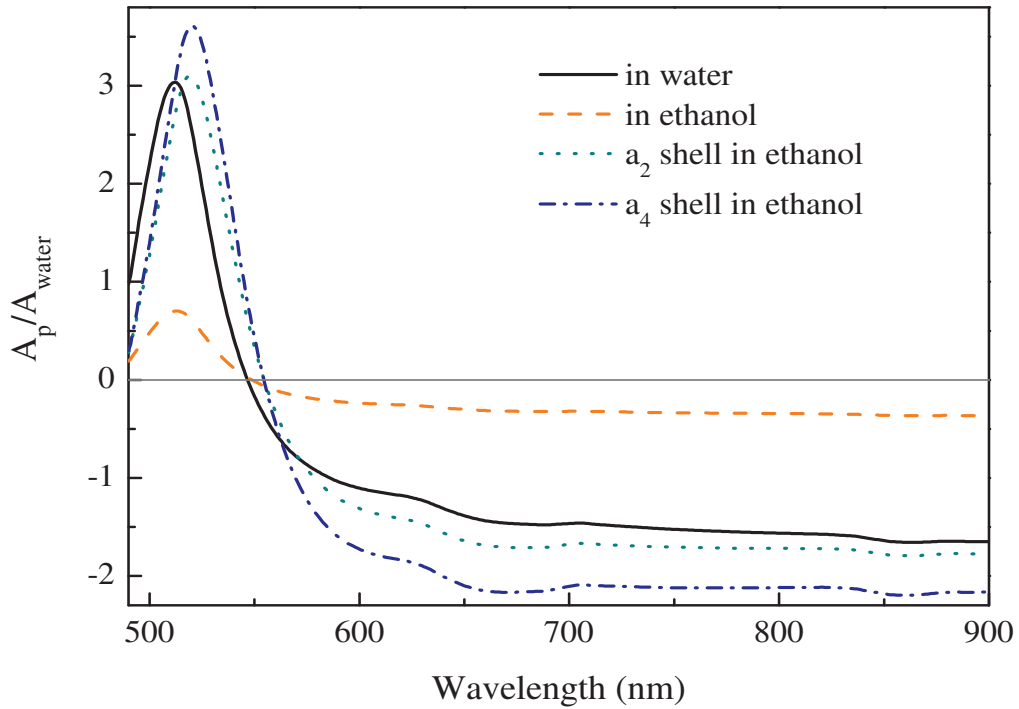


Figure 4.10: Ratio of the metal vs. solvent contribution to optical signals, A_p/A_{sol} , for $D = 18.5$ nm bare gold nanospheres in water (full black line) and ethanol (orange dashed-line) and for gold-silica core-shell particles with shell thicknesses $a_2 = 12.4$ nm (green dotted line) and $a_3 = 18.5$ nm (blue dash-dotted line) in ethanol.

the ratio between contributions of the metal particle and the solvent response A_p/A_{sol} for bare gold nanospheres in water or ethanol, as well as core-shell gold-silica particles in ethanol for two different shell thicknesses. For all systems there is a wavelength for which $A_p = 0$, where the pump-probe response is exclusively produced by the solvent. At shorter

wavelengths, the metal response is amplified on a very small bandwidth (~ 50 nm), which is hard to distinguish in a practical experiment. Towards longer wavelengths, $|A_p/A_{sol}|$ increases until reaching a relatively constant value far from the SPR. For a good reproduction of the optical response of all studied systems, probing in the infrared is therefore preferable as the metal and solvent contributions show little dependence on the specific probe wavelength.

Comparison of the different ratios in the infrared (Fig. 4.10) shows that in the case of Au nanoparticles in a liquid solvent the amplitudes $|A_p|$ and $|A_{sol}|$ are comparable, yielding a non-negligible impact of the liquid to the signal. This effect is much stronger in ethanol than in water, conversely to a glassy environment (e.g. silica shell), where the matrix response can be neglected far from the plasmon resonance due to its small value of $d\epsilon/dT$ (see Sec. 4.3.2) [19].

The dotted and dash-dotted lines in Fig. 4.10 correspond to core-shell nanospheres in ethanol with silica shell thicknesses a_2 and a_3 . They show an increasing amplitude of $|A_p/A_{sol}|$ with increasing shell thickness, yielding a decreasing impact of the solvent. In the following we therefore assume that the solvent response can be neglected for all core-shell samples except for the smallest shell ($a_1 = 3.39$ nm), where one can show that the solvents still impact the absorption change $\Delta\alpha$.

The complete modeling of the time-resolved optical modifications was performed using Eq. (4.26). The resulting relative transmission change $\Delta T/T$ (see Eq. (1.78)), could thus be computed by calculating the time and position-dependent temperature change of the different materials ΔT_p , ΔT_S and ΔT_{sol} of the composite system (Sec. 4.2) and the weighting coefficients in the multi-shell approach A_p , A_{S_i} and A_{sol_i} .

4.4 Results

4.4.1 Thermal conductance at gold-liquid interfaces

The models for the temperature dynamics and their impact on the optical response of the samples, developed in the previous sections, allow a quantitative analysis of the experimental results. We report here for the first time the extraction of the thermal interface conductance G of colloidal metal nanoparticles taking into account heat transfer in all parts of the system.

For spherical bare gold nanoparticles in water and ethanol, the full model (Eq. (4.26)) has been used to describe the transient absorption signal as a sum of metal and solution response, taking into account the temperature distribution of the liquid. Figs. 4.11(a) and 4.11(b) show the experimental signals obtained for gold nanospheres in water and ethanol for a probe wavelength of 820 nm, thus far from the surface plasmon resonance. In

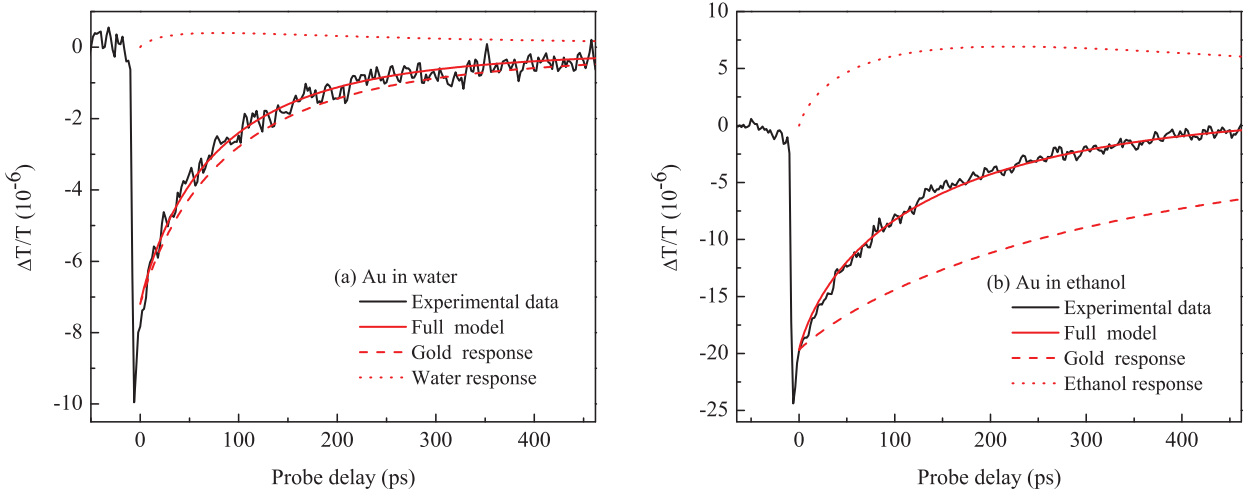


Figure 4.11: Experimental (full black line) and simulated (full red line, Eq. (4.26)) time-resolved transient transmission change for bare $D = 18.5$ nm gold nanospheres in water (a) and ethanol (b) ($\lambda_p = 540$ nm, $\lambda_{pr} = 820$ nm and $F \approx 40 \mu\text{J}/\text{cm}^2$). The gold (red dashed line) and solvent (red dotted line) contributions to the simulated signal are also shown.

order to model the long delay decay of the signal, a χ^2 minimization procedure has been performed with two free parameters, namely the thermal interface conductance G and a general amplitude A , the latter being necessary due to uncertainties in the initial heating and concentration of the sample. Besides the result of the fitting procedure (full red line in Figs. 4.11(a) and 4.11(b)), we also plotted the dynamics of the respective contributions of gold and solvent. As expected, the solvent contribution to the full signal is not negligible, its amplitude being significantly larger for ethanol than for water, due to the larger temperature dependence of its refractive index (see Sec. 4.3.2).

A very good agreement between experimental data and simulated signals could be obtained for both solvents (Figs. 4.11(a) and 4.11(b)), using the following interface conductance values for the gold-water and gold-ethanol interfaces, respectively:

$$G_{Au-H_2O} = (113 \pm 10) \frac{MW}{m^2 K} \quad G_{Au-EtOH} = (40 \pm 10) \frac{MW}{m^2 K}. \quad (4.27)$$

For comparison, we also fitted the signals assuming proportionality to the metal excess temperature ΔT_p only. Only the experimental data for bare gold in water could be reproduced with this simplified model, yielding however a different value for the thermal conductance $\tilde{G}_{Au-H_2O} \approx 175 \text{ MW}/(\text{m}^2 \text{ K})$. This turned out to be not possible for the description of the kinetics of gold nanospheres in ethanol, no value of $\tilde{G}_{Au-EtOH}$ leading to a good reproduction of the experimental signals. In the present experimental configuration (infrared probing), the contributions of metal and solvent have opposite signs (see Fig. 4.10) which leads to an acceleration of the decay of the time-resolved signals. G is

thus easily overestimated if the solvent contribution is not taken into account. Note that this effect is larger for an ethanol solvent than a water one, compensating for a slower heat evacuation in ethanol, which leads to almost similar experimental signals in Figs. 4.11(a) and 4.11(b).

The value of G_{Au-H_2O} (113 MW/(m² K)) is in very good agreement with the extracted value for the gold-water interface conductance in Ref. [226](105 MW/(m² K)), where X-rays have been used to probe G , whereas it is slightly smaller compared to other optical pump-probe experiments [217, 218, 222, 224]. The interface conductance obtained without consideration of the water temperature dynamics, \tilde{G}_{Au-H_2O} , is in better agreement with these literature values, which confirms the presumption that values in the past were slightly misleading due to the common assumption of signal linearity to the particle temperature. Changing the solvent to ethanol decreases the interface conductance $G_{Au-EtOH}$ (40 MW/(m² K)) as compared to water, which is the same trend as in previous studies on metal nanoparticles in organic solvents [220, 223]. However, in this work, Au nanoparticles in water and ethanol were stabilized with different surfactants (see Sec. 4.1.1), and values for the two samples should thus be compared with caution.

4.4.2 Probe wavelength-dependent optical response

We measured the time-resolved signals of bare gold nanospheres in ethanol for different probe wavelengths. The setup allowed to keep a constant pump beam of 410 nm, and to change the wavelength of the probe beam independently. Fig. 4.12 represents the experimental data together with the simulated signals, using again the full model with similar parameters as in Sec. 4.4.1. The sample response consists of the sum of metal and solvent contributions, which are shown as well. All experiments were reproduced using the interface conductance $G_{Au-EtOH}$ extracted with the 820 nm probe within the given error bars (Fig. 4.11(b) and Eq. (4.27)). To include possible uncertainties in the probe wavelength, as well as small shifts in the position of the sample SPR, due to nanoparticle size and morphology dispersion, a variation of the probe wavelength of 5 nm at most to the blue or red was allowed for the simulations. A very good reproduction of the signals is obtained for all probe wavelengths larger than 540 nm. In this region, the optical response of metal and solvent feature opposite signs, leading to a fast decrease of the signals for probe wavelengths in the IR, as observable at 820 nm (Fig. 4.11(b)) or 600 nm (Fig. 4.12(a)). With decreasing wavelength, the ethanol contribution becomes more important, yielding a sign change in the transient signals as observable for probe wavelengths at 560 nm (Fig. 4.12(b)) and 550 nm (Fig. 4.12(c)). The simulation of the signals is less precise at 530 nm (Fig. 4.12(e)), this wavelength being very close to the position of the SPR of the

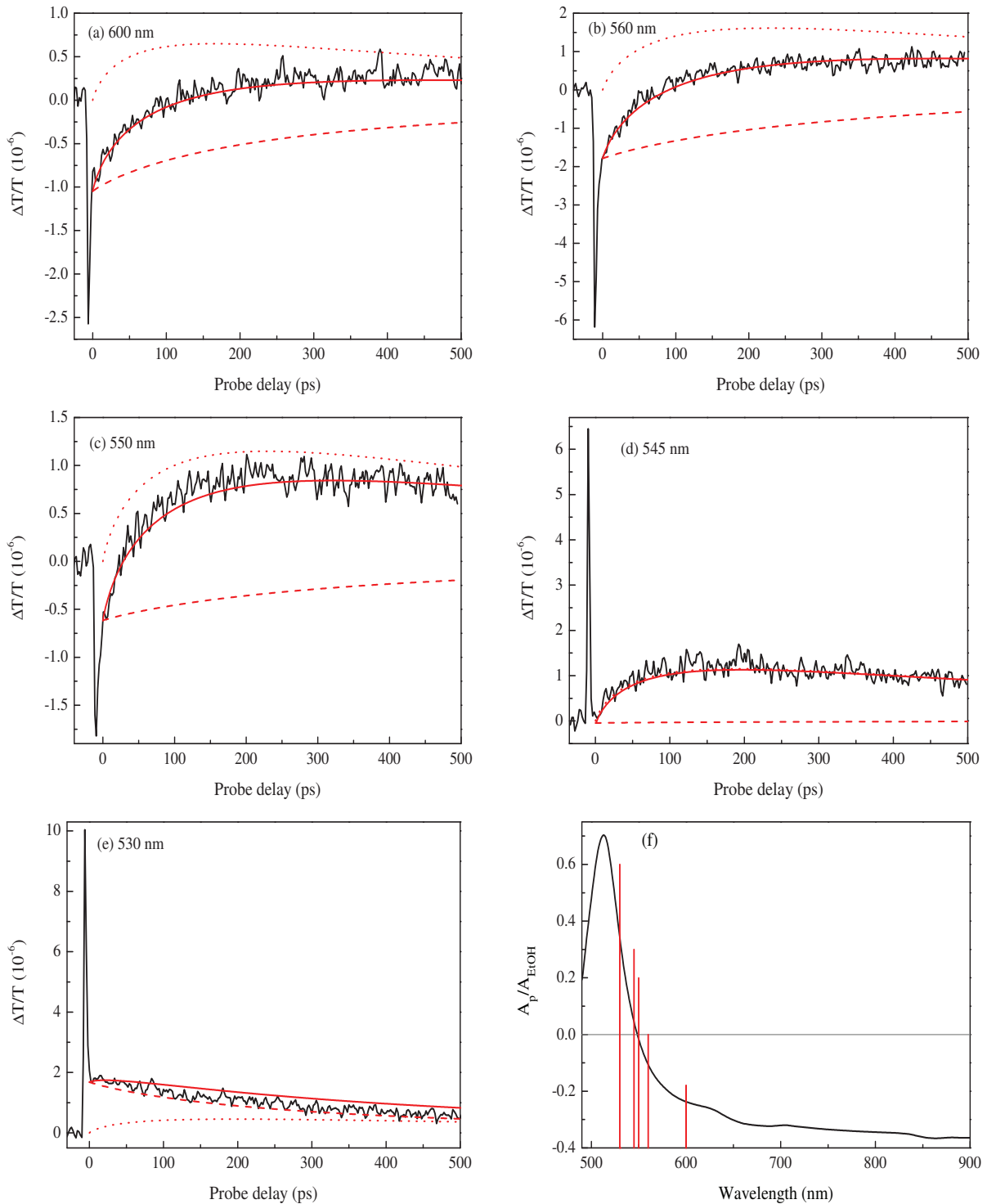


Figure 4.12: Pump-probe relative transmission change $\Delta T/T$ of bare gold nanoparticles ($D = 18.5$ nm) in ethanol at probe wavelengths 600 nm (a), 560 nm (b), 550 nm (c), 545 nm (d) and 530 nm (e). Experimental data (full black line), simulated full response (full red line), also decomposed into its distinct gold (red dashed line) and ethanol contributions (red dotted line). For all signals the pump wavelength was tuned to 410 nm and $F \approx 20 \mu\text{J}/\text{cm}^2$. (f) A_p/A_{EtOH} ratio (see Sec. 4.3.3) and positions of chosen probe wavelengths (red vertical lines).

system. The optical response is hence extremely sensitive to the exact position of the resonance peak as well as its width, due to the derivatives of the absorption spectrum with respect to the dielectric constants (Fig. 4.9). As in this model we did not introduce any nanoparticle size or shape dispersion, uncertainties in the proportion between particle and solvent response remain in this wavelength range. Most probably at $\lambda_{pr} = 530$ nm we overestimate the contribution of ethanol to the signal, the metal contribution (red dashed line in Fig. 4.12(e)) being in better agreement with experiment than the full response.

An important effect is observable at 545 nm (Fig. 4.12(d)). For this wavelength A_p (Fig. 4.12(f)) vanishes, which is equivalent to no contribution of the gold particle to the transient $\Delta T/T$. The long decay response of the signal is thus exclusively ascribed to the consecutive heating and heat evacuation in ethanol.

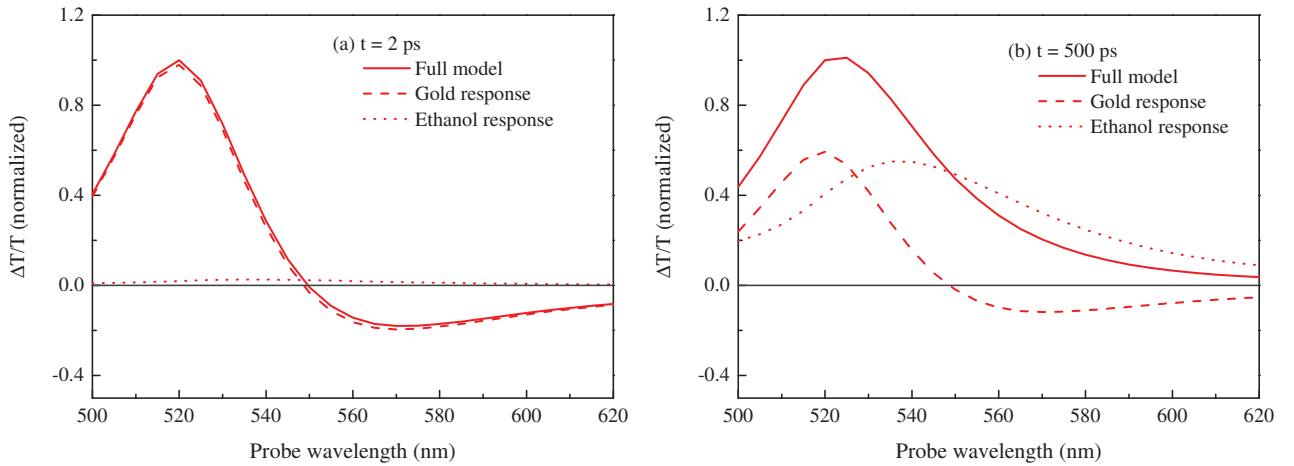


Figure 4.13: Simulated (simulated line) normalized transient transmission change ($G = 40 \text{ MW}/(\text{m}^2 \text{ K})$) for bare Au nanoparticles in water as a function of probe wavelength for a probe delay of 2 ps (a) and 500 ps (b). Red dashed and dotted lines correspond to the gold and ethanol contribution to the signal, respectively.

The probe wavelength dependence of time-resolved experiments is more explicit in Figs. 4.13(a) and 4.13(b), where the simulated normalized transmission change and the separated gold and ethanol contributions are plotted for two fixed time delays ($G = 40 \text{ MW}/(\text{m}^2 \text{ K})$). Because of the time necessary for the solvent to heat, the contribution of ethanol is weak for a short time delay (Fig. 4.13(a), 2 ps). For a longer time delay (Fig. 4.13(b), 500 ps) its amplitude becomes of the same order as the one of gold. The metal response features a sign change around 545 nm, independently of the time delay as discussed in Sec. 4.4.2. This wavelength, for which the metal contribution vanishes, is therefore experimentally identifiable by a vanishing pump-probe signal for short time delays, as shown in Fig. 4.12(d). Directly measuring the cooling dynamics of the solvent allows a more explicit estimation of the interface conductance G . The position of this wavelength being predictable, this

determination could be exploited for metal nanoparticles in different environments, provided that their dielectric function strongly varies with temperature.

In order to identify the same kind of signal for bare gold particles in water, we slightly varied the probe wavelength around 545 nm, accounting for small differences in the absorption spectrum of nanospheres in water and ethanol (Fig. 4.14). For a probe wavelength of

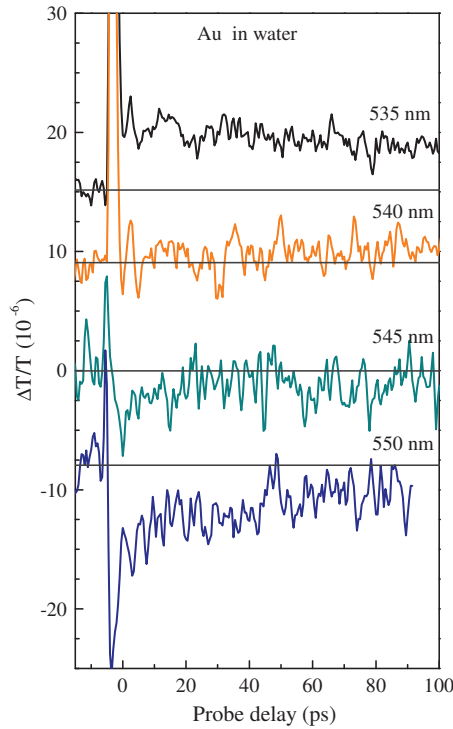


Figure 4.14: Time-resolved long delay relative transmission change for gold particles in water (same conditions as in Fig. 4.13, $\lambda_p = 410$ nm and $F \approx 20$ $\mu\text{J}/\text{cm}^2$). The probe wavelength varies from 535 to 550 nm while pump power and other experimental parameters are similar for all signals. The signals are vertically translated for clarity, their vertical zero position being indicated by a horizontal line.

540 nm, the signal (after the strong peak which corresponds to the metal particle excitation and internal thermalization) vanishes, whereas for the other wavelengths the signal is negative or positive with a slow decay. The wavelength for which the metal part does not contribute to the time-resolved signals has thus shifted from 545 nm to 540 nm for the sample in water. This slight shift is due to the slightly shifted position of the surface plasmon resonance with changing solvent. This is less pronounced in the linear absorption spectra (Fig. 4.2, inset) but becomes clear in the more sensitive ultrafast experiment.

While in the case of bare Au nanoparticles in ethanol, after an initially flat signal one could observe a rise and a subsequent decay corresponding to solvent heating and cooling, we could not observe this structure for water whose optical constant is around ten times less sensitive to heating than the one of ethanol (see Sec. 4.3.2). In the present experimental setup, the signal associated to water is therefore not detectable, the signal to noise ratio being too small.

4.4.3 Thermal conductance at gold-silica and silica-liquid interfaces

In this section the transient transmission signals of gold-silica core-shell particles in water and ethanol are investigated in order to determine the thermal interface conductances G_{Au-S} , G_{S-H_2O} and G_{S-EtOH} at the metal-silica and silica-solvent interfaces, respectively. While experiments have previously been performed on solid-dielectric interfaces [216, 221, 227, 228], to our knowledge no experimental study identifying values for the interface conductances of core-shell nanoparticles has been done by now. The silica-liquid interface is difficult to address experimentally. Both materials being transparent, optical experiments which are most adapted for thermal interface conductance measurements cannot be performed directly and have to be done via excitation of an absorbing medium (Au core here). Experimental values of G for the silica-water and silica-ethanol interfaces are not available.

In contrast to the bare gold particles diluted in a liquid, we now have to treat two interfaces using the equations of Sec. 4.2.3 which allow the determination of ΔT_p , ΔT_S and ΔT_{sol} . Furthermore, even though thermal conductance and volumetric heat capacity of fused silica are well known (see Table 4.1), these quantities can deviate from tabulated values for silica prepared by Stöber method, due to possible porosity. Before discussing the determination of the thermal conductances of the core-shell-solvent interfaces, we first have to analyze the extent of silica porosity in our samples and give an estimation of its impact on the thermal parameters of the silica shells.

4.4.3.a Estimation of the silica porosity

For silica particles synthesized by Stöber method [232], densities have been experimentally observed in the range of 2000 kg/m^3 [249] which is smaller than the value of bulk fused silica (see Table 4.1). Experiments were principally performed on dried particles and the lowered density has been explained by a microporosity of the samples [250]. An estimation of 10-15 % of porosity [251] for silica spheres of a diameter of 80 nm is in good agreement with the measured density. In solution one could imagine an important liquid penetration in the porous silica shell [220], an assumption supported by Refs. [252] and [253] which found water to penetration into small channels of the porous silica.

Porosity and/or liquid penetration is expected to impact the thermal properties of the silica shells, as well as their optical constants derivatives with respect to the temperature. In order to characterize the thermal behavior of silica shells and exclude an important solvent penetration we performed a series of pump-probe experiments varying the probe wavelength around 545 nm for the nanospheres with the thickest silica shells $a_4 = 25.7 \text{ nm}$ (see Sec. 4.1.1) in ethanol, as in this spectral range the contribution of metal to the signal

vanishes (see discussion in the previous section). Fig. 4.15 illustrates the results for the samples in ethanol. An initially vanishing signal is obtained for a probe wavelength of

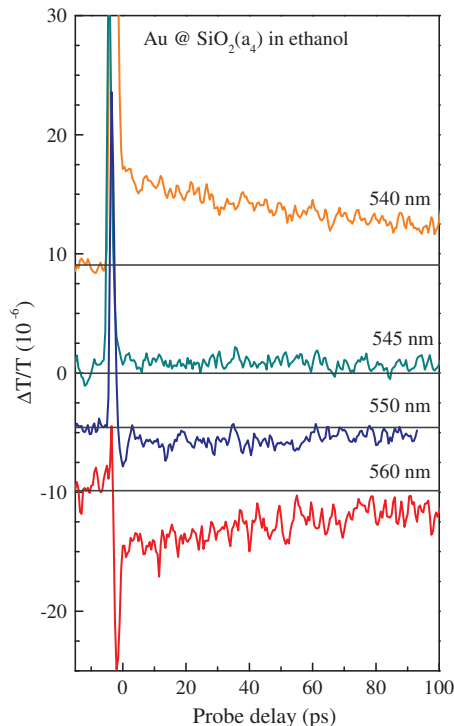


Figure 4.15: Time-resolved long delay relative transmission change for core-shell gold-silica nanospheres ($a_4 = 25.7$ nm) in ethanol. The pump wavelength is set to 410 nm ($F \approx 20 \mu\text{J}/\text{cm}^2$, similar to Fig. 4.14) while the probe wavelength varies around 545 nm.

545 nm, proving that at this wavelength the optical response is insensitive to the temperature of the gold particle. The signal remains flat for longer delays, hence the sensitivity of the optical constant of the shell to temperature increase is too small to be detected in the experiment. This was not the case for bare gold particles in ethanol (see Sec. 4.4.2) and we can, as a consequence, exclude an important liquid penetration in the silica shells (at least for thickest ones).

In the following we will impose 10% (volumic fraction) of solvent penetration in the shells, consistent with measurements on density and porosity of silica synthesized by the Stöber method and our experiment. The volumetric heat capacity c is then estimated as the arithmetic mean of the constituent materials, which leads to:

$$c_{S-H_2O} = 0.9c_S + 0.1c_{H_2O} = 1.77 \times 10^6 \frac{J}{m^3K},$$

$$c_{S-EtOH} = 0.9c_S + 0.1c_{EtOH} = 1.54 \times 10^6 \frac{J}{m^3K},$$
(4.28)

with c_{S-H_2O} the volumetric heat capacity of silica shells in water, c_{S-EtOH} the one of silica shells in ethanol and c_S , c_{H_2O} and c_{EtOH} the tabulated (see Table 4.1) volumetric heat capacities of the respective constituents (fused silica, water and ethanol). In contrast to the heat capacity, the thermal conductivity is not expected to be proportional to the amount of solvent penetration, as it depends in general on the detailed structure of the pores [254] and can strongly differ from the averaged value of the conductivity of the constituents. For these reasons, the thermal conductivity of silica in water Λ_{S-H_2O} and ethanol Λ_{S-EtOH} were left as free parameters.

4.4.3.b Estimation of interface conductances

To limit the quantity of free parameters for a given signal, in a first step we consider the pump-probe measurements on the samples with the thickest silica shell a_4 . In this case, the effect on the dynamics of the second interface conductance is negligible and the system is equivalent to gold particles in an infinite porous silica matrix. It is noteworthy that the remaining free parameters, namely the conductance at the first interface and silica thermal conductivity can be separately determined as they act on different timescales. In Figs. 4.16(a) and 4.16(b) we present the transient transmission signal (P/Pr 540/820 nm) for the core-shell nanoparticles in water and ethanol, respectively. As mentioned before,

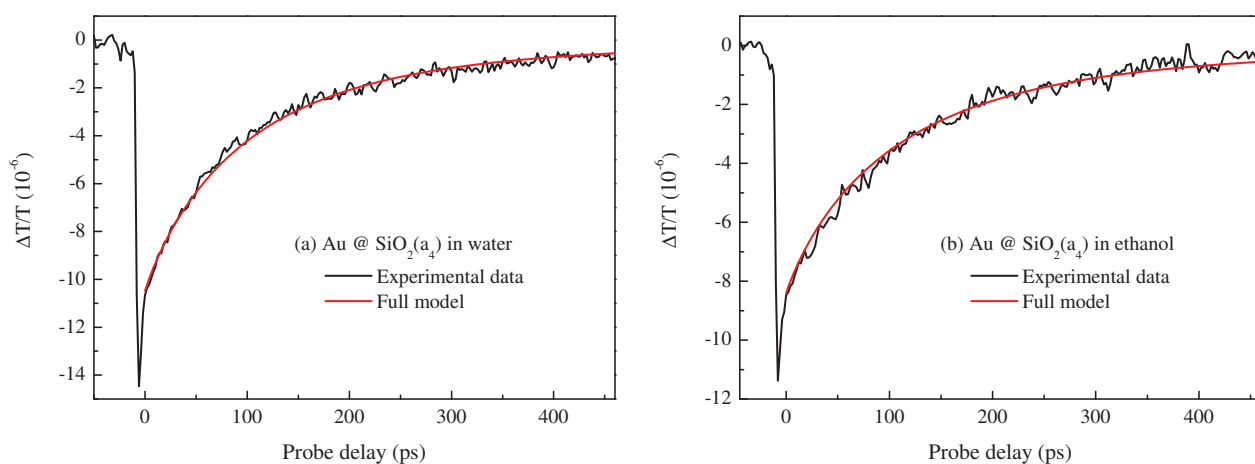


Figure 4.16: Experimental ($\lambda_p = 540$ nm, $\lambda_{pr} = 820$ nm and $F \approx 40 \mu\text{J}/\text{cm}^2$), full black line) and simulated (full red line) pump-probe signals for core-shell gold-silica nanospheres ($D = 18.5$ nm, $a_4 = 25.7$ nm) in water (a) and ethanol (b). Red dashed and dotted lines show the gold and solution contributions, respectively.

these signals are proportional to the metal temperature because of the poor sensitivity of the silica dielectric constant to heating, and the large distance between the solvent and the metal (see Sec. 4.3.3). This accounts for all shell thicknesses except the thinnest one (a_1).

Chapter 4. Thermal relaxation of colloidal gold and gold-silica nanospheres

In order to fit the experimental results, a similar metal-silica thermal interface conductance G_{Au-S} for the particles in water and ethanol was imposed, assuming identical surface conditions. However, an influence of solvent penetration on the thermal conductivity of the shells was considered. The best reproduction of the experimental signals could be obtained with:

$$G_{Au-S} = (104 \pm 20) \frac{MW}{m^2K} \quad \Lambda_{S-H_2O} = 0.9 \frac{W}{mK} \quad \Lambda_{S-EtOH} = 0.73 \frac{W}{mK}. \quad (4.29)$$

The values of the thermal conductivities are around 35% and 45% lower than the one of fused silica (Table 4.1), for the samples immersed in water and ethanol, respectively. This is in good agreement with solvent penetration in the shell, the conductivities of both water and ethanol being smaller than the one of tabulated silica. Furthermore $\Lambda_{S-EtOH} < \Lambda_{S-H_2O}$ featuring the same trend as the conductivities of the two solvents. The thermal conductance at the gold-silica interface is in the same range as the values determined for the gold-water interface before (see Sec. 4.4.1). It is also in good agreement with Ref. [19] (Au-glassy matrix), where similar experimental conditions were used. The discrepancy with other values of G for metal-dielectric interfaces [216, 221, 227, 228] can most probably be explained by the high sensitivity to the precise surface conditions and to the detailed structure of the gold and silica components, as was shown in Ref. [228].

In the following, these values were used for analysis of time-resolved signals with thinner shells in order to determine the conductances at the silica-liquid interfaces G_{S-H_2O} and G_{S-EtOH} , which are the only free parameters left (apart from a multiplying factor for the global amplitude). The samples whose thermal dynamics are most sensitive to the second interface are the ones with the thinnest shell a_1 . Figs. 4.17(a) and 4.17(b) display the corresponding pump-probe signals (same experimental conditions as before) for the two solvents, water and ethanol, along with the respective fits. Here, the ethanol response was included for a good reproduction of the signal (Fig. 4.17(b)), whereas the response of water could be neglected. In contrast to the other investigated interfaces involving metal-liquid or metal-dielectric boundaries, the thermal conductances at the insulator-liquid interfaces were considerably higher. The results from the respective fits revealed:

$$G_{S-H_2O} > 1000 \frac{MW}{m^2K} \quad G_{S-EtOH} = (300 \pm 150) \frac{MW}{m^2K}. \quad (4.30)$$

Only the long delay part of the signals reflects heat evacuation at the second interface. The sensitivity of the fit to this parameter is thus lowered, resulting in important error bars. Especially for the sample in water, only a lower limit of G_{S-H_2O} can be extracted (Fig. 4.17(a)), the fit function varying only slightly for the relatively high interface conductance. For both silica-liquid interfaces, the large conductances are in qualitative

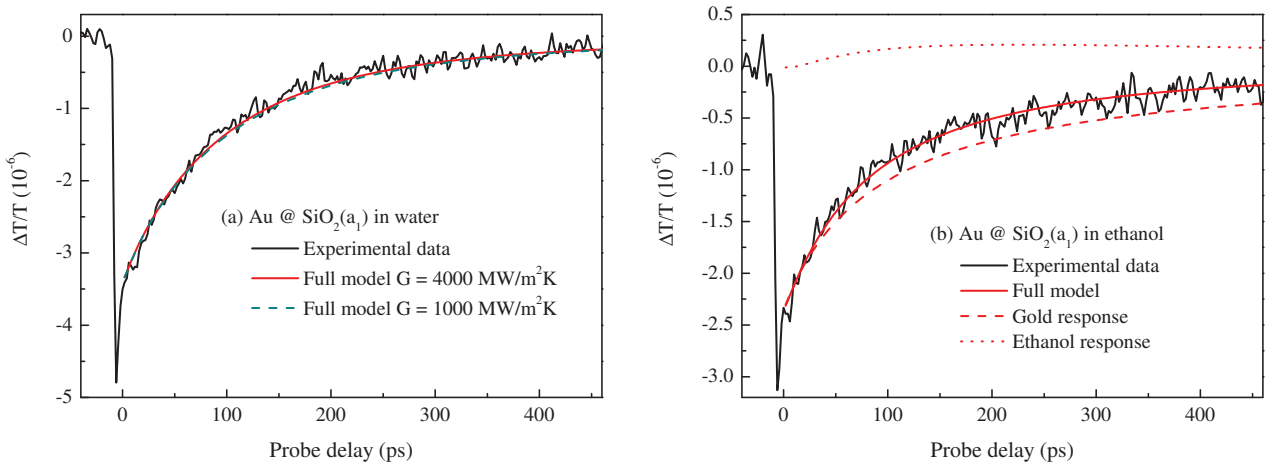


Figure 4.17: Experimental (full black line) transient transmission signals for core-shell gold-silica nanospheres (a_1) in water (a) and ethanol (b), with $\lambda_p = 540$ nm, $\lambda_{pr} = 820$ nm and $F \approx 40$ $\mu\text{J}/\text{cm}^2$ (similar to Figs. 4.16(a) and 4.16(b)). Full red lines correspond to simulated signals for the optimal value of G at the silica-liquid interface, red dashed and dotted lines in (b) describe metal and solvent contributions respectively, green dotted line in (a) is a simulated signal for the lower limit of G .

agreement with molecular dynamics predictions [255, 256]. However, the output of these calculations depending on the algorithm, as well as the chosen parameters of the adjacent liquid layer (interaction strength, wetting angle, polarisability [257]) and the surface conditions (roughness [258], surface functionalization [259],...), a direct comparison with the experiment is delicate.

The thermal interface conductances at the interfaces of the core-shell system, gold-silica and silica-liquid, could thus be estimated via optical pump and probe spectroscopy, albeit with important error bars. These results have been confirmed by the signals of the samples with intermediate shell thicknesses, a_2 and a_3 , which could be reproduced with the same values for interface conductances and thermal conductivity.

4.4.4 Comparison to photoacoustic experiments

The investigations performed to study heat transfer and thermal interface conductances may be exploited to yield information on photoacoustic experiments performed on similar samples [229, 230]. In the last decade, photoacoustic imaging has shown up as a non-invasive diagnostic tool for visualizing biological tissues, through the detection of acoustic waves produced by thermal expansion of tissues absorbing a laser pulse [260]. In this context, the introduction of gold in the medium has shown to be a good contrast agent to enhance photoacoustic signals [229, 230]. In particular, silica coating (0, 18 and 38 nm) of $D = 26$ nm Au nanospheres in aqueous solution led to an increase of the photoacoustic signal which was most pronounced for the thicker shells [230]. The authors suggested an

effective conductance for the gold-silica and silica-water interfaces which would be higher than the bare gold-water one. As a consequence they concluded that heat transfer to the liquid surrounding of the nanoparticles would be more efficient.

From our experiments, we have shown that the interface conductances G_{Au-S} and G_{Au-H_2O} are of the same order. The amount of heat transferred from gold to water and from gold to silica is thus comparable. For a core-shell particle, heat diffuses additionally in the silica shell, and is subsequently transferred to water through an interface with very low thermal resistance ($G_{S-H_2O} \gg G_{Au-S}$). The effective conductance at the surface of the nanospheres is thus definitely smaller for bare Au nanospheres than for core-shell Au-silica nanoparticles (due to diffusion). However, for the experimentally measured thermal parameters, we can compare the water temperature for bare and core-shell particles at a fixed position in the liquid. In Fig. 4.18(a) we show the calculated excess temperature of water for bare

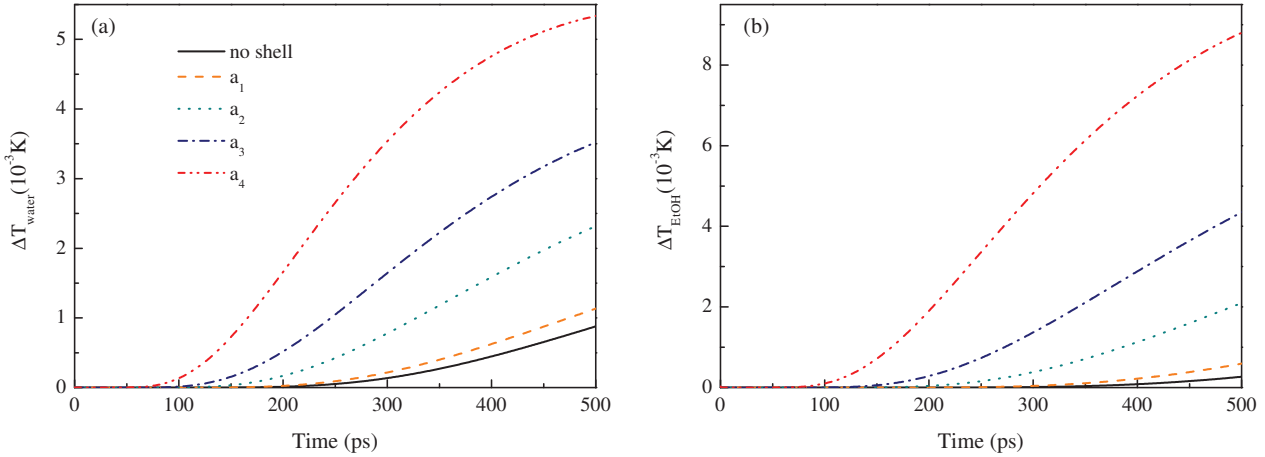


Figure 4.18: Calculated excess temperature of water (a) and ethanol (b) for $D = 18.5$ nm Au nanospheres, bare or coated with silica shells of different thicknesses (a_1, a_2, a_3, a_4) in the corresponding solvent. The initial heating of the gold core was 1 K, the temperature was calculated at a distance of $2D$ from the origin, i.e. ~ 33.5 nm to ~ 11.5 nm far from the external shell of the core-shell particles. Interface conductance and thermal parameters were taken from Secs. 4.4.1 and 4.4.3.b if given and from Table 4.1 otherwise.

gold or core-shell particles (shell thicknesses a_1, a_2, a_3, a_4) at a fixed distance of $2D$ from the particles origin, after initial heating of the metal core of 1 K using the experimental interface conductances and thermal conductivities from Secs. 4.4.1 and 4.4.3.b. Fig. 4.18(a) shows that heating of water at a fixed distance is more efficient with the addition of a silica shell. Furthermore, this effect is stronger for thicker shells, as observed in photoacoustic experiments [229].

The two main reasons for that are related to the different mechanisms governing heat transfer in the systems. Firstly, the thermal conductance G_{S-H_2O} is very high, allowing a very good heat transfer at the silica-water interface: there is almost no loss compared to

the bare particles which have only one interface. Secondly, the thermal diffusivity $\kappa = \Lambda/c$ is larger in porous silica than in water yielding thus more efficient heat conductivity in the shell. The same behavior can also be observed for ethanol (Fig. 4.18(b)), even though G_{S-EtOH} is smaller.

More detailed investigations could be useful to quantitatively interpret these photoacoustic experiments, as a function of different experimental conditions, as the nature of nanoobjects and solvents [230].

4.5 Summary and conclusion

Using time-resolved pump-probe spectroscopy the kinetics of bare gold and silica coated core-shell nanospheres in water and ethanol have been analyzed. As a consequence of a rigorous analysis of both the temperature dynamics in metal, silica and liquid and their impact on the optical properties of the samples, the probe wavelength-dependent dynamics of the time-resolved signals could be quantitatively reproduced. Values for the thermal conductances at gold-liquid, gold-silica and silica-liquid interfaces could subsequently be extracted (Table 4.2).

Table 4.2: Experimental results for G and approximated acoustic mismatch Z_1/Z_2 for the different interfaces. Thermal parameters have been taken from Table 4.1, describing the nanoparticle shells with fused silica.

	Au-H ₂ O	Au-EtOH	Au-S	S-H ₂ O	S-EtOH
G (MW/(m ² K))	113	40	104	> 1000	300
Z_1/Z_2	42	68	4.8	8.8	14

Thermal conductance between solids has often been described by the acoustic mismatch model [214]. The parameter determining the interface conductance is approximately characterized by the acoustic impedance mismatch of the materials on the two sides of the interface Z_1/Z_2 (see Sec. 4.2.1). In Ref. [19], systematic studies of the interface conductance G between metal nanoparticles and glass matrices have been performed and a linear dependence with the acoustic mismatch was found. The determined value of G_{Au-S} and its acoustic mismatch (Table 4.2) are in good agreement with these previous measurements. However, the conductances deduced for solid-liquid interfaces do not agree with this linearity relation. Possibly specific effects of solid/liquid interfaces (e.g. viscosity, presence of surfactants,...), as well as diffuse scattering at the boundary has to be considered.

The simple models of AMM and DMM are not adequate for a global description of different types of interfaces e.g. metal-liquid and dielectric-liquid. Even though the AMM predicts some trends of our measurements, namely a higher conductance for silica-liquid interfaces (due to lower mismatch) than gold-liquid interfaces and higher conductance for

Chapter 4. Thermal relaxation of colloidal gold and gold-silica nanospheres

the liquid interfaces involving water compared to ethanol, it predicts the highest conductance for the metal-silica interface, which has not been demonstrated experimentally. One must not forget that the mechanisms for heat transfer in liquids, dielectrics and metals can be very different (e.g. electronic contributions when metals are involved). For a better reproduction of the different G , more sophisticated models should thus be developed in the future, including also the exact density of states of the different phonon modes. Finally, the measured interface conductances do not only depend on the nature of the materials but also on their stabilizing surfactant molecules. Systematic studies of the parameters influencing heat transfer at interfaces, e.g. coupling of the stabilizing groups at the interfaces, as well as heat propagation along those molecules would be of large fundamental and technological interest.

Conclusion

In this work the ultrafast dynamic processes in noble metal nanoparticles and clusters were studied by time-resolved optical spectroscopy. Electron-electron and electron-lattice interactions, acoustic vibrations and thermal relaxation in metal and hybrid nanoobjects were investigated.

Chapter 2 describes the effects of size reduction on noble metal nanospheres from the few nanometer range to the sub-nanometer range. For this purpose, the electronic interactions in surfactant-free glass-embedded silver clusters (1.1 - 3 nm diameter) and thiol-stabilized gold clusters (25 atoms - 3.5 nm diameter) in solution were investigated via the characterization of their electron gas thermalization and electron-lattice energy transfer times, and their transient absorption spectra. Results for silver nanoparticles could be more precisely interpreted, as these samples constitute less complex systems, due to their optical properties (e.g. interband transitions well separated from the surface plasmon resonance) and to the absence of stabilizing surfactant molecules. For these systems, an increase of the electron-electron and electron-lattice characteristic times with decreasing size was determined for particles smaller than around 2.3 nm, in stark contrast to larger nanoparticles, where a decrease was previously observed. Additionally, an unpredicted spectral shift of their transient absorption spectra occurred. The “small solid” model was not sufficient to explain these modifications and we therefore ascribed them to changes in the electronic energy structure. This onset of quantization effects could be confirmed by simple quantum calculations for electrons confined in a box.

Quantum effects also strongly affected the response of gold clusters, due to their small sizes (down to 25 atoms). Their linear absorption spectra showed strong modifications in the 25-144 Au atom range, which were ascribed to the appearance of molecular-like optical transitions. Modifications in the transient spectra could be correlated to these transitions. The observation of precise characteristic times and their attribution to explicit physical processes appeared to be more complex than in the case of the silver samples. However, similar trends for the characteristic times in the sample consisting of 144 atoms ($D \approx 1.7$ nm) and the small silver samples ($D \approx 2$ nm) compared to larger nanoparticles could be observed, and the onset of the observation of electron energy discretization effects could thus be ascribed to this size. In the future, experimental measurements dis-

Conclusion

criminating the effects of size reduction from other parameters, i.e. surfactant molecules, synthesis method and metal properties (Au vs. Ag), could be done by using different samples, e.g. surfactant-free gold or chemically synthesized silver clusters. Additionally, theoretical work characterizing electronic interactions in more detail is necessary. In this context, a quantum model describing electron-phonon interactions by taking into account the density of electronic states and phonons is currently under development.

The transition from a bulk-like to a molecular-like behavior observed for electronic dynamical properties of metal nanoparticles in the 2 nm size range was in contrast to the experimental observations of their mechanical properties (acoustic vibrations), presented in Chapter 3. Here, size reduction showed few modifications to the diameter-dependent scaling law of the breathing mode periods of thiol-stabilized gold clusters, down to samples consisting of only 25 Au atoms. These could be predicted by classical continuum mechanics, and were also in agreement with atomistic simulations. However, an additional longer vibrational mode was observed, its physical origin still being unclear. Additional theoretical work extending the available computations of the breathing-like vibrational periods could bring more insight into the excitation and detection mechanisms of the different vibrations in these clusters.

The effect of combining two metals was investigated on small (2-3 nm) core-shell Pt/Au and Ni/Ag nanospheres and larger alloyed or core-shell (~ 30 nm) Au-Ag nanoparticles. Measurement of the breathing mode period allowed the experimental discrimination of the structure of the particles (alloy, core/shell, shell/core) in the case of the Pt/Au and Au-Ag samples. Conversely, the morphology suggested for the Ni/Ag core/shell clusters by comparing the measured breathing mode period with elastic modeling was more consistent with a silver core structure, being therefore unexpected. Further analysis of acoustic properties on samples with other compositions or materials, together with an accurate morphology characterization, would be of large interest.

Chapter 4 was devoted to the heat transfer mechanisms between metal nanoparticles and their environment. These were studied on bare and silica-coated gold nanospheres ($D \sim 20$ nm) in a solvent (water or ethanol). The time-resolved measurements were analyzed with a quantitative approach, describing the time and position-dependent temperature increases in metal, silica and solvent and modeling the impact of heating of all parts of this system on the optical pump-probe signal. Due to the temperature sensitivity of the dielectric constants of water and ethanol, a solvent contribution to the signal was found for bare nanoparticles. This was very pronounced in ethanol, where probe-wavelength dependent measurements could be realized, quantifying the relative amplitude of the metal and solvent contributions to the signal. An interesting effect was found for probe wavelengths close to the surface plasmon resonance, where the signal was proportional to solvent temperature, with vanishing contribution of the heated gold nanoparticle.

This effect could be exploited for future local and ultrafast temperature measurements. This detailed description allowed the extraction of reliable values for the interface thermal conductance, a crucial parameter ruling heat transfer at the nanoscale, at gold-liquid, gold-silica and silica-liquid interfaces.

Bibliography

- [1] U. KREIBIG AND M. VOLLMER, *Optical properties of metal clusters*, Springer, Berlin (1995).
- [2] M. JAMET, V. DUPUIS, P. MÉLINON AND G. GUIRAUD, “Structure and magnetism of well defined cobalt nanoparticles embedded in a niobium matrix”, *Physical Review B* **62**, 493 (2000).
- [3] A. CRUT, P. MAIOLI, N. DEL FATTI AND F. VALLÉE, “Acoustic vibrations of metal nano-objects: time-domain investigations”, *Phys. Rep.* DOI:10.1016/j.physrep.2014.09.004 (2014).
- [4] A. CRUT, P. MAIOLI, N. DEL FATTI AND F. VALLÉE, “Time-domain investigation of the acoustic vibrations of metal nanoparticles: size and encapsulation effects”, *Ultrasonics* DOI:10.1016/j.ultras.2014.02.013 (2014).
- [5] C. VOISIN, D. CHRISTOFILOS, P. LOUKAKOS, N. DEL FATTI, F. VALLÉE, J. LERMÉ, M. GAUDRY, E. COTTANCIN, M. PELLARIN AND M. BROYER, “Ultrafast electron-electron scattering and energy exchanges in noble-metal nanoparticles”, *Phys. Rev. B* **69**, 195416 (2004).
- [6] S. I. BOZHEVOLNYI, V. S. VOLKOV, E. DEVAUX, J.-Y. LALUET AND T. W. EBBESEN, “Channel plasmon subwavelength waveguide components including interferometers and ring resonators”, *Nature* **440**, 508 (2006).
- [7] S. A. MAIER, M. L. BRONGERSMA, P. G. KIK, S. MELTZER, A. A. G. REQUICHA AND H. A. ATWATER, “Plasmonics-a route to nanoscale optical devices”, *Adv. Mater.* **13**, 1501 (2001).
- [8] D. P. O’NEAL, L. R. HIRSCH, N. J. HALAS, J. D. PAYNE AND J. L. WEST, “Photo-thermal tumor ablation in mice using near infrared-absorbing nanoparticles”, *Cancer Lett.* **209**, 171 (2004).
- [9] A. M. GOBIN, M. H. LEE, N. J. HALAS, W. D. JAMES, R. A. DREZEK AND J. L. WEST, “Near-infrared resonant nanoshells for combined optical imaging and photothermal cancer therapy”, *Nano Lett.* **7**, 1929 (2007).
- [10] S. K. HASHMI AND G. J. HUTCHINGS, “Gold catalysis”, *Angew. Chem. Int. Ed.* **45**, 7896 (2006).
- [11] M. SHEKHAR, J. WANG, W.-S. LEE, W. D. WILLIAMS, S. M. KIM, E. A. STACH, J. T. MILLER, W. N. DELGASS AND F. H. RIBEIRO, “Size and support

Bibliography

- effects for the water-gas shift catalysis over gold nanoparticle supported on model Al₂O₃ and TiO₂”, *J. Am. Chem. Soc.* **134**, 4700 (2012).
- [12] A. S. ARICÒ, P. BRUCE, B. SCROSATI, J.-M. TARASCON AND W. VAN SCHALKWIJK, “Nanostructured materials for advanced energy conversion and storage devices”, *Nature Mater.* **4**, 366 (2005).
- [13] R. ALAYAN, L. ARNAUD, A. BOURGEY, M. BROYER, E. COTTANCIN, J. R. HUNTZINGER, J. LERMÉ, J.-L. VIALLE, M. PELLARIN AND G. GUIRAUD, “Application of a static quadrupole deviator to the deposition of size-selected cluster ions from a laser vaporization source”, *Rev. Sci. Instrum.* **75**, 2461 (2004).
- [14] A. PEREZ, P. MÉLINON, V. DUPUIS, L. BARDOTTI, B. MASENELLI, F. TOURNUS, B. PRÉVEL, J. TUAILLON-COMBES, E. BERNSTEIN, A. TAMION, N. BLANC, D. TAÏNOFF, O. BOISRON, G. GUIRAUD, M. BROYER, M. PELLARIN, N. DEL FATTI, F. VALLÉE, E. COTTANCIN, J. LERMÉ, J.-L. VIALLE, C. BONNET, P. MAIOLI, A. CRUT, C. CLAVIER, J. L. ROUSSET AND F. MORFIN, “Functional nanostructures from clusters”, *Int. J. Nanotechnology* **7**, 523 (2010).
- [15] M. ZHU, E. LANNI, N. GARG, M. E. BIER AND R. JIN, “Kinetically controlled, high-yield synthesis of Au₂₅ clusters”, *J. Am. Chem. Soc.* **130**, 1138 (2008).
- [16] C. VOISIN, D. CHRISTOFILOS, N. DEL FATTI, F. VALLÉE, B. PRÉVEL, E. COTTANCIN, J. LERMÉ, M. PELLARIN AND M. BROYER, “Size-dependent electron-electron interactions in metal nanoparticles”, *Phys. Rev. Lett.* **85**, 2200 (2000).
- [17] C. VOISIN, N. DEL FATTI, D. CHRISTOFILOS AND F. VALLÉE, “Ultrafast electron dynamics and optical nonlinearities in metal nanoparticles”, *J. Phys. Chem. B* **105**, 2264 (2001).
- [18] A. ARBOUET, C. VOISIN, D. CHRISTOFILOS, P. LANGOT, N. DEL FATTI, F. VALLÉE, J. LERMÉ, G. CELEP, E. COTTANCIN, M. GAUDRY, M. PELLARIN, M. BROYER, M. MAILLARD, M. P. PILENI AND M. TREGUER, “Electron-phonon scattering in metal clusters”, *Phys. Rev. Lett.* **90**, 177401 (2003).
- [19] V. JUVÉ, M. SCARDAMAGLIA, P. MAIOLI, A. CRUT, S. MERABIA, L. JOLY, N. DEL FATTI AND F. VALLÉE, “Cooling dynamics and thermal interface resistance of glass-embedded metal nanoparticles”, *Phys. Rev. B* **80**, 195406 (2009).
- [20] D. G. CAHILL, P. V. BRAUN, G. CHEN, D. R. CLARKE, S. FAN, K. E. GOODSON, P. KEBLINSKI, W. P. KING, G. D. MAHAN, A. MAJUMDAR, H. J. MARIS, S. R. PHILLPOT, E. POP AND L. SHI, “Nanoscale thermal transport. II. 2003-2012”, *Appl. Phys. Rev.* **1**, 011305 (2014).
- [21] C. BOHREN AND D. R. HUFFMAN, *Absorption and scattering of light by small particles*, Wiley, New York (1998).
- [22] N. W. ASHCROFT AND N. D. MERMIN, *Solid state physics*, Cornell University (1976).
- [23] “<http://www.phys.ufl.edu/fermisurface/>”, .

-
- [24] J. D. JACKSON, *Classical electrodynamics*, John Wiley & Sons Ltd. (1962).
- [25] P. JOHNSON AND R. CHRISTY, “Optical constants of the noble metals”, *Phys. Rev. B* **6**, 4370 (1972).
- [26] E. D. PALIK, *Handbook of optical constants of solids*, Academic Press, Orlando (1985).
- [27] J. H. WEAVER AND H. P. R. FREDERIKSE, *CRC Handbook of chemistry and physics*, CRC Press (1977).
- [28] N. P. BLANCHARD, C. SMITH, D. S. MARTIN, D. J. HAYTON, T. E. JENKINS AND P. WEIGHTMAN, “High-resolution measurements of the bulk dielectric constants of single crystal gold with application to reflection anisotropy spectroscopy”, *Phys. Status Solidi C* **0**, 2931 (2003).
- [29] R. L. OLMON, B. SLOVICK, T. W. JOHNSON, D. SHELTON, S.-H. OH, G. D. BOREMAN AND M. B. RASCHKE, “Optical dielectric function of gold”, *Phys. Rev. B* **86**, 235147 (2012).
- [30] P. BILLAUD, J.-R. HUNTZINGER, E. COTTANCIN, J. LERMÉ, M. PELLARIN, L. ARNAUD, M. BROYER, N. DEL FATTI AND F. VALLÉE, “Optical extinction spectroscopy of single silver nanoparticles”, *Eur. Phys. J. D* **43**, 271 (2007).
- [31] J. B. SMITH AND H. EHRENREICH, “The optical dependence of the relaxation time in metals”, *Phys. Rev. B* **25**, 923 (1982).
- [32] P. ALLEN, “Theory of thermal relaxation of electrons in metals”, *Phys. Rev. Lett.* **59**, 1460 (1987).
- [33] C.-Y. TSAI, C.-Y. TSAI, C.-H. CHEN, T.-L. SUNG, T.-Y. WU AND F.-P. SHIH, “Theoretical model for intravalley and intervalley free-carrier absorption in semiconductor lasers: beyond the classical Drude model”, *IEEE J. Quant. Electron.* **34**, 552 (1998).
- [34] F. VALLÉE AND N. DEL FATTI, *Challenges and advances in computational chemistry and physics*, Springer (2013).
- [35] T. STOLL, P. MAIOLI, A. CRUT, N. DEL FATTI AND F. VALLÉE, “Advances in femto-nano-optics: ultrafast nonlinearity of metal nanoparticles”, *Eur. Phys. J. D* (2014).
- [36] N. DEL FATTI, “Dynamique électronique femtoseconde dans les systèmes métalliques massifs et confinés”, Ph.D. thesis, Ecole Polytechnique (1999).
- [37] R. N. GURZHI, “Mutual electron correlations in metal optics”, *Sov. Phys. JETP* **35**, 673 (1959).
- [38] A. KAWABATA AND R. KUBO, “Electronic properties of fine metallic particles”, *J. Phys. Soc. Jpn.* **21**, 1765 (1966).

Bibliography

- [39] V. JUVÉ, M. F. CARDINAL, A. LOMBARDI, A. CRUT, P. MAIOLI, J. PÉREZ-JUSTE, L. M. LIZ-MARZÁN, N. DEL FATTI AND F. VALLÉE, “Size-dependent surface plasmon resonance broadening in nonspherical nanoparticles: single gold nanorods”, *Nano Lett.* **13**, 2234 (2013).
- [40] F. HACHE, D. RICARD AND C. FLYTZANIS, “Optical nonlinearities of small metal particles: surface-mediated resonance and quantum size effects”, *J. Opt. Soc. Am. B: Opt. Phys.* **3**, 1647 (1986).
- [41] N. DEL FATTI, F. VALLÉE, C. FLYTZANIS, Y. HAMANAKA AND A. NAKAMURA, “Electron dynamics and surface plasmon resonance nonlinearities in metal nanoparticles”, *Chem. Phys.* **251**, 215 (2000).
- [42] H. BAIDA, P. BILLAUD, S. MARHABA, D. CHRISTOFILOS, E. COTTANCIN, A. CRUT, J. LERMÉ, P. MAIOLI, M. PELLARIN, M. BROYER, N. DEL FATTI, F. VALLÉE, A. SÁNCHEZ-IGLESIAS, I. PASTORIZA-SANTOS AND L. LIZ-MARZÁN, “Quantitative determination of the size dependence of surface plasmon resonance damping in single Ag@SiO₂ nanoparticles”, *Nano Lett.* **9**, 3463 (2009).
- [43] J. LERMÉ, H. BAIDA, C. BONNET, M. BROYER, E. COTTANCIN, A. CRUT, P. MAIOLI, N. DEL FATTI, F. VALLÉE AND M. PELLARIN, “Size dependence of the surface plasmon resonance damping in metal nanospheres”, *J. Phys. Chem. Lett.* **1**, 2922 (2010).
- [44] J. LERMÉ, “Size evolution of the surface plasmon resonance damping in silver nanoparticles: confinement and dielectric effects”, *J. Phys. Chem. C* **115**, 14098 (2011).
- [45] G. BASSANI AND F. PASTORI-PARRAVICINI, *Electronic states and optical transitions in solids*, Pergamon Press, New York (1975).
- [46] M. DRESSEL AND G. GRUNER, *Electrodynamics of solids: optical properties of electrons in matter*, Cambridge University Press, Cambridge, New York (2002).
- [47] R. ROSEI AND D. W. LYNCH, “Thermomodulation spectra of Al, Au, and Cu”, *Phys. Rev. B* **5**, 3883 (1972).
- [48] R. ROSEI, “Temperature modulation of the optical transitions involving the Fermi surface in Ag: theory”, *Phys. Rev. B* **10**, 474 (1974).
- [49] M. GUERRISI, R. ROSEI AND P. WINSEMIUS, “Splitting of the interband absorption edge in Au”, *Phys. Rev. B* **12**, 557 (1975).
- [50] N. E. CHRISTENSEN, “Band structure of silver and optical interband transitions”, *Phys. Status Solidi B* **54**, 551 (1972).
- [51] T. RANGEL, D. KECIK, P. E. TREVISANUTTO, G.-M. RIGNANESE, H. VAN SWYGENHOVEN AND V. OLEVANO, “Band structure of gold from many-body perturbation theory”, *Phys. Rev. B* **86**, 125125 (2012).
- [52] N. V. SMITH, “Photoelectron energy spectra and the band structures of noble metals”, *Phys. Rev. B* **3**, 1862 (1971).

- [53] D. BRUST, “Band-theoretic model for the photoelectric effect in silicon”, *Phys. Rev.* **139**, 489 (1965).
- [54] H. EHRENREICH AND H. R. PHILIPP, “Optical properties of Ag and Cu”, *Phys. Rev.* **128**, 1622 (1962).
- [55] F. MUELLER AND J. PHILLIPS, “Electronic spectrum of crystalline copper”, *Phys. Rev.* **157**, 600 (1967).
- [56] N. CHRISTENSEN AND B. SERAPHIN, “Relativistic band calculation and the optical properties of gold”, *Phys. Rev. B* **4**, 3321 (1971).
- [57] R. ROSEI, C. CULP AND J. WEAVER, “Temperature modulation of the optical transitions involving the Fermi surface in Ag: experimental”, *Phys. Rev. B* **10**, 484 (1974).
- [58] L. LIZ-MARZÁN, “Tailoring surface plasmons through the morphology and assembly of metal nanoparticles”, *Langmuir* **22**, 32 (2006).
- [59] V. MYROSHNYCHENKO, J. RODRÍGUEZ-FERNÁNDEZ, I. PASTORIZA-SANTOS, A. M. FUNSTON, C. NOVO, P. MULVANEY, L. M. LIZ-MARZÁN AND F. J. GARCÍA DE ABAJO, “Modelling the optical response of gold nanoparticles.”, *Chem. Soc. Rev.* **37**, 1792 (2008).
- [60] G. MIE, “Beiträge zur Optik trüber Medien, speziell kolloidaler Metallösungen”, *Ann. Phys.* **25**, 377 (1908).
- [61] N. DEL FATTI, C. VOISIN, F. CHEVY, F. VALLÉE, C. FLYTZANIS AND F. VALLÉE, “Coherent acoustic mode oscillation and damping in silver nanoparticles”, *J. Chem. Phys.* **110**, 11484 (1999).
- [62] F. VALLÉE, *Nanomaterials and Nanochemistry*, Springer Verlag, Heidelberg (2007).
- [63] H. HÖVEL, S. FRITZ, A. HILGER, U. KREIBIG AND M. VOLLMER, “Width of cluster plasmon resonances: bulk dielectric functions and chemical interface damping.”, *Phys. Rev. B* **48**, 18178 (1993).
- [64] J. PÉREZ-JUSTE, I. PASTORIZA-SANTOS, L. M. LIZ-MARZÁN AND P. MULVANEY, “Gold nanorods: synthesis, characterization and applications”, *Coord. Chem. Rev.* **249**, 1870 (2005).
- [65] O. MUSKENS, G. BACHELIER, N. DEL FATTI, F. VALLÉE, A. BRIOUDE, X. JIANG AND M.-P. PILENI, “Quantitative absorption spectroscopy of a single gold nanorod”, *J. Phys. Chem. C* **112**, 8917 (2008).
- [66] A. LOMBARDI, M. LOUMAIGNE, A. CRUT, P. MAIOLI, N. DEL FATTI, F. VALLÉE, M. SPUCH-CALVAR, J. BURGIN, J. MAJIMEL AND M. TRÉGUER-DELAPIERRE, “Surface plasmon resonance properties of single elongated nano-objects: gold nanobipyramids and nanorods”, *Langmuir* **28**, 9027 (2012).
- [67] C. KITTEL, *Introduction to solid state physics*, Eight Edition (1995).

Bibliography

- [68] N. DEL FATTI, C. VOISIN, M. ACHERMANN, S. TZORTZAKIS, D. CHRISTOFOLOS AND F. VALLÉE, “Nonequilibrium electron dynamics in noble metals”, *Phys. Rev. B* **61**, 956 (2000).
- [69] M. I. KAGANOV, I. M. LIFSHITZ AND L. V. TANATAROV, “Relaxation between electrons and the crystalline lattice”, *Sov. Phys. JETP* **4**, 173 (1957).
- [70] S. I. ANISIMOV, B. L. KAPELIOVICH AND T. L. PERELMAN, “Electron emission from metal surfaces exposed to ultrashort laser pulses”, *Sov. Phys. JETP* **39**, 375 (1974).
- [71] N. DEL FATTI, A. ARBOUET AND F. VALLÉE, “Femtosecond optical investigation of electron-lattice interactions in an ensemble and a single metal nanoparticle”, *Appl. Phys. B* **84**, 175 (2006).
- [72] D. MONGIN, “Spectroscopie ultrarapide de nanoparticules métalliques et hybrides”, Ph.D. thesis, Université Claude Bernard Lyon 1 (2012).
- [73] F. STIETZ, J. BOSBACH, T. WENZEL, T. VARTANYAN, A. GOLDMANN AND F. TRAGER, “Decay times of surface plasmon excitation in metal nanoparticles by persistent spectral hole burning”, *Phys. Rev. Lett.* **84**, 5644 (2000).
- [74] B. LAMPRECHT, J. R. KRENN, A. LEITNER AND F. R. AUSSENEGG, “Resonant and off-resonant light-driven plasmons in metal nanoparticles studied by femtosecond-resolution third-harmonic generation”, *Phys. Rev. Lett.* **83**, 4421 (1999).
- [75] B. LAMPRECHT, A. LEITNER AND F. R. AUSSENEGG, “SHG studies of plasmon dephasing in nanoparticles”, *Appl. Phys. B* **68**, 419 (1999).
- [76] E. KNOESEL, A. HOTZEL AND M. WOLF, “Ultrafast dynamics of hot electrons and holes in copper: excitation, energy relaxation, and transport effects”, *Phys. Rev. B* **57**, 12812 (1998).
- [77] R. MATZDORF, A. GERLACH, F. THEILMANN, G. MEISTER AND A. GOLDMANN, “New lifetime estimates for d-band holes at noble metal surfaces”, *Appl. Phys. B* **68**, 393 (1999).
- [78] J. M. ZIMAN, *Electrons and phonons: the theory of transport phenomena in solids*, Oxford Classic Texts in the Physical Sciences (1960).
- [79] C.-K. SUN, F. VALLÉE, L. H. ACIOLI, E. P. IPPEN AND J. FUJIMOTO, “Femtosecond-tunable measurement of electron thermalization in gold”, *Phys. Rev. B* **50**, 15337 (1994).
- [80] J. HODAK, A. HENGLEIN AND G. HARTLAND, “Photophysics of nanometer sized metal particles: electron-phonon coupling and coherent excitation of breathing vibrational modes”, *J. Phys. Chem. B* **104**, 9954 (2000).
- [81] P. WINSEMIUS, M. GUERRISI AND R. ROSEI, “Splitting of the interband absorption edge in Au: temperature dependence”, *Phys. Rev. B* **12**, 4570 (1975).

- [82] G. PARKINS, W. LAWRENCE AND R. CHRISTY, "Intraband optical conductivity $\sigma(\omega, T)$ of Cu, Ag, and Au: contribution from electron-electron scattering", *Phys. Rev. B* **23**, 6408 (1981).
- [83] M. HU, X. WANG, G. V. HARTLAND, P. MULVANEY, J. P. JUSTE AND J. E. SADER, "Vibrational response of nanorods to ultrafast laser induced heating: theoretical and experimental analysis", *J. Am. Chem. Soc.* **125**, 14925 (2003).
- [84] G. V. HARTLAND, "Optical studies of dynamics in noble metal nanostructures", *Chem. Rev.* **111**, 3858 (2011).
- [85] M. OTTER, "Temperaturabhängigkeit der optischen Konstanten massiver Metalle", *Z. Physik* **161**, 539 (1960).
- [86] B. PALPANT, M. RASHIDI-HUYEH, B. GALLAS, S. CHENOT AND S. FISSON, "Highly dispersive thermo-optical properties of gold nanoparticles", *Appl. Phys. Lett.* **90**, 223105 (2007).
- [87] R. B. WILSON, B. A. APGAR, L. W. MARTIN AND D. G. CAHILL, "Thermoreflectance of metal transducers for optical pump-probe studies of thermal properties", *Opt. Express* **20**, 28829 (2012).
- [88] M. RASHIDI-HUYEH AND B. PALPANT, "Counterintuitive thermo-optical response of metal-dielectric nanocomposite materials as a result of local electromagnetic field enhancement", *Phys. Rev. B* **74**, 075405 (2006).
- [89] N. DEL FATTI, R. BOUFFANAIS, F. VALLÉE AND C. FLYTZANIS, "Nonequilibrium electron interactions in metal films", *Phys. Rev. Lett.* **81**, 922 (1998).
- [90] O. L. MUSKENS, N. DEL FATTI AND F. VALLÉE, "Femtosecond response of a single metal nanoparticle", *Nano Lett.* **6**, 552 (2006).
- [91] J. LERMÉ, M. PELLARIN, E. COTTANCIN, M. GAUDRY, M. BROYER, N. DEL FATTI, F. VALLÉE AND C. VOISIN, "Influence of lattice contraction on the optical properties and the electron dynamics in silver clusters", *Eur. Phys. J. D* **17**, 213 (2001).
- [92] C. D. GRANT, A. M. SCHWARTZBERG, Y. YANG, S. CHEN AND J. Z. ZHANG, "Ultrafast study of electronic relaxation dynamics in Au₁₁ nanoclusters", *Chem. Phys. Lett.* **383**, 31 (2004).
- [93] S. A. MILLER, J. M. WOMICK, J. F. PARKER, R. W. MURRAY AND A. M. MORAN, "Femtosecond relaxation dynamics of Au₂₅L₁₈ - monolayer-protected clusters", *J. Phys. Chem. C* **113**, 9440 (2009).
- [94] H. QIAN, M. Y. SFEIR AND R. JIN, "Ultrafast relaxation dynamics of [Au₂₅(SR)₁₈]^q nanoclusters : effects of charge state", *J. Phys. Chem. C* **114**, 19935 (2010).
- [95] S. H. YAU, O. VARNAVSKI, J. D. GILBERTSON, B. CHANDLER, G. RAMAKRISHNA AND T. I. GOODSON, "Ultrafast optical study of small gold monolayer protected clusters: a closer look at emission", *J. Phys. Chem. C* **114**, 15979 (2010).

Bibliography

- [96] M. Y. SFEIR, H. QIAN, K. NOBUSADA AND R. JIN, “Ultrafast relaxation dynamics of rod-shaped 25-atom gold nanoclusters”, *J. Phys. Chem. C* **115**, 6200 (2011).
- [97] T. D. GREEN AND K. L. KNAPPENBERGER, “Relaxation dynamics of Au₂₅L₁₈ nanoclusters studied by femtosecond time-resolved near infrared transient absorption spectroscopy”, *Nanoscale* **4**, 4111 (2012).
- [98] C. YI, M. A. TOFANELLI, C. J. ACKERSON AND K. L. KNAPPENBERGER, “Optical properties and electronic energy relaxation of metallic Au₁₄₄(SR)₆₀ nanoclusters.”, *J. Am. Chem. Soc.* **135**, 18222 (2013).
- [99] C. MANZONI, D. POLLI AND G. CERULLO, “Two-color pump-probe system broadly tunable over the visible and the near infrared with sub-30 fs temporal resolution”, *Rev. Sci. Instrum.* **77**, 023103 (2006).
- [100] D. POLLI, L. LÜER AND G. CERULLO, “High-time-resolution pump-probe system with broadband detection for the study of time-domain vibrational dynamics”, *Rev. Sci. Instrum.* **78**, 103108 (2007).
- [101] G. DELLA VALLE, M. CONFORTI, S. LONGHI, G. CERULLO AND D. BRIDA, “Real-time optical mapping of the dynamics of nonthermal electrons in thin gold films”, *Phys. Rev. B* **86**, 155139 (2012).
- [102] D. BRIDA, C. MANZONI, G. CIRMI, D. POLLI AND G. CERULLO, “Tracking ultrafast energy flow in molecules using broadly tunable few-optical-cycle pulses”, *IEEE J. Sel. Top. Quant. Electron.* **18**, 329 (2012).
- [103] M. HILLENKAMP, G. DI DOMENICANTONIO AND C. FELIX, “Monodispersed metal clusters in solid matrices: a new experimental setup”, *Rev. Sci. Instrum.* **77**, 025104 (2006).
- [104] K. UCHIDA, S. KANEKO, S. OMI, C. HATA, H. TANJI, Y. ASAHARA, A. J. IKUSHIMA, T. TOKIZAKI AND A. NAKAMURA, “Optical nonlinearities of a high concentration of small metal particles dispersed in glass: copper and silver particles”, *J. Opt. Soc. Am. B: Opt. Phys.* **11**, 1236 (1994).
- [105] C. VOISIN, “Etude femtoseconde de la dynamique électronique et vibrationnelle dans des nanoparticules métalliques”, Ph.D. thesis, Ecole Polytechnique (2001).
- [106] J. A. A. J. PERENBOOM, P. WYDER AND F. MEIER, “Electronic properties of small metallic particles”, .
- [107] R. KUBO, “Electronic properties of metallic fine particles I”, *J. Phys. Soc. Jpn.* **17**, 975 (1962).
- [108] H. E. SAUCEDA, D. MONGIN, P. MAIOLI, A. CRUT, M. PELLARIN, N. DEL FATTI, F. VALLÉE AND I. L. GARZÓN, “Vibrational properties of metal nanoparticles: atomistic simulation and comparison with time-resolved investigation”, *J. Phys. Chem. C* **116**, 25147 (2012).

-
- [109] C.-K. SUN, F. VALLÉE, L. ACIOLI, E. IPPEN AND J. FUJIMOTO, “Femtosecond investigation of electron thermalization in gold”, *Phys. Rev. B* **48**, 365 (1993).
- [110] F. ABELÉS, *Advanced optical techniques*, North-Holland, Amsterdam (1967).
- [111] U. KREIBIG, “Anomalous frequency and temperature dependence of the optical absorption of small gold particles”, *Journal de physique. Colloque* **38**, 97 (1977).
- [112] D. PINES AND P. NOZIÈRES, *The theory of quantum liquids*, Benjamin, New York (1966).
- [113] W. EKARDT, “Work function of small metal particles: self-consistent spherical jellium-background model”, *Phys. Rev. B* **29**, 1558 (1984).
- [114] A. LIEBSCH, “Surface-plasmon dispersion and size dependence of Mie resonance: silver versus simple metals”, *Phys. Rev. B* **48**, 11317 (1993).
- [115] J. LERMÉ, B. PALPANT, B. PRÉVEL, M. PELLARIN, M. TREILLEUX, J.-L. VIALLE, A. PEREZ AND M. BROYER, “Quenching of the size effects in free and matrix-embedded silver clusters”, *Phys. Rev. Lett.* **80**, 5105 (1998).
- [116] G. SITJA, S. LE MOAL, M. MARSAULT, G. HAMM, F. LEROY AND C. R. HENRY, “Transition from molecule to solid state: reactivity of supported metal clusters.”, *Nano Lett.* **13**, 1977 (2013).
- [117] C. M. AIKENS, “Origin of discrete optical absorption spectra of M25(SH)18-nanoparticles (M=Au, Ag)”, *J. Phys. Chem. C* **112**, 19797 (2008).
- [118] G. H. WOHRLE, M. G. WARNER AND J. E. HUTCHISON, “Ligand exchange reactions yield subnanometer, thiol-stabilized gold particles with defined optical transitions”, *J. Phys. Chem. B* **106**, 9979 (2002).
- [119] H. HÄKKINEN, “Atomic and electronic structure of gold clusters: understanding flakes, cages and superatoms from simple concepts”, *Chem. Soc. Rev.* **37**, 1847 (2008).
- [120] S. LINK, A. BEEBY, S. FITZGERALD, M. A. EL-SAYED, T. G. SCHAAFF AND R. L. WHETTEN, “Visible to infrared luminescence from a 28-atom gold cluster”, *J. Phys. Chem. B* **106**, 3410 (2002).
- [121] G. RAMAKRISHNA, O. VARNAVSKI, J. KIM, D. LEE AND T. GOODSON, “Quantum-sized gold clusters as efficient two-photon absorbers”, *J. Am. Chem. Soc.* **130**, 5032 (2008).
- [122] H. QIAN AND R. JIN, “Controlling nanoparticles with atomic precision: the case of Au₁₄₄(SCH₂CH₂Ph)₆₀”, *Nano Lett.* **9**, 4083 (2009).
- [123] Y. LEVI-KALISMAN, P. D. JADZINSKY, N. KALISMAN, H. TSUNOYAMA, T. TSUKUDA, D. A. BUSHNELL AND R. D. KORNBERG, “Synthesis and characterization of Au₁₀₂(p-MBA)₄₄ nanoparticles”, *J. Am. Chem. Soc.* **133**, 2976 (2011).

Bibliography

- [124] H. QIAN AND R. JIN, “Ambient synthesis of Au₁₄₄(SR)₆₀ nanoclusters in methanol”, *Chem. Mater.* **23**, 2209 (2011).
- [125] A. DASS, “Faradaurate nanomolecules: a superstable plasmonic 76.3 kDa cluster”, *J. Am. Chem. Soc.* **133**, 19259 (2011).
- [126] H. QIAN, Y. ZHU AND R. JIN, “Atomically precise gold nanocrystal molecules with surface plasmon resonance”, *Proc. Natl. Acad. Sci. U.S.A.* **109**, 696 (2012).
- [127] M. ZHU, C. M. AIKENS, F. J. HOLLANDER, G. C. SCHATZ AND R. JIN, “Correlating the crystal structure of a thiol-protected Au₂₅ cluster and optical properties”, *J. Am. Chem. Soc.* **130**, 5883 (2008).
- [128] M. W. HEAVEN, A. DASS, P. S. WHITE, K. M. HOLT AND R. W. MURRAY, “Crystal structure of the gold nanoparticle [N(C₈H₁₇)₄][Au₂₅(SCH₂CH₂Ph)₁₈]”, *J. Am. Chem. Soc.* **130**, 3754 (2008).
- [129] P. D. JADZINSKY, G. CALERO, C. J. ACKERSON, D. A. BUSHNELL AND R. D. KORNBERG, “Structure of a thiol monolayer-protected gold nanoparticle at 1.1 Å resolution”, *Science* **318**, 430 (2007).
- [130] R. L. WHETTEN AND R. C. PRICE, “Nano-golden order”, *Science* **318**, 407 (2007).
- [131] O. LOPEZ-ACEVEDO, J. AKOLA, R. L. WHETTEN, H. GRÖNBECK AND H. HÄKKINEN, “Structure and bonding in the ubiquitous icosahedral metallic gold cluster Au₁₄₄(SR)₆₀”, *J. Phys. Chem. C* **113**, 5035 (2009).
- [132] D. BAHENA, N. BHATTARAI, U. SANTIAGO, A. TLAHUICE-FLORES, A. PONCE, S. B. H. BACH, B. YOON, R. L. WHETTEN, U. LANDMAN AND M. JOSE-YACAMAN, “STEM electron diffraction and high-resolution images used in the determination of the crystal structure of the Au₁₄₄(SR)₆₀ cluster”, *J. Phys. Chem. Lett.* **4**, 975 (2013).
- [133] S. H. YAU, O. VARNAVSKI AND T. I. GOODSON, “An ultrafast look at Au nanoclusters”, *Acc. Chem. Res.* **46**, 1506 (2013).
- [134] M. WALTER, J. AKOLA, O. LOPEZ-ACEVEDO, P. D. JADZINSKY, G. CALERO, C. J. ACKERSON, R. L. WHETTEN, H. GRÖNBECK AND H. HÄKKINEN, “A unified view of ligand-protected gold clusters as superatom complexes”, *Proc. Natl. Acad. Sci. U.S.A.* **105**, 9157 (2008).
- [135] E. HULKKO, O. LOPEZ-ACEVEDO, J. KOIVISTO, Y. LEVI-KALISMAN, R. D. KORNBERG, M. PETTERSSON AND H. HÄKKINEN, “Electronic and vibrational signatures of the Au₁₀₂(p-MBA)₄₄ cluster”, *J. Am. Chem. Soc.* **133**, 3752 (2011).
- [136] M. ZHU, W. T. ECKENHOFF, T. PINTAUER AND R. JIN, “Conversion of anionic [Au₂₅(SCH₂CH₂Ph)₁₈]- cluster to charge neutral cluster via air oxidation”, *J. Phys. Chem. C* **112**, 14221 (2008).
- [137] R. PHILIP, P. CHANTHARASUPAWONG, H. QIAN, R. JIN AND J. THOMAS, “Evolution of nonlinear optical properties: from gold atomic clusters to plasmonic nanocrystals”, *Nano Lett.* **12**, 4661 (2012).

- [138] A. DESIREDDY, B. E. CONN, J. GUO, B. YOON, R. N. BARNETT, B. M. MONAHAN, K. KIRSCHBAUM, W. P. GRIFFITH, R. L. WHETTEN, U. LANDMAN AND T. P. BIGIONI, “Ultrastable silver nanoparticles”, *Nature* **501**, 399 (2013).
- [139] H. G. CRAIGHEAD, “Nanoelectromechanical systems”, *Science* **290**, 1532 (2000).
- [140] K. L. EKINCI AND M. L. ROUKES, “Nanoelectromechanical systems”, *Rev. Sci* **76**, 61101 (2005).
- [141] C. VOISIN, N. DEL FATTI, D. CHRISTOFILOS AND F. VALLÉE, “Time-resolved investigation of the vibrational dynamics of metal nanoparticles”, *Appl. Surf. Sci.* **164**, 131 (2000).
- [142] P. V. RUIJGROK, P. ZIJLSTRA, A. L. TCHEBOTAREVA AND M. ORRIT, “Damping of acoustic vibrations of single gold nanoparticles optically trapped in water.”, *Nano Lett.* **12**, 1063 (2012).
- [143] K. YU, P. ZIJLSTRA, J. E. SADER, Q.-H. XU AND M. ORRIT, “Damping of acoustic vibrations of immobilized single gold nanorods in different environments”, *Nano Lett.* **13**, 2710 (2013).
- [144] T. A. MAJOR, A. CRUT, B. GAO, S. S. LO, N. DEL FATTI, F. VALLÉE AND G. V. HARTLAND, “Damping of the acoustic vibrations of a suspended gold nanowire in air and water environments”, *Phys. Chem. Chem. Phys.* **15**, 4169 (2013).
- [145] T. A. MAJOR, S. S. LO, K. YU AND G. V. HARTLAND, “Time-resolved studies of the acoustic vibrational modes of metal and semiconductor nano-objects”, *J. Phys. Chem. Lett.* **5**, 866 (2014).
- [146] T. KRAUSS AND F. WISE, “Coherent acoustic phonons in a semiconductor quantum dot”, *Phys. Rev. Lett.* **79**, 5102 (1997).
- [147] J. H. HODAK, A. HENGLEIN AND G. V. HARTLAND, “Size dependent properties of Au particles: coherent excitation and dephasing of acoustic vibrational modes”, *J. Chem. Phys.* **111**, 8613 (1999).
- [148] V. JUVÉ, A. CRUT, P. MAIOLI, M. PELLARIN, M. BROYER, N. DEL FATTI AND F. VALLÉE, “Probing elasticity at the nanoscale: terahertz acoustic vibration of small metal nanoparticles”, *Nano Lett.* **10**, 1853 (2010).
- [149] H. E. SAUCEDA, F. SALAZAR, L. A. PÉREZ AND I. L. GARZÓN, “Size and shape dependence of the vibrational spectrum and low-temperature specific heat of Au nanoparticles”, *J. Phys. Chem. C* **117**, 25160 (2013).
- [150] A. TLAHUICE-FLORES, R. L. WHETTEN AND M. JOSE-YACAMAN, “Vibrational normal modes of small thiolate-protected gold clusters”, *J. Phys. Chem. C* **117**, 12191 (2013).
- [151] G. V. HARTLAND, “Coherent vibrational motion in metal particles: determination of the vibrational amplitude and excitation mechanism”, *J. Chem. Phys.* **116**, 8048 (2002).

Bibliography

- [152] O. VARNAVSKI, G. RAMAKRISHNA, J. KIM, D. LEE AND T. GOODSON, “Critical size for the observation of quantum confinement in optically excited gold clusters”, *J. Am. Chem. Soc.* **132**, 16 (2010).
- [153] O. VARNAVSKI, G. RAMAKRISHNA, J. KIM, D. LEE AND T. GOODSON, “Optically excited acoustic vibrations in quantum-sized monolayer-protected gold clusters”, *ACS Nano* **4**, 3406 (2010).
- [154] H. LAMB, “On the vibrations of an elastic sphere”, *Proc. London Math. Soc.* **1**, 189 (1881).
- [155] L. D. LANDAU AND E. M. LIFSHITZ, *Theory of elasticity*, Pergamon Press, Oxford, New York, 2nd. edition (1970).
- [156] A. CRUT, P. MAIOLI, N. DEL FATTI AND F. VALLÉE, “Anisotropy effects on the time-resolved spectroscopy of the acoustic vibrations of nanoobjects”, *Phys. Chem. Chem. Phys.* **11**, 5882 (2009).
- [157] V. A. DUBROVSKIY AND V. S. MOROCHNIK, “Nonstationary scattering of elastic waves by spherical inclusion”, *Earth Phys.* **17**, 494 (1981).
- [158] A. S. KIRAKOSYAN AND T. V. SHAHBAZIAN, “Vibrational modes of metal nanoshells and bimetallic core-shell nanoparticles”, *J. Chem. Phys.* **129**, 34708 (2008).
- [159] A. CRUT, V. JUVÉ, D. MONGIN, P. MAIOLI, N. DEL FATTI AND F. VALLÉE, “Vibrations of spherical core-shell nanoparticles”, *Phys. Rev. B* **83**, 205430 (2011).
- [160] A. NELET, A. CRUT, A. ARBOUET, N. DEL FATTI, F. VALLÉE, H. PORTALES, L. SAVIOT AND E. DUVAL, “Acoustic vibrations of metal nanoparticles: high order radial mode detection”, *Appl. Surf. Sci.* **226**, 209 (2004).
- [161] A. ARBOUET, N. DEL FATTI AND F. VALLÉE, “Optical control of the coherent acoustic vibration of metal nanoparticles”, *J. Chem. Phys.* **124**, 144701 (2006).
- [162] D. MONGIN, V. JUVÉ, P. MAIOLI, A. CRUT, N. DEL FATTI, F. VALLÉE, A. SANCHEZ-IGLESIAS, I. PASTORIZA-SANTOS AND L. M. LIZ-MARZÁN, “Acoustic vibrations of metal-dielectric core-shell nanoparticles”, *Nano Lett.* **11**, 3016 (2011).
- [163] C. GUILLON, P. LANGOT, N. DEL FATTI, F. VALLÉE, A. S. KIRAKOSYAN, T. V. SHAHBAZIAN, T. CARDINAL AND M. TREGUER, “Coherent acoustic vibration of metal nanoshells”, *Nano Lett.* **7**, 138 (2007).
- [164] D. MAZURENKO, X. SHAN, J. STIEFELHAGEN, C. GRAF, A. VAN BLAADEREN AND J. DIJKHUIS, “Coherent vibrations of submicron spherical gold shells in a photonic crystal”, *Phys. Rev. B* **75**, 161102 (2007).
- [165] J. H. HODAK, A. HENGLEIN AND G. V. HARTLAND, “Coherent excitation of acoustic breathing modes in bimetallic core-shell nanoparticles”, *J. Phys. Chem. B* **104**, 5053 (2000).

- [166] J. E. SADER, G. V. HARTLAND AND P. MULVANEY, “Theory of acoustic breathing modes of coreshell nanoparticles”, *J. Phys. Chem. B* **106**, 1399 (2002).
- [167] H. PORTALES, L. SAVIOT, E. DUVAL, M. GAUDRY, E. COTTANCIN, M. PELLARIN, J. LERMÉ AND M. BROYER, “Resonant Raman scattering by quadrupolar vibrations of Ni-Ag core-shell nanoparticles”, *Phys. Rev. B* **65**, 165422 (2002).
- [168] L. WANG, A. KIYA, Y. OKUNO, Y. NIIDOME AND N. TAMAI, “Ultrafast spectroscopy and coherent acoustic phonons of Au-Ag core-shell nanorods”, *J. Chem. Phys.* **134**, 54501 (2011).
- [169] M. F. CARDINAL, D. MONGIN, A. CRUT, P. MAIOLI, B. RODRÍGUEZ-GONZÁLEZ, J. PÉREZ-JUSTE, L. M. LIZ-MARZÁN, N. DEL FATTI AND F. VALLÉE, “Acoustic vibrations in bimetallic Au@Pd core-shell nanorods”, *J. Phys. Chem. Lett.* **2**, 613 (2012).
- [170] H. PORTALES, L. SAVIOT, E. DUVAL, M. GAUDRY, E. COTTANCIN, J. LERMÉ, M. PELLARIN, M. BROYER, B. PRÉVEL AND P. E. TREVISANUTTO, “Resonance and composition effects on the Raman scattering from silver-gold alloy clusters”, *Eur. Phys. J. D* **16**, 197 (2001).
- [171] S. ADICHTCHEV, S. SIROTKIN, G. BACHELIER, L. SAVIOT, S. ETIENNE, B. STEPHANIDIS, E. DUVAL AND A. MERMET, “High-order vibration modes of bimetallic Ag-Au nanoparticles embedded in glass”, *Phys. Rev. B* **79**, 201402 (2009).
- [172] H. PETROVA, C.-H. LIN, M. HU, J. CHEN, A. R. SIEKKINEN, Y. XIA, J. E. SADER AND G. V. HARTLAND, “Vibrational response of Au-Ag nanoboxes and nanocages to ultrafast laser-induced heating”, *Nano Lett.* **7**, 1059 (2007).
- [173] F. CALVO, “Influence of size, composition, and chemical order on the vibrational properties of gold-silver nanoalloys”, *J. Phys. Chem. C* **115**, 17730 (2011).
- [174] F. CALVO, “Correction to Influence of size, composition, and chemical order on the vibrational properties of gold-silver nanoalloys”, *J. Phys. Chem. C* **116**, 7607 (2012).
- [175] B. DACOSTA FERNANDES, M. SPUCH-CALVAR, H. BAIDA, M. TRÉGUER-DELAPIERRE, J. OBERLÉ, P. LANGOT AND J. BURGİN, “Acoustic vibrations of Au nano-bipyramids and their modification under Ag deposition: a perspective for the development of nanobalances”, *ACS Nano* 7630–7639 (2013).
- [176] S. LINK, Z. L. WANG AND M. A. EL-SAYED, “Alloy formation of gold-silver nanoparticles and the dependence of the plasmon absorption on their composition”, *J. Phys. Chem. B* **103**, 3529 (1999).
- [177] B. RODRÍGUEZ-GONZÁLEZ, A. SANCHEZ-IGLESIAS, M. GIERSIG AND L. M. LIZ-MARZÁN, “AuAg bimetallic nanoparticles: formation, silica-coating and selective etching”, *Faraday Discuss.* **125**, 133 (2004).

Bibliography

- [178] M. GAUDRY, J. LERMÉ, E. COTTANCIN, M. PELLARIN, J.-L. VIALLE, M. BROYER, B. PRÉVEL, P. E. TREVISANUTTO AND P. MÉLINON, “Optical properties of $(\text{Au}_x\text{Ag}_{1-x})_n$ clusters embedded in alumina: evolution with size and stoichiometry”, *Phys. Rev. B* **64**, 85407 (2001).
- [179] M. B. CORTIE AND A. M. McDONAGH, “Synthesis and optical properties of hybrid and alloy plasmonic nanoparticles”, *Chem. Rev.* **111**, 3713 (2011).
- [180] R. FERRANDO, J. JELLINEK AND R. L. JOHNSTON, “Nanoalloys: from theory to applications of alloy clusters and nanoparticles.”, *Chem. Rev.* **108**, 845 (2008).
- [181] G. BARCARO, M. BROYER, N. DURANTE, A. FORTUNELLI AND M. STENER, “Alloying effects on the optical properties of AgAu nanoclusters from TDDFT calculations”, *J. Phys. Chem. C* **115**, 24085 (2011).
- [182] X. LÓPEZ LOZANO, C. MOTTET AND H.-C. WEISSKER, “Effect of alloying on the optical properties of AgAu nanoparticles”, *J. Phys. Chem. C* **117**, 3062 (2013).
- [183] B. RODRÍGUEZ-GONZÁLEZ, A. BURROWS, M. WATANABE, C. J. KIELY AND L. M. LIZ-MARZÁN, “Multishell bimetallic AuAg nanoparticles: synthesis, structure and optical properties”, *J. Mater. Chem.* **15**, 1755 (2005).
- [184] W. BENTEN, N. NILIUS, N. ERNST AND H.-J. FREUND, “Photon emission spectroscopy of single oxide-supported Ag-Au alloy clusters”, *Phys. Rev. B* **72**, 45403 (2005).
- [185] E. COTTANCIN AND M. PELLARIN, “Optical probes of the chemical structure in nanoalloys”, in F. CALVO (editor), “Nanoalloys: From Fundamentals to Applications”, Springer (2013).
- [186] C. L. YAWS, *Chemical properties handbook: physical, thermodynamic, environmental, transport, safety, and health related properties for organic and inorganic chemicals*, McGraw Hill, New York (1999).
- [187] M. GAUDRY, E. COTTANCIN, M. PELLARIN, J. LERMÉ, L. ARNAUD, J. HUNTZINGER, J.-L. VIALLE, M. BROYER, J. L. ROUSSET, P. E. TREVISANUTTO AND P. MÉLINON, “Size and composition dependence in the optical properties of mixed (transition metal/noble metal) embedded clusters”, *Phys. Rev. B* **67**, 155409 (2003).
- [188] E. COTTANCIN, M. GAUDRY, M. PELLARIN, J. LERMÉ, L. ARNAUD, J. R. HUNTZINGER, J.-L. VIALLE, P. E. TREVISANUTTO, P. MÉLINON, J.-L. ROUSSET AND M. BROYER, “Optical properties of mixed clusters: comparative study of Ni/Ag and Pt/Ag clusters”, *Eur. Phys. J. D* **24**, 111 (2003).
- [189] B. N. WANJALA, J. LUO, B. FANG, D. MOTT AND C.-J. ZHONG, “Gold-platinum nanoparticles: alloying and phase segregation”, *J. Mater. Chem.* **21**, 4012 (2011).
- [190] A. HENGLEIN, “Preparation and optical absorption spectra of Au-core Pt-shell and Pt-core Au-shell colloidal nanoparticles in aqueous solution”, *J. Phys. Chem. B* **104**, 2201 (2000).

- [191] B. H. MORROW AND A. STRIOLO, “Supported bimetallic Pt-Au nanoparticles: structural features predicted by molecular dynamics simulations”, *Phys. Rev. B* **81**, 155437 (2010).
- [192] E. COTTANCIN, G. CELEP, J. LERMÉ, M. PELLARIN, J. R. HUNTZINGER, J.-L. VIALLE AND M. BROYER, “Optical properties of noble metal clusters as a function of the size: comparison between experiments and a semi-quantal theory”, *Theor. Chem. Acc.* **116**, 514 (2006).
- [193] J. BELLONI, M. MOSTAFAVI, H. REMITA, J.-L. MARIGNIER, DELCOURT AND MARIE-ODILE, “Radiation-induced synthesis of mono- and multi-metallic clusters and nanocolloids”, *New J. Chem.* **22**, 1239 (1998).
- [194] M. BROYER, E. COTTANCIN, J. LERMÉ, M. PELLARIN, N. DEL FATTI, F. VALLÉE, J. BURGIN, C. GUILLON AND P. LANGOT, “Optical properties and relaxation processes at femtosecond scale of bimetallic clusters”, *Faraday Discuss.* **138**, 137 (2008).
- [195] M. HARB, F. RABILLOUD AND D. SIMON, “Structural, electronic, magnetic and optical properties of icosahedral silver-nickel nanoclusters”, *Phys. Chem. Chem. Phys.* **12**, 4246 (2010).
- [196] F. RABILLOUD, “UV-visible absorption spectra of metallic clusters from TDDFT calculations”, *Eur. Phys. J. D* **67**, 18 (2013).
- [197] M. PELTON, J. E. SADER, J. BURGIN, M. LIU, P. GUYOT-SIONNEST AND D. GOSZTOLA, “Damping of acoustic vibrations in gold nanoparticles”, *Nature Nanotech.* **4**, 492 (2009).
- [198] R. MARTY, A. ARBOUET, C. GIRARD, A. MLAYAH, V. PAILLARD, V. K. LIN, S. L. TEO AND S. TRIPATHY, “Damping of the Acoustic Vibrations of Individual Gold Nanoparticles.”, *Nano Lett.* **11**, 3301 (2011).
- [199] M. PELTON, D. CHAKRABORTY, E. MALACHOSKY, P. GUYOT-SIONNEST AND J. E. SADER, “Viscoelastic flows in simple liquids generated by vibrating nanostructures”, *Phys. Rev. Lett.* **111**, 244502 (2013).
- [200] A. GAMBETTA, C. MANZONI, E. MENNA, M. MENEGHETTI, G. CERULLO, G. LANZANI, S. TRETIAK, A. PIYATINSKI, A. SAXENA, R. L. MARTIN AND A. R. BISHOP, “Real-time observation of nonlinear coherent phonon dynamics in single-walled carbon nanotubes”, *Nature Phys.* **2**, 515 (2006).
- [201] H. LEDBETTER, “Monocrystal elastic constants and derived properties of the cubic and the hexagonal elements”, in “Handbook of Elastic Properties of Solids, Liquids, and Gases, Vol. 2”, Academic Press, New York (2001).
- [202] G. W. C. KAYE AND T. H. LABY, *Tables of physical and chemical constants*, Longman, 16th edition (1995).
- [203] G. SIMMONS AND H. WANG, *Single crystal elastic constants and calculated aggregate properties: a handbook*, M.I.T. Press, Cambridge, 2nd edition (1971).

Bibliography

- [204] S. S. CHOUHAN, G. PAGARE, S. P. SANYAL AND M. RAJAGOPALAN, “First principles study on structural, electronic and elastic properties of AgX and AuX (X=Mg, Sc, Zn and Cd) intermetallic compounds”, *Comput. Mater. Sci.* **65**, 58 (2012).
- [205] S. S. CHOUHAN, G. PAGARE, M. RAJAGOPALAN AND S. P. SANYAL, “First principles study of structural, electronic, elastic and thermal properties of YX (X = Cd, In, Au, Hg and Tl) intermetallics”, *Solid State Sci.* **14**, 1004 (2012).
- [206] Q. WU AND S. LI, “Alloying element additions to Ni₃Al: site preferences and effects on elastic properties from first-principles calculations”, *Comput. Mater. Sci.* **53**, 436 (2012).
- [207] G. STENUIT AND S. FAHY, “First-principles calculations of the mechanical and structural properties of GaN_xAs_{1-x}: lattice and elastic constants”, *Phys. Rev. B* **76**, 35201 (2007).
- [208] N. ZOTOV AND A. LUDWIG, “First-principles calculations of the elastic constants of FePt alloys”, *Intermetallics* **16**, 113 (2008).
- [209] D. POLLI, I. LISIECKI, H. PORTALES, G. CERULLO AND M.-P. PILENI, “Low sensitivity of acoustic breathing mode frequency in Co nanocrystals upon change in nanocrystallinity”, *ACS Nano* **5**, 5785 (2011).
- [210] H. PORTALES, N. GOUBET, L. SAVIOT, S. ADICHTCHEV, D. B. MURRAY, A. MERMET, E. DUVAL AND M. P. PILENI, “Probing atomic ordering and multiple twinning in metal nanocrystals through their vibrations”, *Proc. Natl. Acad. Sci. U.S.A.* **105**, 14784 (2008).
- [211] J. H. HODAK, A. HENGLEIN AND G. V. HARTLAND, “Tuning the spectral and temporal response in PtAu core-shell nanoparticles”, *J. Chem. Phys.* **114**, 2760 (2001).
- [212] A. TLAHUICE-FLORES, “Normal modes of Au₂₅(SCH₃)₁₈- , Ag₁₂Au₁₃(SCH₃)₁₈- and Au₂₅(SCH₃)₁₈-clusters”, *Mol. Simul.* 1–4 (2013).
- [213] S.-K. PARK, K.-C. MIN, C. LEE, S. K. HONG, Y. KIM AND N.-S. LEE, “Intermolecular hydrogen bonding and vibrational analysis of N, N-dimethylformamide hexamer cluster”, *Bull. Korean Chem. Soc.* **30** (2009).
- [214] E. SWARTZ AND R. POHL, “Thermal boundary resistance”, *Rev. Mod. Phys.* **61**, 605 (1989).
- [215] D. G. CAHILL, W. K. FORD, K. E. GOODSON, G. D. MAHAN, A. MAJUMDAR, H. J. MARIS, R. MERLIN AND S. R. PHILLPOT, “Nanoscale thermal transport”, *J. Appl. Phys.* **93**, 793 (2003).
- [216] R. J. STONER AND H. J. MARIS, “Kapitza conductance and heat flow between solids at temperatures from 50 to 300 K”, *Phys. Rev. B* **48**, 16373 (1993).
- [217] O. WILSON, X. HU, D. G. CAHILL AND P. BRAUN, “Colloidal metal particles as probes of nanoscale thermal transport in fluids”, *Phys. Rev. B* **66**, 224301 (2002).

- [218] Z. GE, D. G. CAHILL AND P. V. BRAUN, “AuPd metal nanoparticles as probes of nanoscale thermal transport in aqueous solution”, *J. Phys. Chem. B* **108**, 18870 (2004).
- [219] Z. GE, Y. KANG, T. A. TATON, P. V. BRAUN AND D. G. CAHILL, “Thermal transport in Au-core polymer-shell nanoparticles”, *Nano Lett.* **5**, 531 (2005).
- [220] M. HU, X. WANG, G. V. HARTLAND, V. SALGUEIRIÑO MACEIRA AND L. M. LIZ-MARZÁN, “Heat dissipation in gold-silica core-shell nanoparticles”, *Chem. Phys. Lett.* **372**, 767 (2003).
- [221] H.-K. LYEON AND D. G. CAHILL, “Thermal conductance of interfaces between highly dissimilar materials”, *Phys. Rev. B* **73**, 144301 (2006).
- [222] A. J. SCHMIDT, J. D. ALPER, M. CHIESA, G. CHEN, S. K. DAS AND K. HAMAD-SCHIFFERLI, “Probing the gold nanorod-ligand-solvent interface by plasmonic absorption and thermal decay”, *J. Phys. Chem. C* **112**, 13320 (2008).
- [223] J. PARK, J. HUANG, W. WANG, C. J. MURPHY AND D. G. CAHILL, “Heat transport between Au nanorods, surrounding liquids, and solid supports”, *J. Phys. Chem. C* **116**, 26335 (2012).
- [224] J. HUANG, J. PARK, W. WANG, C. J. MURPHY AND D. G. CAHILL, “Ultrafast thermal analysis of surface functionalized gold nanorods in aqueous solution”, *ACS nano* **7**, 589 (2012).
- [225] Z. GE, D. G. CAHILL AND P. BRAUN, “Thermal conductance of hydrophilic and hydrophobic interfaces”, *Phys. Rev. Lett.* **96**, 186101 (2006).
- [226] A. PLECH, V. KOTAIDIS, S. GRÉSILLON, C. DAHMEN AND G. VON PLESSEN, “Laser-induced heating and melting of gold nanoparticles studied by time-resolved X-ray scattering”, *Phys. Rev. B* **70**, 195423 (2004).
- [227] R. J. STEVENS, A. N. SMITH AND P. M. NORRIS, “Measurement of thermal boundary conductance of a series of metal-dielectric interfaces by the transient thermorefectance technique”, *J. Heat Transfer* **127**, 315 (2005).
- [228] R. KATO AND I. HATTA, “Thermal conductivity and interfacial thermal resistance: measurements of thermally oxidized SiO₂ films on a silicon wafer using a thermorefectance technique”, *Int. J. Thermophys.* **29**, 2062 (2008).
- [229] Y.-S. CHEN, W. FREY, S. KIM, P. KRUIZINGA AND S. EMELIANOV, “Silica-coated gold nanorods as photoacoustic signal nano-amplifiers”, *Nano Lett.* **11**, 348 (2012).
- [230] Y.-S. CHEN, W. FREY, S. AGLYAMOV AND S. EMELIANOV, “Environment-dependent generation of photoacoustic waves from plasmonic nanoparticles”, *Small* **8**, 47 (2012).

Bibliography

- [231] A. PLECH, S. KÜRBITZ, K.-J. BERG, G. GRAENER, G. BERG, S. GRÉSILLON, M. KAEMPFE, J. FELDMANN, M. WULFF AND G. VON PLESSEN, “Time-resolved X-ray diffraction on laser-excited metal nanoparticles”, *Eur. Phys. Lett.* **61**, 762 (2003).
- [232] L. M. LIZ-MARZÁN, M. GIERSIG AND P. MULVANEY, “Synthesis of nanosized gold-silica core-shell particles”, *Langmuir* **12**, 4329 (1996).
- [233] E. G. DWIGHT, *American Institute of Physics Handbook*, New York, third edition (1972).
- [234] N. B. VARGAFTIK, *Handbook of physical properties of liquids and gases*, Hemisphere, New York (1975).
- [235] A. PLECH, V. KOTAIDIS, M. LORENC AND M. WULFF, “Thermal dynamics in laser excited metal nanoparticles”, *Chem. Phys. Lett.* **401**, 565 (2005).
- [236] H. S. CARLSLAW AND J. C. JAEGER, *Conduction of heat in solids*, Oxford University Press, Oxford (1959).
- [237] F. COOPER, “Heat transfer from a sphere to an infinite medium”, *Int. J. Heat Mass Transfer.* **20**, 991 (1977).
- [238] C. W. NAN, R. BIRRINGER, D. R. CLARKE AND H. GLEITNER, “Effective thermal conductivity of particulate composites with interfacial thermal resistance”, *J. Appl. Phys.* **81**, 6692 (1997).
- [239] G. SEIFERT, T. PATZLAFF AND H. GRAENER, “Size dependent ultrafast cooling of water droplets in microemulsions by picosecond infrared spectroscopy”, *Phys. Rev. Lett.* **88**, 147402 (2002).
- [240] K. SETOURA, D. WERNER AND S. HASHIMOTO, “Optical scattering spectral thermometry and refractometry of a single gold nanoparticle under CW laser excitation”, *J. Phys. Chem. C* **116**, 15458 (2012).
- [241] M. RASHIDI-HUYEH, M. SHIRDEL HAVAR AND B. PALPANT, “Thermo-optical properties of embedded silver nanoparticles”, *J. Appl. Phys.* **112**, 103101 (2012).
- [242] F. VALLÉE AND N. DEL FATTI, “Ultrafast nonlinear plasmonics”, in T. V. SHAHBAZIAN AND M. I. STOCKMAN (editors), “Plasmonics: Theory and Applications”, 167–205, SpringerLink (2013).
- [243] N. V. VOSHCHINNIKOV AND J. S. MATHIS, “Calculating cross sections of composite interstellar grains”, *Astrophys. J.* **526**, 257 (1999).
- [244] V. G. FARAFONOV AND M. V. SOKOLOVSKAJA, “Construction of the Rayleigh approximation for axysymmetric multilayered particles, making use of the eigenfunctions of the laplace operator”, *J. Math. Sci.* **194**, 104 (2013).
- [245] I. MALITSON, “Interspecimen comparison of the refractive index of fused silica”, *J. Opt. Soc. Am.* **55**, 1205 (1965).

- [246] M. DAIMON AND A. MASUMURA, “Measurement of the refractive index of distilled water from the near-infrared region to the ultraviolet region”, *Appl. Opt.* **46**, 3811 (2007).
- [247] J. RHEIMS, J. KÖSER AND T. WRIEDT, “Refractive-index measurements in the near-IR using an Abbe refractometer”, *Meas. Sci. Technol.* **8**, 601 (1997).
- [248] R. J. RIOBÓO, M. PHILIPP, M. A. RAMOS AND J. K. KRÜGER, “Concentration and temperature dependence of the refractive index of ethanol-water mixtures: influence of intermolecular interactions”, *Eur. Phys. J. E* **30**, 19 (2009).
- [249] A. VAN BLAADEREN AND A. KENTGENS, “Particle morphology and chemical microstructure of colloidal silica spheres made from alkoxyxilanes”, *J. Non-Cryst. Solids* **149**, 161 (1992).
- [250] F. BALAS, M. RODRÍGUEZ-DELGADO, C. OTERO-AREAN, F. CONDE, E. MATE-SANZ, L. ESQUIVIAS, J. RAMÍREZ-CASTELLANOS, J. GONZALEZ-CALBET AND M. VALLET-REGÍ, “Structural characterization of nanosized silica spheres”, *Solid State Sci.* **9**, 351 (2007).
- [251] G. H. BOGUSH, M. A. TRACY AND C. F. ZUKOSKY IV, “Preparation of monodisperse silica particles: control of size and mass fraction”, *J. Non-Cryst. Solids* **104**, 95 (1988).
- [252] A. LABROSSE AND A. BURNEAU, “Characterization of porosity of ammonia catalysed alkoxyxilane silica”, *J. Non-Cryst. Solids* **221**, 107 (1997).
- [253] Y. J. WONG, L. ZHU, W. S. TEO, Y. W. TAN, Y. YANG, C. WANG AND H. CHEN, “Revisiting the Stöber method : inhomogeneity in silica shells”, *J. Am. Chem. Soc.* **133**, 11422 (2011).
- [254] G. GESELE, J. LINSMEIER, V. DRACH, J. FRICKE AND R. ARENS-FISCHER, “Temperature-dependent thermal conductivity of porous silicon”, *J. Phys. D: Appl. Phys.* **30**, 2911 (1997).
- [255] J. V. GOICOCHEA, M. HU, B. MICHEL AND D. POULIKAKOS, “Surface functionalization mechanisms of enhancing heat transfer of solid-liquid interfaces”, *J. Heat Transfer* **133**, 082401 (2011).
- [256] M. HU, J. V. GOICOCHEA, B. MICHEL AND D. POULIKAKOS, “Thermal rectification of water/functionalized silica interfaces”, *Appl. Phys. Lett.* **95**, 151903 (2009).
- [257] X. CHEN, A. MUNJIZA, K. ZHANG AND D. WEN, “Molecular dynamics simulation of heat transfer from a gold nanoparticle to a water pool”, *J. Phys. Chem. C* **118**, 1285 (2013).
- [258] S. MERABIA, “Thermal boundary conductance across rough interfaces probed by molecular dynamics”, *Phys. Rev. B* **89**, 054309 (2014).
- [259] P. A. SCHOEN, B. MICHEL, A. CURIONI AND D. POULIKAKOS, “Hydrogen-bond enhanced thermal energy transport at functionalized, hydrophobic and hydrophilic silicawater interfaces”, *Chem. Phys. Lett.* **476**, 271 (2009).

Bibliography

- [260] K. S. VALLURU, B. K. CHINNI AND N. A. RAO, “Photoacoustic imaging: opening new frontiers in medical imaging”, *J. Clin. Imaging Sci.* **1**, 24 (2011).

Résumé: Nous avons étudié par spectroscopie pompe-sonde résolue en temps la réponse optique ultrarapide d'agrégats de très petite taille (< 2 nm), pour lesquelles une transition d'un comportement de type solide à un comportement moléculaire est attendue. Les modifications des processus de thermalisation interne (interactions électrons-électrons et électrons-phonons) avec la réduction de taille ont été étudiées dans des nanosphères d'argent triées en masse entourées de silice, et dans des échantillons d'or atomiquement définis stabilisés par des surfactants. Ces expériences ont mis en évidence les effets de confinement quantique des états électroniques sur la cinétique électronique. L'étude des vibrations acoustiques de nanoparticules dans le même régime de taille a été effectuée. Les vibrations observées dans les agrégats d'or sont dominées par leur mode de respiration radial avec une période proportionnelle à leur diamètre, en analogie avec les nanoparticules plus grandes. Le mode de respiration observé sur les nanoobjets bimétalliques de type cœur/couronne Pt-Au et Ni-Ag est en accord quantitatif avec les estimations du modèle élastique macroscopique, malgré une épaisseur de couronne monoatomique. La spectroscopie résolue en temps a également été utilisée pour étudier le transfert de chaleur à travers l'interface d'une nanoparticule sphérique. Dans ce but, l'évacuation de la chaleur dans des nanoparticules d'or, nues ou enrobées de silice, en solution colloïdale a été étudiée expérimentalement et modélisée de manière quantitative grâce à la prise en compte de la contribution de l'environnement (échauffement du solvant) au signal optique.

Abstract: We used ultrafast time-resolved pump-probe spectroscopy to experimentally investigate the optical response of small metal nano-objects in the few nanometer range (< 2 nm), where a transition from a small solid behaviour to a molecular one is expected. The modification of the intrinsic thermalization processes (electron-electron and electron-phonon interactions) has been studied both on glass-embedded mass-selected silver samples and chemically synthesized ligand-stabilized atomic-defined gold clusters. Electron gas internal thermalization and cooling with the lattice are shown to be affected by size reduction and the concomitant discretization of electronic states. The acoustic response in the same small size range has been investigated. Vibrations of gold clusters were characterized by a quasi-breathing mode scaling with their size, in analogy with larger nanoparticles. The breathing mode of bimetallic core/shell Pt-Au and Ni-Ag nanospheres appeared to be in good quantitative agreement with predictions of continuous elastic models, despite the monoatomic thickness of the layer shell. The same time-resolved approach was used to investigate heat transfer through the nanoparticles interfaces. In this context, heat evacuation of bare or silica-encapsulated gold nanospheres in solution was monitored, and the contribution of solvent heating to the optical signal was quantitatively reproduced, by the development of a precise model.